

**Bauhaus-Universität Weimar**

**Numerical Simulation Models for  
Thermoelastic Damping Effects**

Numerische Simulationsmodelle für thermoelastische  
Dämpfungseffekte

**Dissertation**

zur Erlangung des akademischen Grades  
Doktor-Ingenieur (Dr.-Ing.)

an der Fakultät Bauingenieurwesen  
der Bauhaus-Universität Weimar

vorgelegt von

**Christin Zacharias**

geboren am 05.04.1990 in Sangerhausen

Gutachter: Prof. Dr.-Ing. habil. Carsten Könke  
Prof. Dr.-Ing. habil. Raimund Rolfes  
Prof. Dr.-Ing. Christian Guist

Tag der Disputation: 05.10.2022



# Vorwort

Die vorliegende Promotionsschrift entstand während meiner Tätigkeit als wissenschaftliche Mitarbeiterin am Institut für Strukturmechanik der Bauhaus-Universität Weimar. Während dieser Zeit habe ich sowohl beruflich als auch privat in vielfacher Hinsicht Unterstützung erfahren, für die ich mich an dieser Stelle herzlich bedanken möchte.

Mein besonderer Dank gilt Professor Carsten Könke für die wissenschaftliche Betreuung und Unterstützung. Neben den konstruktiven fachlichen Diskussionen, ohne die ein Gelingen der Arbeit nicht möglich gewesen wäre, weiß ich insbesondere die Möglichkeiten und Freiheiten sehr zu schätzen, die mir die Arbeit am Lehrstuhl geboten hat.

Ich möchte mich herzlich bei Professor Raimund Rolfes für das Interesse an meiner Arbeit und die Begutachtung der Dissertation bedanken.

Besonders bedanken möchte ich mich bei Professor Christian Guist für die intensive Begleitung des Vorhabens über die letzten Jahre. In zahlreichen Gesprächen hat er sowohl bedeutende inhaltliche Impulse eingebracht als auch stets den Blick aus der Praxis bewahrt und damit die Motivation und Ausrichtung der Arbeit geprägt. Dieser fachliche Rahmen war eine wertvolle Unterstützung bei der Entstehung dieser Promotionsschrift.

Teile der in dieser Arbeit verwendeten CAD-Daten wurden mir freundlicherweise von der BMW Group zur Verfügung gestellt, wofür ich mich ausdrücklich bedanken möchte.

Des Weiteren möchte ich mich herzlich bei meinen Kolleg\*innen am ISM und der MFPA Weimar bedanken, die mir sowohl fachlich als auch persönliche eine unermessliche Unterstützung waren. Die freundschaftliche Arbeitsatmosphäre lässt mich die vergangenen Jahre in bester Erinnerung behalten.

Von ganzem Herzen möchte ich meiner Familie und meinen Freund\*innen für die Geduld, Rücksichtnahme und Motivation während der letzten Jahre danken. Insbesondere meine Mutter hat mich über viele Jahre in allen Lebenslagen unterstützt, gefördert und mir durch ihren unerschütterlichen Glauben in meine Fähigkeiten die Sicherheit gegeben, diesen Weg zu gehen.

Ganz besonders möchte ich mich bei meinem Partner Stefan für den großen Rückhalt, das Verständnis und die Zuversicht bedanken, die für die Vollendung dieser Arbeit unerlässlich waren.

Weimar, April 2022

Christin Zacharias



# Abstract

Finite Element Simulations of dynamically excited structures are mainly influenced by the mass, stiffness, and damping properties of the system, as well as external loads. The prediction quality of dynamic simulations of vibration-sensitive components depends significantly on the use of appropriate damping models. Damping phenomena have a decisive influence on the vibration amplitude and the frequencies of the vibrating structure. However, developing realistic damping models is challenging due to the multiple sources that cause energy dissipation, such as material damping, different types of friction, or various interactions with the environment. This thesis focuses on thermoelastic damping, which is the main cause of material damping in homogeneous materials. The effect is caused by temperature changes due to mechanical strains. In vibrating structures, temperature gradients arise in adjacent tension and compression areas. Depending on the vibration frequency, they result in heat flows, leading to increased entropy and the irreversible transformation of mechanical energy into thermal energy.

The central objective of this thesis is the development of efficient simulation methods to incorporate thermoelastic damping in finite element analyses based on modal superposition. The thermoelastic loss factor is derived from the structure's mechanical mode shapes and eigenfrequencies. In subsequent analyses that are performed in the time and frequency domain, it is applied as modal damping.

Two approaches are developed to determine the thermoelastic loss in thin-walled plate structures, as well as three-dimensional solid structures. The realistic representation of the dissipation effects is verified by comparing the simulation results with experimentally determined data. Therefore, an experimental setup is developed to measure material damping, excluding other sources of energy dissipation. The three-dimensional solid approach is based on the determination of the generated entropy and therefore the generated heat per vibration cycle, which is a measure for thermoelastic loss in relation to the total strain energy. For thin plate structures, the amount of bending energy in a modal deformation is calculated and summarized in the so-called Modal Bending Factor (MBF). The highest amount of thermoelastic loss occurs in the state of pure bending. Therefore, the MBF enables a quantitative classification of the mode shapes concerning the thermoelastic damping potential. The results of the developed simulations are in good agreement with the experimental results and are appropriate to predict thermoelastic loss factors. Both approaches are based on modal superposition with the advantage of a high computational efficiency. Overall, the modeling of thermoelastic damping represents an important component in a comprehensive damping model, which is necessary to perform realistic simulations of vibration processes.



# Kurzfassung

Die Finite-Elemente Simulation von dynamisch angeregten Strukturen wird im Wesentlichen durch die Steifigkeits-, Massen- und Dämpfungseigenschaften des Systems sowie durch die äußere Belastung bestimmt. Die Vorhersagequalität von dynamischen Simulationen schwingungsanfälliger Bauteile hängt wesentlich von der Verwendung geeigneter Dämpfungsmodelle ab.

Dämpfungsphänomene haben einen wesentlichen Einfluss auf die Schwingungsamplitude, die Frequenz und teilweise sogar die Existenz von Vibrationen. Allerdings ist die Entwicklung von realitätsnahen Dämpfungsmodellen oft schwierig, da eine Vielzahl von physikalischen Effekten zur Energiedissipation während eines Schwingungsvorgangs führt. Beispiele hierfür sind die Materialdämpfung, verschiedene Formen der Reibung sowie vielfältige Wechselwirkungen mit dem umgebenden Medium. Diese Dissertation befasst sich mit thermoelastischer Dämpfung, die in homogenen Materialien die dominante Ursache der Materialdämpfung darstellt. Der thermoelastische Effekt wird ausgelöst durch eine Temperaturänderung aufgrund mechanischer Spannungen. In der schwingenden Struktur entstehen während der Deformation Temperaturgradienten zwischen benachbarten Regionen unter Zug- und Druckbelastung. In Abhängigkeit von der Vibrationsfrequenz führen diese zu Wärmeströmen und irreversibler Umwandlung mechanischer in thermische Energie.

Die Zielstellung dieser Arbeit besteht in der Entwicklung recheneffizienter Simulationsmethoden, um thermoelastische Dämpfung in zeitabhängigen Finite-Elemente Analysen, die auf modaler Superposition beruhen, zu integrieren. Der thermoelastische Verlustfaktor wird auf der Grundlage der mechanischen Eigenformen und -frequenzen bestimmt. In nachfolgenden Analysen im Zeit- und Frequenzbereich wird er als modaler Dämpfungsgrad verwendet.

Zwei Ansätze werden entwickelt, um den thermoelastischen Verlustfaktor in dünnwandigen Plattenstrukturen, sowie in dreidimensionalen Volumenbauteilen zu simulieren. Die realitätsnahe Vorhersage der Energiedissipation wird durch die Verifizierung an experimentellen Daten bestätigt. Dafür wird ein Versuchsaufbau entwickelt, der eine Messung von Materialdämpfung unter Ausschluss anderer Dissipationsquellen ermöglicht.

Für den Fall der Volumenbauteile wird ein Ansatz verwendet, der auf der Berechnung der Entropieänderung und damit der erzeugte Wärmeenergie während eines Schwingungszyklus beruht. Im Verhältnis zur Formänderungsenergie ist dies ein Maß für die thermoelastische Dämpfung. Für dünne Plattenstrukturen wird der Anteil an Biegeenergie in der Eigenform bestimmt und im sogenannten modalen Biegefaktor (MBF) zusammengefasst. Der maximale Grad an thermoelastischer Dämpfung kann im Zustand reiner Biegung auftreten, sodass der MBF eine quantitative Klassifikation der Eigenformen hinsichtlich ihres thermoelastischen Dämpfungspotentials zulässt.

---

Die Ergebnisse der entwickelten Simulationsmethoden stimmen sehr gut mit den experimentellen Daten überein und sind geeignet, um thermoelastische Dämpfungsgrade vorherzusagen. Beide Ansätze basieren auf modaler Superposition und ermöglichen damit zeitabhängige Simulationen mit einer hohen Recheneffizienz. Insgesamt stellt die Modellierung der thermoelastischen Dämpfung einen Baustein in einem umfassenden Dämpfungsmodell dar, welches zur realitätsnahen Simulation von Schwingungsvorgängen notwendig ist.

# Contents

<b>List of Figures</b>	<b>xi</b>
<b>List of Tables</b>	<b>xv</b>
<b>Notation</b>	<b>xvii</b>
<b>1 Introduction</b>	<b>1</b>
1.1 Motivation . . . . .	1
1.2 Objectives and Methods . . . . .	3
1.3 Structure of the Thesis . . . . .	4
<b>2 Physics and Mechanical Models of Damping</b>	<b>7</b>
2.1 Introduction . . . . .	7
2.2 Sources of Vibration Damping . . . . .	8
2.2.1 Physical Material Effects . . . . .	8
2.2.1.1 Point Defects . . . . .	9
2.2.1.2 Grain Boundaries . . . . .	10
2.2.1.3 Thermoelasticity on Microscopic and Macroscopic Scale . . . . .	10
2.2.1.4 Empirical Values for Material Damping . . . . .	11
2.2.2 Friction . . . . .	11
2.2.3 Air and Radiation Damping . . . . .	12
2.3 Mechanical Damping Models . . . . .	13
2.3.1 Viscous Damping . . . . .	14
2.3.2 Hysteretic Damping . . . . .	18
2.3.3 Coloumb Friction . . . . .	19
2.3.4 Modal Damping . . . . .	20
2.3.5 Rayleigh Damping . . . . .	23
<b>3 Thermoelasticity and Thermoelastic Damping</b>	<b>25</b>
3.1 Introduction . . . . .	25
3.2 Fundamentals of Thermoelasticity . . . . .	25
3.2.1 Basic Equations for Linear Thermoelastic Coupling . . . . .	25
3.2.2 Differential Equations of Thermoelastic Coupling . . . . .	28
3.3 Thermoelastic Damping . . . . .	29
3.3.1 Rate of Dissipated Energy . . . . .	33
3.3.2 Rate of Generated Heat . . . . .	38
3.3.3 Thermoelastic Damping in Plate Structures . . . . .	42

---

3.4	Thermoelastic Coupling in Finite Element Analysis . . . . .	45
3.4.1	Elastic Solid Element . . . . .	46
3.4.2	Thermoelastic Solid Element . . . . .	49
3.4.3	Finite Element Analysis of Dynamically Excited Systems . . .	51
3.4.3.1	Time Domain . . . . .	52
3.4.3.2	Frequency Domain . . . . .	53
3.4.3.3	Mode Superposition . . . . .	54
3.5	Summary and Research Questions . . . . .	55
<b>4</b>	<b>Experimental studies</b>	<b>59</b>
4.1	Introduction . . . . .	59
4.2	Experimental Samples . . . . .	59
4.2.1	Material . . . . .	59
4.2.2	Rectangular Plate . . . . .	60
4.2.3	Protection Plate . . . . .	61
4.2.4	Gearbox Casing . . . . .	63
4.3	Measurement of Damping using Decay Experiments . . . . .	64
4.3.1	Approaches in the literature . . . . .	64
4.3.2	Suspension and Excitation . . . . .	66
4.3.3	Measurement . . . . .	69
4.3.4	Analysis . . . . .	70
4.3.4.1	Fast Fourier Transformation . . . . .	70
4.3.4.2	Filters in Signal Processing . . . . .	73
4.3.4.3	Exponential Fit . . . . .	74
4.4	Results . . . . .	75
4.4.1	Dependence on the Amplitude . . . . .	75
4.4.2	Dependence on the Air Pressure . . . . .	76
4.4.3	Damping Ratios in Vacuum and under Atmospheric Pressure .	78
4.4.3.1	Rectangular Plate . . . . .	78
4.4.3.2	Protection Plate . . . . .	80
4.4.3.3	Gearbox Casing . . . . .	82
4.5	Summary and Discussion . . . . .	85
<b>5</b>	<b>Thermoelastic damping based on generated heat</b>	<b>87</b>
5.1	Introduction . . . . .	87
5.2	Theoretical Background - Thermoelastic Heat Generation . . . . .	88
5.3	Method . . . . .	91
5.4	Results . . . . .	94
5.4.1	Beam Structure . . . . .	94
5.4.2	Plate Structure . . . . .	99
5.4.2.1	Numerical Model . . . . .	99
5.4.2.2	Generated Heat . . . . .	99
5.4.2.3	Comparison with Experimental Data . . . . .	100
5.4.2.4	Effect of the Damping Ratio on the Stresses in the Component . . . . .	104
5.4.2.5	Comparison with Fully Coupled Simulation . . . . .	106
5.4.3	Gearbox Casing . . . . .	107
5.4.3.1	Numerical Model . . . . .	107

---

---

5.4.3.2	Generated Heat . . . . .	107
5.4.3.3	Comparison with Experiments . . . . .	109
5.4.3.4	Effect of the Damping Ratio on the Stresses in the Component . . . . .	110
5.4.3.5	Comparison with Fully Coupled Simulation . . . . .	112
5.5	Discussion . . . . .	114
<b>6</b>	<b>Thermoelastic damping based on modal bending energy</b>	<b>117</b>
6.1	Introduction . . . . .	117
6.2	Fundamentals of Plate Theories and Shell Models . . . . .	118
6.2.1	Plate theory . . . . .	118
6.2.2	Shell Elements . . . . .	121
6.3	Method - Derivation and Implementation . . . . .	123
6.4	Results . . . . .	127
6.4.1	Rectangular Plate . . . . .	127
6.4.1.1	Numerical Model . . . . .	127
6.4.1.2	Modal Bending Factor . . . . .	127
6.4.1.3	Comparison of the MBF Approach with Experiments	129
6.4.1.4	Comparison of the MBF Approach with the Entropy Approach . . . . .	130
6.4.2	Protection Plate . . . . .	132
6.4.2.1	Numerical Model . . . . .	132
6.4.2.2	Modal Bending Factor . . . . .	133
6.4.2.3	Comparison of the MBF Simulation with Experiments	133
6.4.2.4	Comparison of the MBF Simulation with a Fully Thermoelastically Coupled Simulation . . . . .	135
6.4.3	Application on a Literature Example . . . . .	137
6.5	Summary and Discussion . . . . .	140
<b>7</b>	<b>Conclusion and Outlook</b>	<b>143</b>
7.1	Summary and Conclusion . . . . .	143
7.2	Outlook . . . . .	147
	<b>Bibliography</b>	<b>148</b>
	<b>A Measurement and Excitation Schemes of the Components</b>	<b>163</b>
A.1	Rectangular Plate . . . . .	164
A.2	Protection Plate . . . . .	165
A.3	Gearbox Casing . . . . .	166
	<b>Publications by the Author</b>	<b>166</b>



# List of Figures

1.1	Examples of vibration-sensitive structures . . . . .	2
1.2	Finite element computational process based on modal superposition . . . . .	4
2.1	Classification of damping phenomena . . . . .	8
2.2	Relaxation spectrum according to Lazan [14] . . . . .	9
2.3	Point defects in lattice structure . . . . .	10
2.4	Typical hysteresis loop for dry friction according to [29] . . . . .	12
2.5	Under-critically, over-critically and critically damped decay curves . . . . .	15
2.6	Decay curve of a viscously damped free vibration . . . . .	15
2.7	Hysteresis loop of a viscously damped system . . . . .	17
2.8	Free vibration with friction damping . . . . .	20
2.9	Hysteresis loop of a system with friction damping . . . . .	20
2.10	Rayleigh damping . . . . .	24
3.1	Relationship between stresses in the beam during vibration, distribution of temperature changes and dissipated energy. . . . .	31
3.2	Mechanism of thermoelastic damping . . . . .	32
3.3	Relationship between the loss factor and the relevant natural frequency relative to the appropriate thermal relaxation time . . . . .	32
4.1	Rectangular aluminium plate . . . . .	60
4.2	Photo of the protection plate . . . . .	62
4.3	Position of the protection plate (red) in the rear axle of an automobile [137] . . . . .	62
4.4	Component designed for the experiments, inspired by a gearbox casing . . . . .	63
4.5	Gearbox casing suspended in the vacuum chamber . . . . .	63
4.6	Thermoelastic damping in copper wires . . . . .	65
4.7	Flow chart for the determination of the modal experimental setup . . . . .	67
4.8	Measurement and excitation schemes for the first three eigenmodes of the investigated components . . . . .	68
4.9	Automatic impulse hammer . . . . .	68
4.10	Automatic impulse hammer installed in the vacuum chamber . . . . .	68
4.11	Frequency spectrum for a measurement of the rectangular aluminum plate according to the experimental scheme for the first mode shape. . . . .	69
4.12	Frequency spectrum for a measurement of the rectangular aluminum plate according to the experimental scheme for the second mode shape. . . . .	69
4.13	Processing scheme of the recorded signal . . . . .	71
4.14	Pass-band and stop-band ranges for different filtering classes . . . . .	73
4.15	Filter tolerance scheme . . . . .	74

---

4.16	Exponential fit of the decay curve . . . . .	75
4.17	Damping ratio as a function of excitation amplitude for the rectangular plate . . . . .	76
4.18	Damping ratio as a function of excitation amplitude for the protection plate . . . . .	76
4.19	Damping ratio as a function of air pressure for the rectangular plate .	77
4.20	Damping ratio as a function of air pressure for the protection plate .	77
4.21	Experimental results rectangular plate . . . . .	79
4.22	Experimental results protection plate . . . . .	81
4.23	Experimental results for the gearbox casing . . . . .	84
4.24	Experimental results for the gearbox casing in the vacuum . . . . .	84
5.1	Flow chart for numerical solution procedure of entropy based loss factor	91
5.2	Displacement, stress, temperature variation and generated heat due to thermoelastic coupling in a beam structure . . . . .	96
5.3	Thermoelastic damping in beam structures . . . . .	97
5.4	Peak frequencies of loss factor curves as well as corresponding eigenvectors of the heat equation . . . . .	98
5.5	Mode shapes and energy transformation of plate structure . . . . .	100
5.6	Comparison of simulated and experimentally determined damping ratios	101
5.7	Comparison of experiment and simulation (entropy approach) in time and frequency domain . . . . .	102
5.8	Von Mises stress in harmonically excited rectangular aluminum plate model . . . . .	105
5.9	Comparison of entropy approach with fully coupled simulation - plate structure . . . . .	107
5.10	Discretization of the gearbox casing with hexahedron and tetrahedron solid elements. The elements C3D20 and C3D10 in ABAQUS use quadratic interpolation functions and have three Degree of Freedom (DOF) per node. . . . .	108
5.11	Mode shapes, hydrostatic stress and dissipated energy in gearbox casing	108
5.12	Comparison of the simulated and experimentally determined damping ratios - gearbox casing . . . . .	110
5.13	Von Mises stress in the harmonically excited aluminum gearbox casing	111
5.14	Comparison of entropy approach with fully coupled simulation - gearbox casing structure . . . . .	113
5.15	Comparison of nodal displace - model with modal damping and fully coupled model . . . . .	114
5.16	Excitation and measurement point for fully coupled simulation . . . .	114
6.1	Four-node shell element . . . . .	122
6.2	Flow chart for determination of the loss factor using the modal bending factor . . . . .	126
6.3	Shell model of the rectangular plate structure . . . . .	127
6.4	Displacement, strain and modal bending factor of the rectangular plate	128
6.5	Mode shapes and modal bending factor of rectangular plate . . . . .	129
6.6	Overview of the modal bending factors (MBF) of the eigenmodes considered in experiment and simulation for the rectangular plate. . .	131

---

6.7	Comparison of the simulated and experimentally determined damping ratios for the rectangular plate structure . . . . .	131
6.8	Comparison of modal bending factor and generated heat calculated by the entropy approach in the plate structure . . . . .	132
6.9	Shell model of the protection plate. For the numerical analysis, a model with 80 722 elements and an approximate edge length of approximately 1 mm is used. The shell thickness is set to 1 mm. . . . .	133
6.10	Displacement, strain and modal bending factor of the protection plate	134
6.11	Mode shapes and modal bending factor of the protection plate . . . . .	134
6.12	Comparison of the MBF simulation results for the protective plate with experimental results . . . . .	135
6.13	Excitation point of force F in the full thermoelastically coupled simulation of the protection plate. . . . .	136
6.14	Comparison of the MBF simulation of the protective plate with the fully thermoelastically coupled simulation in ANSYS . . . . .	137
6.15	Mode shapes and modal bending factor of a circular disc . . . . .	139
6.16	Comparison of MBF simulation of circular disc with experimental results of Cagnoli et al. [122] . . . . .	140
7.1	Flow chart for numerical solution procedure . . . . .	144
A.1	Measurement and excitation schemes for the eigenmodes of the rectangular plate . . . . .	164
A.2	Measurement and excitation schemes for the eigenmodes of the protection plate . . . . .	165
A.3	Measurement and excitation schemes for the eigenmodes of the gearbox casing . . . . .	166



# List of Tables

2.1	Empirical values for the material damping ratio of aluminium in the literature . . . . .	11
4.1	Material parameters of aluminium alloy AlMg4.5Mn0.7 [136] . . . . .	60
4.2	Eigenfrequencies and mode shapes of the rectangular plate . . . . .	61
4.3	Eigenfrequencies and mode shapes of the protection plate . . . . .	62
4.4	Eigenfrequencies and mode shapes of the gearbox casing . . . . .	64
4.5	Air damping in rectangular plate . . . . .	80
4.6	Air damping in protection plate . . . . .	82
4.7	Air damping in protection plate . . . . .	83
5.1	Element sizes of beam models . . . . .	95
5.2	Comparison of simulated and experimentally determined damping ratios	101
5.3	Computing time for a frequency-domain analysis using a direct solution procedure with fully coupled thermoelastic elements and a mode superposition solution procedure with modal damping . . . . .	115
6.1	Comparison of simulated and experimentally determined damping ratios	130
6.2	Material parameters of brass alloy with 64% Cu and 36% Zn [176] . .	138
6.3	Computing time in CPU seconds for the calculation of the damping ratios of the rectangular aluminum plate using the Modal Bending Factor (MBF) approach in comparison to the entropy approach . . .	141
6.4	Computing times in CPU seconds for a harmonic analysis of the protection plate using the MBF approach and mode superposition compared with a fully thermoelastically coupled harmonic analysis . . . .	141



# Notation

---

## Capital latin letters

---

$A$	area
$\mathbf{B}_e$	strain-displacement matrix
$\mathbf{B}_{th}$	matrix including derivatives of thermal shape functions
$\mathbf{C}$	damping matrix
$\tilde{\mathbf{C}}$	generalized damping matrix
$\mathbf{C}_{th}$	damping matrix, thermal
$\mathbf{C}_{th,e}$	damping matrix, elastic
$D$	bending stiffness of a plate
$E$	Young's modulus
$E_d$	total strain energy
$\mathbf{E}, E_{ijkl}$	elastic stiffness tensor
$E_S$	total strain energy
$\hat{F}$	maximal amplitude of force
$F_D$	damping force
$F$	force
$F_F$	Coulomb friction force
$F_H$	Helmholtz free energy
$F_N$	normal force
$F_S$	stiffness force
$G$	shear modulus
$G_f$	frequency response of a filter function (gain)
$H$	strength of inner heat source
$I$	second moment of area
$\mathbf{I}$	identity matrix
$I_T$	thermal moment

---

$\mathbf{K}$	stiffness matrix
$\mathbf{K}_c$	complex stiffness matrix
$\mathbf{K}_e$	elastic stiffness matrix
$\mathbf{K}_{e,th}$	thermoelastic stiffness matrix
$\tilde{\mathbf{K}}$	generalized stiffness matrix
$\mathbf{K}_{th}$	thermoelastic stiffness matrix
$L$	right-hand side of weak form PDE
$M$	bending moment
$\mathbf{M}$	mass matrix
$M_e$	elastic bending moment
$\tilde{\mathbf{M}}$	generalized mass matrix
$M_t$	thermal bending moment
$N$	number of samples in a block
$\mathbf{N}_e$	matrix of shape functions for displacement DOF
$N_i$	shape function
$\mathbf{N}_{th}$	matrix of shape functions for temperature DOF
$P_R$	power of radiated sound
$Q_d$	quality factor
$Q$	generated heat
$S$	entropy
$S_e$	external entropy
$S_p$	internal entropy production
$T$	absolute temperature
$T_0$	temperature in reference state
$V$	volume
$W^{def}$	work of deformation
$W_D$	total dilation energy
$X$	Fourier transform

---

### Small latin letters

---

$s_p$	specific internal entropy production
$a$	left-hand side weak form PDE
$\mathbf{b}, b_i$	vector of body forces
$\mathbf{b}_e$	elastic forces

---

$\mathbf{b}_m$	modal forces
$b$	body forces
$\mathbf{b}_{th}$	thermal forces
$c$	viscous damping
$c_{crit}$	critical damping
$c_i$	diagonal entry of the generalized damping matrix
$c_n$	Fourier coefficient
$c_S$	speed of sound
$c_V$	heat capacity at constant volume
$d$	width of a beam
$\mathbf{d}, d_{ij}$	rate of deformation tensor
$f_D$	frequency shift in laser Doppler vibrometry
$f$	frequency
$g$	hysteretic damping coefficient
$h$	thickness of a beam
$k$	stiffness
$k_0$	stiffness of the elastic stick deformation
$k^*$	complex stiffness
$k_i$	diagonal entry of the generalized stiffness matrix
$k_s$	stiffness of the deformation in macro-slip
$l$	length of a beam
$l_1, l_2$	length and width of a plate
$m$	mass
$m_i$	diagonal entry of the generalized mass matrix
$n$	number of nodes
$n$	number of samples
$\mathbf{n}$	normal vector
$n_p$	number of particles
$p$	number of spectral lines
$\mathbf{q}, q_i$	heat flux
$r$	strength of heat source per unit mass
$s$	specific entropy
$s_e$	specific external entropy
$\mathbf{t}, t_i$	surface tension

---

---

$u$	displacement
$\mathbf{u}, u_i$	displacement vector
$u_0$	initial displacement
$u_F$	static deformation due to $F_F$
$\hat{u}$	amplitude of displacement
$\mathbf{v}, v_i$	nodal displacement vector
$\tilde{v}$	surface velocity, spatially averaged
$v$	displacement
$w$	deflection of a plate
$\mathbf{x}$	vector of coordinates
$\mathbf{y}, y_i$	modal displacement vector

---

## Capital greek letters

---

$\Gamma$	surface
$\Gamma_{el}$	surface with mechanical boundary conditions
$\Gamma_{th}$	surface with thermal boundary conditions
$\Delta t$	time step
$\Lambda$	logarithmic decrement
$\Phi$	matrix of eigenvectors
$\Psi$	internal energy
$\Omega$	excitation frequency
$\Omega^2$	matrix of eigenvalues
$\Omega$	circular excitation frequency

---

## Small greek letters

---

$\alpha_H$	integration parameter HHT-method
$\alpha$	coefficient of thermal expansion
$\alpha_R$	Rayleigh coefficient for mass proportional damping
$\boldsymbol{\beta}, \beta_{ij}$	matrix of thermoelastic coupling coefficients
$\beta$	thermoelastic coupling coefficient
$\beta_N$	Newmark integration parameter
$\beta_R$	Rayleigh coefficient for stiffness proportional damping

---

$\gamma$	shear strain
$\gamma_j$	$j^{\text{th}}$ eigensolution of heat equation (thermal mode)
$\gamma_N$	Newmark integration parameter
$\delta_{ij}$	Kronecker delta
$\boldsymbol{\varepsilon}, \varepsilon_{ij}$	strain tensor
$\varepsilon_{ij}$	component of the strain tensor
$\varepsilon$	strain
$\zeta$	damping ratio
$\zeta_l$	lower damping ratio
$\zeta_i$	damping ratio of mode shape i
$\zeta_m$	modal damping ratio
$\zeta_u$	upper damping ratio
$\eta$	thermoelastic loss factor
$\eta_B$	thermoelastic loss factor for pure bending
$\eta_{Pl}$	thermoelastic loss factor for a plate
$\theta$	temperature increment above reference
$\boldsymbol{\theta}$	vector of nodal temperatures
$\kappa$	thermal conductivity
$\lambda$	Lamé constant
$\lambda_e$	eigenvalue of equation of motion
$\lambda_w$	wavelength of laser beam
$\mu$	Lamé constant
$\mu_B$	modal bending factor
$\mu_F$	coefficient of friction
$\mu_R$	radiation efficiency
$\nu$	Poisson's ratio
$\rho$	density
$\boldsymbol{\sigma}, \sigma_{ij}$	stress tensor
$\sigma$	stress
$\tau$	period length of the undamped vibration
$\tau_D$	period length of the damped vibration
$\tau_F$	sampling interval in the DFT
$\tau_i$	relaxation time
$\varphi_j$	$j^{\text{th}}$ eigenvector of heat equation

---

$\varphi$	phase shift
$\varphi_0$	phase angle at $t = 0$
$\Phi$	eigenvector
$\phi_x, \phi_y, \phi_z$	rotation angles in plates
$\psi$	specific internal energy
$\chi$	thermal diffusivity
$\omega_{th}$	thermal eigenfrequency
$\omega$	circular frequency
$\omega_0$	circular eigenfrequency
$\omega_c$	cut-off frequency of a filter
$\omega_{cl}$	low cut-off frequency of a filter
$\omega_{ch}$	high cut-off frequency of a filter
$\omega_D$	circular eigenfrequency of damped system
$\omega_m$	medium frequency of a filter

## Abbreviations

<b>BEM</b>	Boundary Element Method
<b>CAD</b>	Computer Aided Design
<b>DFT</b>	Discrete Fourier Transformation
<b>DOF</b>	Degree of Freedom
<b>EOM</b>	Equation of Motion
<b>FDM</b>	Finite Difference Method
<b>FE</b>	Finite Element
<b>FEM</b>	Finite Element Method
<b>FFT</b>	Fast Fourier Transformation
<b>IDFT</b>	Inverse Discrete Fourier Transformation
<b>IFFT</b>	Inverse Fast Fourier Transformation
<b>LDV</b>	Laser-Doppler Vibrometer
<b>MBF</b>	Modal Bending Factor
<b>MDOF</b>	Multi-Degree-Of-Freedom System
<b>SDOF</b>	Single-Degree-Of-Freedom System
<b>TED</b>	Thermoelastic Damping

# Chapter 1

## Introduction

### 1.1 Motivation

The simulation of dynamically excited systems is of exceptional significance in nearly every engineering discipline. In the context of digitalization, creating virtual models in the development process is becoming increasingly important. Therefore, the dynamical behavior of structures in all operating states should be predicted realistically and monitored by digital models from the planning stage throughout the service life.

For vibration-sensitive components, the correct prediction of the vibrational behavior relying on virtual models without calibration on a physical object is challenging. A decisive factor is the realistic assumption of damping. Damping phenomena have a considerable effect on the vibration amplitude, time history, or even the existence of vibrations. The integration of realistic damping models is indispensable for accurate Finite Element (FE) analyses and, therefore, the design and optimization of dynamically excited structures. Typical fields of application are machine- and structural dynamics, system dynamics, or technical acoustics [1]. Examples of vibration-sensitive structures from various engineering disciplines are shown in Figure 1.1. Undesired and especially unpredictable vibrations can cause a large variety of problems. Whereas the stability of the structure is at risk in civil engineering, in mechanical or automotive engineering, problems often arise in acoustics or fatigue strength. In micro- and nanomechanics, oscillators perform desired vibrations, and high damping ratios cause restrictions in the functionality.

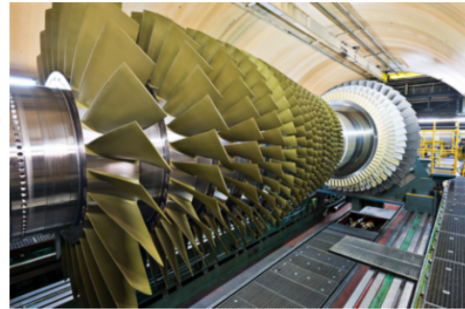
The development of appropriate damping models is complex because vibration damping is based on various physical effects. Energy dissipation in mechanical vibrations can arise, for example, through friction processes at contacts or within the component. Besides this internal friction, other physical phenomena that cause

energy dissipation occur within the material, e. g. thermoelastic or electromagnetic effects. In the interaction with the environment, radiation damping or friction against the surrounding medium can occur [2].

Simplified mechanical models are used in most applications, such as viscous damping or Rayleigh damping. These are based on damping characteristics that summarize all sources of energy dissipation. This global use of empirically determined data from literature or experience often leads to inaccuracies in the result. The alternative is extensive experimental investigation before simulation, which contradicts the essential idea of the digital development process. Therefore, there is a demand to develop damping models that both guarantee a realistic representation of the vibration behavior of components and are practicable to integrate into existing simulation procedures. In order to enable a quantitative prediction of vibrations, the various sources of damping should be taken under consideration.



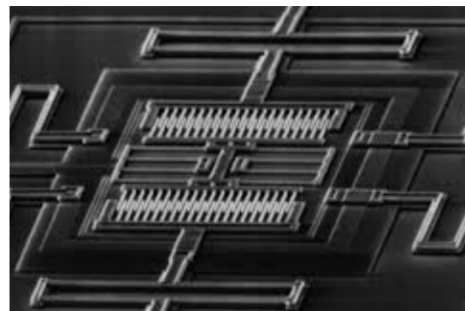
(a) Electric motor [3]



(b) Gas turbine [4]



(c) Millenium Bridge, London [5]



(d) Micro resonator [6]

**Figure 1.1:** Examples of vibration-sensitive structures. In the field of civil engineering, undesired vibrations caused by wind or traffic typically affect the stability and serviceability of structures. Besides fatigue strength, noise emissions are particularly undesired effects of vibrations in mechanical or automotive engineering. Concerning micro- and nanomechanics, damping control impacts the quality factor of oscillators.

## 1.2 Objectives and Methods

This work focuses on the modeling of material damping in metals and thus provides a component for developing a comprehensive damping model. The considered physical effect is thermoelasticity, i. e. the coupling of the temperature field with the elastic field. It has been almost a century since Clarence Zener defined Thermoelastic Damping (TED) in his pioneering work [7]. The author developed a formula for the use on thin beams, which is still the basis for numerous other studies until today. In addition, he proved experimentally that in metals, the material damping can be determined precisely with his calculation and that thermoelasticity is thus the dominant contribution to material damping [8].

Since then, intensive research has been conducted to develop analytical and numerical models to include TED in dynamical calculations. However, the analytical models are often limited to simple geometries, such as beams, rings, rectangular plates or circular discs. Numerical FE models, such as those proposed by Serra et al. [9], usually use full thermoelastically coupled system matrices, resulting in computationally expensive simulations. Moreover, the publications of the last few years have been predominantly focused on micro- and nanostructures since thermoelasticity is the dominant energy loss on the micro-scale [10].

In assembled macrostructures, such as automotive components, friction in joints is usually the dominant source for energy loss. However, it can be shown that e.g. the acoustics of thin plates are strongly influenced by TED [11]. In addition, material damping represents an essential part modeling of the complete damping behavior. Therefore, two approaches are provided in this work that enable an effective calculation of TED in metallic macro structures.

Both methods can be included easily in the FE simulation process. They are based on the calculation of modal damping ratios from the eigenmodes of a structure. The role of modal damping in the practical calculation process based on modal superposition is illustrated in 1.2. Modal superposition is widely used in FE analyses in the time and frequency domain for linear simulations since the procedure is much less computationally expensive than direct solvers. Modal damping provides a damping ratio for each underlying mode shape.

The calculation of the modal damping ratios is preceded by a structural modal analysis. Dependent on the type of the structural model (two- or three-dimensional) follows the determination of the thermoelastic loss factors, which is a measure for the damping of the structure and can easily be converted into a damping ratio. These

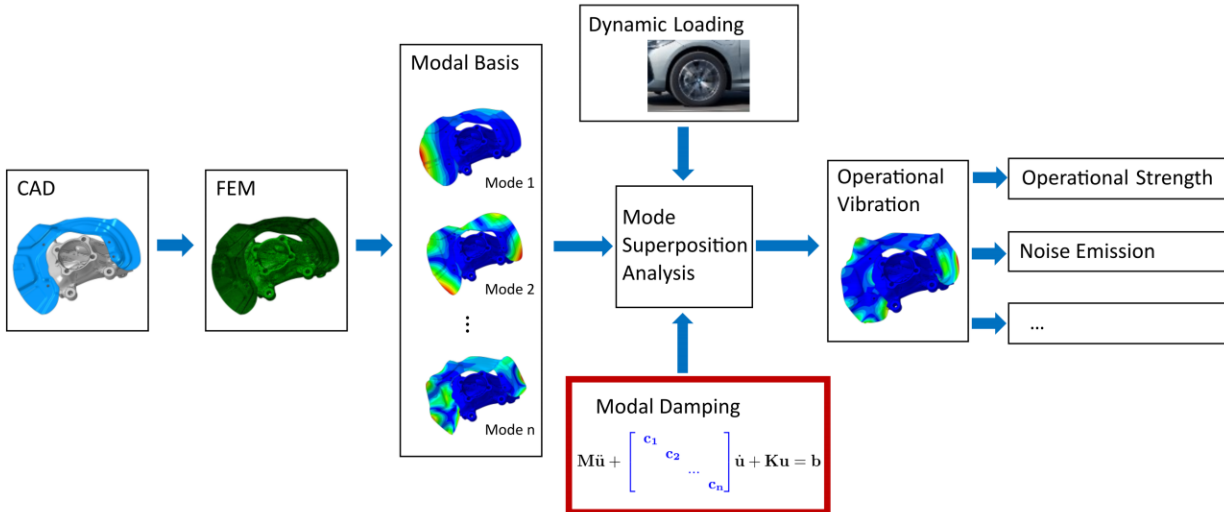


**Figure 1.2:** Finite element computational process based on modal superposition. Preceded by a modal analysis, simulations in time and frequency domain can be performed for linear problems. Modal damping provides damping ratios for each mode shape. These parameters can be empirical or experimental data, or simulated values. Two approaches to calculate modal damping ratios are presented in this thesis. Illustration based on [12]

values are used in subsequent dynamical analyses.

In order to verify the developed simulations, the results are compared to physical experiments. For this purpose, a test setup is designed to determine material damping by recording the decay of dynamically excited structures. The challenge of the experimental setup is the exclusion of other damping sources such as friction or radiation damping. Therefore the tests are realized in a vacuum environment using special support conditions.

Both the simulations and the experiments are performed on a specimen with simple geometry (rectangular plate). Two additional components from the industrial context with more complex geometries are investigated to demonstrate a practical application. A thin protection plate from automotive industry is used for the two-dimensional surface approach. Furthermore, a structure is designed based on a gearbox case for testing the solid method.

### 1.3 Structure of the Thesis

The theoretical background and the state of the art for the main topics of this thesis are summarized in two chapters. Chapter 2 provides a classification of damping phenomena with respect to the sources and modeling of energy dissipation. First, the principal physical effects causing damping are shortly described. Concerning

damping models, some widely used simplified approaches are outlined, including modal damping.

Since the focus in this work is set on TED, the theory of thermoelasticity is derived, and important approaches for TED in the literature are explained in Chapter 3. Furthermore, the application of thermoelastic coupling in FE simulations is described. In this context, the fundamentals simulating dynamically excited vibrations are summarized. The chapter closes with highlighting open research questions.

Chapter 4 presents the experimental studies carried out to determine damping properties. The investigated components are introduced and the experimental setup is explained in detail. The results of the experiments, that are used repeatedly in the following chapters, are exhibited and discussed.

Chapter 5 is devoted to the simulation of TED in solid modeled structures. The method of using entropy and generated heat to determine the energy loss is described and the results for beam structures, a rectangular plate and the gearbox case are calculated. The damping parameters are compared to experiments, analytical models and fully coupled simulations.

In Chapter 6, the method to include TED in the simulation of two-dimensional surface structures discretized by shell elements is presented. Therefore, the calculation of bending energy is derived from the plate theory. The approach is developed on the example of the rectangular plate and verified on a real automotive component. Furthermore, the method is compared to experimental results from literature.

Chapter 7 summarizes and discusses the results of the experimental and numerical studies of this thesis. An outlook regarding further research possibilities in the field of damping models is provided.



# Chapter 2

## Physics and Mechanical Models of Damping

### 2.1 Introduction

Damping is defined as the transformation of mechanical energy into lower energy forms, usually into thermal energy [2] effecting the reduction or prevention of mechanical oscillations. Damping or energy dissipation is caused by a wide variety of sources. Likewise, there are various approaches to consider damping effects in the modeling of vibrating structures. Many terms and parameters concerning damping are not used uniformly in the literature. In this chapter, an attempt is made to classify dissipation effects according to the physical sources and mechanical models. Concerning the sources of damping, a classification is made based on the VDI guideline 3830 [1]. The damping is called internal if the damping force and the reaction force act within the system boundaries. The damping is external if the reaction force acts outside the system boundaries. Internal damping includes physical effects within the material (material damping) and friction in joints. Friction at bearings or suspensions is classified as external, as well as dissipation due to air resistance and radiation damping. An overview is given in figure 2.1.

In the first part of this chapter, material damping, friction, and radiation damping are explained. Particular emphasis is placed on physical effects in the micro-and macrostructure of the material as a basis for the following chapters.

Subsequently, mechanical models that are frequently used in engineering practice are explained. As standard methods, viscous and hysteretic damping, as well as Coulomb friction, are described. For the case of Multi-Degree-Of-Freedom System (MDOF) systems, as they usually occur in the simulation of dynamically excited systems, modal damping and Rayleigh damping are presented. Usually, the calculation does not distinguish between the individual damping causes (except for

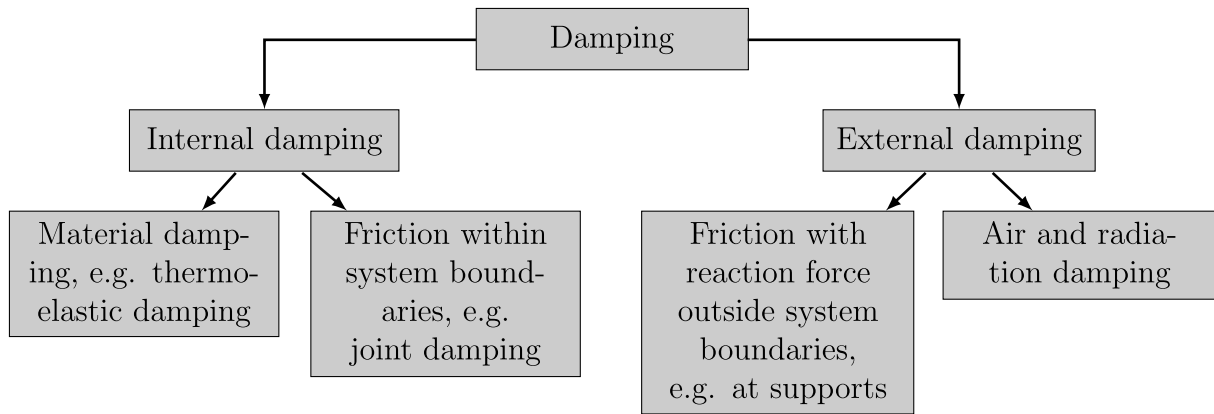


**Figure 2.1:** Classification of damping phenomena, based on [1]

Coulomb friction). The outlined approaches are idealized models concerning all sources of energy dissipation. Therefore, no direct assignment can be drawn between the physical effects and the mechanical models.

## 2.2 Sources of Vibration Damping

### 2.2.1 Physical Material Effects

Material damping results from physical effects in the material structure on the micro and macro scale, causing anelasticity. Typical sources for anelastic behavior in solids are defects and imperfections in the lattice structure resulting in microplastic deformations. Furthermore, energy is dissipated by thermomechanical or electromechanical effects. In fluids, viscous flow losses can occur [1]. A good overview of several mechanisms is given in [13] or [14]. Lazan [14] provided a relaxation spectrum including the most important material dissipation effects over a wide range of vibration frequencies or temperatures (see figure 2.2).

This schematic diagram shows the loss factor  $\eta$  as a function of the vibration frequency for a hypothetical material. Several peaks occur in characteristic frequency ranges due to different physical effects, the so-called relaxation peaks.

Imperfections in the crystal structure and grain boundaries usually induce peaks in low frequency ranges ( $< 1 \times 10^{-1}$  Hz). In higher frequencies, the relaxation in the material is dominated by thermoelastic losses on the macro- and microscale. In this thesis, frequencies in the range of approximately 30 - 3000 Hz are considered. In this interval, the principal loss mechanism is macro-thermoelasticity.

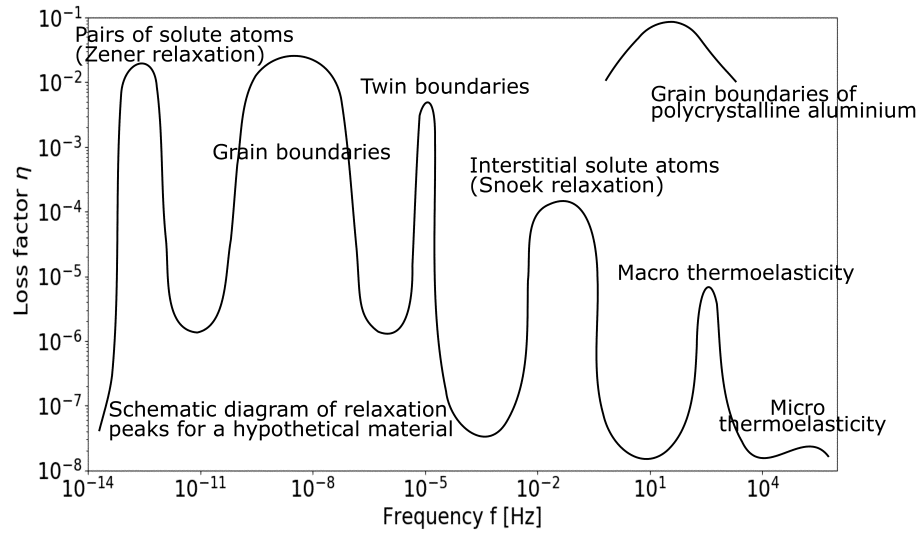


**Figure 2.2:** Relaxation spectrum according to Lazan [14]. The loss factor  $\eta$  is shown as a function of frequency. Due to different physical effects relaxation peaks occur in characteristic frequency ranges. Imperfections in the lattice structure, such as grain boundaries, are dominant in low frequency ranges whereas thermoelastic losses arise in higher frequencies.

### 2.2.1.1 Point Defects

The lattice structure of metals can have various types of defects and imperfections that affect the mechanical behavior of the material. A detailed description can be found in [15]. These impurities cause a local asymmetry in the structure and, therefore, anelastic behavior. The crystal imperfections can be the result of removed atoms (vacancy), substituted atoms of the same or different species (substitutional atom), or additional atoms of the same or different species (interstitial atom). These kinds of point defects are shown in figure 2.3.

Two significant phenomena related to the crystal lattice structure are the Snoek relaxation and the Zener relaxation. The Snoek effect [16] is based on the rearrangement of interstitial solute atoms, e.g., carbon atoms in an iron lattice, under the effect of elastic stress. In the unstrained condition, the atoms are distributed statistically uniform. Due to cyclic stress excitation, the structure is strained elastically, resulting in a reorientation of the gaps in the lattice structure. Therefore solute atoms diffuse to new positions causing microplastic deformations.

The Zener relaxation [17, 18] is closely related to the Snoek effect and concerns the reorientation of solute atom pairs under the impact of cyclic stress. The relaxation time is comparatively long at room temperature. Therefore the Zener relaxation occurs at very low frequencies (see figure 2.2) or high temperatures.

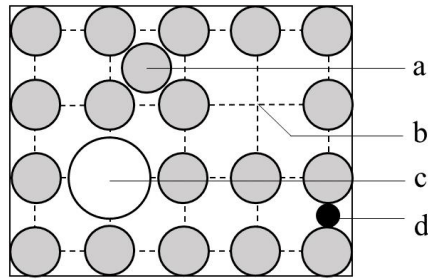


**Figure 2.3:** Point defects in lattice structure (according to [13]): a) self-interstitial atom, b) vacancy, c) substitutional atom, d) foreign-interstitial atom

### 2.2.1.2 Grain Boundaries

Grain boundaries are two-dimensional defects in the crystal lattice. At two adjacent crystals, shear stress along the boundary causes slip and anelastic strain due to grain boundary sliding. The dissipation energy is proportional to the product of shear stress and anelastic shear strain rate. The highest amount of internal friction due to stress relaxation occurs when the excitation frequency corresponds to the reciprocal stress relaxation time across grain boundaries. In addition to frequency, the energy loss also depends on temperature and grain size. The impact of grain-boundary relaxation increases in materials with fine grains or at high temperatures [19]. In 1947, Kê [20] showed experimentally the existence of relaxation curves in polycrystalline aluminum that do not occur in single-crystal aluminum. In metals with only a few significant boundary imperfections, the relaxation time is much longer and, therefore, the peak frequency much smaller.

So-called twin boundaries arise between two crystals of the same type, and a high degree of symmetry exists. Therefore the relaxation time is smaller and the frequency slightly higher than for usual grain boundaries (see figure 2.2).

### 2.2.1.3 Thermoelasticity on Microscopic and Macroscopic Scale

In this thesis, the main focus is set on TED. It is the dominant source of material damping for room temperature and in the considered frequency range (30 - 3000 Hz). Therefore, this effect will be explained in detail in the next chapter and is only mentioned here for the sake of completeness.

Due to the coupling of elastic stresses and strains with thermal variables, a mechanically stressed body produces local temperature variations depending upon local stress levels. Temperature gradients within the specimen cause heat flows that lead to internal friction and energy dissipation. These temperature gradients can exist on a macroscopic scale between different regions (Macrothermoelasticity). Furthermore, temperature gradients on a microscopic scale are produced due to different orientations of neighboring grains, even under macroscopically uniform stress. This

difference in temperature results in micro-thermal currents and energy dissipation (Microthermoelasticity) [18].

#### 2.2.1.4 Empirical Values for Material Damping

In some literature references, general values for material damping ratios are given. Usually, these are empirical data obtained from experiments. Often, the material damping is considered a specific material parameter without considering the dependence on, for example, the vibration frequency or shape and the environmental conditions. Therefore, significant differences occur between particular references. Table 2.1 gives some examples of material damping characteristics in aluminum. The range extends over several orders of magnitude from  $\zeta = 1.5 \times 10^{-6}$  to  $\zeta = 1 \times 10^{-3}$ .

**Table 2.1:** Empirical values for the material damping ratio of aluminium in the literature. If another damping parameter, such as the loss factor, is given, it is converted into the damping ratio.

Reference	damping ratio $\zeta$
Cremer: <i>Structure Borne sound</i> [21]	
longitudinal	$5 \times 10^{-5}$
flexural	$1.5 \times 10^{-5} - 1 \times 10^{-4}$
de Silva: <i>Vibration Damping</i> [2]	$1 \times 10^{-5} - 1 \times 10^{-3}$
Adams et al.: <i>Building better products with finite element analysis</i> [22]	$4 \times 10^{-4}$
Gaul: <i>Werkstoff- und Fügestellendämpfung</i> [23]	$8 \times 10^{-5}$

### 2.2.2 Friction

Friction is an important mechanism causing energy dissipation in bolted, clamped, or riveted joints or bearings and guides. The effect significantly influences the damping behavior of an assembled structure. In many technical systems, friction damping accounts for up to 90% of the total damping, as emphasized by Beards [24].

For a general overview of friction and joint damping in relation to other types of damping, the reader is referred to relevant textbooks concerning vibration damping as [2, 25] or the VDI guideline 3830 [1]. The review articles of Wenzel [26], Ibrahim and Pettit [27] or Gaul and Nitsche [28] give a thorough overview of the physical mechanism as well as experimental studies and modeling of joint damping.

Relative displacements of the contact surfaces cause friction damping in joints. The effect is called dry friction if no medium is applied between the mating surfaces.

The dry friction process can be described in three stages: stick, micro-slip, and macro-slip. The displacements in the contact depend mainly on the tangential force,

the joint's contact stress, and the surface properties. The surfaces stick together with a low tangential load and a high contact pressure, and elastic deformations with the stiffness  $k_0$  occur in the asperities. If the tangential force increases, small area relative movements arise (micro-slip). When the movement covers the entire contact surface, the effect is called macro-slip, and the deformation has the stiffness  $k_s$ . Figure 2.4 shows the hysteresis loop of this non-linear process.

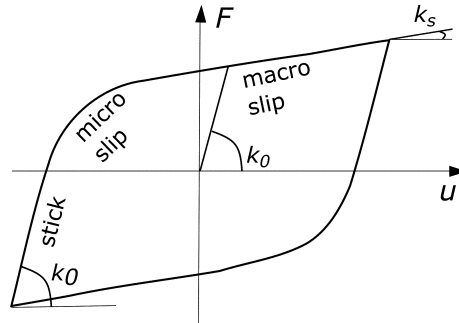


**Figure 2.4:** Typical hysteresis loop for dry friction according to [29]

The procedure can be idealized to a piece-wise linear behavior using the Coulomb friction model. This approach is described in section 2.3.3. A very comprehensive review of analytical joint friction models is provided by Mathis et al. [30]. Concerning numerical modeling, the use of zero-thickness elements has shown to be a promising approach in the literature. Geisler [31] describes in his dissertation an implementation using these contact elements with an elastic slip model. Gaul et al. take up a similar approach in several publications [23, 32–35].

### 2.2.3 Air and Radiation Damping

Whenever a structure vibrates in a fluid, energy dissipation mechanisms occur. According to the VDI guideline 3830, two effects can be distinguished in this context:

- Interactions between the vibrating solid and the surrounding medium
- Acoustical radiation

The deflections of the structure's surface cause a movement in the surrounding medium. The velocity of the oscillation is proportional to the pressure in the fluid. At the same time, the environmental pressure affects the frequency and damping of the mechanical vibration [36, 37].

One way to account for these interactions in the calculation is to represent the influence of the surrounding medium by an added mass. This approach was derived in the field of hydraulic engineering by Westergaard in 1933 [38]. Conca et al. [39] developed a framework for using added mass effects in fluid-structure-interaction in numerical simulations. In this method, the influence of the surrounding medium

is represented by an added mass and an added damping. The added mass effect impacts the frequency and the amplitudes of the vibration. Further dissipation due to the viscous fluid is considered using added damping factors. This approach has been extended and advanced numerous times and is still used in current research [40–42].

Sound radiation describes the release of kinetic energy from a vibrating structure and the associated change in sound pressure in the environmental medium. Concerning acoustic loss, the radiation efficiency  $\mu_R$  is a widely used measure in engineering acoustics. This ratio is calculated in terms of the radiated power  $P_R$ , the surface of the body  $A$  and the spatially averaged mean-square velocity  $\tilde{v}$  [21, 43]

$$\mu_R = \frac{P_R}{\rho c_S A \tilde{v}^2} \quad (2.2.1)$$

with the speed of sound  $c_S$  and the density of the medium  $\rho$ . For simple geometries, e. g. spheres, plates or pistons, there are analytical approaches to determine the acoustic radiation power. They can serve as a basis for estimating the acoustic loss of real bodies.

In the numerical simulation, fluid-structure interaction can be realized by the Finite Element Method (FEM) and the Boundary Element Method (BEM). Whereas the solid is usually described by finite elements, both approaches can be considered for the fluid. In general, finite fluid volumes are modeled by finite elements and infinite acoustic spaces by boundary elements [44]. The BEM usually offers an advantage in computational efficiency since significantly fewer degrees of freedom are considered [45, 46].

## 2.3 Mechanical Damping Models

This section provides a short overview of widely used models for damping effects. In this context, damping parameters used in the present work and their interrelations are presented as well. Especially the viscous damping model and its extension to modal damping in MDOF systems form the basis for the methods introduced in the chapters 5 and 6.

For a more thorough treatment of the topic the reader is referred to one of numerous textbooks available. Damping modeling is especially considered in Nashif [25] and De Silva [2], whereas books focussing on structural dynamics provide a broader view, e.g. Chopra [47], Petersen [48] or Clough and Penzien [49].

### 2.3.1 Viscous Damping

Viscous damping is the most commonly used method for modelling energy dissipation in mechanical vibration. The model is mathematically convenient and agrees well with numerous physical experiments [50]. The concept of a viscous damper goes back to Rayleigh [51] and is defined as proportional to the velocity of the vibration. In the literature, the term rate-dependent damping is often used as well.

Initially, viscous damping is described using the single-degree-of-freedom system. The Equation of Motion (EOM) that describes the vibration of a mechanical system mathematically, is formulated as follows:

$$m\ddot{u}(t) + c\dot{u}(t) + ku(t) = 0 \quad . \quad (2.3.1)$$

This homogeneous differential equation holds for a free vibration without an excitation force on the right-hand side. In the viscous damping model there is a linear dependency between the damping force  $F_D$  and the velocity  $\dot{u}$ . The damping coefficient  $c$  has the unit Ns/m and represents all effects causing energy dissipation in the system.

$$F_D = c\dot{u} \quad (2.3.2)$$

To solve the EOM the ansatz  $u = e^{\lambda_e t}$  is used that fulfills the differential equation for each  $t$ . The characteristic equation is

$$\lambda_e^2 + \frac{c}{m}\lambda_e + \frac{k}{m} = 0 \quad (2.3.3)$$

with the solutions

$$\lambda_{e1,2} = -\frac{c}{2m} \pm \sqrt{\left(\frac{c}{2m}\right)^2 + \frac{k}{m}} \quad . \quad (2.3.4)$$

Dependent on the radicant under the square root, a distinction is made between under-critically, over-critically or critically damped systems (see figure 2.5). If the radicant becomes zero, the critical damping  $c_{crit}$  is obtained.

$$c_{crit} = 2\sqrt{km} = 2m\omega_0 \quad (2.3.5)$$

The value  $\omega_0 = \sqrt{\frac{k}{m}}$  is the circular eigenfrequency of the undamped system. Dependent on the critical damping, the damping ratio  $\zeta$  is defined, which is a widely used damping parameter in structural dynamics.

$$\zeta = \frac{c}{c_{crit}} \quad (2.3.6)$$

With the damping ratio  $\zeta$  the eigenfrequency of the system is slightly shifted to the damped eigenfrequency  $\omega_D = \omega\sqrt{1-\zeta^2}$ . If  $\zeta > 1$  the vibration is over-critically damped. Therefore, no free oscillation occurs. In the case of critical damping ( $\zeta = 1$ ) the initial amplitude is damped immediately.

In an under-critically or weakly damped system, the radicant is negative and the damping ratio is  $\zeta < 1$ . The result is a free oscillation with an amplitude decreasing exponentially over time. The solution of the EOM for a free vibration is

$$u = e^{-\zeta\omega t}(A \cos(\omega\sqrt{1-\zeta^2}t) + B \sin(\omega\sqrt{1-\zeta^2}t)) \quad . \quad (2.3.7)$$

The constants  $A$  and  $B$  can be determined from the initial displacement  $u_0$  and the initial velocity  $\dot{u}_0$ . Due to the effect of the function  $e^{-\zeta\omega t}$  the curve decays exponentially. For the special case of a weakly damped oscillation it can be assumed that damped eigenfrequency is similar to the undamped eigenfrequency ( $\omega = \omega_D$ ). This graph is shown in figure 2.6 with an initial displacement of  $u_0 = 1$  and an initial velocity of  $\dot{u}_0 = 0$ . The corresponding solution of the EOM is:

$$u = e^{-\zeta\omega t}(u_0 \cos(\omega\sqrt{1-\zeta^2}t)) \quad . \quad (2.3.8)$$

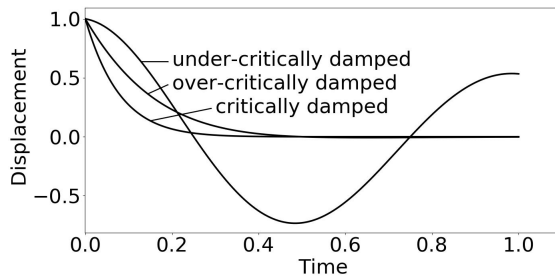


**Figure 2.5:** Under-critically, over-critically and critically damped decay curves of a free vibration with a frequency of 2 Hz and an initial displacement  $x_0$ .

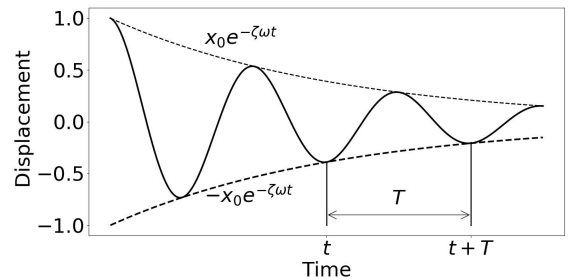


**Figure 2.6:** Decay curve of a viscously damped free vibration with the damping ratio  $\zeta$ . The envelope of the curve is  $\pm x_0 e^{-\zeta\omega t}$ .

In relation to the decay curve shown in Figure 2.6, a further damping parameter can be defined. The logarithmic decrement  $\Lambda$  is especially used to determine damping from experimental data. To calculate  $\Lambda$ , the amplitudes at two specific points in time are considered. The period length of the damped vibration  $\tau_D$  depends on the damping ratio  $\zeta$ :

$$\tau_D = \frac{\tau}{\sqrt{1-\zeta^2}} \quad . \quad (2.3.9)$$

The natural logarithm of the ratio of the deflection  $u$  at the time points  $t$  and  $t + \tau_D$  gives the logarithmic decrement.

$$\Lambda = \ln \frac{u(t)}{u(t + \tau_D)} \quad (2.3.10)$$

If  $u$  is substituted by the enveloping exponential function, the following equation can be established.

$$\Lambda = \ln \frac{e^{-\zeta\omega_D t}}{e^{-\zeta\omega_D(t+\tau_D)}} = \ln e^{\zeta\omega_D\tau_D} = \frac{2\pi\zeta}{\sqrt{1-\zeta^2}} \quad (2.3.11)$$

In weakly damped systems  $\zeta \ll 1$  the relationship between the damping parameters can be described by

$$\Lambda = 2\pi\zeta \quad (2.3.12)$$

If the oscillation is forced by an external force, the EOM becomes an inhomogeneous differential equation. The most basic scenario is harmonic excitation with an excitation frequency  $\Omega$  and a force amplitude  $\hat{F}$ .

$$m\ddot{u}(t) + c\dot{u}(t) + ku(t) = \hat{F} \sin(\Omega t) \quad (2.3.13)$$

The complementary solution  $u_c$  is equal to equation 2.3.7, i.e. the solution of the homogeneous EOM. This part of the displacement function represents the free vibration. After the decay of this part, the system remains in a state of harmonic vibration (steady-state vibration) in the excitation frequency  $\Omega$ . This particular solution  $u_p$  of the EOM can be determined with a harmonic ansatz.

$$u_c = e^{-\zeta\omega_D t} (A \cos(\omega_D t) + B \sin(\omega_D t)) \quad (2.3.14)$$

$$u_p = \hat{u} \sin(\Omega t - \varphi) \quad (2.3.15)$$

The angle  $\varphi$  is the phase lag between the excitation force and the response displacement. Differentiating and substituting the ansatz function into the EOM gives the solutions for the phase lag and the amplitude of the steady-state vibration.

$$\hat{u} = \frac{\hat{F}}{\sqrt{(k - m\Omega^2)^2 + c^2\Omega^2}} \quad (2.3.16)$$

$$\tan \varphi = \frac{c\Omega}{k - m\Omega^2} \quad (2.3.17)$$

During a stationary vibration there is no decay. The energy delivered by the excitation force is dissipated by the viscous damper. A steady-state oscillation can be illustrated by a hysteresis loop either in a stress-strain diagram or in a force-displacement diagram (see figure 2.7). In the case of viscous damping, the hysteresis loop takes the form of an ellipse. The inclination of the ellipse corresponds to the stiffness  $k$  of the system, whereas the enclosed area is a measure of the dissipated energy in one vibration cycle. The dissipated energy can be expressed as the integral

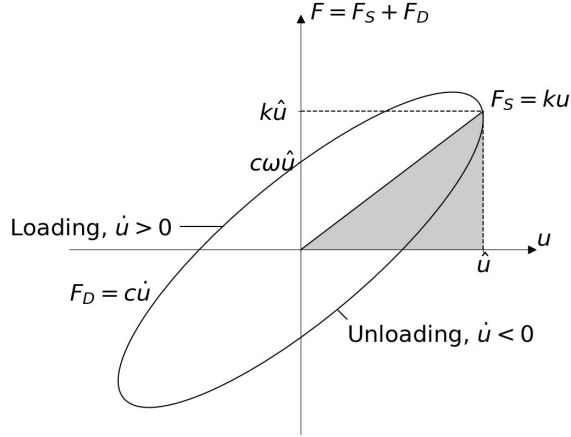


**Figure 2.7:** Hysteresis loop of a viscously damped system. The shaded area characterizes the total strain energy. The area enclosed by the curve describes the dissipated energy. The inclination of the ellipse corresponds to the stiffness  $k$ . The stiffness force  $F_S$  is  $ku_0$  at the point of maximum deflection. The maximum damping force is  $F_D = c\omega_D u_0$ .

of the damping force over the vibration displacement. The value is proportional to the square of the maximum displacement  $\hat{u}$  as shown in equation 2.3.18.

$$E_d = \int F_D du = \int_0^{2\pi/\omega} (c\dot{u})u dt = \int_0^{2\pi/\omega} c \cos(\Omega t - \varphi)^2 \hat{u}^2 \Omega^2 dt = c\pi\Omega\hat{u}^2 \quad (2.3.18)$$

The loss factor  $\eta$  is defined as the ratio of the damping energy  $E_d$  to the total strain energy  $E_S = \frac{k\hat{u}^2}{2}$  for maximal deflection  $\hat{u}$ . The reciprocal of the loss factor is called the quality factor  $Q_d$ .

$$\eta = \frac{E_d}{2\pi E_S} \quad Q_d = \frac{2\pi E_S}{E_d} \quad (2.3.19)$$

The definitions in 2.3.19 are generally applicable and not restricted to viscous damping. However, if the derivation in 2.3.18 is used as a basis (i.e. viscous damping with an elliptical hysteresis curve), the following relationship between the damping parameters can be established.

$$\eta = \frac{2c\pi\Omega\hat{u}^2}{2\pi k\hat{u}^2} = \frac{c}{m\omega} \frac{\Omega}{\omega} = 2\zeta \frac{\Omega}{\omega} \quad (2.3.20)$$

If the excitation frequency equals the eigenfrequency (case of resonance) the loss factor is calculated as follows.

$$\eta = 2\zeta \quad (2.3.21)$$

### 2.3.2 Hysteretic Damping

Although viscous (rate-dependent) damping is the most commonly used mechanical approach to model energy dissipation, there are numerous methods in the literature to formulate rate-independent damping. In 1927 Kimball and Lovell [52] showed experimentally that many materials exhibit a type of energy loss that is independent of the excitation frequency. Theodorsen and Garrick [53] developed a mathematical framework for a type of damping force that is in phase with the vibration velocity, but its magnitude is proportional to the amplitude of the oscillation. The term "hysteretic damping" for this phenomenon was first mentioned by Bishop et al. [54] in 1960. Based on this, various damping models were developed, e.g. complex stiffness by Soroka [55], a linear visco-elastic damper by Caughey [56] or a non-linear hysteretic model by Reid [57]. "Hysteretic damping" is not used uniformly in the literature and includes a variety of mechanical approaches. The complex stiffness method is presented here as an example.

In order to avoid the dissipated energy being dependent on the frequency, the damping term in the EOM is divided by the excitation frequency. It is proportional to the stiffness  $k$  and in phase with the velocity of the vibration  $\dot{u}$ .

$$F_D = \frac{gk}{\Omega} \dot{u} \quad (2.3.22)$$

Therefore the complex stiffness term  $k^*$  can be introduced.

$$k^* = (1 + ig)k \quad (2.3.23)$$

This approach assumes a harmonic excitation force with the frequency  $\Omega$ , i.e. it is only defined for the steady-state response of a vibrating system. The inhomogeneous EOM can be rewritten as

$$m\ddot{u} + k^*u = \hat{F} \sin(\Omega t). \quad (2.3.24)$$

With the ansatz function defined in equation 2.3.17 the amplitude of the steady-state vibration  $\hat{u}$  and the phase angle  $\varphi$  can be calculated.

$$u = \hat{u} \sin(\Omega t - \varphi) \quad (2.3.25)$$

$$\hat{u} = \frac{\hat{F}}{k \sqrt{(1 - \frac{\Omega^2}{\omega^2})^2 + g^2}} \quad (2.3.26)$$

$$\tan \varphi = \frac{g}{1 - \frac{\Omega^2}{\omega^2}} \quad (2.3.27)$$

Exactly as in the EOM, in the calculation of the damping energy the damping coefficient  $c$  is replaced by  $\frac{gk}{\Omega}$ .

$$E_d = \pi g k \hat{u}^2 \quad (2.3.28)$$

Besides the frequency independence of the dissipated energy, the solutions of a harmonically excited oscillation with viscous and hysteretic damping differ only slightly.

### 2.3.3 Coloumb Friction

If (dry) friction is the dominant damping mechanism in a system, the approach of viscous or hysteretic damping with exponential decay is not suitable. In these cases, the model of Coulomb friction is used. For free vibrations, the friction damped EOM is

$$m\ddot{u} + ku = \pm F_F \quad (2.3.29)$$

with the friction force  $F_F = \mu_F F_N$ . In this context,  $F_N$  is the normal force between the sliding surfaces and  $\mu_F$  is the coefficient of friction, which is a material parameter and depends on the type and condition of the surface. The direction of the friction force opposes the direction of motion. Although Coulomb friction is defined to be independent of velocity, the direction of  $F_F$  is indicated by the sign of the vibration velocity  $\dot{u}$ .

$$m\ddot{u} + ku = \text{sgn}(\dot{u})\mu_F F_N \quad (2.3.30)$$

The solution for this EOM is

$$u = A \cos(\omega_0 t) + B \sin(\omega_0 t) \pm u_F \quad (2.3.31)$$

with  $u_F$  as the static deformation due to the friction force  $F_F$ . The constants  $A$  and  $B$  are determined using the initial conditions. Figure 2.8 exhibits an example of the decay curve for an oscillation with the following assumptions: The system has an initial deflection of  $u(0) = u_0$  and an initial velocity of  $\dot{u} = 0$ . The constants  $A$  and  $B$  are

$$A = u_0 - u_F \quad B = 0 \quad (2.3.32)$$

and therefore the solution is

$$u = (u_0 - u_F) \cos(\omega_0 t) + u_F. \quad (2.3.33)$$

The solution for  $u$  is valid for the first half-cycle of the vibration ( $0 \leq t \leq \pi/\omega_0$ ) till the velocity of the vibration  $\dot{u}$  becomes zero and changes sign. At that point the

system has a deflection of  $u = -u_0 + 2u_F$ . For the next half period, the EOM must be re-solved with new initial conditions. The constants are

$$A = u_0 - 3u_F \qquad B = 0 \qquad (2.3.34)$$

and therefore the solution is

$$u = (u_0 - 3u_F) \cos(\omega_0 t) - u_F. \qquad (2.3.35)$$

This equation is valid until the sign of the velocity changes again ( $\pi/\omega_0 \leq t \leq 2\pi/\omega_0$ ). This scheme continues for the following oscillation cycles.

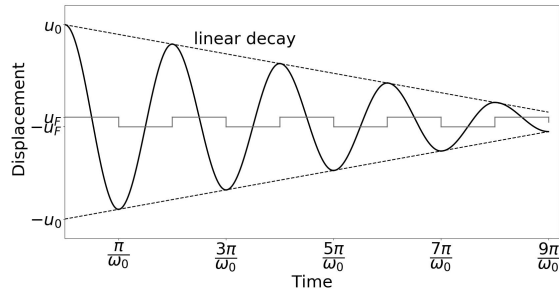


**Figure 2.8:** Decay curve of a free vibration with Coulomb friction damping. The envelope of the curve is a linear function.

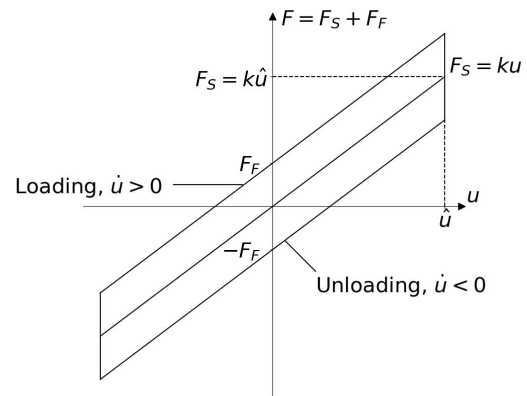


**Figure 2.9:** Hysteresis loop of a system with friction damping. The inclination of the loop corresponds to the stiffness  $k$ . The friction force  $F_F$  characterizes the width of the rectangular loop.

Since the governing equation changes every half-cycle of the vibration, a solution for a forced oscillation is complicated and is beyond the scope of this thesis. Further information can be found in pertinent textbooks, as [47, 48, 58].

However, a comparison to viscous damping can be given using the hysteresis loop and the dissipated energy per vibration cycle. Due to the sudden change of sign, the hysteresis curve of the oscillation damped by friction is a parallelogram, as shown in figure 2.9. The enclosed area is equal to the dissipated energy, therefore it is

$$E_d = 4F_F \hat{u}. \qquad (2.3.36)$$

### 2.3.4 Modal Damping

Modal damping is based on the assumption that each eigenmode in a MDOF system is individually damped. The modal damping force is proportional to the modal velocity of each eigenform. Therefore, the prerequisite for applying modal damping is a transformation of the EOM into modal coordinates. The transformation matrix

for this procedure contains the eigenmodes of the MDOF system. To determine the eigenmodes or natural modes, the undamped EOM for a free vibration is solved.

$$\mathbf{M}\ddot{\mathbf{u}} + \mathbf{K}\mathbf{u} = 0 \quad (2.3.37)$$

With the ansatz function

$$\mathbf{u} = \boldsymbol{\Phi}e^{i\omega t} \quad (2.3.38)$$

the generalized eigenproblem can be formulated.

$$\mathbf{K}\boldsymbol{\Phi} = \omega^2\mathbf{M}\boldsymbol{\Phi} \quad (2.3.39)$$

The eigenvalue  $\omega^2$  and the eigenvector  $\boldsymbol{\Phi}$  are obtained by solving the characteristic equation

$$\det(\mathbf{K} - \omega^2\mathbf{M}) = 0. \quad (2.3.40)$$

The results are  $n$  eigensolutions. Theoretically, one eigenfrequency and eigenform can be determined for each DOF  $n$ . The square root of the eigenvalue,  $\omega_i$ , corresponds to the  $i^{\text{th}}$  natural frequency of the system, while  $\boldsymbol{\Phi}_i$  characterises the  $i^{\text{th}}$  eigenmode, i.e. the arbitrarily scalable deformation figure of the system. Depending on the application, the eigenvectors can be normalized differently. Most common is the orthonormalization with respect to the mass matrix, i.e. the modal masses are scaled to unity. In this case each eigenvector satisfies the relations

$$\boldsymbol{\Phi}_i^T \mathbf{M} \boldsymbol{\Phi}_j = \begin{cases} 1 & \text{if } i = j \\ 0 & \text{if } i \neq j \end{cases} \quad \boldsymbol{\Phi}_i^T \mathbf{K} \boldsymbol{\Phi}_j = \begin{cases} \omega^2 & \text{if } i = j \\ 0 & \text{if } i \neq j \end{cases}. \quad (2.3.41)$$

The eigenvectors are combined as columns of a matrix  $\boldsymbol{\Phi}$ , so the following relations apply.

$$\boldsymbol{\Phi}^T \mathbf{M} \boldsymbol{\Phi} = \mathbf{I} \quad \boldsymbol{\Phi}^T \mathbf{K} \boldsymbol{\Phi} = \boldsymbol{\Omega}^2 \quad (2.3.42)$$

The matrix  $\boldsymbol{\Omega}^2$  contains the eigenvalues, i.e. the squares of the eigenfrequencies on the main diagonal.

$$\boldsymbol{\Omega}^2 = \begin{bmatrix} \omega_1^2 & & & \\ & \omega_2^2 & & \\ & & \ddots & \\ & & & \omega_n^2 \end{bmatrix} \quad (2.3.43)$$

With the transformations

$$\mathbf{u}(t) = \boldsymbol{\Phi}\mathbf{y}(t) \quad \dot{\mathbf{u}}(t) = \boldsymbol{\Phi}\dot{\mathbf{y}}(t) \quad \ddot{\mathbf{u}}(t) = \boldsymbol{\Phi}\ddot{\mathbf{y}}(t) \quad (2.3.44)$$

the EOM for an undamped system can be formulated as follows

$$\mathbf{M}\Phi\ddot{\mathbf{y}} + \mathbf{K}\Phi\mathbf{y} = \mathbf{b} \quad . \quad (2.3.45)$$

The components of the vectors  $\mathbf{y}$  and  $\dot{\mathbf{y}}$  are referred to as modal displacements and modal accelerations respectively. With the left multiplication of  $\Phi^T$  we get

$$\Phi^T\mathbf{M}\Phi\ddot{\mathbf{y}} + \Phi^T\mathbf{K}\Phi\mathbf{y} = \Phi^T\mathbf{b} = \mathbf{b}_m \quad . \quad (2.3.46)$$

The expressions  $\Phi^T\mathbf{M}\Phi$  and  $\Phi^T\mathbf{K}\Phi$  are summarized to the generalized mass and generalized stiffness matrices  $\tilde{\mathbf{M}}$  and  $\tilde{\mathbf{K}}$ . These square matrices are diagonal with the main diagonal entries  $m_i$  and  $k_i$ , respectively. The result is an equation system with n decoupled equations of motion in the form of a Single-Degree-Of-Freedom System (SDOF) equation.

$$m_i\ddot{y}_i(t) + k_i y_i(t) = b_{mi}. \quad (2.3.47)$$

If the eigenmodes are mass-normalized, according to equation 2.3.42, the EOM is simplified to

$$\ddot{\mathbf{y}}(t) + \mathbf{\Omega}^2\mathbf{y}(t) = \mathbf{b}_m. \quad (2.3.48)$$

Since  $\mathbf{\Omega}^2$  is a diagonal matrix, the equation system is decoupled, and the EOM for each eigenmode can be solved independently.

It is convenient to still deal with decoupled equations if damping is included. Therefore the transformation shown in equation 2.3.46 is applied to the damped EOM.

$$\Phi^T\mathbf{M}\Phi\ddot{\mathbf{y}} + \Phi^T\mathbf{C}\Phi\dot{\mathbf{y}} + \Phi^T\mathbf{K}\Phi\mathbf{y} = \Phi^T\mathbf{b} = \mathbf{b}_m. \quad (2.3.49)$$

The generalized damping matrix  $\tilde{\mathbf{C}} = \Phi^T\mathbf{C}\Phi$  is diagonal with the entries  $c_i$  on the main diagonal. Therefore the single equations of motion of the equation system are formulated similar to the damped SDOF equations.

$$m_i\ddot{y}_i(t) + c_i\dot{y}_i(t) + k_i y_i(t) = b_{mi} \quad (2.3.50)$$

If equation 2.3.50 is divided by the modal mass  $m_i$  the simplified form

$$\ddot{y}_i(t) + 2\zeta_i\omega_i\dot{y}_i(t) + \omega_i^2 y_i(t) = \frac{b_{mi}}{m_i} \quad (2.3.51)$$

is set up. The modal damping ratio  $\zeta_i$  is calculated similar to equation 2.3.6.

$$\zeta_i = \frac{c_i}{2\omega_i m_i} \quad (2.3.52)$$

The concept of a decoupled equation system with one damping ratio per mode shape gives the possibility to determine and apply damping parameters on a modal basis. This approach is the basis for all experimental and numerical studies in this thesis. For the sake of clarity,  $\zeta_m$  is used as the symbol for the modal damping ratio in the following chapters.

### 2.3.5 Rayleigh Damping

If there is no experimental, empirical or otherwise derived data to use as modal damping ratios, it is possible to obtain a proportional damping matrix. Furthermore, it can be necessary to formulate a damping matrix instead of single damping ratios, e.g. in the case of nonlinear response simulations. A simple method of constructing the damping matrix is mass and stiffness proportional damping by multiplying the mass or stiffness matrix with a constant  $\alpha_R$  or  $\beta_R$  respectively. To get a diagonal damping matrix and retain the decoupled equation system, the generalized mass and stiffness matrices are used.

$$\tilde{\mathbf{C}} = \alpha_R \tilde{\mathbf{M}} \qquad \tilde{\mathbf{C}} = \beta_R \tilde{\mathbf{K}} \qquad (2.3.53)$$

With 2.3.52 the relationship of the modal damping ratio  $\zeta_i$  to  $\alpha_R$  and  $\beta_R$  can be derived.

$$c_i = 2\omega_i m_i \zeta_i = \alpha_R m_i \qquad c_i = \beta_R k_i = \beta_R \omega_i^2 m_i \qquad (2.3.54)$$

$$\zeta_i = \frac{\alpha_R}{2\omega_i} \qquad \zeta_i = \frac{\beta_R \omega_i}{2} \qquad (2.3.55)$$

Obviously, the damping ratio related to the mass is inversely proportional to the frequency, whereas the stiffness damping ratio is directly proportional to frequency. Neither of the two models is appropriate in an MDOF system with a wide range of considered eigenfrequencies. A pervasive approach in practice, Rayleigh damping, is a combination of mass- and stiffness-proportional damping. A superposition of the above methods determines the damping matrix. The damping ratio is calculated as follows

$$\zeta_i = \frac{\alpha_R}{2\omega_i} + \frac{\beta_R \omega_i}{2} \qquad (2.3.56)$$

In this context  $\alpha_R$  and  $\beta_R$  are called Rayleigh coefficients. With this model, lower frequencies are mainly damped by mass proportional damping and higher frequencies are influenced by stiffness proportional damping. The damping ratio  $\zeta$  dependent on the frequency is shown graphically in figure 2.10. The coefficients  $\alpha_R$  and  $\beta_R$  can be determined if two damping ratios  $\zeta_a$  and  $\zeta_b$  with the appropriate frequencies,  $\omega_a$

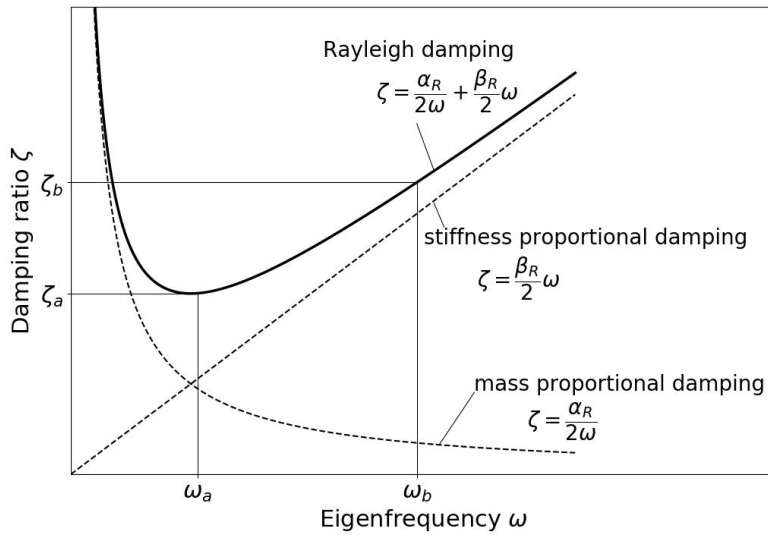


**Figure 2.10:** Graphical representation of the Rayleigh damping concept. The damping ratio  $\zeta$  is calculated by the superposition of mass- and stiffness-proportional damping. Therefore, low frequencies are mainly influenced by the mass proportional damping term. Higher frequency ranges are mainly damping stiffness-proportionally.

and  $\omega_b$ , are known. Usually, two eigenmodes of the system are used.

$$\begin{Bmatrix} \zeta_a \\ \zeta_b \end{Bmatrix} = \frac{1}{2} \begin{bmatrix} \frac{1}{\omega_a} & \omega_a \\ \frac{1}{\omega_b} & \omega_b \end{bmatrix} \begin{Bmatrix} \alpha_R \\ \beta_R \end{Bmatrix} \quad (2.3.57)$$

The accuracy of the model depends essentially on the considered eigenmodes. For the use of Rayleigh damping in practice, applying the fundamental frequency of an MDOF system as  $\omega_a$  is recommended, and one higher eigenfrequency that contributes significantly to the dynamic response as  $\omega_b$  [49]. The two related damping ratios,  $\zeta_a$  and  $\zeta_b$ , are represented precisely by the model. All frequencies between  $\omega_a$  and  $\omega_b$  show a lower damping ratio. For frequencies higher than  $\omega_b$ , the damping increases monotonically with the frequency. Therefore very high eigenmodes are eliminated if Rayleigh damping is used.

# Chapter 3

## Thermoelasticity and Thermoelastic Damping

### 3.1 Introduction

A change of the temperature in a body results in a state of strain and stress. Conversely, loading of the body produces a temperature field. A part of the mechanical strain energy is converted into heat. The first complete description of the coupling of the temperature field and the elastic field was deduced by Biot in 1956 [59]. Later, detailed derivations were given by Nowacki [60, 61] and Parkus [62].

In the present chapter, the fundamentals of thermoelastic coupling are outlined based on the first and second laws of thermodynamics. Afterward, the effect of thermoelastic damping is described. Since a mechanical vibration causes cyclic strains in a solid, oscillating temperature gradients occur. The resulting heat flows lead to irreversible transformations of mechanical energy to thermal energy and therefore damping in the material.

Finally, the implementation of thermoelastic coupling in FE formulations is presented. In this context, the fundamentals of the numerical simulation of dynamically excited structures are summarized. The chapter closes with a discussion of open research questions.

### 3.2 Fundamentals of Thermoelasticity

#### 3.2.1 Basic Equations for Linear Thermoelastic Coupling

According to the first law of thermodynamics, the total energy of a system and its environment is conserved. The mechanical work  $W^{def}$  performed on the system, and

the heat  $Q$  supplied to it are stored as the internal energy  $\Psi$ .

$$d\Psi = dW^{def} + dQ \quad (3.2.1)$$

The heat  $Q$  is a combination of the heat flux in direction  $i$ ,  $q_i$  and the strength of an inner heat source. The quantity of heat generated in unit time by an inner heat source  $H$  is

$$dQ = q_{i,i} + H \quad (3.2.2)$$

The internal energy  $\Psi$  is a state variable, i.e., it depends only on the state of the system at one instant and not on the process arriving at the given state. In contrast,  $W^{def}$  and  $Q$  depend on the process during a change of state [63].

Systems in thermodynamic equilibrium are characterized by a set of  $n + 2$  independent state variables. For two of these quantities, the number of particles  $n_p$  and the entropy  $S$  are assumed. The other  $n$  values are kinematic state variables depending on the type of the system. For a gas  $n = 1$  and the kinematic state variable is the volume  $V$ . For a solid  $n = 6$  and the additional state variables are the six independent components of the strain tensor  $\varepsilon_{ij}$ , so that  $\Psi = \Psi(n_p, \varepsilon_{ij}, S)$ .

$$\varepsilon_{ij} = \left\{ \varepsilon_{11} \quad \varepsilon_{22} \quad \varepsilon_{33} \quad \varepsilon_{12} \quad \varepsilon_{13} \quad \varepsilon_{23} \right\} \quad (3.2.3)$$

Since in the framework of this thesis only solids are considered the number of particles is always set to be constant, so in the following  $\Psi = \Psi(\varepsilon_{ij}, S)$  is used.

Based on the second law of thermodynamics it can be shown that the temperature  $T$  is given by the derivative of the internal energy  $\Psi$  with respect to the entropy  $S$ . Similar to this definition the elastic stress  $\sigma_{ij}$  can be defined.

$$\left. \frac{\partial \Psi}{\partial S} \right|_{\varepsilon_{ij}} = T \quad (3.2.4)$$

$$\left. \frac{\partial \Psi}{\partial \varepsilon_{ij}} \right|_S = \sigma_{ij} \quad (3.2.5)$$

By setting up the total differential of the internal energy  $\Psi$  and substituting equations 3.2.4 and 3.2.5 a formulation for the entropy can be found.

$$d\Psi = \left. \frac{\partial \Psi}{\partial S} \right|_{\varepsilon_{ij}} dS + \left. \frac{\partial \Psi}{\partial \varepsilon_{ij}} \right|_S d\varepsilon_{ij} \quad (3.2.6)$$

$$d\Psi = T dS + \sigma_{ij} d\varepsilon_{ij} \quad (3.2.7)$$

$$dS = \frac{d\Psi}{T} - \sigma_{ij} d\varepsilon_{ij} \quad (3.2.8)$$

In Equation 3.2.7 the first term on the right hand side refers to the supplied heat  $dQ$  and the second term refers to the mechanical deformation work  $dW^{def}$ . Hence, the entropy can be defined dependent on heat and temperature.

$$T dS = dQ \quad (3.2.9)$$

To further specify the thermoelastic interaction, it is useful to introduce the Helmholtz free energy  $F_H$ . It is calculated as

$$F_H = \Psi - TS \quad . \quad (3.2.10)$$

The independent variables are now the temperature  $T$  and  $\varepsilon_{ij}$  instead of  $S$  and  $\varepsilon_{ij}$ . By building the total differential and substituting equation 3.2.7 we get:

$$dF_H = d\Psi - T dS - S dT \quad (3.2.11)$$

$$dF_H = \sigma_{ij} d\varepsilon_{ij} - S dT \quad (3.2.12)$$

Therefore it can be shown that the stress tensor  $\sigma_{ij}$  is conjugated to the strain tensor  $\varepsilon_{ij}$  in the same way as the entropy  $S$  is conjugated to the temperature  $T$ .

$$\sigma_{ij} = \frac{\partial F_H}{\partial \varepsilon_{ij}} \quad S = -\frac{\partial F_H}{\partial T} \quad (3.2.13)$$

The expression for Helmholtz free energy in the vicinity of the equilibrium state ( $\varepsilon_{ij} = 0, T = T_0$ ) is derived using a multivariant Taylor series expansion assuming that the free energy, entropy and stress vanish in this case ( $F_H(0, T_0) = 0, S(0, T_0) = 0, \sigma_{ij}(0, T_0) = 0$ ). This is described in detail in [64].

$$F_H(\varepsilon_{ij}, T) = \frac{1}{2} E_{ijkl} \varepsilon_{ij} \varepsilon_{kl} - \beta_{ij} \varepsilon_{ij} \theta + \frac{c_V}{2T_0} T^2 \quad (3.2.14)$$

The elastic stiffness tensor  $E_{ijkl}$ , the thermoelastic coupling constant  $\beta$  and the heat capacity at constant volume  $c_V$  are defined as follows:

$$E_{ijkl} = \frac{\partial^2 F_H(0, T_0)}{\partial \varepsilon_{ij} \partial \varepsilon_{kl}} \quad \beta_{ij} = -\frac{\partial^2 F_H(0, T_0)}{\partial \varepsilon_{ij} \partial \theta} \quad c_V = T_0 \frac{\partial^2 F_H(0, T_0)}{\partial T^2} \quad (3.2.15)$$

These quantities  $E_{ijkl}$  and  $\beta_{ij}$  depend on the material properties. If an isotropic material is considered they are given by

$$E_{ijkl} = \lambda \delta_{ij} \delta_{kl} + \mu (\delta_{ik} \delta_{jl} + \delta_{il} \delta_{jk}) \quad (3.2.16)$$

$$\beta_{ij} = \alpha (3\lambda + 2\mu) \delta_{ij} = \beta \delta_{ij} \quad (3.2.17)$$

where  $\alpha$  is the thermal expansion coefficient,  $\lambda$ ,  $\mu$  are the Lamé coefficients,  $\delta_{ij}$  is the Kronecker delta and  $\beta$  is referred to as thermoelastic coupling coefficient. On this basis an expression for the thermoelastic stress as well as the entropy can be obtained.

$$\sigma_{ij} = \frac{\partial F_H}{\partial \varepsilon_{ij}} = 2\mu\varepsilon_{ij} + (\lambda\varepsilon_{kk} - \beta T)\delta_{ij} \quad (3.2.18)$$

$$S = -\frac{\partial F_H}{T} = \beta_{ij}\varepsilon_{ij} + \frac{c_V}{T_0}T \quad (3.2.19)$$

Equation 3.2.18 gives the relation between stress, strain and temperature, the Duhamel-Neumann relation. It should be emphasized that only the normal stresses ( $\sigma_{11}, \sigma_{22}, \sigma_{33}$ ) show a coupling to the thermal field. The shear stresses ( $\sigma_{12}, \sigma_{13}, \sigma_{23}$ ) are not thermoelastically coupled.

$$\sigma_{11} = 2\mu\varepsilon_{11} + \lambda\varepsilon_{kk} - \beta T \quad (3.2.20)$$

$$\sigma_{22} = 2\mu\varepsilon_{22} + \lambda\varepsilon_{kk} - \beta T \quad (3.2.21)$$

$$\sigma_{33} = 2\mu\varepsilon_{33} + \lambda\varepsilon_{kk} - \beta T \quad (3.2.22)$$

$$\sigma_{12} = \mu\varepsilon_{12} \quad (3.2.23)$$

$$\sigma_{23} = \mu\varepsilon_{23} \quad (3.2.24)$$

$$\sigma_{13} = \mu\varepsilon_{13} \quad (3.2.25)$$

Here  $\varepsilon_{kk}$  is the trace of the strain tensor  $\varepsilon_{kk} = \varepsilon_{11} + \varepsilon_{22} + \varepsilon_{33}$ . Solving equation 3.2.18 with respect to the strain  $\varepsilon_{ij}$  leads to

$$\varepsilon_{ij} = \alpha T \delta_{ij} + \frac{1}{2\mu} \left( \sigma_{ij} - \frac{\lambda}{3\lambda + 2\mu} \sigma_{kk} \delta_{ij} \right) \quad (3.2.26)$$

Furthermore, the strains can be expressed in terms of the displacement.

$$\varepsilon_{ij} = \frac{1}{2}(u_{i,j} + u_{j,i}) \quad (3.2.27)$$

### 3.2.2 Differential Equations of Thermoelastic Coupling

The complete set of differential equations of thermoelasticity consists of four equations. The stress/strain field is based on the EOM:

$$\sigma_{ij,j} + b_i = \rho \ddot{u}_i \quad (3.2.28)$$

The variable  $b_i$  indicates the body forces. They will be neglected in the following considerations. By inserting equations 3.2.18 and 3.2.27 the coupled differential equation for three-dimensional solids can be developed.

$$\mu u_{i,jj} + (\lambda + \mu)u_{j,ji} = \beta T_{,i} + \rho \ddot{u}_i \quad (3.2.29)$$

Besides the displacement  $\mathbf{u}$  also the temperature  $T$  and the thermoelastic coupling constant  $\beta$  occurs which realizes a coupling to the temperature field.

By inserting equation 3.2.2 into equation 3.2.9 the following expression is obtained.

$$T dS = -q_{i,i} + H \quad . \quad (3.2.30)$$

Under the assumption that no external heat source influences the thermal conduction the equation reduces to:

$$T dS = -q_{i,i} \quad . \quad (3.2.31)$$

The heat flux  $q_i$  is defined by Fourier's law of heat conduction:

$$q_i = -\kappa T_{,i} \quad (3.2.32)$$

$$T dS = \kappa T_{,ii} \quad . \quad (3.2.33)$$

The expression for the entropy (equation 3.2.19) is substituted into 3.2.33. This results in the thermoelastically coupled heat equation.

$$T(\beta d\varepsilon_{kk} + \frac{c_V}{T_0} dT) = \kappa T_{,ii} \quad (3.2.34)$$

For the calculation of TED, it is assumed that the temperature changes are very small compared to the reference temperature. Therefore, it is acceptable to replace  $T$  with  $T_0$  on the left-hand side. This results in a one-way coupling. The strain field is decoupled from the temperature field.

$$T_0 \beta d\varepsilon_{kk} + c_V dT = \kappa T_{,ii} \quad (3.2.35)$$

### 3.3 Thermoelastic Damping

Thermoelastic damping (TED) results from thermal currents, which balance the temperature gradient between stretched and compressed component regions. When a solid is deformed, e.g. during structural vibration, it is taken out of equilibrium by building an excess of potential and kinetic energy. In a thermoelastic solid there is a coupling effect between the elastic strain field and the temperature field. In

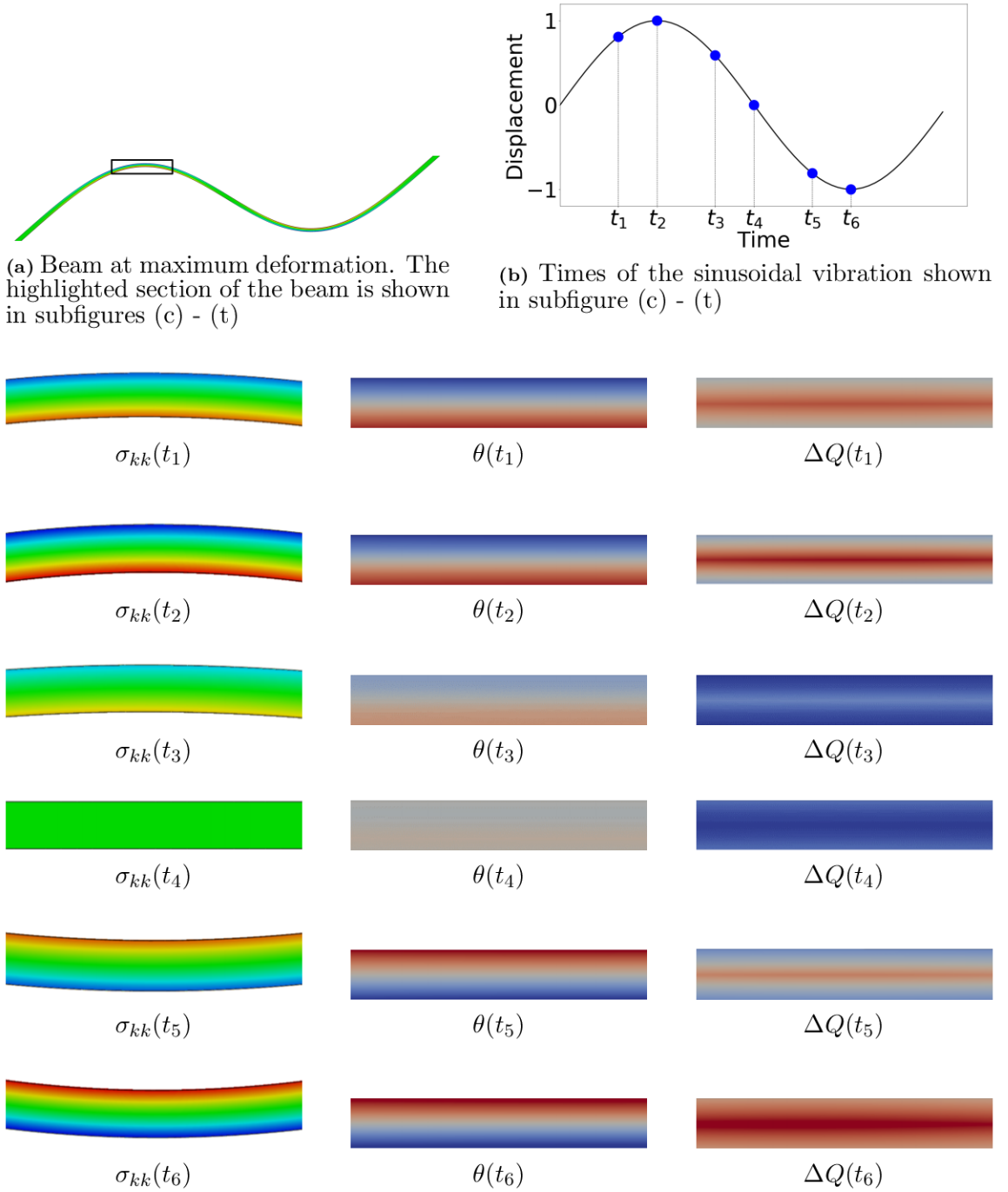
compressed areas the temperature increases and in stretched areas it decreases. The resulting local temperature gradient causes irreversible heat flows that set the body back to its equilibrium state. They lead to an increase in entropy, a transformation of mechanical to thermal energy and therefore a dissipation of energy in the solid.

Figure 3.1 demonstrates a series of hydrostatic stress distributions  $\sigma_{kk} = \sigma_{xx} + \sigma_{yy} + \sigma_{zz}$  during the vibration of a beam in accordance with the temperature change  $\theta$  and the transformed, i. e. the dissipated energy  $Q$ . Exemplary, a thin beam of size 400 mm x 10 mm x 3 mm is chosen. The results are an extract from a simulation outlined in chapter 5.4.1. Subfigure 3.1a shows the beam in its second mode shape deformation. To illustrate the thermoelastic effect clearly, only a small detail is exhibited in the other subfigures.

If the beam oscillates in a steady-state vibration, the deformation of each point follows a sine curve. The stress and temperature distribution, as well as the thermal energy, are analyzed at six time points in the vibration cycle. All three quantities are normalized to unity with a constant scale for all time steps. During the beam bending, the stretched fibers decrease in temperature. On the opposite edge, the compressed fibers warm up. The neutral axis remains constant in temperature. Due to the temperature gradient, heat flows from the warm side of the beam to the cold side.

These heat fluxes cause an increase in entropy and, therefore, the irreversible transformation of mechanical energy into thermal energy. The maximum energy dissipating is in the middle fiber of the beam section. After one half-cycle of the vibration, the beam is unstressed, and the temperature gradient has vanished. In the second part of the sinusoidal vibration, the stress distribution and the temperature variations invert. The heat flows in the opposite direction. Nevertheless, the spatial distribution of dissipated energy looks similar with a high amount of energy transformation in the middle fibers.

The temperature gradient equalizes in a characteristic relaxation time  $\tau_i$ . The relaxation time corresponds to one eigensolution of the heat conduction equation in frequency domain. Physically, the eigenvector of the heat equation is a characteristic temperature distribution. The inverse of the corresponding eigenvalue is the relaxation time, i. e. the time the solid needs to return to the thermodynamic equilibrium state. Regarding the amount of dissipated energy, there is a close relationship between the dominant thermal relaxation time and the natural frequency of the component.



**Figure 3.1:** Relationship between stresses in the beam during vibration, distribution of temperature changes and dissipated energy. The beam is vibrating sinusoidally. In subfigure (a) the beam in the state of maximal deflection is shown ( $t = \pi/4$ ). In subfigure (b) the illustrated times of the vibration are indicated. Subfigure (c) - (t) exhibit the hydrostatic stress  $\sigma_{kk} = \sigma_{xx} + \sigma_{yy} + \sigma_{zz}$ , the temperature change due to the thermoelastic coupling and the resulting dissipated, i. e. transformed, energy at different time points. For the sake of clarity, these quantities are only plotted for the part marked in (a). The figures of the hydrostatic stress show the deformed state of the beam part. The values for all quantities are normalized to unity.

$\tau_i \ll \frac{1}{\omega}$ : If the relaxation time is much smaller than the inverse of the relevant eigenfrequency, the vibration is adiabatic. The deformation is too fast to enable the compensation of the temperature gradient. Therefore the amount of dissipated energy is small.

$\tau_i \gg \frac{1}{\omega}$ : If the relaxation time is much greater than the inverse of the relevant eigenfrequency, the vibration is isothermal. The low velocity of vibration results in thermal exchange with the environment. The amount of dissipated energy is small.

$\tau_i \approx \frac{1}{\omega}$ : The highest loss factors are obtained when the relaxation time approximately coincides with the reciprocal of the natural frequency. The period length is exactly sufficient to bring the system back to equilibrium by heat flows.

This behavior is illustrated in figure 3.3. The loss factor as a function of the vibration frequency shows a clear peak if the frequency equals the inverse of the relaxation time. The actual relaxation results from a superposition of all eigenmodes. Practically, the analysis is often limited to the first one.

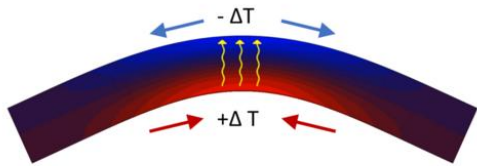


**Figure 3.2:** Mechanism of TED: Compressed regions are heated and stretched regions are cooled. The resulting irreversible heat flux causes an increase in entropy and energy dissipation.

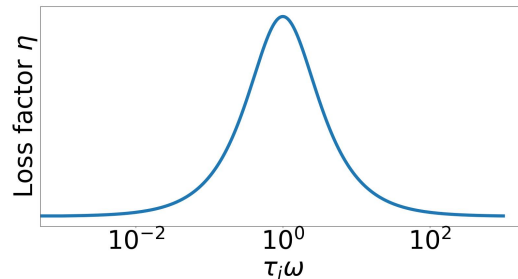


**Figure 3.3:** Relationship between the loss factor and the relevant natural frequency relative to the appropriate thermal relaxation time. The thermoelastic loss is maximized if the period length  $1/\omega$  matches the relaxation time  $\tau_i$ .

A large number of the studies on TED carried out to date can be traced back to the pioneering work of Zener in 1937 and 1938. He defined two procedures for calculating the thermomechanical loss factor [7, 65], which almost all later developed methods are based on.

1. The first (dynamical) approach is based on the difference in phase between the stresses and corresponding strains. To calculate the dissipated energy, the coupled thermoelastic heat equation is solved in the complex domain. The loss

factor is equal to the ratio of the imaginary and the real part of the solution. This approach is explained in chapter 3.3.1.

2. The second approach involves the calculation of dissipated energy. By solving the heat equation and analysing the heat flows, the amount of mechanical energy converted into heat can be determined. The loss factor is obtained from the quotient of the dissipated energy to the total strain energy. This method is described in detail in chapter 3.3.2.

Both approaches are related and can result in similar expressions.

The analytical methods were initially developed for one dimensional structures (beams and rods). Later, intensive research was conducted to extend the approaches to more complex geometries. A special focus was placed on the consideration of thin plate structures, as this opens up a wide range of possible applications. For this reason, this development is described separately in chapter 3.3.3.

### 3.3.1 Rate of Dissipated Energy

In his first publication concerning TED in 1937 Zener derived the formula for a thin bending beam [7]. Assuming the mechanical wavelength to be long compared to the thickness of the beam the only relevant heat conduction is in the thickness direction. Furthermore, only the displacement in the transverse direction  $u_z$  and the stresses in the longitudinal direction  $\sigma_{xx}$  are taken into account. Therefore the problem is reduced to one dimension.

In equation 3.2.28 the equation of motion for a continuous system was given. Considering the assumptions of a bending beam with one dimensional heat conduction, the EOM is reduced to

$$\rho \ddot{u}_z + \frac{\partial^2 M}{\partial x^2} = b \quad . \quad (3.3.1)$$

Due to the one dimensional problem, the density  $\rho$  is defined here as mass per unit length. The elastic stress is expressed in terms of the bending moment  $M(x, t)$ . Zener defined the thermoelastic loss factor  $\eta$  as the quotient of the imaginary and real part of the derivative of the bending moment.

$$\eta = \left| \frac{\text{Im} \frac{\partial^2 M}{\partial x^2}}{\text{Re} \frac{\partial^2 M}{\partial x^2}} \right| \quad (3.3.2)$$

The bending moment consists of a mechanical or elastic part  $M_e$  and a thermal part  $M_t$ . It is calculated as

$$M = M_e + M_t \quad (3.3.3)$$

$$M = EI \frac{\partial^2 u_z}{\partial x^2} + \alpha d \int_{-h/2}^{h/2} (T - T_0) dz \quad (3.3.4)$$

with the width of the beam  $d$ , the thickness  $h$  and the second moment of inertia  $I = \frac{dh^3}{12}$  for a beam with a rectangular section. In order to determine the thermal moment  $M_t$ , it is necessary to calculate the temperature distribution across the beam. Therefore the thermoelastically coupled heat equation is solved (see equation 3.2.34).

$$\frac{\partial \theta}{\partial t} = \chi \frac{\partial^2 \theta}{\partial z^2} - \beta T_0 \frac{\partial \varepsilon_{xx}}{\partial t} \quad (3.3.5)$$

In this version of the differential equation the unknown function is the temperature increment above the reference temperature  $\theta(\mathbf{x}, t) = T - T_0$ . The variable  $\chi = \frac{\kappa}{\rho c_V}$  denotes the thermal diffusivity. The normal strain  $\varepsilon_{xx}$ , that is the only considered strain in this one dimensional equation, is replaced by the second derivative of the displacement  $u_z$ . Since only harmonic oscillations are considered, this quantity can be expressed in frequency domain.

$$\varepsilon_{xx} = -z \frac{\partial^2 u_z}{\partial x^2} \quad (3.3.6)$$

$$u_z(\mathbf{x}, t) = \bar{u}_z(\mathbf{x}) e^{i\omega t} \quad (3.3.7)$$

$$\frac{\partial \theta}{\partial t} = \chi \frac{\partial^2 \theta}{\partial z^2} - \left( i\omega \beta T_0 \frac{\partial^2 \bar{u}_z}{\partial x^2} \right) z e^{i\omega t} \quad (3.3.8)$$

Adiabatic conditions are assumed for the vibration of the beam. Therefore no heat flow across the surface to and from the surrounding air occurs. The temperature gradient is set to zero at the upper and lower boundary and the boundary conditions are

$$\frac{\partial \theta}{\partial z} = 0 \quad \text{at} \quad z = \pm \frac{h}{2}. \quad (3.3.9)$$

By separation of variables, a general solution as a trigonometric series is obtained that fulfils the spatial boundary condition. The sinus term corresponds to the series of thermal eigenmodes, i.e. the spatial distribution of the heat flow during vibration.

For the sake of clarity, this term is denoted by  $\gamma_j$  in the following.

$$\theta = \sum_{k=1}^{\infty} g_k(t) \sin \left[ (2k+1) \frac{\pi}{h} z \right] \quad (3.3.10)$$

$$\theta = \sum_{k=1}^{\infty} g_k(t) \gamma_j \quad (3.3.11)$$

The expression for  $\theta$  is substituted into equation 3.3.8.

$$\sum_{k=1}^{\infty} \dot{g}_k(t) \gamma_j + \chi \sum_{k=1}^{\infty} g_k(t) \gamma_j \left[ (2k+1) \frac{\pi}{h} \right]^2 = -i\omega\beta T_0 \frac{\partial^2 u_z}{\partial x^2} z e^{i\omega t} \quad (3.3.12)$$

Both sides are multiplied by  $\gamma_j$  and integrated across the beam. Since  $\int_{-h/2}^{h/2} \gamma_j^2 dz = \frac{h}{2}$  the following solution for  $g_k$  is obtained.

$$\sum_{k=1}^{\infty} g_k(t) = -\frac{i\omega\beta T_0 \frac{\partial^2 \bar{u}_z}{\partial x^2} e^{i\omega t} s_k}{i\omega + \omega_{th}} \quad (3.3.13)$$

$$s_k = \frac{2}{h} \int_{-\frac{h}{2}}^{\frac{h}{2}} z \sin \left[ (2k+1) \frac{\pi}{h} z \right] dz \quad (3.3.14)$$

$$\omega_{th} = \chi \left[ (2k+1) \frac{\pi}{h} \right]^2 \quad (3.3.15)$$

The frequency  $\omega_{th}$  is equal to the inverse value of the relaxation time  $\tau_i$ . The time dependent thermal bending moment  $M_t$  can also be transferred into the frequency domain. By inserting the solution for  $\theta$  a formula for the explicit calculation of the bending moment is derived.

$$M_t(\mathbf{x}, t) = \bar{M}_t(\mathbf{x}) e^{i\omega t} \quad (3.3.16)$$

$$\bar{M}_t(\mathbf{x}) = \alpha d \beta T_0 \frac{1}{2} h \sum_{k=1}^{\infty} \frac{\partial^2 u_z}{\partial x^2} \frac{i\omega}{\omega_{th} + i\omega} s_k^2 \quad (3.3.17)$$

In combination with the elastic bending moment  $M_e$  the loss factor  $\eta$  can be determined by dividing the imaginary and real part of the total bending moment.

$$\eta = \frac{\alpha \frac{\beta T_0}{E} \sum_{k=1}^{\infty} \frac{\omega_{th} \omega}{\omega_{th}^2 + \omega^2} \frac{6s_k^2}{h^2}}{1 + \frac{\beta T_0}{E} \sum_{k=1}^{\infty} \frac{\omega^2}{\omega_{th}^2 + \omega^2} \frac{6s_k^2}{h^2}} \quad (3.3.18)$$

$$\frac{6s_k^2}{h^2} = \frac{96}{\pi^4(2k+1)^4} \quad (3.3.19)$$

It can be shown that  $\frac{6s_k^2}{h^2}$  becomes 0.9855 for  $k = 0$  and approximately 0 for all other  $k$ . Therefore it is reasonable in this special case of one dimensional beam bending to reduce the sum to the first term of the series. By substituting the thermoelastic coupling coefficient  $\beta$  the well-established formula to calculate TED is obtained.

$$\eta = \frac{E\alpha^2 T_0}{\rho c_V} \frac{\omega_{th} \omega}{\omega_{th}^2 + \omega^2} \quad (3.3.20)$$

The first term is only material dependent and is denoted as relaxation strength. It describes the maximal possible energy dissipation for the material with specific thermodynamic properties. The second part is frequency-dependent and depicts the Debye peak. The maximal loss coefficient occurs if the mechanical vibration frequency  $\omega$  is equal to the reciprocal value of the thermal relaxation time  $\omega_{th} = 1/\tau_i$ .

In 1962 Chadwick [66] developed an extension of Zener's method to three-dimensional homogeneous structures based on his theory of linear thermoelasticity [67]. He obtained the solution of the coupled differential equations by means of a series expansion of orthonormal eigenfunctions for the displacement and temperature. In a second publication, the author applied this theory to the special cases of thin rods and thin plates [68]. This is explained in detail in chapter 3.3.3. At the same time, another approach for the calculation of TED in three-dimensional solids was published by Alblas [69]. The analysis is also based on modal decomposition, but further boundary conditions and the coupling of several eigenmodes are considered. Therefore the author provided a more general theory, which is, however, much more complex. In 1980 Alblas expanded his approach and added new application examples [70].

In 2000 Lifshitz et al. [71] presented a further development of Zener's approach by not limiting the solution to the first thermal mode and thus achieving more accurate

results. The thermoelastic loss factor is calculated as

$$\eta = \frac{T_0 E \alpha}{\rho c_V} \left( \frac{6}{\xi^2} - \frac{6}{\xi^3} \frac{\sinh \xi + \sin \xi}{\cosh \xi + \cos \xi} \right) \quad (3.3.21)$$

$$\text{with } \xi = d \sqrt{\frac{\omega_0}{2\chi}} \quad . \quad (3.3.22)$$

The parameter  $\xi$  is a dimensionless variable dependent on the eigenfrequency. The deviation of the solution for the loss factor is less than 2% from the Zener model. Furthermore, the authors focused on beams of micro and nano scale size. This was the basis for numerous further publications in the following years for the field of micro resonators. In principle, the same assumptions and boundary conditions as for macro beams can be used here. The condition, is that the thickness of the micro beam does not fall below a critical value, which is defined as the mean free path of a thermal phonon.

Guo et al. [72] showed that the thermoelastic effect in microbeam resonators is much larger than the air damping effect. The authors used an eigenmode analysis of the coupled equations to get the complex frequencies where the energy dissipation is equal to the imaginary part. They analyzed the frequency shift between elastic and thermoelastic beams and pointed out the size effect in particular. With decreasing beam thickness they noted an increasing frequency shift that is related to increased attenuation. Sun et al. [73] confirmed these results. They used similar analysis as well as integral transformation to solve the coupled thermoelastic equations. The authors considered beams under several thermal and mechanical boundary conditions.

Since the thermoelastic effect was identified as the dominant loss mechanism in microbeams, intensive research considering various aspects has been done in the following years. In addition to the one-layered structures the thermoelastic coupling in two- and three-layered beams were also considered [74–77]. Besides straight flexural beams, also ring structures with flexural vibrations were investigated [78–80]. Furthermore, several studies focussed on nonlinear aspects [81–83] or prestressed microbeams [84, 85]. In 2006 De et al. [86] modified the theory of Lifshitz and Roukes for the case of electrostatically actuated microbeams by substituting the right-hand side of the thermoelastic heat equation by an electrostatic force.

Shieh [87] developed an approach to calculate TED in beams based on Timoshenko theory. This allows the application to thick beams. In the system of thermoelastically coupled differential equations, both the shear deformation and the angle of

rotation of the normal to the beam axis are included. Additionally, heat fluxes in the longitudinal direction are included and the thermal boundary conditions at both ends of the beam are defined. The author uses a two-way coupling to describe not only the changes in the temperature field but also the effects of the thermoelastic coupling on the structural vibrations. The results are presented for beams of different slenderness and set in comparison with Zener's theory. For slender beams ( $h/l \ll 1$ ) the influence of shear deformation is hardly present. As the thickness/length ratio increases, it becomes more important. In addition, a dependence on the excitation frequency is shown. In the vicinity of the peak frequency, the theory agrees very well with Zener's calculation. With increasing excitation frequency, deviations of up to 13 % arise. In a second publication Shieh [88] generalized his theory and considered numerous boundary conditions. In 2015 Parayil et al. [89] extended the approach by a FE solution for the thermoelastic coupling in Timoshenko beams.

### 3.3.2 Rate of Generated Heat

In a further publication in 1938 Zener introduced a second approach to calculate the thermoelastic loss factor of a thin bending beam [65]. Based on the entropy generation due to stress inhomogeneities in a thermoelastic solid, he calculated the amount of mechanical energy that is transformed into heat in one vibration cycle. This derivation results in the same formula as the calculation of dissipated mechanical energy as shown in the following. The author uses only thermodynamical considerations to calculate TED. As a starting point the rate of entropy change  $\dot{S}$  caused by irreversible heat conduction in a solid is given in terms of the heat flux  $q_i$  and the temperature  $T$  [90]. The absolute temperature  $T$  is the sum of ambient temperature  $T_0$  and the temperature variation  $\theta$ .

$$\dot{S} = \int_V -\frac{q_{i,i}}{T} dV \quad (3.3.23)$$

By introducing Fourier's law (see equation 3.2.32) with the thermal conductivity  $\kappa$  the following expression is obtained:

$$\dot{S} = \int_V \kappa \frac{T_{,ii}}{T} dV \quad . \quad (3.3.24)$$

For small temperature fluctuations compared to the ambient temperature  $T_0$  the entropy rate can directly be converted into generated heat.

$$\dot{Q} = \dot{S}T_0 \quad (3.3.25)$$

$$\dot{Q} = \int_V \kappa T_0 \frac{T_{,ii}}{T} dV \quad (3.3.26)$$

By integrating over one period the rise in heat content per cycle is obtained which is equal to the dissipated energy.

$$\Delta Q = \frac{2\pi}{\omega} \left\langle \int_V \kappa T_0 \frac{T_{,ii}}{T} dV \right\rangle \quad (3.3.27)$$

Here  $\langle f(t) \rangle = \frac{1}{t_2 - t_1} \int_{t_1}^{t_2} f(t) dt$  denotes the time average of the function. Applying the thermoelastically coupled heat equation (see equation 3.2.34)  $\kappa T_{,ii}$  can be replaced by  $T_0 \beta \dot{\varepsilon}_{kk} + c_V \dot{\theta}$ . Furthermore,  $T^{-1}$  is substituted by the Taylor series expansion in the vicinity of the ambient temperature  $T_0$ .

$$T^{-1} \approx T_0^{-1} - \theta T_0^{-1} \quad (3.3.28)$$

Assuming very small temperature variations compared to the ambient temperature ( $\theta \ll T_0$ ) the only term producing a non-zero integral over one vibration cycle is  $\beta \dot{\varepsilon}_{kk} \theta$ .

$$\Delta Q = \frac{2\pi}{\omega} \beta \left\langle \int_V \theta \dot{\varepsilon}_{kk} dV \right\rangle \quad (3.3.29)$$

The temperature fluctuation  $\theta$  as well as the volumetric deformation  $\varepsilon_{kk}$  are harmonic functions and can therefore be written as

$$\theta(x, y, z, t) = \bar{\theta}(x, y, z) e^{i\omega t} \quad (3.3.30)$$

$$\varepsilon_{kk}(x, y, z, t) = \bar{\varepsilon}(x, y, z) e^{i\omega t} \quad (3.3.31)$$

By replacing  $\theta$  and  $\varepsilon_{kk}$  in equation 3.3.29 and choosing a suitable time origin,  $\bar{\varepsilon}$  can be made real and  $\bar{\theta}$  complex in general. After calculating the time average, equation 3.3.29 becomes

$$\Delta Q = \beta \int_0^{2\pi/\omega} \int_V -\omega \bar{\varepsilon} \sin(\omega t) \bar{\theta} [\cos(\omega t) + i \sin(\omega t)] dV dt \quad (3.3.32)$$

With

$$\int_0^{2\pi/\omega} \sin^2(\omega t) dt = \frac{\pi}{\omega} \quad \int_0^{2\pi/\omega} \sin(\omega t) \cos(\omega t) dt = 0 \quad (3.3.33)$$

this results in

$$\Delta Q = \pi\beta \int_V \bar{\varepsilon} \operatorname{Im}(\bar{\theta}) dV \quad . \quad (3.3.34)$$

Furthermore, the coupled heat equation 3.2.34 is transformed into the frequency domain:

$$\chi \bar{\theta}_{,ii} - i\omega \bar{\theta} - i\omega \frac{\beta T_0}{c_V} \bar{\varepsilon} = 0 \quad (3.3.35)$$

with the thermal diffusivity  $\chi = \frac{\kappa}{\rho c_V}$ . One approach to solve equation 3.3.35 is the modal decomposition of  $\bar{\theta}(x, y, z)$  into a set of eigenfunctions  $\varphi_j$  that fulfill the Helmholtz equation under the desired boundary conditions.

$$(\nabla^2 + \gamma_j) \varphi_j = 0 \quad (3.3.36)$$

with the eigenvalue  $\gamma_j = \frac{\omega_j}{\chi}$  of the  $j^{\text{th}}$  eigenmode. The quantities  $\bar{\theta}$  and  $\bar{\varepsilon}$  can be decomposed with respect to the orthogonal basis of the vectors  $\varphi_j$ .

$$\bar{\theta} = \sum_j \hat{\theta}_j \varphi_j(x, y, z) \quad (3.3.37)$$

$$\bar{\varepsilon} = \sum_j \hat{\varepsilon}_j \varphi_j(x, y, z) \quad (3.3.38)$$

In general the modal coordinates  $\hat{\theta}_j$  and  $\hat{\varepsilon}_j$  respectively are complex and determined by substituting 3.3.37 into the coupled heat equation (eq. 3.3.35).

$$(\chi \nabla^2 - i\omega) \sum_{j=1}^{\infty} \hat{\theta}_j \varphi_j + i\omega \frac{\beta T_0}{c_V} \bar{\varepsilon} = 0 \quad (3.3.39)$$

The equation is multiplied with the eigenfunction  $\varphi_k$  and integrated over the solid.

$$\int \underbrace{\varphi_k (\chi \nabla^2 + \omega_k - i\omega - \omega_k)}_{=0} \sum_{j=1}^{\infty} \hat{\theta}_j \varphi_j dV + \int \varphi_k i\omega \frac{\beta T_0}{c_V} \bar{\varepsilon} dV = 0 \quad (3.3.40)$$

Due to the orthogonality of the thermal eigenvectors  $\langle \varphi_j, \varphi_k \rangle = \delta_{jk}$  where  $\langle, \rangle$  symbolizes the inner product, the sum term becomes  $\hat{\theta}_j$  if  $\varphi_k = \varphi_j$  and vanishes for all other cases. The equation is solved with respect to  $\theta_j$ .

$$\hat{\theta}_j = \frac{\int \varphi_j \bar{\varepsilon}_{kk} dV i\omega \frac{\beta \alpha T_0}{c_V}}{(i\omega + \omega_j)} = \frac{\beta \alpha T_0}{c_V} \int \varphi_j \bar{\varepsilon}_{kk} dV \frac{i\omega}{i\omega + \omega_j} \quad (3.3.41)$$

Then the imaginary part of  $\hat{\theta}_j$  can be derived.

$$\text{Im}(\hat{\theta}) = \frac{\beta T_0}{c_V} \int_V \bar{\varepsilon} \varphi_j dV \frac{\omega \omega_j}{\omega^2 + \omega_j^2} \quad (3.3.42)$$

For the heat transformation per cycle the following term is obtained.

$$\Delta Q = \pi \frac{\beta^2 T_0}{c_V} \left( \int_V \bar{\varepsilon} \varphi_j dV \right)^2 \frac{\omega \omega_j}{\omega^2 + \omega_j^2} \quad (3.3.43)$$

The thermoelastic loss factor  $\eta$  is defined as the ratio of dissipated energy  $\Delta Q$  with respect to the total dilation energy  $W_D$ .

$$\eta = \frac{1}{2\pi} \frac{\Delta Q}{W_D} \quad (3.3.44)$$

$$W_D = \frac{1}{2} \int_V \sigma_{kk} \varepsilon_{kk} dV \quad (3.3.45)$$

The dilation energy  $E_s$  is calculated using the stresses and strains causing volume change. Rotational deformations are not connected to the thermal field and therefore neglected in the calculation. For a beam structure (one dimensional) the dilation energy can be obtained by

$$W_D = \frac{1}{2} E \int_V \varepsilon_{kk}^2 dV \quad (3.3.46)$$

and the thermoelastic coupling constant is  $\beta = \alpha E$ . Therefore equation 3.3.44 can be transformed to

$$\eta = \frac{E \alpha^2 T_0}{\rho c_V} \sum_i \frac{\left( \int_V \bar{\varepsilon} \varphi_j dV \right)^2}{\int_V \bar{\varepsilon}^2 dV} \frac{\omega_j \omega}{\omega_j^2 + \omega^2} \quad (3.3.47)$$

The eigenvectors  $\varphi_j$  form a complete orthonormal base, therefore the following relation is satisfied [91].

$$\sum_{i=1}^{\infty} \frac{\left( \int_V \bar{\varepsilon} \varphi_j dV \right)^2}{\int_V \bar{\varepsilon}^2 dV} = 1 \quad (3.3.48)$$

The resulting equation for the thermoelastic loss in a thin bending beam is consistent with equation 3.3.20, but was derived based on the entropy generation during a thermomechanical vibration cycle.

$$\eta = \frac{E \alpha^2 T_0}{\rho c_V} \frac{\omega_j \omega}{\omega_j^2 + \omega^2} \quad (3.3.49)$$

In 1994 Kinra et al. [92] derived an approach similar to Zener to calculate the produced entropy in a mechanical vibration based on the second law of thermodynamics. The authors applied the method to a beam with flexural vibration as well as a rod with a thermoelastic interface and therefore heterogeneous material properties. For validation they used numerical results and experimental data from an own previous publication [93]. Some years later Bishop et al. [94] extended this approach to laminated sections of flexural beams.

Duwel et al. [95] presented a weakly coupled approach based on the entropy generation of one vibration cycle. The authors used the eigenvalue solution of the thermoelastically coupled heat equation to calculate the transferred mechanical energy and determine the quality factor (inverse of the loss factor) of silicon microresonators. The method is built on the derivation of Zener presented in this chapter. The results are compared to analytical solutions, fully coupled numerical solutions and experimental data from literature.

Chandorkar et al. [96] developed an analytical formula to obtain the thermoelastic loss factor in plate-like microstructures. The authors focussed on the dependency of the energy loss on the mode shape and used a projection of the structural mode shapes on the thermal mode shapes to calculate mode-dependent weighting factors. The approach is based on entropy generation and results in a weighted sum of Zener formulas. They applied the expression on structures with flexural, torsional and bulk modes. Due to the projection they considered more than one thermal mode (unlike Zener) and proved that in multi-dimensional structures there is not only one dominant relaxation time.

Hao et al. [97, 98] derived an entropy based formulation for the TED in thin resonators with variable geometry. For the first time the authors cover anisotropic material with their theory. They formulate a numerical algorithm to include TED in commercial FE analyses by first simulating the mechanical strains and energy and using them as a source term in a transient thermal simulation. They verified the approach on microresonators with simple and complex geometry like tuning forks or disc resonators.

Tai et al. [99] provided an analytical model to calculate the entropy generation and TED in flexural beams. Later, the authors extended their method on plate structures under various boundary conditions [100] and ring structures [101].

### **3.3.3 Thermoelastic Damping in Plate Structures**

In the decades following Zener's pioneering publications, intensive research has been conducted to find analytical formulas for calculating TED beyond its application in thin beams. Although formulations for arbitrary bodies easily become complex and

cumbersome, considerable progress has been made for thin plates. In the following, the developments of thermoelastic plate theories as well as approaches for the simplified determination of TED in plates are presented.

In 1961 Ignaczak and Nowacki [102, 103] derived the basic equations of thermoelastic coupling in plates in the case of thermally induced transversal vibrations. In a later standard reference, Nowacki provides a detailed derivation of thermoelastic plate equations for the plane strain and plane stress cases and discusses numerous examples [60]. However, the temperature is solved via the uncoupled heat conduction equation, which neglects the influence of the strain field on the temperature change. In this case of one-way coupling the application is limited to thermal excitation.

Chadwick [68] developed a two-way coupled equation system by reducing his general three-dimensional theory to plate structures [66]. The author gives formulations for longitudinal and flexural vibrations. The equation for flexural vibration can be described as an extension of the Kirchhoff plate equation by a thermal coupling term.

$$D\Delta^2 w + D\alpha(1 + \nu)\Delta I_T + \rho h w_{,tt} = 0 \quad (3.3.50)$$

$$c_V \theta_t - \kappa \Delta \theta - \frac{z\alpha T E}{1 - \nu} \Delta w_t = 0 \quad (3.3.51)$$

In this closed pair of partial differential equations  $D = \frac{Eh^3}{12(1 - \nu^2)}$  is the bending stiffness of the plate. The thermal moment  $I_T$  is calculated as

$$I_T = \frac{1}{I} \int_{-h/2}^{h/2} z\theta \, dz. \quad (3.3.52)$$

with the second moment of inertia  $I$ . In most of the research studies subsequently published, equation 3.3.50 for calculating plate deflection is used. However, different approaches have been developed to determine the temperature distribution in the plate. In 1989, Langnese and Lions [104] provided a thorough theory that takes into account various boundary conditions. In comparison to Chadwick's method, the temperature  $\theta$  in the thermoelastically coupled heat equation (equation 3.3.51) is replaced by a thermal moment which is defined to be independent of the  $z$ -coordinate. For simplification, a linear temperature distribution in  $z$  is assumed. This approach was used as a starting point for many further studies of thermoelastic plate equations (e.g.[105–107]). Most of the authors did not focus on the mechanical application but on mathematical considerations of the coupled differential equations. However, e.g. Kim [108] and Enomoto [109] proved an exponential decay in time mathematically. Simmonds [110] developed a thermoelastic plate model which is described by a single

differential equation concerning the plate deflection. The thermoelastic component was introduced similar to a viscous damper. This equation is a simplification of the Langnese model at the cost of the accuracy of the damping effect. The thermoelastic loss behaviour results in a monotonically increasing function dependent on the frequency, which agrees with the peak behaviour of the other models only in low frequency ranges.

Norris [111] also developed a single equation for plate deflection with viscoelastic behaviour for isotropic and orthotropic plates. In the case of isotropic materials, the TED terms are included in the bending stiffness, which results in a complex-valued stiffness term. In a following publication [112], the author compared his formulation to three other thermoelastic plate theories mentioned before [66, 104, 110] considering the effects for the attenuation of flexural waves.

Furthermore, procedures for a simplified calculation of general structures have been developed over the last two decades. In 2002 Houston et al. [113, 114] and Photiadis et al. [115] calculated the thermoelastic loss factor due to transverse thermal currents in microscale resonators. The authors used Zener's formula for thin bending beams as a basis and adapted it to mode shapes of a plate which include torsional components besides bending. The flexural part in the resonant modes is calculated by using the ratio of bending energy to total strain energy. This "modal participation factor" reduces the damping ratio according to Zener to a mode-dependent loss factor. The results are validated with experimental values.

In 2005 Norris et al. [111] published a comprehensive model of TED in plate structures. First the authors extended the approach of [114] by including lateral strains and therefore considering the two-dimensional state of stress. Furthermore they introduce a formulation for orthotropic plates using direction dependent material parameters (Young's modulus, Poisson's ratio, thermal expansion coefficient).

Nayfeh et al. [116] developed a numerical expression for the thermoelastic loss in microplates of general shapes and boundary conditions. The authors reduced the thermoelastically coupled heat equation to a temperature flow in thickness direction and solved the differential equation system by a perturbation method. They especially considered electrostatic loading.

Sun and Tohmyoh [117] derived an analytical expression for circular thin plates in out-of-plane vibration. The result is similar to the expression of Lifshitz and Roukes' equation for the calculation of TED in thin beams (see equation 3.3.22), but includes the effect of lateral strains in plate deformation. Initially the authors considered axisymmetric vibrations. In a later publication Sun and Saka [118] extended and verified the approach for non-axisymmetric mode shapes of circular plates. In their derivation they assumed the strain in thickness direction of the plate to be zero ( $\varepsilon_{zz} = 0$ ) according to the Kirchhoff plate theory. Li et al. [119]

used this approach and considered in addition the case of  $\varepsilon_{zz} \neq 0$ .

Tai et al. applied their model of entropy generation [100] (see chapter 3.3.2) to thin microplates. The approach shows a good agreement to other analytical and numerical models but does not consider the torsional part of the mode shapes in plate structures, just like the methods in [117–119]. Therefore the authors extended their model in order to consider the coupling effect between torsion and bending [120]. This results in a calculation similar to [114] and [111] using the ratio of flexural energy to total strain energy. The same approach was validated by Metcalf et al. [121]. The authors compared analytically determined damping ratios to experimental values and showed that TED can be calculated effectively using the Zener formula in combination with a modal participation factor.

Cagnoli et al. [122] conducted a series of experiments on circular silicon plates and investigated the mode dependent TED. They derived a formula for the general thermoelastic loss in cylinders equivalent to approach of Zener. Furthermore they define mode families to classify the damping behaviour with respect to the mode shapes and also use the flexural (or dilational) energy to calculate the thermoelastic loss.

### 3.4 Thermoelastic Coupling in Finite Element Analysis

For complex structures, analytical solution methods often reach computational limits. With respect to numerical solution methods, the finite element method will be considered in this thesis as one of the most widely used numerical solution techniques in engineering. There are numerous methods for coupling mechanical and thermal problems in FEM [123–126]. However, the point of correct representation of thermoelastic damping is often neglected.

One promising approach was presented in 2009 by Serra and Bonaldi [9]. The authors developed fully coupled thermoelastic elements and set their focus on the implementation of damping terms. The method was realized in the FE software ANSYS for plate and solid elements. The FE formulation is outlined in detail since the ANSYS solution is used for the verification of the new approaches in this thesis. As a basis, the deduction of the element formulation for an elastic solid element is presented, followed by the thermoelastic element according to Serra and Bonaldi. The derivation is shown by the example of a 20-node solid element. At the end of this section, numerical solution techniques for time-dependent FE problems are described. For a thorough insight into the FEM please refer to the books of Bathe [127], Zienkiewicz [128] or Hughes [129].

### 3.4.1 Elastic Solid Element

The governing equation of linear elasticity in local form for a volume  $V$  without damping term is written as

$$\sigma_{ij,j} + b_i = \rho \ddot{u}_i \quad . \quad (3.4.1)$$

The core of the FEM is to find an approximate solution for the differential equation. In a first step, the weak form of the problem is formulated. This form has the advantage that the differential equation does not have to be satisfied at every point, but rather averaged over an integral. In addition, the order of derivatives is reduced by one, so that the solution function in general only has to be simply differentiable. First, the equation is multiplied by an appropriate arbitrary function. One common possibility is the use of a variational term  $\delta u_i$ . Subsequently this product is integrated over the spatial domain  $V$ .

$$\int_V (\sigma_{ij,j} + b_i - \rho \ddot{u}_i) \delta u_i \, dV = 0 \quad (3.4.2)$$

To remove the spatial derivative the first term is integrated by parts and the divergence theorem is applied. Furthermore the derivative of  $\delta u_i$  is substituted using the kinematic relation  $\varepsilon_{ij} = \frac{u_{i,j} + u_{j,i}}{2}$ .

$$\int_V \sigma_{ij,j} \delta u_i \, dV = - \int_V \sigma_{ij} \delta \varepsilon_{ij} \, dV + \int_{\Gamma_{el}} \sigma_{ij} \mathbf{n}_j \delta u_i \, d\Gamma_{el} \quad (3.4.3)$$

For the weak form of the EOM it follows

$$\int_V (b_i - \rho \ddot{u}_i) \delta u_i \, dV - \int_V \sigma_{ij} \delta \varepsilon_{ij} \, dV + \int_{\Gamma_{el}} \sigma_{ij} \mathbf{n}_j \delta u_i \, d\Gamma_{el} = 0. \quad (3.4.4)$$

The displacement  $u$  is approximated with shape functions  $N_i$ . The matrix  $\mathbf{N}_e$  is matrix of shape functions for displacement DOF and has a size of  $3n \times 1$  where  $n$  is the number of nodes in the element. The same approximation is used for the interpolation of the variational field.

$$\mathbf{u} = \mathbf{N}_e \mathbf{v} \quad \delta \mathbf{u} = \mathbf{N}_e \delta \mathbf{v} \quad (3.4.5)$$

where  $\mathbf{v} = \left\{ u_1^1 \quad u_2^1 \quad u_3^1 \quad \dots \quad u_1^{20} \quad u_2^{20} \quad u_3^{20} \right\}$  is the vector of nodal displacements. In an elastic solid element with quadratic shape functions there are twenty nodes with

three DOF each.

$$\mathbf{u} = \begin{Bmatrix} u_1 \\ u_2 \\ u_3 \end{Bmatrix} = \begin{bmatrix} N_1 & 0 & 0 & & N_{20} & 0 & 0 \\ 0 & N_1 & 0 & \dots & 0 & N_{20} & 0 \\ 0 & 0 & N_1 & & 0 & 0 & N_{20} \end{bmatrix} \begin{Bmatrix} u_1^1 \\ u_2^1 \\ u_3^1 \\ \vdots \\ u_1^{20} \\ u_2^{20} \\ u_3^{20} \end{Bmatrix} \quad (3.4.6)$$

To derive the system matrices, each term of equation 3.4.4 is handled separately.

$$\int_V \delta u_i^T \rho \ddot{u}_i dV = \int_V \delta \mathbf{v}^T \mathbf{N}_e^T \rho \mathbf{N}_e \ddot{\mathbf{v}} dV = \delta \mathbf{v}^T \mathbf{M} \ddot{\mathbf{v}} \quad (3.4.7)$$

$$\text{with } \mathbf{M} = \sum_e \int_{V^e} \rho \mathbf{N}_e^T \mathbf{N}_e dV \quad (3.4.8)$$

The mass matrix  $\mathbf{M}$  is built of the density in combination with the shape functions. The integration is done elementwise and summed up over the volume of the solid. The size of  $\mathbf{M}$  is  $3n \times 3n$ .

As a basis for the derivation of the stiffness matrix the kinematic relation and the constitutive law are considered. The nodal displacements are connected to the strains via matrix  $\mathbf{B}_e$ . The matrix contains derivatives of the shape functions and has the size  $6 \times 3n$  (for a three-dimensional solid).

$$\boldsymbol{\varepsilon} = \mathbf{B}_e \mathbf{v} \quad (3.4.9)$$

$$\boldsymbol{\varepsilon} = \begin{Bmatrix} \varepsilon_x \\ \varepsilon_y \\ \varepsilon_z \\ \gamma_{xy} \\ \gamma_{yz} \\ \gamma_{zx} \end{Bmatrix} = \begin{bmatrix} \frac{\partial N_1}{\partial x} & 0 & 0 & & \frac{\partial N_{20}}{\partial x} & 0 & 0 \\ 0 & \frac{\partial N_1}{\partial y} & 0 & & 0 & \frac{\partial N_{20}}{\partial y} & 0 \\ 0 & 0 & \frac{\partial N_1}{\partial z} & \dots & 0 & 0 & \frac{\partial N_{20}}{\partial z} \\ \frac{\partial N_1}{\partial y} & \frac{\partial N_1}{\partial x} & 0 & & \frac{\partial N_{20}}{\partial y} & \frac{\partial N_{20}}{\partial x} & 0 \\ 0 & \frac{\partial N_1}{\partial z} & \frac{\partial N_1}{\partial y} & & 0 & \frac{\partial N_{20}}{\partial z} & \frac{\partial N_{20}}{\partial y} \\ \frac{\partial N_1}{\partial z} & 0 & \frac{\partial N_1}{\partial x} & & \frac{\partial N_{20}}{\partial z} & 0 & \frac{\partial N_{20}}{\partial x} \end{bmatrix} \begin{Bmatrix} u_1^1 \\ u_2^1 \\ u_3^1 \\ \vdots \\ u_1^{20} \\ u_2^{20} \\ u_3^{20} \end{Bmatrix} \quad (3.4.10)$$

The stresses are coupled with the strains via the constitutive or material law. The elasticity tensor  $\mathbf{E}$  depends on the material model.

$$\boldsymbol{\sigma} = \mathbf{E}\boldsymbol{\varepsilon} = \mathbf{E}\mathbf{B}_e\mathbf{v} \quad (3.4.11)$$

The stiffness matrix results from the second term of equation 3.4.4 as follows:

$$\int_V \delta\varepsilon_{ij}^T \sigma_{ij} dV = \int_V \delta\mathbf{v}^T \mathbf{B}_e^T \mathbf{E} \mathbf{B}_e \mathbf{v} dV = \delta\mathbf{v}^T \mathbf{K}_e \mathbf{v} \quad (3.4.12)$$

$$\text{with } \mathbf{K}_e = \sum_e \int_{V^e} \mathbf{B}_e^T \mathbf{E} \mathbf{B}_e dV \quad (3.4.13)$$

The elastic stiffness matrix has a size of  $3n \times 3n$ .

Body forces and tension at the surface of the continuum can be summarized in the force vector  $\mathbf{b}_e$ . The surface tension  $t_i$  is defined with respect to the stress tensor  $\sigma_{ij} = \sigma_{ji}$  and the normal vector of the body surface  $\mathbf{n}_j$ .

$$t_i = \sigma_{ji} \mathbf{n}_j \quad (3.4.14)$$

The force vector is assembled as follows:

$$\int_V \delta u_i^T b_i dV + \int_{\Gamma_{el}} \delta u_i^T t_i d\Gamma_{el} = \int_V \delta\mathbf{v}^T \mathbf{B}_e^T \mathbf{b} dV + \int_{\Gamma_{el}} \delta\mathbf{v}^T \mathbf{B}_e^T \mathbf{t} d\Gamma_{el} = \delta\mathbf{v}^T \mathbf{b}_e \quad (3.4.15)$$

$$\text{with } \mathbf{b}_e = \sum_e \int_{V^e} \mathbf{B}_e^T \mathbf{b} dV + \sum_e \int_{\Gamma_{el}^e} \mathbf{B}_e^T \mathbf{t} d\Gamma_{el} \quad (3.4.16)$$

With the assembled system matrices the discretized form of the (weak) EOM results.

$$\delta\mathbf{v}^T \mathbf{M}\ddot{\mathbf{v}} + \delta\mathbf{v}^T \mathbf{K}_e \mathbf{v} = \delta\mathbf{v}^T \mathbf{b}_e \quad (3.4.17)$$

The variations of the nodal point displacements  $\delta\mathbf{v}$  are arbitrary. Therefore equation 3.4.17 only holds if

$$\mathbf{M}\ddot{\mathbf{v}} + \mathbf{K}_e \mathbf{v} = \mathbf{b}_e \quad (3.4.18)$$

is fulfilled.

### 3.4.2 Thermoelastic Solid Element

In addition to the EOM for an elastic solid 3.4.1 the second governing equation for a thermoelastic solid is the balance equation for entropy (see equation 3.2.31).

$$T_0 \dot{s} + q_{i,i} = 0 \quad (3.4.19)$$

In order to derive the weak form of this equilibrium, the equation is multiplied with the variation of the temperature increment  $\delta\theta$  and integrated over the volume of the solid  $V$ .

$$r \int_V (T_0 \dot{s} + q_{i,i}) \delta\theta \, dV = 0 \quad (3.4.20)$$

On the second term integration by parts and the divergence theorem are applied.

$$\int_V q_{i,i} \delta\theta = - \int_V q_i \delta\theta_{,i} \, dV + \int_{\Gamma_{th}} q_i \mathbf{n}_i \delta\theta \, d\Gamma_{th} \quad (3.4.21)$$

For the weak form of the entropy balance equation it follows

$$\int_V T_0 \dot{s} \delta\theta \, dV - \int_V q_i \delta\theta_{,i} \, dV + \int_{\Gamma_{th}} q_i \mathbf{n}_i \delta\theta \, d\Gamma_{th} = 0. \quad (3.4.22)$$

Equation 3.4.22 is combined with equation 3.4.4 to the weak form of the thermoelastic governing equation. Due to the thermomechanical coupling the stress tensor  $\sigma_{ij}$  and the entropy term  $s$  are substituted by the constitutive equations 3.2.18 and 3.2.19 respectively. Furthermore, Fourier's law is introduced (see equation 3.2.32).

$$\sigma_{ij} = E_{ijkl} \varepsilon_{kl} - \beta\theta \quad (3.4.23)$$

$$s = \beta \varepsilon_{ij} + \frac{c_V}{T_0} \theta \quad (3.4.24)$$

$$q_i = -\kappa \theta_{,i} \quad (3.4.25)$$

$$\begin{aligned} & \int_V \delta \varepsilon_{ij} E_{ijkl} \varepsilon_{kl} \, dV - \int_V \beta \theta \delta \varepsilon_{ij} \, dV + \int_V \delta u_i \rho \ddot{u}_i \, dV \\ & + T_0 \int_V \beta \dot{\varepsilon}_{ij} \delta\theta \, dV + \int_V c_V \dot{\theta} \delta\theta \, dV + \int_V \delta \theta_{,i} \kappa_{ij} \theta_{,j} \, dV \\ & = \int_V b_i \delta u_i \, dV + \int_{\Gamma_{el}} \sigma_{ij} \mathbf{n}_j \delta u_i \, d\Gamma_{el} - \int_{\Gamma_{th}} q_i \mathbf{n}_i \delta\theta \, d\Gamma_{th} \end{aligned} \quad (3.4.26)$$

In addition to the system matrices derived in section 3.4.1 the coupled element contains damping and further stiffness terms as well as thermal boundary forces. In the thermoelastic solid element each node contains four DOF: three mechanical (displacement in x, y and z) and the temperature. Therefore, additional shape functions to interpolate the thermal distribution are introduced and collected in the matrix  $\mathbf{N}_{\text{th}}$ . The vector  $\boldsymbol{\theta} = \{\theta^1 \ \theta^2 \ \dots \ \theta^{20}\}$  consists of the nodal temperatures and has a size of  $n \times 1$ .

$$\boldsymbol{\theta} = \mathbf{N}_{\text{th}}\boldsymbol{\theta} \quad (3.4.27)$$

Therefore  $\mathbf{N}_{\text{th}}$  has a size of  $1 \times n$ .

Due to the thermal and thermoelastic terms in the governing equation that are related to the first derivative of mechanical and thermal DOF, damping elements are included in the system matrices. TED matrix  $\mathbf{C}_{\text{th,e}}$ :

$$T_0 \int_V \delta\theta^T \beta_{ij} \dot{\epsilon}_{ij} dV = T_0 \int_V \delta\theta^T \mathbf{N}_{\text{th}}^T \boldsymbol{\beta} \mathbf{B}_e \dot{\mathbf{v}} dV = T_0 \delta\theta^T \mathbf{C}_{\text{th,e}} \dot{\mathbf{v}} \quad (3.4.28)$$

$$\text{with } \mathbf{C}_{\text{th,e}} = \sum_e \int_{V_e} \mathbf{N}_{\text{th}}^T \boldsymbol{\beta} \mathbf{B}_e dV \quad (3.4.29)$$

Thermal damping matrix  $\mathbf{C}_{\text{th}}$ :

$$\int_V \delta\theta^T c_V \dot{\theta} dV = \int_V c_V \delta\theta^T \mathbf{N}_{\text{th}}^T \mathbf{N}_{\text{th}} \dot{\theta} dV = \delta\theta^T \mathbf{C}_{\text{th}} \dot{\theta} \quad (3.4.30)$$

$$\text{with } \mathbf{C}_{\text{th}} = \sum_e \int_{V_e} c_V \mathbf{N}_{\text{th}}^T \mathbf{N}_{\text{th}} dV \quad (3.4.31)$$

Thermoelastic stiffness matrix:

$$- \int_V \delta \varepsilon_{ij}^T \beta_{ij} \theta dV = - \int_V \delta \mathbf{v}^T \mathbf{B}_e^T \boldsymbol{\beta} \mathbf{N}_{\text{th}} \theta dV = - \delta \mathbf{v}^T \mathbf{K}_{\text{e,th}} \theta \quad (3.4.32)$$

$$\text{with } \mathbf{K}_{\text{e,th}} = \sum_e \int_{V_e} \mathbf{B}_e^T \boldsymbol{\beta} \mathbf{N}_{\text{th}} dV \quad (3.4.33)$$

The matrix  $\boldsymbol{\beta}$  includes the thermoelastic coupling constants and has the size of  $6 \times 1$ . Therefore the coupling matrix  $\mathbf{K}_{\text{e,th}}$  has the size of  $3n \times n$ .

In order to derive the stiffness matrix  $\mathbf{K}_{\text{th}}$  it is necessary to introduce the matrix  $\mathbf{B}_{\text{th}}$  that includes the spatial derivatives of the thermal shape functions and has the size  $3 \times n$ .

$$\nabla \theta = \mathbf{B}_{\text{th}} \boldsymbol{\theta} \quad (3.4.34)$$

$$\int_V \delta\theta_{,i}^T \kappa \theta_{,i} dV = \int_V \delta\theta^T \mathbf{B}_{th}^T \kappa \mathbf{B}_{th} \theta dV = \delta\theta^T \mathbf{K}_{th} \theta \quad (3.4.35)$$

$$\text{with } \mathbf{K}_{th} = \sum_e \int_{V^e} \mathbf{B}_{th}^T \kappa \mathbf{B}_{th} dV \quad (3.4.36)$$

Assuming a prescribed heat flux at the boundary with thermal boundary conditions  $\Gamma_{th}$  the thermal force vector can be assembled as follows:

$$- \int_{\Gamma_{th}} \delta\theta^T q_i \mathbf{n}_i d\Gamma_{th} = - \int_{\Gamma_{th}} \mathbf{N}_{th}^T \delta\theta^T \mathbf{n} \mathbf{q} d\Gamma_{th} = -\delta\theta^T \mathbf{b}_{th} \quad (3.4.37)$$

$$\text{with } \mathbf{b}_{th} = \sum_e \int_{V^e} \mathbf{N}_{th}^T \mathbf{n} \mathbf{q} d\Gamma_{th} \quad (3.4.38)$$

Matrix system for the thermoelastically coupled EOM:

$$\begin{bmatrix} \mathbf{M} & 0 \\ 0 & 0 \end{bmatrix} \begin{Bmatrix} \ddot{\mathbf{v}} \\ \ddot{\theta} \end{Bmatrix} + \begin{bmatrix} 0 & 0 \\ \mathbf{C}_{th,e} & \mathbf{C}_{th} \end{bmatrix} \begin{Bmatrix} \dot{\mathbf{v}} \\ \dot{\theta} \end{Bmatrix} + \begin{bmatrix} \mathbf{K}_e & -\mathbf{K}_{e,th} \\ 0 & \mathbf{K}_{th} \end{bmatrix} \begin{Bmatrix} \mathbf{v} \\ \theta \end{Bmatrix} = \begin{Bmatrix} \mathbf{b}_e \\ \mathbf{b}_{th} \end{Bmatrix} \quad (3.4.39)$$

### 3.4.3 Finite Element Analysis of Dynamically Excited Systems

The EOM shown above for an elastic solid (equation 3.4.18) and a thermoelastic solid (equation 3.4.39) represent mathematically a system of linear differential equations. They can be solved in the time domain, i.e. by a temporal discretization. This transient method is suitable for arbitrary input and responses. Furthermore, the solution can be obtained in the frequency domain. The system is solved for a particular excitation frequency per solution step before considering the next frequency step. This results in a frequency spectrum. In each step input and response are single frequency sinusoidal.

A further distinction can be made concerning the solution procedure. Direct integration methods solve the system of equations in terms of physical DOF without prior transformation. The second procedure, mode superposition, is characterized by a transformation of the equations into modal coordinates. Both methods are introduced in the following.

### 3.4.3.1 Time Domain

In numerical time integration methods, the solution is found at discrete time intervals  $\Delta t$ . There are various techniques considering different approximations of displacement, velocity and acceleration within each time step. The solution technique has an impact on the stability, accuracy and computational cost of the analysis.

In general, explicit and implicit time integration schemes can be distinguished. Using explicit methods the displacement solution for time step  $t + \Delta t$  can be solved directly without an inversion of the stiffness matrix based on the solution of previous time steps. In an implicit time integration, the equation of motion is solved for time step  $t + \Delta t$ . An iterative solution within each time step is necessary. Detailed descriptions of different time integration schemes can be found e.g. in [127, 128, 130].

Typical examples for explicit integration approaches are Finite Difference Method (FDM). The first derivative of the displacement  $\dot{u}$  is approximated by a difference quotient. The forward difference method uses the current and the following time step

$$\dot{u}^t = \frac{u^{t+\Delta t} - u^t}{\Delta t} \quad (3.4.40)$$

and the central difference method considers two time steps from  $t - \Delta t$  to  $t + \Delta t$ .

$$\dot{u}^t = \frac{u^{t+\Delta t} - u^{t-\Delta t}}{2\Delta t} \quad (3.4.41)$$

For the acceleration in the central difference method we get

$$\ddot{u}^t = \frac{u^{t+\Delta t} - 2u^t + u^{t-\Delta t}}{\Delta t^2} \quad (3.4.42)$$

By substituting equation 3.4.42 into the equation of motion, the following formulation is obtained:

$$\left( \frac{1}{\Delta t^2} \mathbf{M} + \frac{1}{2\Delta t} \mathbf{C} \right) \mathbf{u}^{t+\Delta t} = \mathbf{b}^t - \left( \mathbf{K} - \frac{2}{\Delta t^2} \mathbf{M} \right) \mathbf{u}^t - \left( \frac{1}{\Delta t^2} \mathbf{M} - \frac{1}{2\Delta t} \mathbf{C} \right) \mathbf{u}^{t-\Delta t} \quad (3.4.43)$$

Therefore  $u^{t+\Delta t}$  can be solved based on the solutions of the previous time step. Explicit time integration methods are conditionally stable, i. e. the stability depends on the size of the time steps. The solution is computationally less costly than implicit solving approaches, but a large number of short time steps is necessary for a stable solution and a good approximation.

Two solution approaches for implicit time integration methods are presented here. They are often used in commercial FE software [131, 132].

Probably the most common procedure is the method developed by Newmark in 1959

[133] and its derivatives. The displacement  $\mathbf{u}$  and the velocity  $\dot{\mathbf{u}}$  at time  $t + \Delta t$  are approximated using the following formulas.

$$\dot{\mathbf{u}}^{t+\Delta t} = \dot{\mathbf{u}}^t + \Delta t((1 - \gamma_N)\ddot{\mathbf{u}}^t + \gamma_N\ddot{\mathbf{u}}^{t+\Delta t}) \quad (3.4.44)$$

$$\mathbf{u}^{t+\Delta t} = \mathbf{u}^t + \Delta t\dot{\mathbf{u}}^t + \frac{1}{2}(\Delta t)^2((1 - 2\beta_N)\ddot{\mathbf{u}}^t + 2\beta_N\ddot{\mathbf{u}}^{t+\Delta t}) \quad (3.4.45)$$

The integration parameters  $\beta_N$  and  $\gamma_N$  determine the approximation of the acceleration between two time steps. Therefore they influence the accuracy and stability of the solution. Two well established concepts are the linear acceleration method ( $\beta_N = 1/4$  and  $\gamma_N = 1/2$ ) as well as the trapezoidal rule with constant acceleration proposed by Newmark [133] ( $\beta_N = 1/6$  and  $\gamma_N = 1/2$ ). If  $\gamma_N > 1/2$  numerical dissipation is introduced into the model. This can be desirable in some cases, e.g. to ensure stability and convergence or filter out under-resolved high frequencies. Unfortunately the Newmark method can only consider numerical damping inadequately since the adaption of  $\gamma_N$  is related to a loss of accuracy. Therefore improved integration schemes were developed.

Hilber et al. provided the HHT- $\alpha$ -method in 1977 [134]. It was extended by Hughes in 1987 [129]. They used the Newmark algorithm as a basis and introduced the addition integration parameter  $\alpha_H$  into the EOM.

$$\mathbf{M}\ddot{\mathbf{u}}^{t+\Delta t} + (1 + \alpha_H)\mathbf{C}\dot{\mathbf{u}}^{t+\Delta t} - \alpha_H\mathbf{C}\dot{\mathbf{u}}^t + (1 + \alpha_H)\mathbf{K}\mathbf{u}^{t+\Delta t} - \alpha_H\mathbf{K}\mathbf{u}^t = \mathbf{b}^{t+\alpha_H\Delta t} \quad (3.4.46)$$

If  $\alpha_H = 0$  the approach reduces to the Newmark method. Usually it should be set to  $-1/3 \leq \alpha_H \leq 0$  to guarantee unconditional stability. With decreasing  $\alpha_H$  the amount of numerical dissipation increases.

### 3.4.3.2 Frequency Domain

Solution procedures in the frequency domain provide the steady-state amplitude and phase of the system response due to sinusoidal excitation. The equation system is solved in frequency steps with a single harmonic excitation frequency in each step. For the overall solution, a frequency sweep over the desired range is performed.

Based on the EOM, the problem is transformed into frequency domain. The force on the right-hand side of the equation is applied harmonically as expressed by the sine term, where  $\varphi_0$  is the phase angle at time  $t = 0$  and  $\Omega$  is the excitation frequency.

$$\mathbf{M}\ddot{\mathbf{u}} + \mathbf{C}\dot{\mathbf{u}} + \mathbf{K}\mathbf{u} = \hat{\mathbf{b}} \sin(\Omega t + \varphi_0) \quad (3.4.47)$$

The harmonic force can be formulated as complex expression

$$\mathbf{b} = \bar{\mathbf{b}}e^{i\Omega t} \quad (3.4.48)$$

with the complex force amplitude  $\bar{\mathbf{b}} = \hat{\mathbf{b}}e^{i\varphi_0} = \hat{\mathbf{b}}(\cos \varphi_0 + i \sin \varphi_0)$  and the maximum force amplitude  $\hat{\mathbf{b}}$  [135]. Similarly to the force, a complex approach for the displacement is adopted with the complex amplitude  $\bar{\mathbf{u}} = \hat{\mathbf{u}}e^{i\varphi} = \hat{\mathbf{u}}(\cos \varphi + i \sin \varphi)$  and the maximum displacement per DOF  $\hat{\mathbf{u}}$ .

$$\mathbf{u} = \bar{\mathbf{u}}e^{i\Omega t} \quad (3.4.49)$$

By substituting the complex force and displacement expressions the differential equation results in

$$\underbrace{(-\Omega^2\mathbf{M} + i\Omega\mathbf{C} + \mathbf{K})}_{\mathbf{K}_c} \bar{\mathbf{u}}e^{i\Omega t} = \bar{\mathbf{b}}e^{i\Omega t}. \quad (3.4.50)$$

The analytical solution for harmonic problems is derived in detail e.g. in [47, 49, 135].

By summarizing the system matrices to the complex matrix  $\mathbf{K}_c$  equation 3.4.50 can be reduced to

$$\mathbf{K}_c \mathbf{u}_c = \mathbf{b}_c \quad (3.4.51)$$

with the complex displacement  $\mathbf{u}_c$  and the complex excitation force  $\mathbf{b}_c$ . In order to solve equation 3.4.51 numerically the same solver used for static analyses can be used, but under consideration of the complex arithmetic. A well-known example is the LDL<sup>T</sup>-solver. Details are provided e.g. in [127].

### 3.4.3.3 Mode Superposition

In systems with a large number of DOF, the direct solution methods of the equations in the time and frequency domains are a computationally intensive problem. Less costly operations can be realized by transformation into the modal space. The conversion to modal coordinates is described in the section concerning modal damping (see section 2.3.4). The equation system, including the system matrices  $\mathbf{M}$ ,  $\mathbf{K}$  and  $\mathbf{C}$ ,

$$\mathbf{M}\ddot{\mathbf{u}} + \mathbf{C}\dot{\mathbf{u}} + \mathbf{K}\mathbf{u} = \mathbf{b} \quad (3.4.52)$$

is transformed to

$$\tilde{\mathbf{M}}\ddot{\mathbf{y}} + \tilde{\mathbf{C}}\dot{\mathbf{y}} + \tilde{\mathbf{K}}\mathbf{y} = \mathbf{b}_m \quad (3.4.53)$$

with the generalized mass matrix  $\tilde{\mathbf{M}} = \Phi^T \mathbf{M} \Phi$ , the generalized damping matrix  $\tilde{\mathbf{C}} = \Phi^T \mathbf{C} \Phi$  and the generalized stiffness matrix  $\tilde{\mathbf{K}} = \Phi^T \mathbf{K} \Phi$ . Due to the transformation with the matrix of the eigenvectors, the generalized system matrices are

diagonalized. Therefore, the equation system in modal space is decoupled with  $n$  equations of the form of an SDOF equation.

$$m_i \ddot{y}_i(t) + c_i \dot{y}_i(t) + k_i y_i(t) = b_{mi} \quad (3.4.54)$$

If the eigenvectors in the modal matrix are mass-normalized, equation 3.4.54 can be simplified as follows

$$\ddot{y}_i(t) + 2\zeta_i \omega_i \dot{y}_i(t) + \omega_i^2 y_i(t) = \frac{b_{mi}}{m_i} \quad (3.4.55)$$

Equation 3.4.55 is solved  $n$ -times for each mode by using the numerical procedures in the time or frequency domain as described above. Since only SDOF equations are solved, this procedure is computational very efficient. The results are  $n$  modal system responses  $y_i$ . For the total system responses, the superposition of the modal parts is necessary.

$$\mathbf{u}(t) = \sum_{i=1}^n \boldsymbol{\phi}_i y_i \quad (3.4.56)$$

The procedure of modal superposition can be summarized as follows:

1. solution of the eigenvalues and eigenvectors
2. transformation of the system matrices into the modal space
3. solution of  $n$  SDOF equations
4. superposition of the response in each mode

The efficiency of the method depends significantly on the number of considered eigenmodes. Theoretically, the number of available modes equals the number of DOF in the system. However, only a small fraction of eigenmodes is computational necessary for mode superposition in order to obtain a good approximation of the exact solution.

### 3.5 Summary and Research Questions

The damping of a vibrating structure is caused by a variety of sources. One way of classifying them is to distinguish internal and external damping. Internal dissipation mechanisms include physical effects in the material such as thermoelasticity or friction on grain boundaries. Interactions with the environment belong to external sources. Friction can either be internal or external, depending on the location of the acting forces. Simplified mechanical models are usually used in the simulation of vibration processes, which summarize all causes. Typical examples are viscous

damping, hysteretic damping, or Rayleigh damping.

Material damping in homogeneous structures is mainly caused by the thermoelastic effect, i. e. a coupling between the stress and strain field and the temperature field. The so-called thermoelastic damping has been identified as the dominant energy loss mechanism in micro- and nanostructures. Therefore much of the current research on thermoelastic damping pays particular attention to the micro-scale. The amount of literature on TED in macrostructures is very limited. Although friction is considered the principal damping source in macroscopic components, it is of interest to study material damping in monolithic structures and large thin-walled components.

Regarding material damping, empirical values are given in the literature as loss factors or damping ratios that can be used in the time-dependent simulations. However, these are considered as material parameters and not as a function of geometry, vibration mode, or excitation frequency. Therefore the development of material damping models that take into account the characteristics of the component as well as the parameters of the vibration is the main focus of this thesis.

Analytical approaches to determine the thermoelastic damping can be obtained by solving the thermoelastically coupled heat conduction equation as well as the coupled equations of motion. For one-dimensional problems (thin beams), there are well established analytical solutions. When extended to two and three dimensions, the solution quickly becomes very inconvenient. For the case of thin plates, promising analytical approaches were developed if the underlying geometry is straightforward (rectangular and circular plates, rings etc.). It is desirable to find a general method for plate structures in any geometry.

Fully thermoelastically coupled finite elements are available for the numerical simulation of vibration processes with thermoelastic damping. These allow the creation of a damping matrix and can consider the dissipated energy very well. However, with these element formulations a solution is only possible by direct integration methods. In each time or frequency step, the thermoelastically coupled system of equations must be solved. For this reason, the numerical solution using this method is computationally very expensive and not suitable for practical application. This motivates the development of simplified approaches to include thermoelastic damping effects in FE simulations.

Accordingly, the research questions that define the objectives of this thesis can be summarized as follows:

- analyze the thermoelastic damping on macrostructures experimentally and numerically
- develop efficient algorithms to consider thermoelastic damping in FE simulations, preferably in an analysis based on mode superposition
- the methods should be applicable to three-dimensional solid structures as well as thin-walled structures



# Chapter 4

## Experimental studies

### 4.1 Introduction

In this chapter, the experimental studies are presented. For verification of the developed simulation approaches, reliable experimental data are required. In order to be able to measure material damping, a test setup that excludes or minimizes other sources of energy dissipation is developed. The experimental rig must be partially installed in a vacuum chamber, which influences the selection of the components as well as the execution of the experiments.

First, the investigated samples are presented. In order to determine the exact test setup, i.e., the suspension, excitation, and measurement points for each component, a modal analysis is performed numerically. Subsequently, the execution of the experiments and the evaluation of the recorded data are explained. The experimental setup is put in context with approaches in the literature. The measurement results are shown and discussed in various aspects. Finally, possible sources of error in the experiment are listed, which influence the interpretation of the experimental results.

### 4.2 Experimental Samples

#### 4.2.1 Material

In order to ensure comparability and to keep the number of influences low, all test samples should be manufactured from the same material. One of the test objects, a thin protection plate, is actually used in automotive industry. Therefore the material of the plate, an aluminum alloy (AlMg4.5Mn0.7), is used as a template for the production of the other experimental samples. The material data from the manufacturer were used in the simulations [136]. These are listed in Table 4.1.

parameter	value	unit
Young's modulus $E$	$7 \times 10^{10}$	N/m <sup>2</sup>
Poisson's ratio $\nu$	0.34	
density $\rho$	2660	kg/m <sup>3</sup>
thermal conductivity $\lambda$	130	W/mK
heat capacity $C_p$	900	J/K
thermal expansion coefficient $\alpha$	$2.31 \times 10^{-5}$	K <sup>-1</sup>

**Table 4.1:** Material parameters of aluminium alloy AlMg4.5Mn0.7 [136]

## 4.2.2 Rectangular Plate

As a basic example, a rectangular plate structure was chosen. The reduced geometry has advantages for the experimental setup as well as the numerical approaches. The straightforward form and size, as well as the easy to calculate eigenmodes, make it suitable as a basis for the development and verification of the simulation methods. The dimensions were chosen so that the component could be suspended in the vacuum chamber without touching the walls. The plate size used is 300 mm x 200 mm x 3 mm.

As a preparation for the experiments, a numerical modal analysis was performed. The eigenfrequencies and mode shapes for the first sixteen eigenmodes of the rectangular plate are demonstrated in table 4.2. The eigenfrequency analysis was done without boundary conditions, i.e., assuming free support. In the presentation of the eigenmodes, the resulting rigid-body modes are neglected.

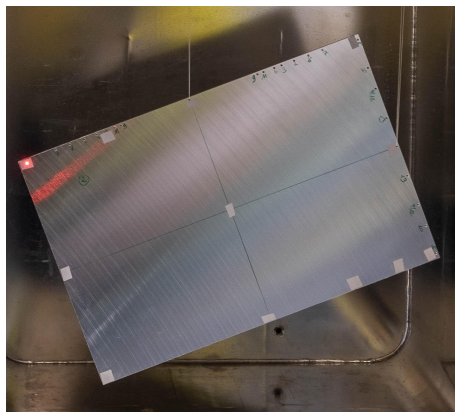
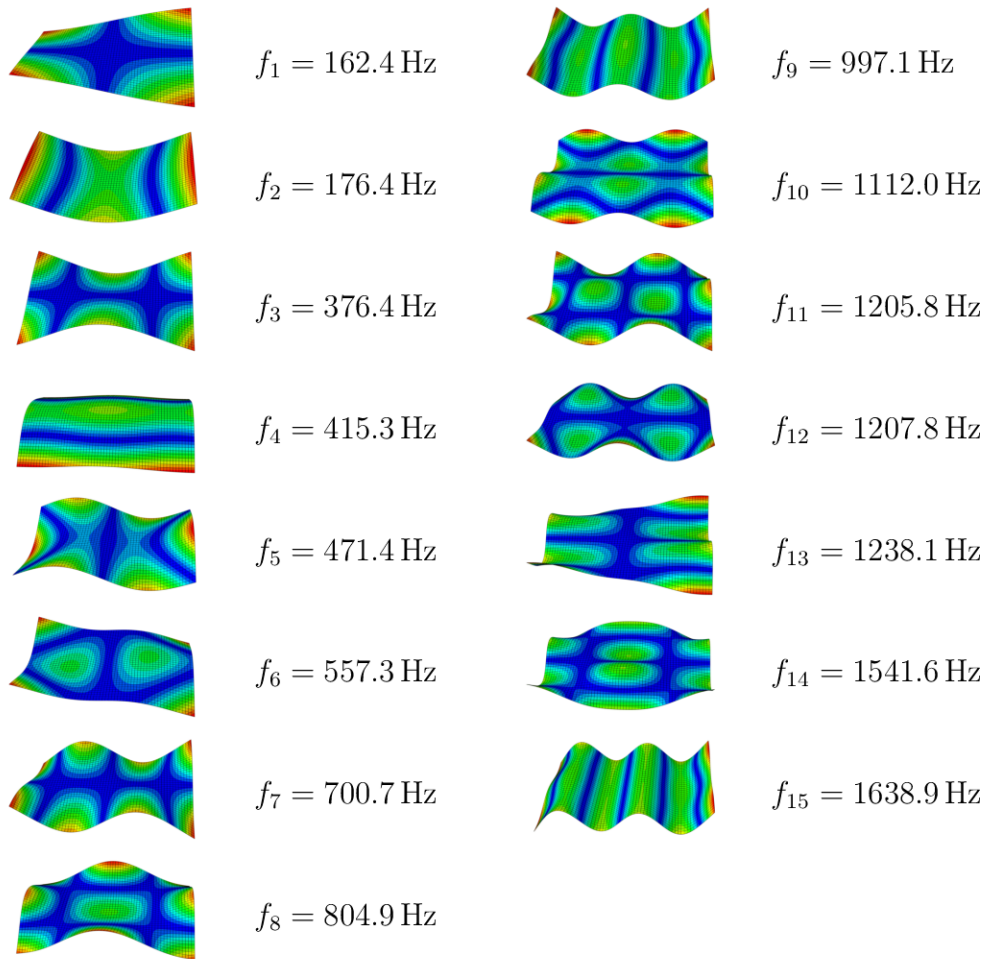


**Figure 4.1:** Rectangular aluminium plate suspended in the vacuum chamber. The dimensions of the plate are 300 mm x 200 mm x 3 mm.

**Table 4.2:** Mode shapes and eigenfrequencies of the first 15 eigenmodes of the rectangular plate, simulation results.



### 4.2.3 Protection Plate

A brake protection plate from the automotive industry has been chosen as a practical example of thin-walled structures. The component is shown in Figure 4.2. In the actual application, the sheet is installed behind the disc brakes and protect them from road dirt and water. Furthermore, it shields the components inside the car chassis from brake heat and dust. Figure 4.3 shows the rear axle of a vehicle. The brake protection plate is marked in red. The sheet has a thickness of one millimeter and a horseshoe-shaped geometry. There are four holes for mounting purposes. Furthermore, the component is covered by numerous ribs and grooves. The dimensions of the sheet are approximately 38 x 34 cm. In the numerical modal analysis preceding the experiments, the first 12 eigenmodes were determined. The results for the frequencies and mode shapes are presented in Table 4.3.



**Figure 4.2:** Photo of the protection plate. The horseshoe-shaped component is covered by numerous ribs and grooves. It has maximal dimensions of 38 cm (width) times 34 cm (height) and a thickness of 1 mm.

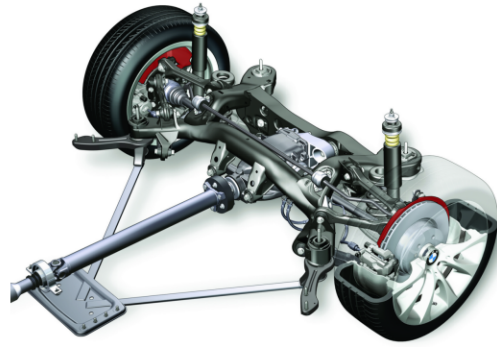
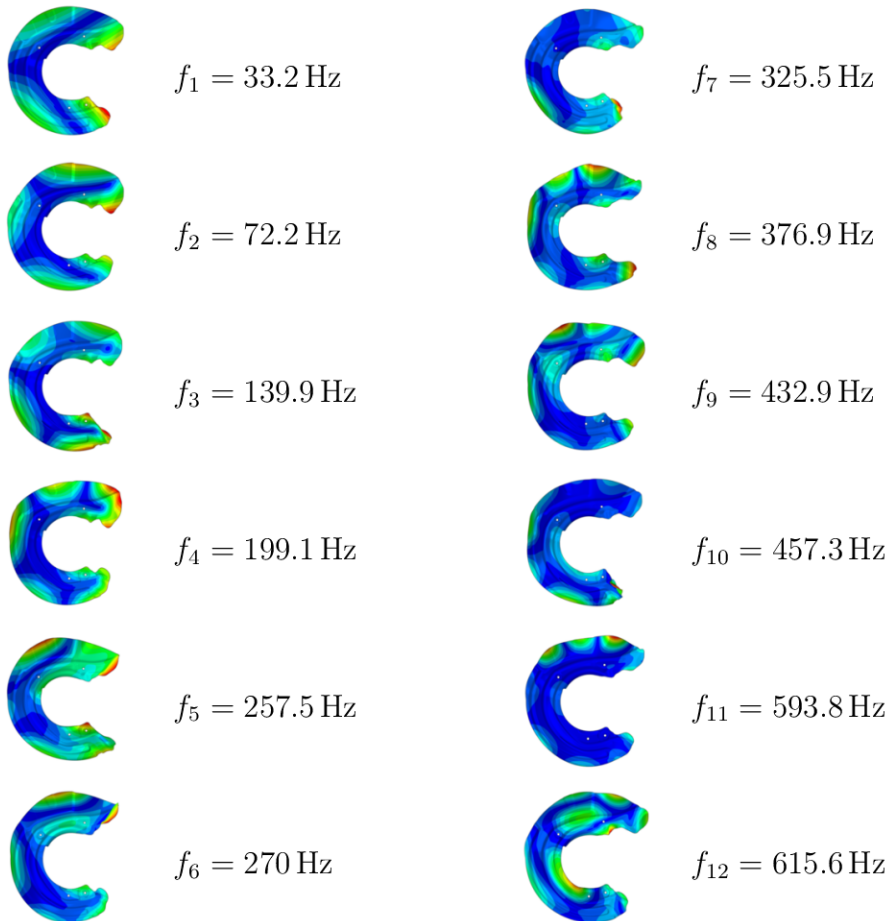


**Figure 4.3:** Position of the protection plate (red) in the rear axle of an automobile [137]

**Table 4.3:** Mode shapes and eigenfrequencies of the first 12 eigenmodes of the protection plate, simulation results.



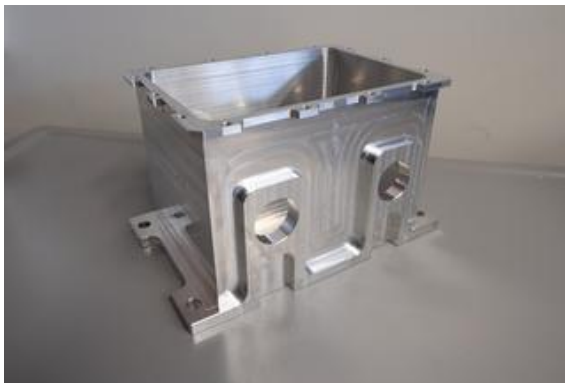
#### 4.2.4 Gearbox Casing

In addition to the thin-walled protection plate, another component should be investigated that has a compact geometry and can preferably be modeled with solid elements. A sample inspired by a gearbox casing was designed to meet the following requirements:

- size and weight must be suitable for suspension in the vacuum chamber
- at least five to six natural frequencies should be smaller than 2500 Hz in order to measure a frequency range comparable to the other components and to ensure that the excitation with the available impulse hammer can be done
- geometric boundary conditions for the manufacturing process must be met (radius, wall thickness etc.)

The result is the casing shown in figure 4.4 and figure 4.5. It has a basic wall thickness of 5 mm and the outer dimensions are 250 mm x 160 mm x 145 mm.

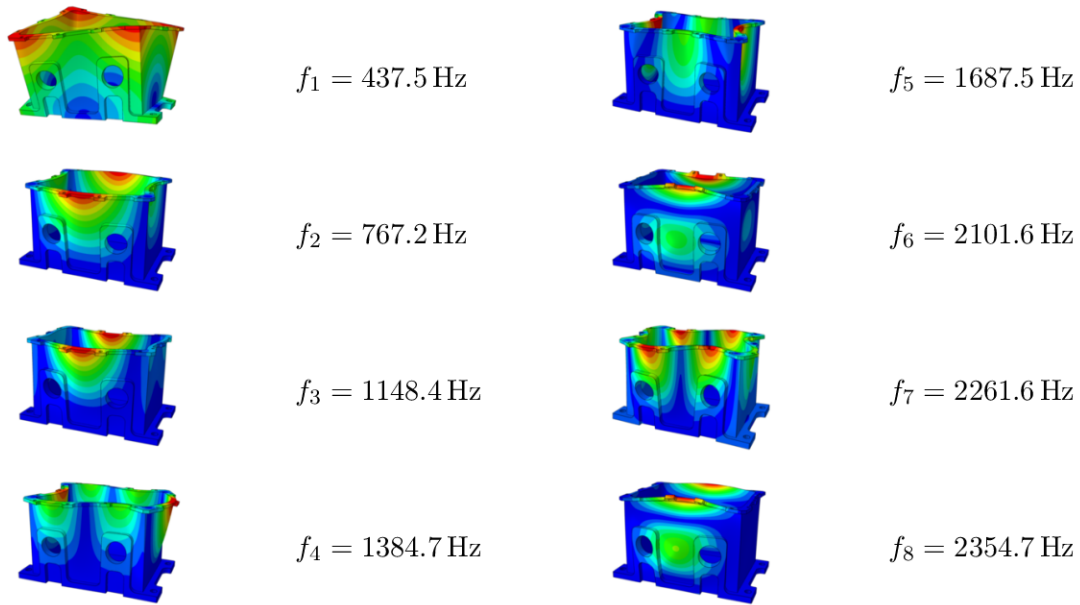
For this geometry, the simulation indicated eight eigenfrequencies and mode shapes smaller than 2500 Hz as shown in Table 4.4.



**Figure 4.4:** The component designed for the experiments was inspired by a gearbox casing.



**Figure 4.5:** Gearbox casing suspended within the vacuum chamber. The excitation is performed by an automatic impulse hammer, installed on a tripod (on the right-hand side).

**Table 4.4:** Eigenfrequencies smaller than 2500 Hz and mode shapes of the gearbox casing, simulation results.

## 4.3 Measurement of Damping using Decay Experiments

### 4.3.1 Approaches in the literature

Precise measurements of material damping require a proper experimental setup concerning the environmental parameters, support conditions, excitation and measurement techniques, and the analysis of the recorded data. The concept of the developed test setup is based on various research studies in the literature.

The first measurements of material damping were published in 1936 by Bennewitz and Rötger [138]. The authors showed an experimental setup for clamped thin wires of different materials (silver, steel, brass, aluminium, glass). The measured frequencies range from 0.5 to 500 Hz. They carefully investigated different mechanisms affecting the measured damping, e.g. the air pressure, although they could not avoid them. The results of the experiments show a clear frequency-dependent material damping behaviour. All curves have a maximum at a peak frequency specific for the material.

In 1938, Zener et al. presented an experimental study [8, 139] to strengthen the theoretical approaches in [7, 65]. The authors emphasized the importance of the support to avoid energy loss by friction especially at low frequencies. Therefore

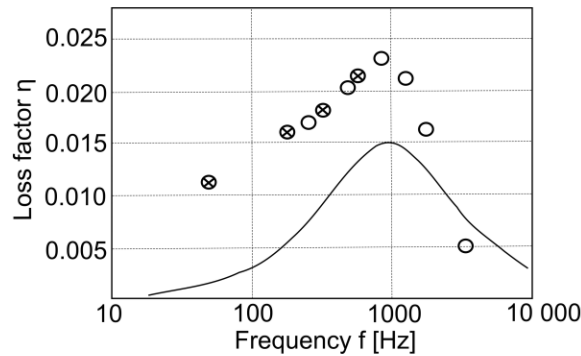


**Figure 4.6:** TED in copper wires according to [8]. The solid curve represents the analytical values. Crossed circles show longer samples (30.5 cm) that are suspended in nodal points. Open circles show shorter samples (13.5 cm) that are clamped at one end.

the test samples, thin copper wires, were suspended in the nodal lines of the mode shapes by thin silk threads. In figure 4.6 their experimental results are compared to the theoretical calculations. It is evident that the experimental loss factors are much higher than the theoretical values. This effect is caused by the influence of air damping, which was not taken into account in their experiments.

The problem of the atmospheric pressure was addressed in a publication of Baker et al. in 1967 [140]. They provided a test rig using a simple vacuum chamber. The test setup was covered by a bell jar and evacuated to the desired pressure. As a result, most later studies were conducted in vacuum.

The experimental studies were extended to new materials and conditions within the next decades. In 1968 Granick and Stern examined the damping behaviour of aluminium beams under different temperature ranges and high and permanent load until the fatigue strength is reached [141]. Gudmundson and Wüthrich conducted similar experiments with different steels [142]. Gibson and Plunkett developed a setup for testing the material damping of forced flexural vibrations in fiber-reinforced composite materials [143].

In 1989 Buser [144] and in 1990 Roszhart [145] introduced experimental studies on microstructures following a similar experimental setup. The authors showed the significance of TED in micro- and nanostructures where it is usually the dominant energy loss effect. This field was extended in several studies to a wide range of materials and geometries, usually on straightforward geometries like beams and plates [146–150], but also on more complex shapes as tuning forks [151].

The majority of research in the last three decades covers the topic of micro- and nanostructures. However, two other fields of application should be mentioned in particular. Cagnoli et al. provided an experimental and theoretical study of TED

in thin circular silicon wafers [122]. The authors set the focus especially on a precise suspension of the samples by using a test setup proposed by [152]. Similar experiments were conducted by Dmitriev et al. [153]. The results of both groups are comparable and they measured the same level of thermoelastic loss.

Furthermore Gibert et al. examined the material damping in turbomachinery blades [154] since these thin structures are vulnerable to high cycle fatigue. They used samples made of a titanium alloy and considered different air pressure conditions. Hentschel et al. [155] developed an experimental setup for these types of objects using a special clamping mechanism and a purpose-built vacuum chamber.

These different approaches from the literature are combined and extended to develop a suitable experimental design for measuring material damping, as described in the following.

### 4.3.2 Suspension and Excitation

The aim of the experimental study is to measure the modal damping, i.e. one damping ratio per mode shape. The experiment is designed to measure the material damping while avoiding other dissipation effects. To eliminate the effect of air and radiation damping, the experiments are conducted in a vacuum chamber with the size of 40 cm x 40 cm x 40cm. This limited space makes the installation of the experimental setup challenging. The available vacuum chamber achieves a medium vacuum with a pressure of approximately 5 mbar.

Another important source of energy dissipation is friction at the supports of the system. Optimally, free support conditions without bearing or suspensions should be aimed at. In practice, this is implemented as close as possible through a nodal suspension. For this purpose, the experiments are preceded by a modal analysis in a standard FEM software. By analyzing the mode shapes, the best locations for the suspension and the excitation of the components can be determined:

- Suspension: The best option to avoid friction at the support is to choose a location without deformation during the vibration. Therefore, the nodal lines of each mode shape are calculated where the modal deflection approaches zero.
- Excitation: To guarantee an efficient excitation of the desired mode, the excitation force is applied at a point of high deflection.

Furthermore, some practical restrictions should be considered. The test samples are suspended on thin elastic threads. For the rectangular plate and the protection plate, small holes are drilled. For the gearbox casing, pre-drilled holes at the bottom are used. The threads should have no further contact with the component.

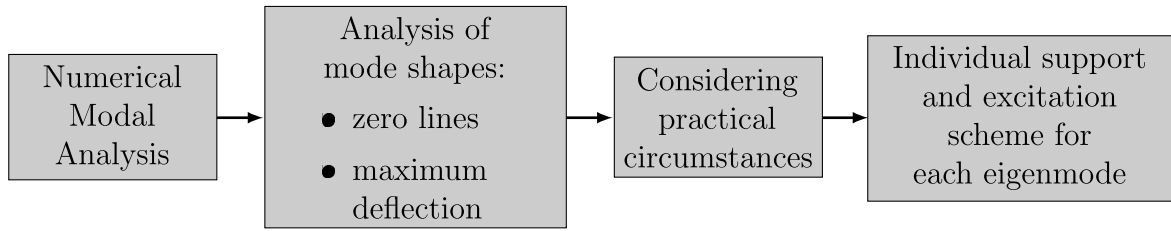


**Figure 4.7:** Flow chart for the determination of the modal experimental setup

Therefore the suspensions are placed close to the edge. Moreover, due to the limited space available, selecting the optimum points is not always possible.

These facts result in an individual scheme for the suspension and excitation points for each eigenmode, taking all practical circumstances into account. In figure 4.7 the procedure for planning the experimental setup for each mode is displayed. Figure 4.8 shows the suspension, measurement and excitation points for the first three modes of the components. The data for the other investigated mode shapes can be found in appendix A.

The excitation force should be applied with as little contact as possible. Furthermore, it should be controllable from the outside of the vacuum chamber. Therefore, an automatic impulse hammer is used (see figures 4.9 and 4.10). The hammer is installed inside the vacuum chamber to hit the excitation point of the desired eigenmode perpendicular to the component surface. After evacuating the vacuum chamber, the impulse can be triggered several times from the outside, but the position of the hammer can no longer be changed. Excitation by an impulse excites a broad frequency band. The shorter the pulse, the more frequencies are excited.

Figures 4.11 and 4.12 illustrate the influence of the excitation point on the frequency spectrum. The rectangular plate is used as an example. Figure 4.11 shows the spectrum in the frequency range of 0 – 800 Hz for a measurement using the scheme for the first eigenfrequency. The plate is suspended in the nodal lines in the middle of two edges. One corner point is excited with the impulse hammer and the vibration velocity is measured on the opposite corner. This point is deflected in almost every mode shape of the plate. Therefore, six of the first seven modes are excited in this measurement. The first eigenfrequency (166.5 Hz) shows the highest peak, but also the second mode (179.2 Hz) is visible. In figure 4.12 the spectrum of the measurement according to the measurement scheme of the second eigenmode is displayed. The suspension points are both on the long edge of the plate in the nodal lines. The component is excited in the middle of the short edge and the measurement location is on the opposite point. Both the excitation and measurement point correspond

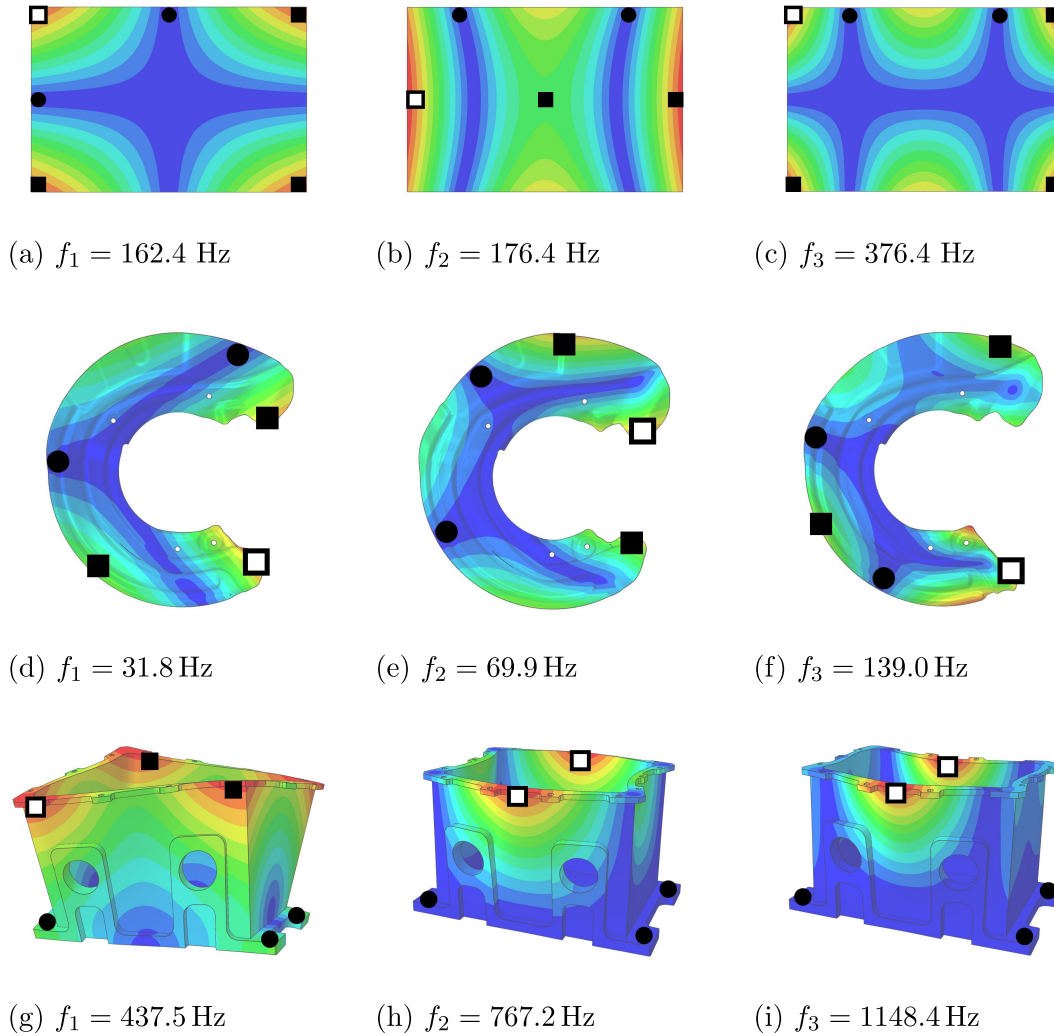


**Figure 4.8:** Measurement schemes for the first three eigenmodes of each component. The locations for the suspension (●) are in the nodal lines. The excitation (□) and measurement (■) points are at the locations with high deflections.

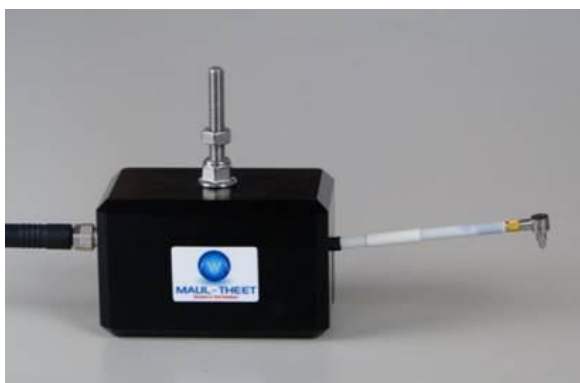


**Figure 4.9:** Automatic impulse hammer

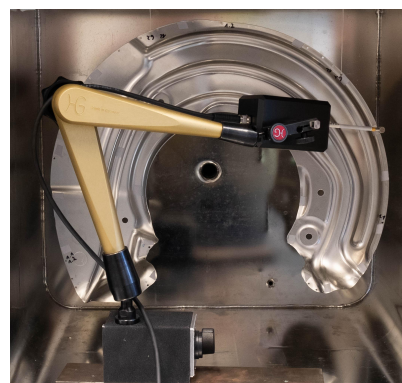


**Figure 4.10:** Experimental setup in the vacuum chamber. The measurement of the protection plate is shown. In the foreground, the automatic impulse hammer is mounted on a tripod.

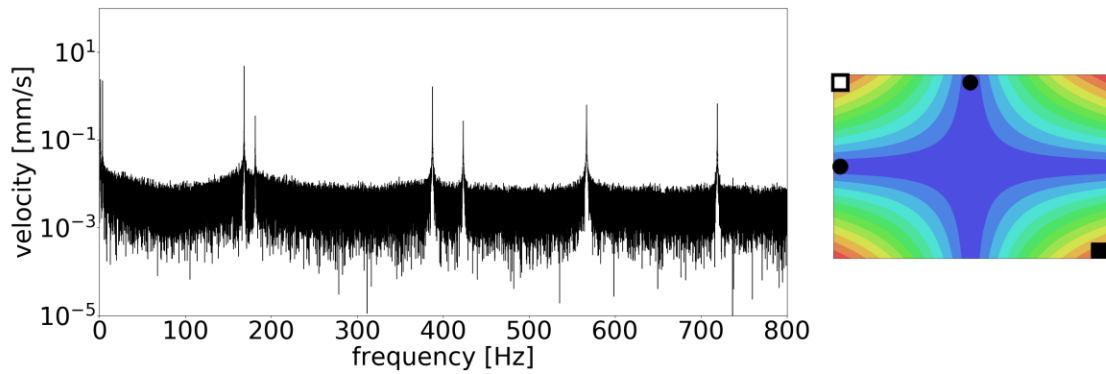


**Figure 4.11:** Frequency spectrum for a measurement of the rectangular aluminum plate according to the experimental scheme for the first mode shape. On the right-hand side the points of suspension (●), excitation (◻) and measurement (◼) are shown. The frequency range of 0 Hz - 800 Hz is demonstrated. Six modes are excited and the first mode ( $f_1 = 162.4$  Hz) is dominant.

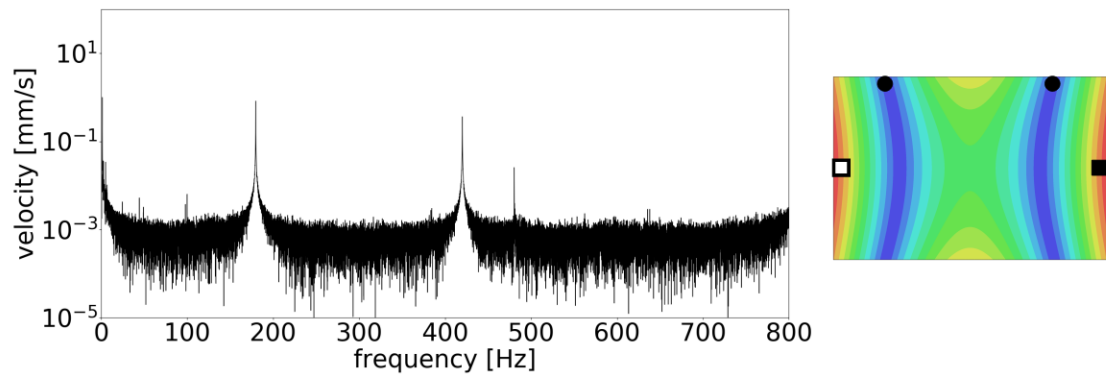


**Figure 4.12:** Frequency spectrum for a measurement of the rectangular aluminum plate according to the experimental scheme for the second mode shape. On the right-hand side the points of suspension (●), excitation (◻) and measurement (◼) are shown. The frequency range of 0 Hz - 800 Hz is demonstrated. Due to the test setup only the second and the fourth mode are clearly visible as peaks in the spectrum.

exactly to a nodal line of the first eigenmode. Therefore, the first eigenfrequency is not visible in the spectrum. Overall, only the second mode and the fourth mode can be clearly excited. Eigenmode five is faintly visible. The other mode shapes can not be investigated with the present measuring scheme.

### 4.3.3 Measurement

The measurement is realized contactless with a Laser-Doppler Vibrometer (LDV) installed outside the vacuum chamber. The laser beam is directed through a glass window in the chamber door to the surface of the component. The reflection is improved by sticking ultra-thin reflector foil onto the component at the measuring points. The mass of the foil can be neglected, therefore it is safe to assume that it does not influence the vibration of the samples.

The principle of an LDV is based on the measurement of a frequency shift. The laser emits at a constant wavelength of  $\lambda_w = 633 \text{ nm}$ . The laser beam is reflected by the vibrating test object. Due to the movement of the component, a Doppler shift is applied to the laser frequency. Compared to the initially emitted wave, the frequency shift is

$$f_D = 2 \frac{|\dot{u}|}{\lambda_w} \quad (4.3.1)$$

with the frequency shift  $f_D$ , the wavelength of the initial wave  $\lambda_w$  and the velocity of the component  $\dot{u}$  [156]. The measurement is done in an integrated interferometer. The emitted and reflected laser beams are superimposed to form an interference pattern. Deviations in the interference pattern allow conclusions about the frequency shift. The recorded variation in laser intensity is independent of the velocity sign. To determine whether the object is approaching or moving away from the vibrometer, so-called heterodyning is used. For this purpose, an additional shift of the light frequency is applied. Depending on the direction of movement during vibration, this modulation frequency is increased or decreased so that a frequency shift can be measured depending on the sign.

Further information on the subject of LDV can be found, for example, in the textbooks of Albrecht et al. [157] or Tomasini et al. [158].

### 4.3.4 Analysis

The recorded data are time signals of the vibration velocity in mm/s. To extract damping parameters, several signal processing steps are necessary. A Fast Fourier Transformation (FFT) is applied to the raw signal to convert the data into the frequency domain. The desired frequencies are filtered and transferred back into the time domain for the analysis of the decay curve. The fundamentals of these algorithms are presented in the following. An overview is given in figure 4.13. For a comprehensive presentation of the topic, the reader is referred to the textbooks available concerning signal processing, e.g. Meyer [159] or Giron-Sierra [160].

#### 4.3.4.1 Fast Fourier Transformation

Periodic signals can be decomposed into sums of trigonometric functions, a Fourier series. In the complex representation this is expressed as follows

$$x(t) = \sum_{n=-\infty}^{\infty} c_n e^{in\omega_0 t} \quad (4.3.2)$$

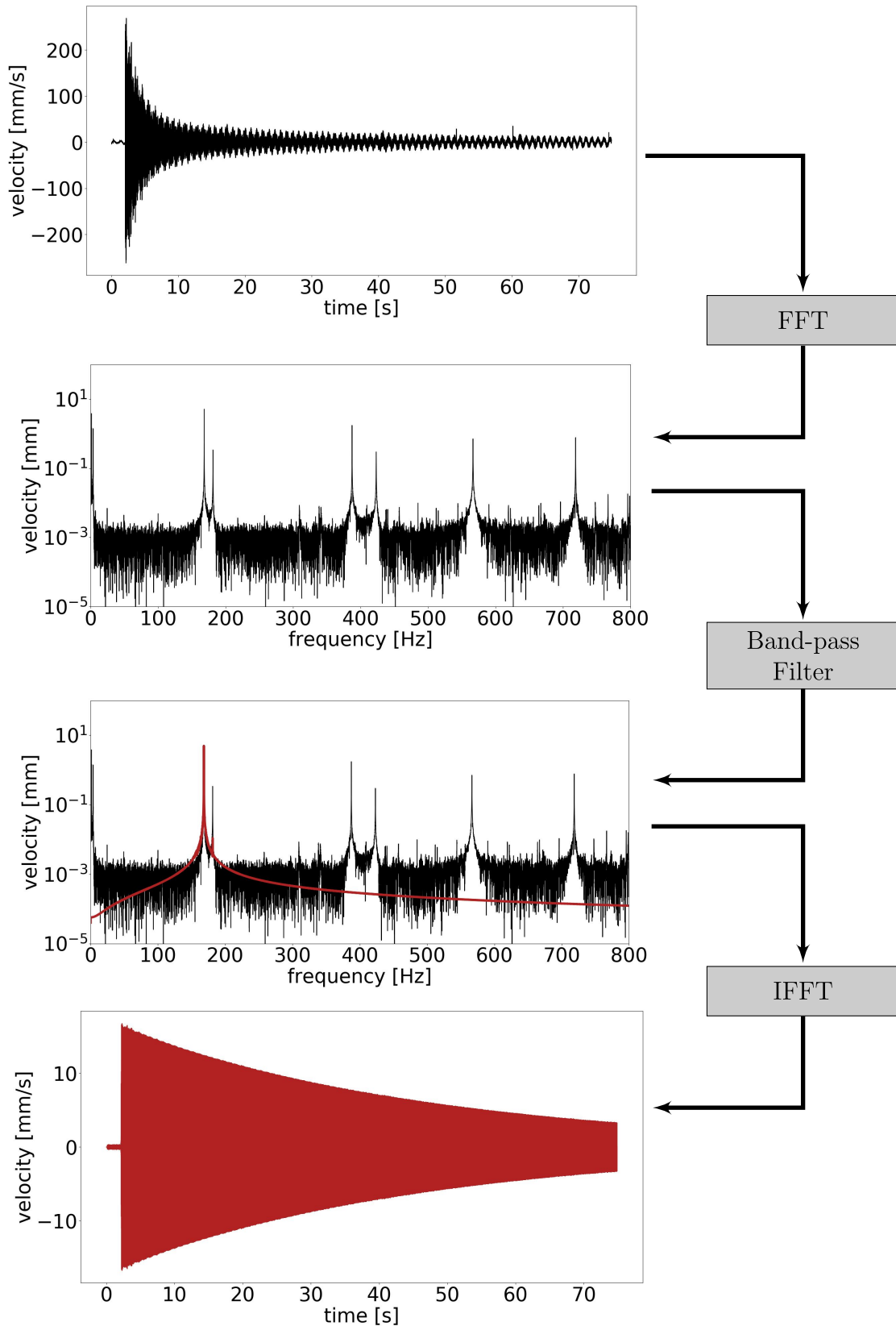


**Figure 4.13:** Processing scheme of the recorded signal. The raw digital signal recorded by the LDV contains the time series of vibration velocities. It is transferred into the frequency domain by a FFT. The result is a discrete frequency spectrum. A band-pass filter is multiplied on the spectrum to isolate the system response in the desired frequency range. Usually, one of the system's eigenfrequencies is in the filter window. The filtered amplitude spectrum (red) is reconverted to the time domain by an Inverse Fast Fourier Transformation (IFFT).

with the Fourier coefficient  $c_n$ .

$$c_n = \frac{1}{\tau} \int_0^{\tau} x(t) e^{-in\omega t} dt \quad (4.3.3)$$

For a periodic signal the result is a discrete frequency spectrum. The distance between the spectral lines is  $\Delta f = \frac{1}{\tau}$ . The Fourier series expansion can not be applied directly to aperiodic signals. Therefore it is assumed that  $\tau \rightarrow \infty$ . The spacing of the lines in the spectrum decreases with increasing period. At infinity, the result is a continuous spectrum, the so-called Fourier spectrum. The function of the spectrum, the Fourier transform is defined as

$$X(\omega) = \int_{-\infty}^{\infty} x(t) e^{i\omega t} dt. \quad (4.3.4)$$

The Fourier transformation enables the conversion of a signal from the time domain to the frequency domain. For a transformation from the frequency spectrum to the time signal, the inverse Fourier transformation is used.

$$x(t) = \frac{1}{2\pi} \int_{-\infty}^{\infty} X(\omega) e^{i\omega t} d\omega \quad (4.3.5)$$

Digital time signals are provided as discrete values. In the processing of digital signals, blocks of  $N$  values are sampled. The Discrete Fourier Transformation (DFT) converts a digital signal of a block length  $N\tau_F$  into the frequency range. The resulting spectrum is a line spectrum with a line distance of  $\Delta f = \frac{1}{N\tau_F}$ . The DFT is defined as

$$X[p] = \sum_{n=0}^{N-1} x[n] e^{-i2\pi \frac{pn}{N}}. \quad (4.3.6)$$

In this equation  $n$  is the number of samples,  $p$  the number of lines,  $x[n]$  the sequence of samples and  $X[p]$  the sequence of amplitudes in the spectrum. For the conversion from the frequency domain into the time domain the Inverse Discrete Fourier Transformation (IDFT) is defined:

$$x[n] = \frac{1}{N} \sum_{p=0}^N X[p] e^{i2\pi \frac{pn}{N}}. \quad (4.3.7)$$

The FFT are widely used in digital signal processing. Mathematically, the FFT is similar to the DFT. However, the method was developed as an efficient algorithm for the calculation of the DFT. The core of the process is a shortening of

the block length, i.e. the sequence of sampled values is decomposed into shorter sequences. This results in a significant reduction in computing time. In principle, a segmentation of the block length  $N$  into any integer blocks is possible. However, it is especially effective if  $N$  is a power of two, as the sub-blocks can be reduced to a block length of two.

#### 4.3.4.2 Filters in Signal Processing

In signal processing, filters are frequency-dependent systems to modify a signal concerning the amplitude or the phase. In contrast to analogue filters, digital filters are composed of mathematical functions applied to sampled signals. Filters allow specific frequency ranges to pass (pass-band) and block other frequency ranges (stop-band). Depending on the cut-off frequencies  $\omega_c$  between pass-band and stop-band, low-pass, high-pass, band-pass and band-stop filters can be distinguished. In figure 4.14 the different types are shown idealised in the frequency domain. A low-pass filter blocks all frequencies higher than the cut-off frequency  $\omega_c$ , a high-pass filter blocks all frequencies lower than  $\omega_c$ , a band-pass filter allows only the frequencies between the low and high cut-off frequencies  $\omega_{cl}$  and  $\omega_{ch}$  to pass and a band-stop blocks this frequency range.

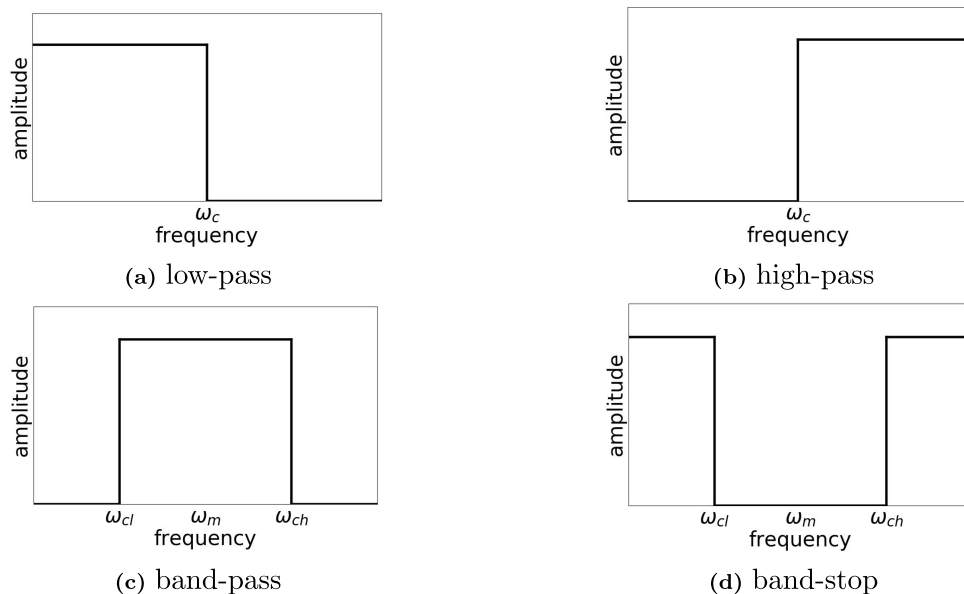


**Figure 4.14:** Pass-band and stop-band ranges for different filtering classes. Low-pass filter block all frequencies higher than a cut-off frequency  $\omega_c$ , high-pass filter block all frequencies lower than  $\omega_c$ , band-pass filter allow only frequencies in a defined range to pass and band-stop filters block frequencies within a defined range.

The theoretical principles are usually derived from the example of a normalised low-pass filter with cut-off frequency one. High-pass, band-pass and band-stop filters with arbitrary cut-off frequencies can be obtained from this basis. With a tolerance

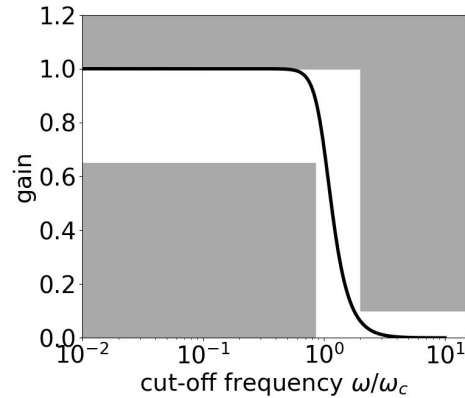


**Figure 4.15:** Filter tolerance scheme. The filter function should be characterized by a flat course in the pass-band and stop-band range, as well as a steep slope in the transition range. In this example, a fourth-order Butterworth filter is shown.

scheme, as shown in figure 4.15, the filter function can be adapted to the requirements concerning the course in the pass-band and stop-band as well as the slope in the transition range. In the present experiments, mainly the Butterworth-filter is used. The function of the filter is shown in Figure 4.15. It is characterized by a flat course in the pass-band. Mathematically, the function is expressed by

$$G_f(\omega) = \frac{1}{\sqrt{1 + \omega^{2n}}} \quad . \quad (4.3.8)$$

Here  $n$  is the filtering degree and  $G_f$  is the frequency response of the filter function (gain). In the figure, a fourth-order filter is shown.

#### 4.3.4.3 Exponential Fit

The result of applying an FFT to the raw signal, multiplying a band-pass filter and a conversion back to the time domain by an IFFT is a time-discrete signal that includes only the portions of the desired frequencies. This signal is cut to the part of the decay curve that should be analyzed, i.e. only the decay curve. Usually, the considered time series begins at the point of the impulse excitation.

In order to calculate the damping ratio, the upper and lower envelopes of the vibration curve are determined. These functions are approximated by an exponential fit. The resulting exponential equations give the lower and upper damping ratios  $\zeta_l$  and  $\zeta_u$ . Usually, these values should not differ significantly. For the final result, the average of both coefficients is calculated. An example is shown in figure 4.16.

An exponential function that corresponds very well to the course of the curve is an indicator of viscous damping behaviour. There may be undesirable friction losses if an exponential curve cannot describe the envelope well. The experimental setup should be checked and optimized in this case.

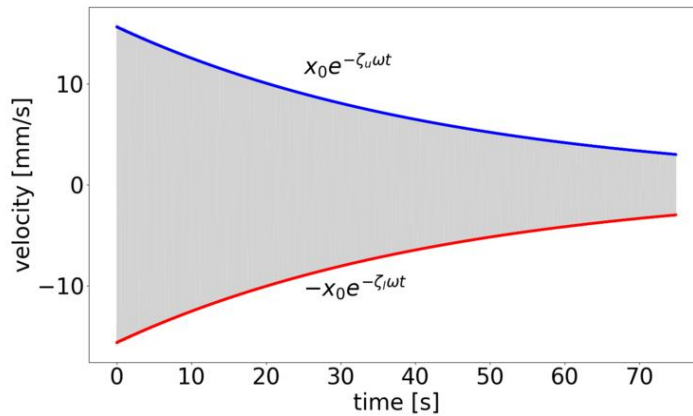


**Figure 4.16:** Exponential fit of the decay curve. The upper and lower envelope of the decay function are approximated by an exponential function. The upper and lower damping ratios  $\zeta_u$  and  $\zeta_l$  should be essentially the same. In this example  $\zeta_u = 2.08452 \times 10^{-5}$  and  $\zeta_l = 2.08453 \times 10^{-5}$ .

## 4.4 Results

### 4.4.1 Dependence on the Amplitude

In some of the studies presented in section 4.3.1, the dependence of the material damping on the vibration amplitude is investigated [138, 141, 143, 155]. In the early work by Bennewitz and Rötger [138], experiments were carried out on metal wires made of four different materials (copper, silver, brass, aluminium) with different diameters (0.9 mm to 1.5 mm). It was shown that there was no dependence of the logarithmic decrement on the amplitude in the case of the aluminium wire. The other samples showed an increasing decrement with increasing amplitude, whereby the slope of the curves differed. However, it is not clear from the data whether the amplitude dependence is due to the different material or the different geometry. Furthermore, the tests were done in the air so that no distinction can be made between the effects of material damping and air damping.

In the publication by Granick and Stern [141] is shown that the damping ratio of aluminium samples in air increases slightly with increasing amplitude. However, if a stress level close to the yield stress is reached in the material, the damping ratio increases drastically. The behaviour at low amplitudes in vacuum and air was investigated in another series of measurements. It was found that the damping ratio in air increases linearly with the amplitude, while the value in vacuum remains almost constant. Gibson and Plunkett [143] obtained similar results for samples made of fibre-reinforced composites.

The results of these studies suggest that the damping ratio does not depend on the amplitude as long as the deformation is small, so the yield stress is not reached. This hypothesis is strengthened by the measurements in the publication of Hentschel et al. [155]

In order to prove this assumption for the present experimental setup and the material used, measurements on the amplitude dependence were carried out. The investigations were done on the rectangular plate and the protective plate in vacuum. For the rectangular plate the measurement scheme for the first eigenmode was used and for the protective plate the scheme for the second mode. With the available impulse hammer velocity amplitudes between 0.9 mm/s and 19.7 mm/s (rectangular plate) and 1.5 mm/s and 26.4 mm/s (protection plate) respectively could be measured. Figures 4.17 and 4.18 show the results of the tests. In both cases, the damping ratio is almost constant with varying amplitude.

For the following series of experiments, it is assumed that the excited amplitudes do not significantly exceed those demonstrated here. Consequently, the damping ratio should not depend on the vibration amplitude. However, it must be taken into account that the measurements were only carried out in vacuum. The conclusions therefore only refer to the material damping. The influence of the amplitude on air and radiation damping can not be derived from the results.

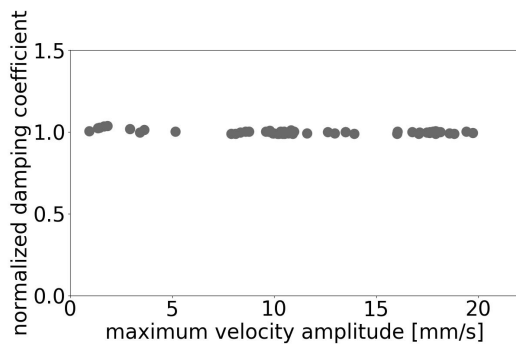


**Figure 4.17:** Normalized damping ratio as a function of excitation amplitude for the rectangular plate. The measurement were performed in vacuum and the measurement scheme for the first eigenmode (see Figure 4.8) was used.

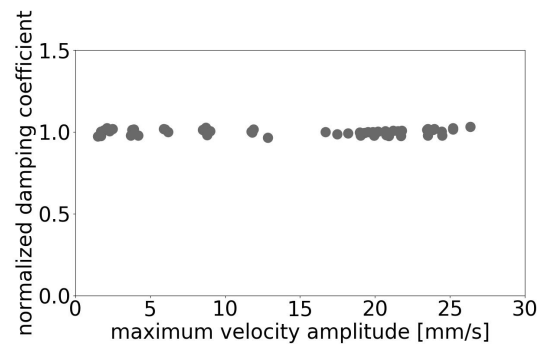


**Figure 4.18:** Normalized damping ratio as a function of excitation amplitude for the protection plate. The measurement were performed in vacuum and the measurement scheme for the second eigenmode (see Figure 4.8) was used.

#### 4.4.2 Dependence on the Air Pressure

A minimum air pressure of approximately 5 mbar can be achieved in the available vacuum chamber. Therefore, it can be assumed that the remaining air produces a small amount of damping, measured in addition to the material damping. In the present experiments, the influence of the air pressure on the damping ratio is investigated.

In the analytical approaches to air damping, as presented in chapter 2.2.3, a linear dependency between damping and air pressure or air density is usually assumed. This relationship could not be completely confirmed in experimental studies [154, 161, 162]. All studies gave comparable results, but the publication of Wesolowski

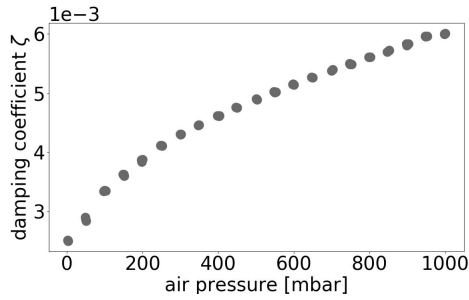


**Figure 4.19:** Damping ratio as a function of air pressure for the rectangular plate. The measurement scheme for the first eigenmode (see 4.8) was used and the air pressure was decreased from atmospheric pressure to approximately 5 mbar in steps of 50 mbar.

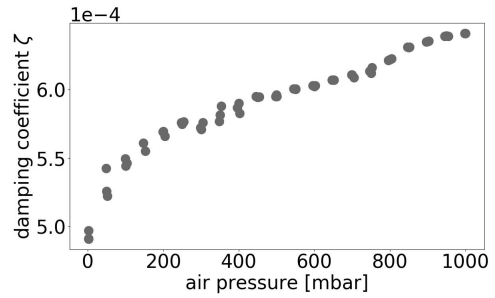


**Figure 4.20:** Damping ratio as a function of air pressure for the protection plate. The measurement scheme for the second eigenmode (see 4.8) was used and the air pressure was decreased from atmospheric pressure to approximately 5 mbar in steps of 50 mbar.

and Barkalov [162] should be emphasized since it presents very comprehensive data concerning the damping ratios under varying air pressure. The authors performed their test on samples made of composite materials and considered different geometries, mode shapes and vibration amplitudes. The absolute air damping ratio varies, but the actual trend is similar in all experiments: With decreasing air pressure, the degree of damping also decreases continuously. However, the curve is not linear, but the slope of the curve becomes steeper in low air pressure ranges.

In order to confirm this correlation on own examples, experiments were performed on the rectangular plate and the protection plate. Therefore the test object was installed in the vacuum chamber, and measurements of the damping ratios were done under atmospheric pressure. Next, the air pressure was reduced step by step to the lowest possible value of approximately 5 mbar. The excitation and measurement point, and the excitation amplitude were kept constant. The aim was to take three measurements every 50 mbar. This criterion could only be approximately fulfilled since the vacuum chamber can not be set precisely to one air pressure. Deviations of  $\pm 3$  mbar occurred.

Figures 4.19 and 4.20 show the results of the investigations. First of all, it can be seen that the variations in the measured values are stronger for the protective plate. In addition, the absolute values of the damping ratio naturally differ between the components. However, the course of the curves is very similar for both objects. There is obviously a dependence of the damping ratio on the air pressure. However, this cannot be assumed to be linear. The slope of the curve is significantly steeper in the range of low air pressures ( $< 200$  mbar) than at medium and high pressures. These results are broadly consistent with the findings in the experimental studies cited above. For the following experiments and especially the comparison with simulation data, it can be assumed that the actual material damping is slightly lower than the measured values. A mathematical correction of the measured values is not

included in the analysis, as there is no linear correlation. Several measurements at different air pressures would be necessary for a good curve approximation. These additional tests are not practicable in the experimental setup.

### **4.4.3 Damping Ratios in Vacuum and under Atmospheric Pressure**

#### **4.4.3.1 Rectangular Plate**

The experimental procedure described above is applied to the three components. The results in vacuum and under atmospheric pressure are compared.

To ensure the reproducibility of the experiments, four identical rectangular plates are tested. For each eigenmode, three or four measurement points are available (see figure 4.8). Furthermore, each measurement is repeated five times. Therefore up to one hundred values are recorded per eigenfrequency. Figure 4.21 shows the results for the damping ratios dependent on the frequency.

As expected, the values measured in air are considerably higher than the vacuum values because of the additional air damping. The measured values of the individual eigenmodes do not follow a monotonous course but vary significantly between the modes. It is also noticeable that the values in air are subject to larger fluctuation than the values in vacuum. A possible explanation for this is the dependency of air damping effects, such as acoustic radiation or moving air mass, on the environment. Depending on the position of the test object in the room and the distances to other objects, variations may occur.

No statement can be made about the extent of air and radiation attenuation based on the tests. Table 4.5 shows the absolute air damping and the relative part of the total measured damping. The values fluctuate randomly from mode to mode and do not follow any pattern. This demonstrates that air damping cannot be predicted generally. A measurement in a vacuum is absolutely necessary to be able to accurately determine the material damping.

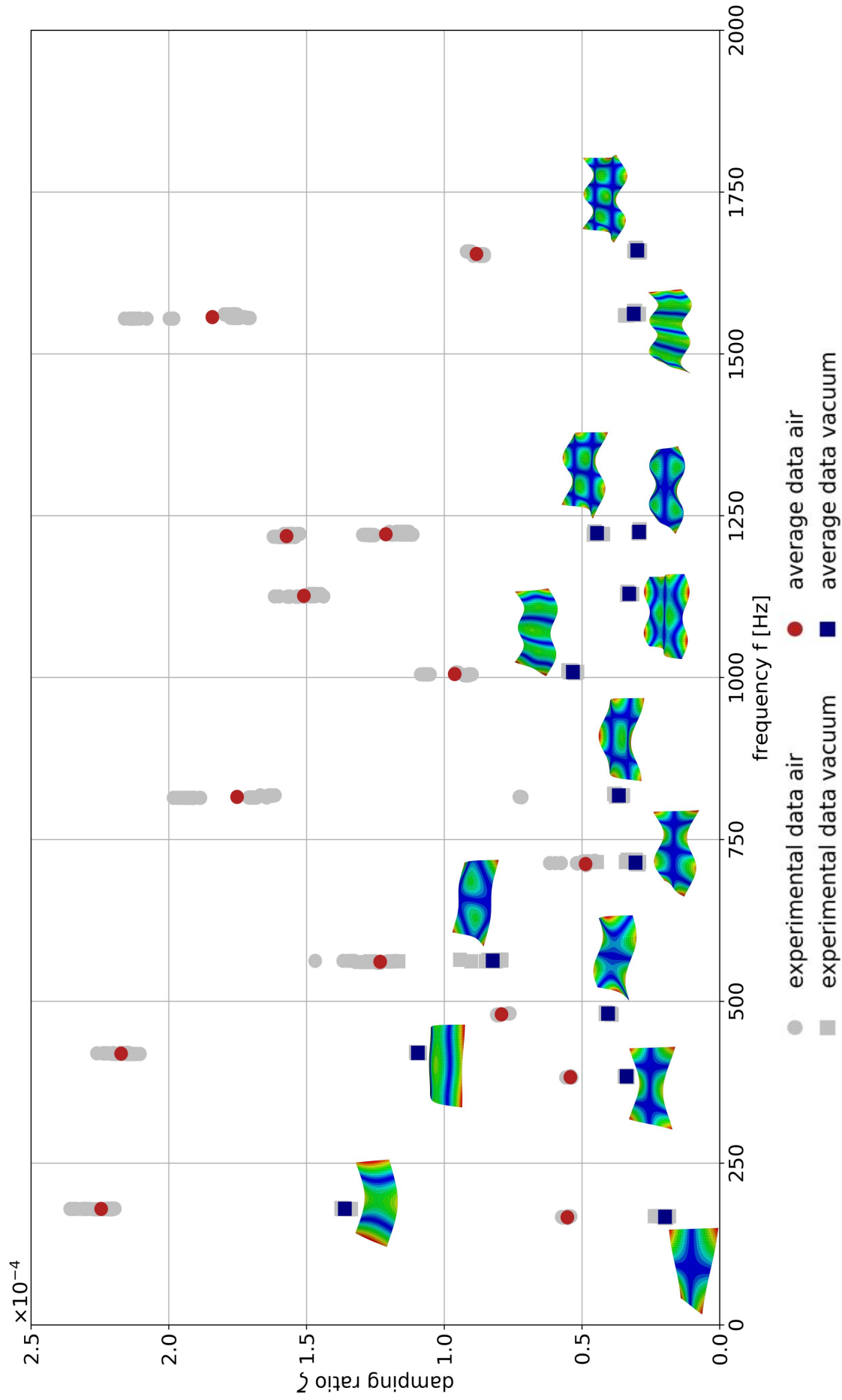


**Figure 4.21:** Experimental results for the damping ratio of the rectangular plate. The grey points show all experimental data. The red dots are the averaged values for the damping ratio under atmospheric pressure for each eigenmode. The blue squares are the averaged values for the damping ratio in vacuum. For each eigenmode, the mode shape is displayed next to the vacuum measurement value.

**Table 4.5:** Comparison of the measured damping ratios under atmospheric pressure ( $\zeta_a$  at frequency  $f_a$ ) and in vacuum ( $\zeta_v$  at frequency  $f_v$ ) for the rectangular plate. The absolute radiation damping  $\zeta_{ra}$  and the relative radiation damping  $\zeta_{rr}$  are calculated. For comparison, also the simulated eigenfrequency  $f_{sim}$  is given.

$f_{sim}$ [Hz]	$f_a$ [Hz]	$\zeta_a$	$f_v$ [Hz]	$\zeta_v$	$\zeta_{ra} = \zeta_a - \zeta_v$	$\zeta_{rr} = \zeta_{ra}/\zeta_a$
162.4	166.5	$5.528 \times 10^{-5}$	167.1	$1.981 \times 10^{-5}$	$3.547 \times 10^{-5}$	0.642
176.4	179.2	$2.245 \times 10^{-4}$	179.9	$1.361 \times 10^{-4}$	$8.848 \times 10^{-5}$	0.394
376.4	383.0	$5.425 \times 10^{-5}$	384.2	$3.374 \times 10^{-5}$	$2.052 \times 10^{-5}$	0.378
415.3	419.1	$2.173 \times 10^{-4}$	420.7	$1.095 \times 10^{-4}$	$1.078 \times 10^{-4}$	0.496
471.4	479.7	$7.926 \times 10^{-5}$	481.1	$4.043 \times 10^{-5}$	$3.883 \times 10^{-5}$	0.490
557.3	561.0	$1.233 \times 10^{-4}$	563.2	$8.231 \times 10^{-5}$	$4.099 \times 10^{-5}$	0.332
700.7	712.2	$4.872 \times 10^{-5}$	714.3	$3.047 \times 10^{-5}$	$1.825 \times 10^{-5}$	0.375
804.9	815.6	$1.752 \times 10^{-4}$	818.1	$3.659 \times 10^{-5}$	$1.387 \times 10^{-4}$	0.791
997.1	1005.4	$9.622 \times 10^{-5}$	1009.0	$5.321 \times 10^{-5}$	$4.301 \times 10^{-5}$	0.447
1112.0	1126.5	$1.510 \times 10^{-4}$	1129.8	$3.284 \times 10^{-5}$	$1.181 \times 10^{-4}$	0.782
1205.8	1218.8	$1.573 \times 10^{-4}$	1223.2	$4.449 \times 10^{-5}$	$1.128 \times 10^{-4}$	0.717
1207.8	1221.7	$1.213 \times 10^{-4}$	1225.3	$2.920 \times 10^{-5}$	$9.205 \times 10^{-5}$	0.759
1541.6	1557.2	$1.842 \times 10^{-4}$	1562.2	$3.115 \times 10^{-5}$	$1.531 \times 10^{-4}$	0.831
1638.9	1654.5	$8.828 \times 10^{-5}$	1660.1	$2.990 \times 10^{-5}$	$5.838 \times 10^{-5}$	0.661

#### 4.4.3.2 Protection Plate

The measurements of the protection plate were performed on two identical components. In each eigenfrequency, two measuring points were available, and each measurement was repeated five times. Figure 4.22 shows the measured damping ratios in air and vacuum. The experimental values are in the same order of magnitude as the damping ratios of the rectangular plate. However, the maximum values are slightly higher.

The damping ratios measured in air show a greater spread than the vacuum values. Compared to the rectangular plate, however, the variation is considerably smaller. This can probably be attributed to the smaller number of measured values. The measured damping ratios follow an increasing curve with a maximum at approximately 260 Hz. For higher frequencies, the trend of the damping ratios is decreasing. The air and radiation damping is generally smaller than in the preceding measurements on the rectangular plate. However, the relative values (absolute radiation damping divided by damping ratio under atmospheric pressure) fluctuate significantly between 9 % and 53 %, as shown in Table 4.6. Accordingly, no conclusion can be made about the dependence of the air and radiation damping on the eigenfrequency.

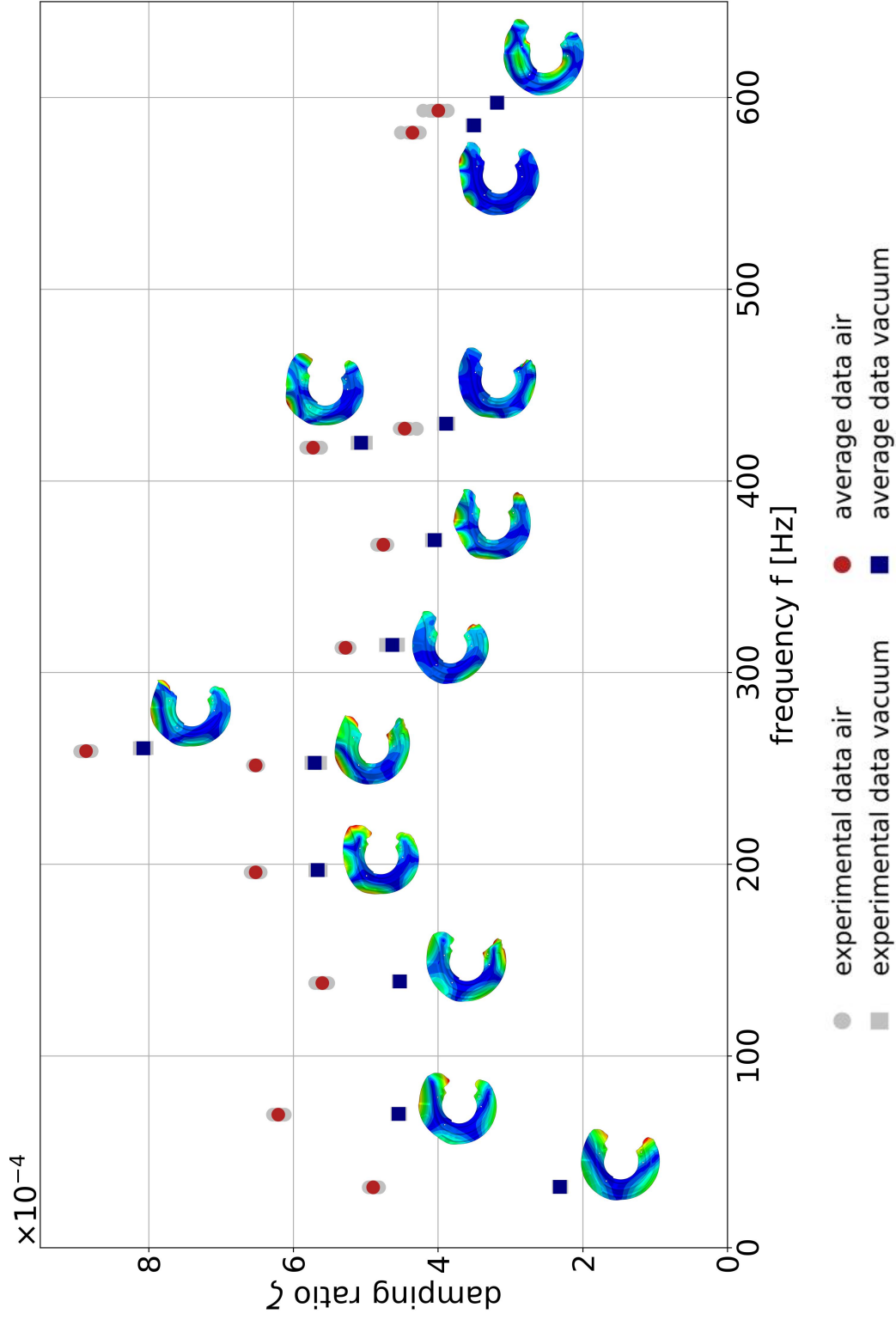


**Figure 4.22:** Experimental results for the damping ratio of the protection plate. The grey points show all experimental data. The red dots are the averaged values for the damping ratio under atmospheric pressure for each eigenmode. The blue squares are the averaged values for the damping ratio in vacuum. For each eigenmode, the mode shape is displayed next to the vacuum measurement value.

**Table 4.6:** Comparison of the measured damping ratios under atmospheric pressure ( $\zeta_a$  at frequency  $f_a$ ) and in vacuum ( $\zeta_v$  at frequency  $f_v$ ) for the protection plate. The absolute radiation damping  $\zeta_{ra}$  and the relative radiation damping  $\zeta_{rr}$  are calculated. For comparison, also the simulated eigenfrequency  $f_{sim}$  is given.

$f_{sim}$ [Hz]	$f_a$ [Hz]	$\zeta_a$	$f_v$ [Hz]	$\zeta_v$	$\zeta_{ra} = \zeta_a - \zeta_v$	$\zeta_{rr} = \zeta_{ra}/\zeta_a$
33.2	31.5	$4.896 \times 10^{-4}$	31.8	$2.316 \times 10^{-4}$	$2.581 \times 10^{-4}$	0.53
72.2	69.4	$6.208 \times 10^{-4}$	69.9	$4.545 \times 10^{-4}$	$1.663 \times 10^{-4}$	0.27
139.9	138.1	$5.603 \times 10^{-4}$	139.0	$4.529 \times 10^{-4}$	$1.074 \times 10^{-4}$	0.19
199.1	195.8	$6.521 \times 10^{-4}$	197.1	$5.664 \times 10^{-4}$	$8.567 \times 10^{-5}$	0.13
257.5	251.6	$6.524 \times 10^{-4}$	253.1	$5.703 \times 10^{-4}$	$8.205 \times 10^{-5}$	0.13
270.0	259.0	$8.866 \times 10^{-4}$	260.7	$8.072 \times 10^{-4}$	$7.936 \times 10^{-5}$	0.09
325.5	313.0	$5.282 \times 10^{-4}$	314.6	$4.631 \times 10^{-4}$	$6.508 \times 10^{-5}$	0.12
376.9	366.7	$4.760 \times 10^{-4}$	369.2	$4.048 \times 10^{-4}$	$7.116 \times 10^{-5}$	0.15
432.9	417.4	$5.730 \times 10^{-4}$	419.9	$5.062 \times 10^{-4}$	$6.680 \times 10^{-5}$	0.12
457.3	427.2	$4.462 \times 10^{-4}$	429.9	$3.888 \times 10^{-4}$	$5.747 \times 10^{-5}$	0.13
593.8	581.7	$4.354 \times 10^{-4}$	585.6	$3.503 \times 10^{-4}$	$8.506 \times 10^{-5}$	0.20
615.6	593.1	$3.999 \times 10^{-4}$	597.4	$3.182 \times 10^{-4}$	$8.168 \times 10^{-5}$	0.20

#### 4.4.3.3 Gearbox Casing

Concerning the gearbox casing, the experimental studies included the measurement of the damping ratios on two identical components in vacuum and under atmospheric pressure. Due to the dimensions and the weight of the sample, several challenges occurred. It was complicated to reach the corresponding excitation points with the impulse hammer and at the same time enable a laser measurement from outside of the chamber. Therefore, as mentioned in section 4.3.2, the casing was suspended in the existing openings at the bottom for all mode shapes. This solution represents a good compromise between the theoretically best suspension points and the practical circumstances.

Two or three measuring points were used per eigenmode, and each experiment was repeated five times. Figure 4.23 provides the measured damping ratio in vacuum and in air dependent on the frequency. It is apparent from this diagram that the air and radiation damping becomes dominant, especially in the mode shapes three to eight. The exact numerical values can be found in Table 4.7. The relative part of the air damping exceeds 96 % at eigenfrequency three and remains on a high level. In the experiments concerning the eighth mode shape, it was not possible to record a decay curve under atmospheric pressure. A possible explanation is the high damping in air that completely eliminates the vibration. Furthermore, the excitation amplitude using the available automatic impulse hammer might be too small to produce a measurable curve.

The damping ratios in air show a considerable variation. These fluctuating measure-

**Table 4.7:** Comparison of the measured damping ratios under atmospheric pressure ( $\zeta_a$  at frequency  $f_a$ ) and in vacuum ( $\zeta_v$  at frequency  $f_v$ ) for the gearbox casing. The absolute radiation damping  $\zeta_{ra}$  and the relative radiation damping  $\zeta_{rr}$  are calculated. For comparison, also the simulated eigenfrequency  $f_{sim}$  is given.

$f_{sim}$ [Hz]	$f_a$ [Hz]	$\zeta_a$	$f_v$ [Hz]	$\zeta_v$	$\zeta_{ra} = \zeta_a - \zeta_v$	$\zeta_{rr} = \zeta_{ra}/\zeta_a$
437.5	444.1	$7.213 \times 10^{-5}$	444.5	$2.600 \times 10^{-5}$	$4.613 \times 10^{-5}$	0.64
767.2	774.0	$9.062 \times 10^{-5}$	776.6	$1.447 \times 10^{-5}$	$7.615 \times 10^{-5}$	0.84
1148.4	1156.0	$3.722 \times 10^{-4}$	1158.5	$1.430 \times 10^{-5}$	$3.579 \times 10^{-4}$	0.96
1384.7	1392.3	$2.351 \times 10^{-3}$	1400.3	$1.406 \times 10^{-5}$	$2.337 \times 10^{-3}$	0.99
1687.5	1708.3	$1.285 \times 10^{-3}$	1706.4	$1.395 \times 10^{-5}$	$1.271 \times 10^{-3}$	0.99
2101.6	2124.1	$2.916 \times 10^{-4}$	2128.0	$1.208 \times 10^{-5}$	$2.795 \times 10^{-4}$	0.96
2261.6	2280.7	$8.583 \times 10^{-4}$	2275.3	$1.216 \times 10^{-5}$	$8.462 \times 10^{-4}$	0.99
2354.7	-	-	2380.4	$1.253 \times 10^{-5}$	-	-

ment values can possibly be explained by the effects causing air damping. Besides the acoustical radiation, the moved air mass impacts the energy dissipation as well. During the vibration a pressure waves forms inside the gearbox casing. The intensity depends on the direction and magnitude of the excitation force as well as the position of the component in the chamber. Further investigations concerning air and radiation damping were not carried out as part of this thesis.

In order to obtain a clear visual representation of the material damping, figure 4.24 only shows the damping ratios in vacuum. Compared to the measured values of the plate components, the order of magnitude of the damping ratios is significantly lower. In the first mode the highest damping ratio is  $2.6 \times 10^{-5}$ . The values of the eigenfrequencies two to eight are considerably lower and show a slightly decreasing trend.

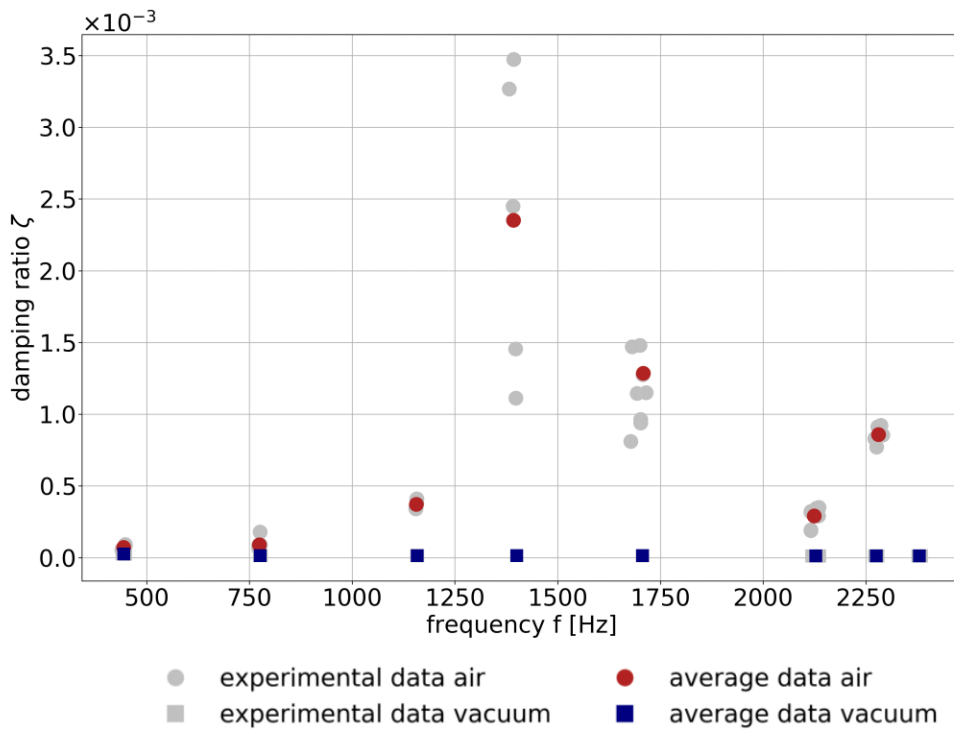


**Figure 4.23:** Experimental results for the damping ratio of the gearbox casing. The grey points show all experimental data. The red dots are the averaged values for the damping ratio under atmospheric pressure for each eigenmode. The blue squares are the averaged values for the damping ratio in vacuum.

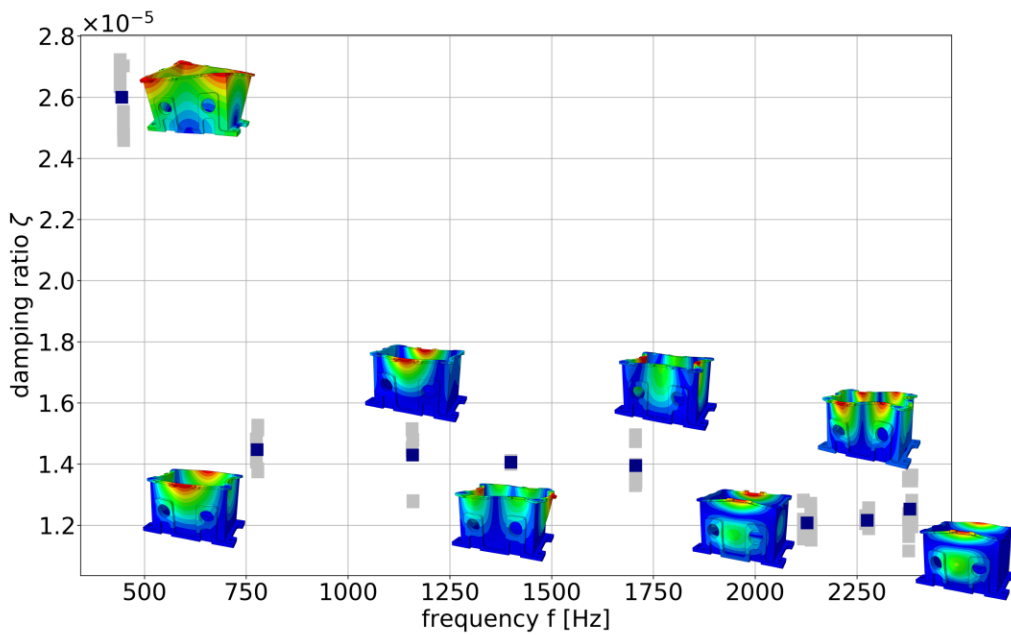


**Figure 4.24:** Experimental results for the damping ratio of the gearbox casing in the vacuum. The gray points show all experimental data. The blue squares are the averaged values for the damping ratio. For each eigenmode, the mode shape is displayed next to the vacuum measurement value.

## 4.5 Summary and Discussion

The experiments presented here have the aim to measure material damping under the exclusion of other damping sources. Therefore, a suitable test setup was developed. The measurements were done in a vacuum chamber to avoid air and radiation damping. Suspension, excitation and measuring points were adapted for each mode shape to guarantee that frictions losses are minimized at the supports and that the mode shapes are excited effectively. The measurement was done contactless with a LDV that recorded time series of vibration velocities. The resulting signal is cut and filtered, and the damping ratio can be determined by applying an exponential fit to the decay curve.

Overall, the experiments are very well suited for determining the material damping ratios. The tests show good repeatability. The results show only minor fluctuations due to the change of the measuring point as well as the change between (identical) components. It can be assumed that there are no significant friction losses, as exponential decay curves were observed in all measurements. This is an indicator of viscous damping behaviour.

It has been shown that the vibration amplitude does not influence the damping ratio. This result is limited to the material damping determined in vacuum. Furthermore, in the framework of this chapter only small amplitudes were tested. Based on the literature review, it can be assumed that the air damping is dependent on the vibration amplitude. Furthermore, significant changes in the damping behaviour usually occur at higher amplitudes if the material's yield stress is reached.

Comparative measurements between air and vacuum have shown that air and radiation losses usually influence damping behavior. Depending on the component, air damping accounts for up to 99 % of the total damping. In addition, a non-linear relationship between air pressure and damping ratio has been demonstrated. These results conclude that the experimental determination of the material damping must necessarily take place in a vacuum.

The influence of the air pressure is significant, especially in the range of low pressures ( $< 200$  mbar). Since the available vacuum chamber only achieves a medium vacuum with a minimum pressure of approx. 5 mbar, it can be assumed that the actual material damping is slightly lower than the measured values. The determined damping ratios always include a minor part of air and radiation damping.

In order to avoid friction damping at the supports, the test objects were suspended in the zero lines of the considered eigenmode. This concept is effective in excluding support losses but quite sensitive to inaccuracies. If the exact zero line can not be used for practical reasons, considerable energy losses occur due to relative movements at the suspension during the vibration. Therefore particular care should be

taken when choosing the support points.

Overall, it is highly probable that the actual material damping values are systematically lower than the measured values due to the factors mentioned above. This should be taken into account when comparing experimental data with simulation data.

# Chapter 5

## Thermoelastic damping based on generated heat

### 5.1 Introduction

This chapter presents a concept for models that are discretized with solid elements. On the one hand, this general approach can be used to model compact components. On the other hand, also thin-walled structures are often modeled with solid elements for convenience reasons in practical use. The method presented is based on the principle of converting mechanical energy into heat during an oscillation. In this context, the thermoelastic loss factor is defined as the ratio of generated heat, i.e. dissipated energy, to total strain energy. The energy converted into heat is directly related to the internal entropy production in the solid during a mechanical vibration. Therefore, the method will be denoted as “entropy approach” in the following chapters.

First, the theoretical background of entropy generation is outlined. The method and the used algorithm are presented subsequently. As a prestudy, the procedure is applied to thin beam structures. This enables direct comparison to the analytical Zener approach [7, 65].

A more detailed consideration follows for two additional components. The plate structure introduced in chapter 4 is modeled with finite solid elements. This model is used to calculate the modal damping ratios according to the entropy approach. Furthermore, dynamically excited oscillations in the time and frequency domain are simulated. Since detailed experimental data are available for the plate structure, the model allows the verification of the entropy method. Additionally, the results are compared to the fully thermoelastically coupled FEM solution.

As a practical application example, the three-dimensional box structure also presented in chapter 4 is analyzed. The results of the calculated damping ratios and

simulated frequency spectra are compared to experimental data and fully coupled simulations.

The results are discussed, and the method is evaluated with regard to its accuracy and practical applicability.

## 5.2 Theoretical Background - Thermoelastic Heat Generation

The internal entropy production can be calculated based on the second law of thermodynamics. The formulation of constitutive equations for simple materials based on the entropy principle was proposed by Coleman and Noll [163–165]. The relevant aspects for the case of a thermoelastic solid are presented below. A detailed description of this topic can be found in [166] or [63].

By considering a solid from a thermodynamic point of view, at least one further non-mechanical property is assigned to each point in the material, e.g. the absolute temperature or the entropy. The temperature in the continuum is defined as a temperature field and can have spatial and temporal variations. Extensive thermodynamic state variables, as well as derived variables, can be expressed in the local form. For example, the specific entropy  $s$  or the specific internal energy  $\psi$  are defined as

$$S = \int_V \rho s \, dV \qquad \Psi = \int_V \rho \psi \, dV \quad . \quad (5.2.1)$$

Furthermore, the specific external entropy  $s_e$  and the specific internal entropy production  $s_p$  can be derived in the same way. Specific variables can be considered as variable per unit mass.

According to the second law of thermodynamics, the entropy of an isolated system always has to increase (irreversible process) or stay constant (reversible process). If heat is transferred to the system by an external or distributed heat source, this relation is expressed by the so-called Clausius-Planck inequality.

$$\dot{S} \geq \dot{S}_e = \frac{\dot{Q}}{T} \quad (5.2.2)$$

Here  $\dot{Q}$  is the rate of heat transfer to the system whereas  $T$  refers to the temperature of the heat source. In continuum mechanics, per definition, the boundary points are always in equilibrium with the external heat source and the internal heat source is always in equilibrium with the material points [63]. Therefore the temperature of the body is equal to the temperature of the heat source and  $T$  is used generally.

The rate of heat transfer consists of two parts, the specific strength of the heat source  $r$ , i.e. the quantity of emitted heat per unit mass, and the heat flux  $\mathbf{q}$  over the surface  $A$ .

$$\dot{Q} = \int_V \rho r \, dV - \int_{\partial V} \mathbf{q} \cdot \mathbf{n} \, dA \quad (5.2.3)$$

Equation 5.2.3 is substituted into 5.2.2 and the divergence theorem is applied on the heat flux term. The condition for the resulting equation is the continuous differentiability of  $\mathbf{q}$ .

$$\int_V \rho \dot{s} \geq \int_V \frac{\rho r}{T} \, dV - \int_{\partial V} \frac{\mathbf{q} \cdot \mathbf{n}}{T} \, dA \quad (5.2.4)$$

$$\int_V \rho \dot{s} \geq \int_V \frac{\rho r}{T} \, dV - \int_V \nabla \cdot \frac{\mathbf{q}}{T} \, dV \quad (5.2.5)$$

Since the inequality must be fulfilled for every point in the continuum, it is formulated in local form as

$$\dot{s} \geq \dot{s}_e = \frac{r}{T} - \frac{1}{T} \nabla \cdot \frac{\mathbf{q}}{T} \quad (5.2.6)$$

Equation 5.2.6 represents a form of the second law of thermodynamics and is called Clausius-Duhem inequality. The difference between the specific external entropy  $s_e$  and the specific total entropy  $s$  is the specific internal entropy production  $\dot{s}_p$ .

$$\dot{s}_p = \dot{s} - \dot{s}_e \quad (5.2.7)$$

$$\dot{s}_p \geq 0 \quad (5.2.8)$$

$$T \rho \dot{s}_p = T \rho \dot{s} - r \rho + \nabla \cdot \mathbf{q} - \mathbf{q} \cdot \frac{\nabla T}{T} \geq 0 \quad (5.2.9)$$

Using the first law of thermodynamics in local form, the terms  $\nabla \cdot \mathbf{q} - r \rho$  can be replaced as follows.

$$\nabla \cdot \mathbf{q} - r \rho = \boldsymbol{\sigma} \dot{\boldsymbol{\varepsilon}} - \rho \dot{\psi} \quad (5.2.10)$$

$$T \rho \dot{s}_p = T \rho \dot{s} + \boldsymbol{\sigma} \dot{\boldsymbol{\varepsilon}} - \rho \dot{\psi} - \mathbf{q} \cdot \frac{\nabla T}{T} \geq 0 \quad (5.2.11)$$

Equation 5.2.11 represents the Clausius-Duhem inequality in a general form and must be fulfilled for every admissible process. The combination with constitutive equations for special material models allows the formulation of relations between different continuum fields [166]. In the following, a thermoelastic material with independent state variables strain  $\boldsymbol{\varepsilon}$  and entropy  $S$  is assumed. Therefore, the equations established in chapter 3.2 concerning the internal energy  $\Psi = \Psi(\boldsymbol{\varepsilon}, S)$  can

be applied.

$$d\Psi = \left. \frac{\partial\Psi}{\partial S} \right|_{\boldsymbol{\varepsilon}} dS + \left. \frac{\partial\Psi}{\partial \boldsymbol{\varepsilon}} \right|_S d\boldsymbol{\varepsilon} = T\dot{s} + \boldsymbol{\sigma}\dot{\boldsymbol{\varepsilon}} \quad (5.2.12)$$

In local form equation 5.2.12 is written as

$$\rho\dot{\psi} = \rho T\dot{s} + \boldsymbol{\sigma}\dot{\boldsymbol{\varepsilon}} \quad . \quad (5.2.13)$$

By introducing equation 5.2.13 into 5.2.11 the relation between the inner entropy production rate and the temperature field is determined.

$$T\rho\dot{s}_p = -\mathbf{q}\frac{\nabla T}{T} \geq 0 \quad (5.2.14)$$

$$\dot{s}_p = -\frac{\mathbf{q}}{T\rho} \frac{\nabla T}{T} \quad (5.2.15)$$

Substituting Fourier's law (see equation 3.2.32)  $\mathbf{q} = -\kappa\nabla T$  the following form can be derived.

$$\dot{s}_p = \frac{\kappa(\nabla T)^2}{\rho T^2} \quad (5.2.16)$$

The local entropy is transformed into the global entropy by multiplying the density of the material and integrating over the volume.

$$\dot{S}_p = \int_V \kappa \frac{(\nabla T)^2}{T^2} dV \quad (5.2.17)$$

Assuming the relationship between internal entropy production and heat production  $\dot{S}_p T = \dot{Q}$  we get

$$\dot{Q} = \int_V \kappa \frac{(\nabla T)^2}{T} dV \quad (5.2.18)$$

and considering one vibration cycle from  $t = 0$  to  $t = T$  the formula for the calculation of the generated heat  $\Delta Q$  is determined.

$$\Delta Q = \frac{2\pi}{\omega} \left\langle \int_V \kappa \nabla T \frac{\nabla T}{T_0} dV \right\rangle \quad (5.2.19)$$

Here  $\langle f(x) \rangle = \frac{1}{T} \int_0^T f(t) dt$  denotes the time average of the function. The thermoelastic loss factor  $\eta$  is defined as the ratio of generated thermal energy  $\Delta Q$  to total strain energy  $E_S$ .

$$\eta = \frac{1}{2\pi} \frac{\Delta Q}{E_S} \quad (5.2.20)$$

### 5.3 Method

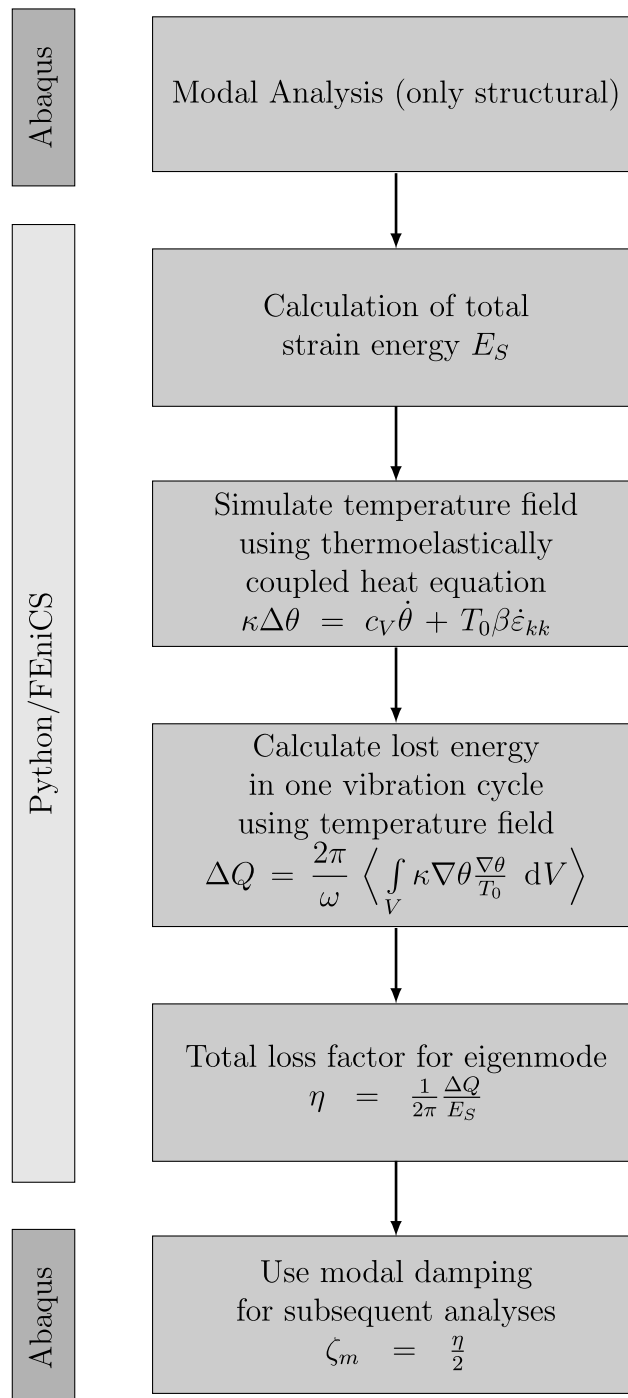


**Figure 5.1:** Flow chart for the numerical solution procedure of the entropy based loss factor

The calculation of the loss factor and the modal damping ratio, respectively, is embedded into a FE simulation procedure. The algorithm calculating the modal damping values is implemented based on an eigenfrequency analysis. These modal parameters are used in subsequent FE analyses in the time or frequency domain. Figure 5.1 demonstrates a flowchart showing the complete procedure.

The eigenfrequency analysis is performed only in the structural domain. It can be done in any commercial FE software. The examples presented in this thesis were solved in ABAQUS using the Lanczos eigensolver. The number of extracted eigenmodes depends on the geometry and discretization of the component as well as the subsequent dynamic analysis. In the presented examples, the eigenvectors are normalized to the maximal displacement. It does not matter for the calculation of the loss factor if the mode shapes are mass or displacement normalized because all further calculations are based on relative values. The strain components are determined per node using the displacement field, and the nodal strain vectors, shown in equation 5.3.1, are exported for the next steps implemented in Python.

$$\boldsymbol{\varepsilon} = \left\{ \varepsilon_{11} \quad \varepsilon_{22} \quad \varepsilon_{33} \quad 2\varepsilon_{12} \quad 2\varepsilon_{23} \quad 2\varepsilon_{13} \right\} \quad (5.3.1)$$

First, the total strain energy is determined. The necessary stress tensor is connected to the strain tensor via the three-dimensional elastic Hooke's law with the elasticity tensor  $\mathbf{E}$ .

$$E_S = \frac{1}{2} \int_V \boldsymbol{\sigma} \boldsymbol{\varepsilon} \, dV \quad (5.3.2)$$

$$\boldsymbol{\sigma} = \mathbf{E} \boldsymbol{\varepsilon} \quad (5.3.3)$$

Due to the thermoelastic coupling, the temperature field results directly from the strain field. The negative sign appears due to the nature of the thermoelastic effect: if a solid is stretched, the material decreases in temperature. If the solid is compressed, the temperature increases. This relation is described by the Thomson-effect [92, 167]:

$$\frac{\partial \theta}{\partial t} = -T_0 \frac{\beta}{c_V} \frac{\partial \varepsilon_{kk}}{\partial t} \quad (5.3.4)$$

In the next step the heat flow during a mechanical oscillation is determined. Therefore, one vibration cycle is considered. In order to solve the thermoelastically coupled heat equation, the vibration cycle is discretized in time steps.

The analysis of the heat equation is realized using the open-source FE library FEniCS. This toolbox allows the solution of partial differential equation in Python in a FE procedure based on the weak form of the problem. Whereas the spatial discretization is done in finite elements, the time derivatives are discretised by a

finite difference algorithm (see chapter 3.4.3) as described exemplarily in [168].

$$\dot{\theta} = \frac{\theta^{n+1} - \theta^n}{dt} \quad (5.3.5)$$

$$\dot{\varepsilon}_{kk} = \frac{\varepsilon_{kk}^{n+1} - \varepsilon_{kk}^n}{dt} \quad (5.3.6)$$

The coupled heat equation results in

$$\kappa \nabla^2 \theta = c_V \frac{\theta^{n+1} - \theta^n}{dt} + T_0 \beta \frac{\varepsilon_{kk}^{n+1} - \varepsilon_{kk}^n}{dt} \quad (5.3.7)$$

$$\theta^n = \theta^{n+1} - \frac{\kappa}{c_V} \nabla^2 \theta dt + \frac{T_0 \beta}{c_V} (\varepsilon_{kk}^{n+1} - \varepsilon_{kk}^n) \quad (5.3.8)$$

To derive the weak form of the equation, all terms are multiplied by a weighting function  $v$  and integrated over the volume of the solid. The second derivative, which is indicated by the Laplace operator, is resolved by partial integration.

$$\int_V \theta^n v dV = \int_V \theta^{n+1} v dV - dt \frac{\kappa}{c_V} \int_V \Delta \theta^{n+1} v dV + \frac{T_0 \beta}{c_V} \int_V (\varepsilon_{kk}^{n+1} - \varepsilon_{kk}^n) v dV \quad (5.3.9)$$

$$\begin{aligned} \int_V \theta^n v dV &= \int_V \theta^{n+1} v dV - dt \frac{\kappa}{c_V} \left[ \int_V \nabla \theta^{n+1} \nabla v dV - \int_{\partial V} v \frac{\partial \theta^{n+1}}{\partial n} d\Gamma \right] \\ &+ \frac{T_0 \beta}{c_V} \int_V (\varepsilon_{kk}^{n+1} - \varepsilon_{kk}^n) v dV \end{aligned} \quad (5.3.10)$$

The calculation of TED in the material is based on the assumption of adiabatic conditions, i.e., there is no heat flow over the surface of the solid. Therefore the following condition applies:

$$\int_{\partial V} v \frac{\partial \theta^{n+1}}{\partial n} d\Gamma = 0 \quad (5.3.11)$$

Two factors influence the variation in temperature in each time step:

- the heat flow from the previous time step
- the amount of heat added by thermoelastic coupling due to strain differences.

A time-dependent strain is applied for this purpose. The strain field from the mode shapes is considered to be the maximum value and is adapted to the oscillation by

applying the sine function.

$$\varepsilon_{kk}(t) = \varepsilon_{kk}^{\max} \sin(2\pi ft) \quad (5.3.12)$$

For the implementation, the weak form of the differential equation 5.3.10 is transformed into a standard form  $a = L$  with the left-hand side  $a$  including the unknown variable  $\theta^{n+1}$  and the right-hand side  $L$  including the known temperature  $\theta$  from the previous time step.

$$a = \int_V \theta^{n+1} v \, dV - dt \frac{\kappa}{c_V} \int_V \nabla \theta^{n+1} \nabla v \, dV \quad (5.3.13)$$

$$L = \int_V \theta^n v \, dV - \frac{T_0 \beta}{c_V} \int_V (\varepsilon_{kk}^{n+1} - \varepsilon_{kk}^n) v \, dV \quad (5.3.14)$$

The generated heat per time step is calculated using the resulting temperature field according to equation 5.2.18. By integrating over one period the heat generated in one vibration cycle is determined. The thermoelastic loss factor is defined as the ratio of the heat generation to the total strain energy, see equation 5.2.20. Based on the loss factor, other damping parameters can easily be determined, e.g. the modal damping ratio  $\zeta_m$ , for use in subsequent FE simulations.

$$\zeta_m = \frac{\eta}{2} \quad (5.3.15)$$

## 5.4 Results

### 5.4.1 Beam Structure

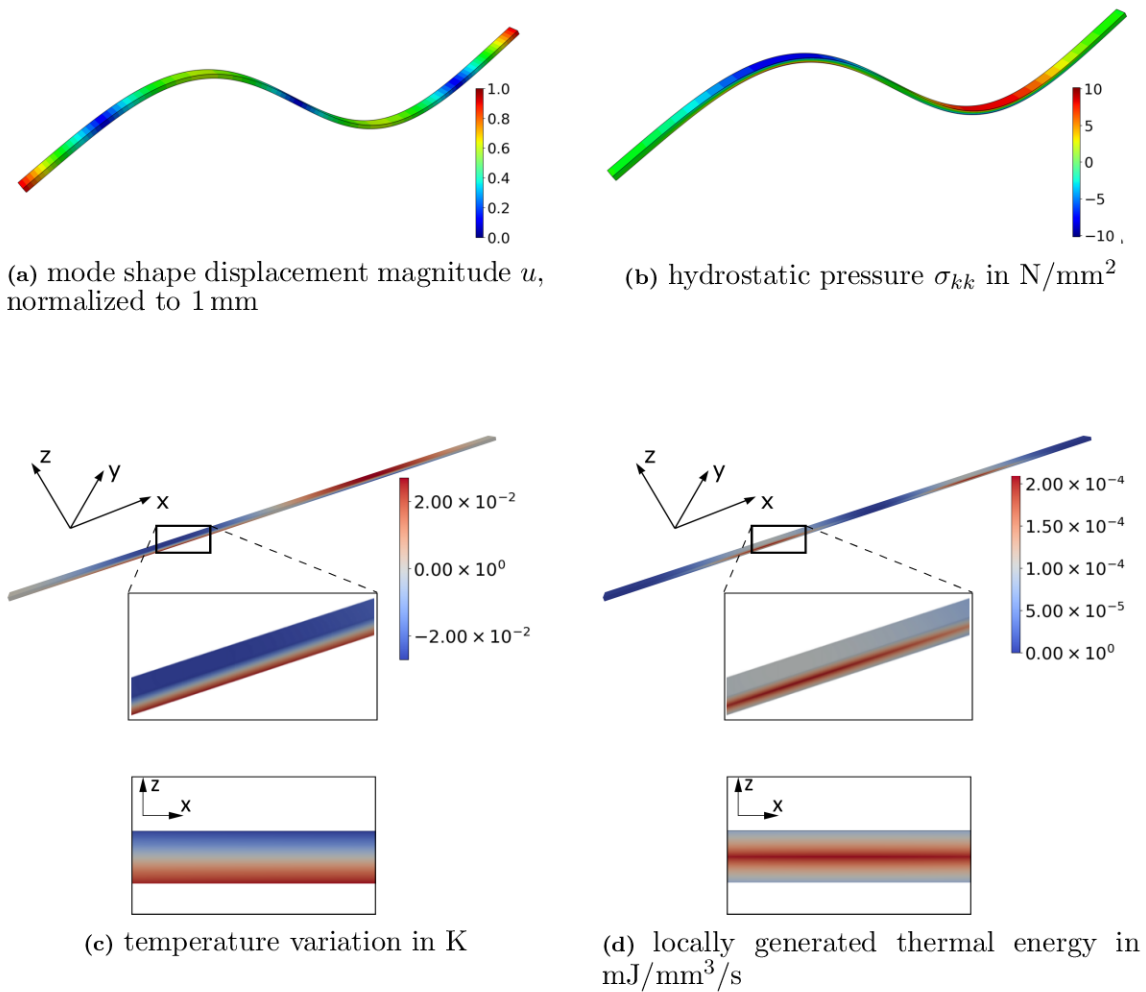
In order to verify the method it was first applied to thin beam structures and the results were compared to the analytical solution according to Zener [65]. This allows analyzing the temperature distribution, heat flow and entropy generation on the example of a simple structure. Therefore 16 thin beams were modeled with solid elements. All of the structures have a length of 400 mm and different widths (40 mm, 10 mm, 5 mm, 3 mm) and thicknesses (3 mm, 1.5 mm, 1 mm, 0.5 mm). The element size of the meshes is given in table 5.1.

Figure 5.2 shows the results for the beam of width  $d = 10$  mm and thickness  $h = 3$  mm. It displays the absolute values of the displacement magnitude, hydrostatic stress distribution  $\sigma_{kk}$ , temperature variation  $\theta$  and generated heat  $\Delta Q$  for the second eigenmode at  $f_2 = 272.4$  Hz. The hydrostatic stress is chosen because

**Table 5.1:** Element size of the meshes for the different beam models. At the top of each cell the element size in plane direction is given and at the bottom the number of elements in thickness direction.

Width: Thickness:	40 mm	10 mm	5 mm	3 mm
3 mm	4 mm 4	2 mm 4	2 mm 4	1 mm 4
1.5 mm	4 mm 4	2 mm 4	2 mm 4	1.5 mm 4
1 mm	4 mm 4	2 mm 4	1.5 mm 4	1 mm 4
0.5 mm	4 mm 4	2 mm 4	1 mm 4	0.5 mm 4

the temperature field is only effected by normal stress components, as derived in chapter 3.2. The mode shape is displacement-normalized to 1 mm. It is apparent that the temperature distribution is equivalent to the stress field due to the thermo-elastic coupling. The highest temperatures variation appears on the outer fibres of the beam whereas in the middle fibres of the beam no temperature change occurs. Since the thermal energy generation results from the heat flow mainly in the thickness direction, it becomes maximal in the center of the beam and vanishes on the outside, as shown in the theoretical consideration in chapter 3.3. The loss factor  $\eta$  was subsequently calculated from the generated thermal energy using the formula 5.2.20. The results of the frequency-dependent loss factor are organized into four diagrams in figure 5.3. Concerning geometry parameters, only the thickness influences the analytical solution for a thin beam (see formulas 3.3.20 and 3.3.15). Therefore beams of identical thickness are compared directly in the same diagram. Furthermore, the analytically calculated graph for the appropriate thickness is demonstrated in the plot. The analytical formula represents the behavior of a pure bending beam assuming one-dimensional heat conduction. For the analyzed beam structures one loss factor per eigenmode is calculated. In the figure, only the bending modes are displayed. The frequency axis is scaled logarithmically for reasons of visualization. The peak frequency of the analytical graph corresponds to the first eigenvalue of the heat equation. In the thinner beams ( $h = 0.5$  mm and  $h = 1$  mm), the left and the right branch of this curve are covered with sample points of the simulated loss factor. In the beams with a thickness of 1.5 mm and 3 mm, the eigenfrequencies are higher, thus only the descending branch of the peak is represented. The mechanical eigenfrequency of the beam depends on the length and the thickness, but not on the width. Therefore, all four beams of the same width have the same eigenfrequencies. Concerning the impact of the width, it should be distinguished between thick and thin beams. In the samples with a thickness of  $h = 1.5$  mm and  $h = 3$  mm, no varia-



**Figure 5.2:** Graphical representation of the absolute displacement, stress, temperature variation and generated heat due to thermoelastic coupling in the second mode shape ( $f_2 = 272.4 \text{ Hz}$ ) of the beam with size  $400 \text{ mm} \times 10 \text{ mm} \times 3 \text{ mm}$ .

tion are visible between the points of different widths (see figures 5.3c and 5.3d). In the structure with a thickness of 1 mm in figure 5.3b, the widest beam ( $d = 40 \text{ mm}$ ) show slightly higher loss factors than the other examples. In the thin beam with a thickness of 0.5 mm in figure 5.3a this difference becomes significant. From this it can be concluded that the mechanical behavior of the component shifts towards the plate structure with a smaller  $h/d$  ratio. As explained in chapter 6.3, the loss factor increases in case of two-axial bending. Compared to the analytical solution, two deviations are noticeable:

- Especially in subfigures 5.3a and 5.3b it can be seen that the analytical one-dimensional solution has lower peak frequencies than the numerical solution. The peaks of the numerical models with three-dimensional heat conduction are shifted to the right.

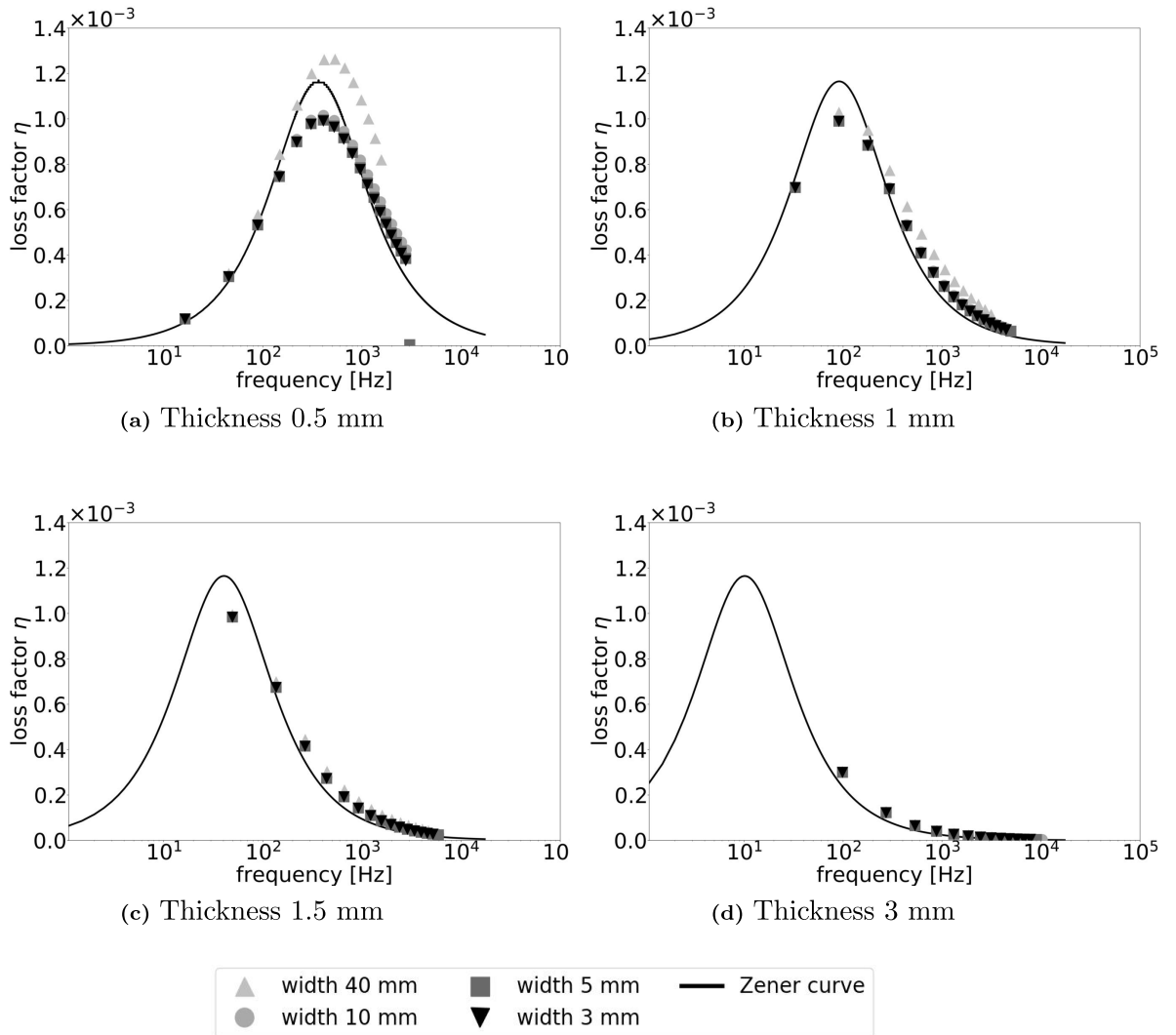


**Figure 5.3:** Comparison of the loss factors  $\eta$  calculated using the entropy approach with the analytical solution according to Zener [65] for 16 beams with varying widths and thicknesses. All beams have a length of 400 mm. In each diagram, four beams of the same thickness are plotted with the corresponding analytical curve.

- The height of the peak is lower in the numerical models.

Both facts can be explained by the modeling approach. In the three-dimensional numerical model the dominant heat flux is not necessarily a single flow in thickness direction. To verify this assumption the heat flow at the peak frequency is analyzed. Therefore the eigenvalues of the heat equation are determined numerically at a beam of width  $d = 10$  mm and thickness  $h = 3$  mm.

The thermal eigenvalue represents the reciprocal of the characteristic thermal decay time, i.e. the time till the temperature gradients are equalized. To be precise, it is not a frequency, as the thermal relaxation is not an oscillating process. In order to emphasize the connection to the mechanical natural frequency, the term “peak

frequency” is nevertheless used and it is given in Hertz. The thermal eigenvector is the corresponding temperature distribution. Parts of the results are shown in figure 5.4 and related to the loss factor curves of figure 5.3.

In the vicinity of the analytically determined peak frequency (365.8 Hz), two thermal eigenvectors were found for the 3D solid modeled beam. One has a single temperature gradient in the thickness direction (see figure 5.4b). The corresponding eigenvalue exactly matches the analytical peak frequency. Furthermore, another eigenvector with an eigenvalue of 407.9 Hz occurs. This value agrees with the peak frequency of the 3D loss factor simulations. Obviously, this is the dominant heat flow in the solid beam model. The temperature distribution shows a gradient in the thickness and width direction (see figure 5.4c). Therefore the heat flows in two dimensions during the decay time. The analytical model assumes one-dimensional heat conduction and the peak frequency is a characteristic value for a specific thickness. In the solid model, there is no concentrated heat flow over the thickness of the beam. Therefore the height of the analytical peak is not achieved.

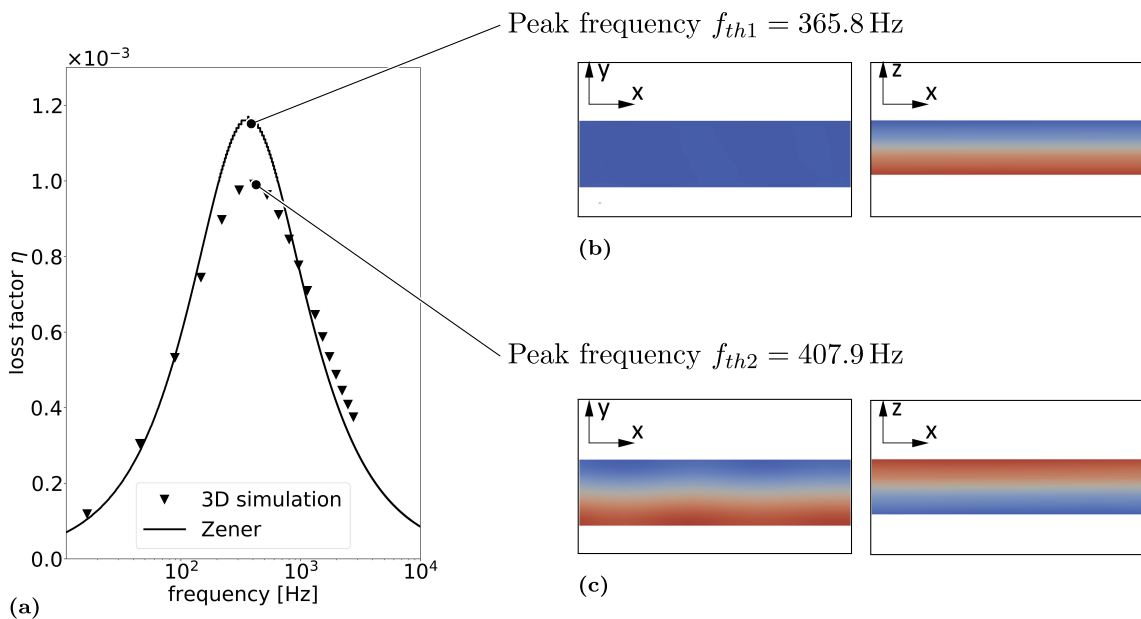


**Figure 5.4:** Peak frequencies of the analytical solution according to Zener [65] and the numerical solution of the 3D solid modeled beam (subfigure (a)), as well as the corresponding eigenvectors of the heat equation. At a frequency of 365.8 Hz, the thermal relaxation time corresponds to one-dimensional heat flow in thickness direction. Subfigure (b) shows the temperature gradients in width (xy-plane) and thickness direction (xz-plane) at a frequency of 365.8 Hz, i.e., a thermal relaxation time of  $1/365.8$  s. For a frequency of 407.9 Hz, the corresponding thermal eigenvector implies a two-dimensional heat conduction in thickness and width direction. Subfigure (c) shows the temperature gradients in width (xy-plane) and thickness direction (xz-plane) at a frequency of 407.9 Hz, i.e., a thermal relaxation time of  $1/407.9$  s.

## 5.4.2 Plate Structure

### 5.4.2.1 Numerical Model

In the next step, the rectangular aluminum plate presented in chapter 4 was modeled and the entropy approach to simulate the TED was applied. The structure was discretized with 20-node solid elements using quadratic interpolation functions. The solid elements have 3 translational DOF per node. For the in-plane direction, an edge length of 2 mm was used. In thickness direction, the plate was divided into 4 layers of elements to avoid shear locking effects. Therefore in total the mesh contains 60 000 elements for the plate of size 300 mm x 200 mm x 3 mm.

For the analyses performed in ABAQUS, solid elements with the name C3D20 were used.

### 5.4.2.2 Generated Heat

The basis for all subsequent steps is an eigenfrequency analysis. Following the workflow shown in figure 5.1 the eigenmodes are determined in ABAQUS and exported to Python. Additionally, the normalized stresses and strains due to the modal deformations are determined. In the framework of the entropy approach the generated heat during one vibration cycle in the appropriate frequency is simulated. Figure 5.5 provides the correlation among the mode shape of the plate structure, the hydrostatic stress distribution  $\sigma_{kk} = \sigma_{xx} + \sigma_{yy} + \sigma_{zz}$  and the generated heat  $\Delta Q$  in three specific mode shapes.

Since the eigenmodes are normalized vectors, the amplitudes are not significant and all quantities are scaled to the maximal value in the figure. The vibration of the plate follows a sine curve over time and the results are shown at time  $t = T/4$ , i.e. at the time step of maximum deflection and maximum stress level.

Furthermore, the figures (g) - (i) display a cut on the mid-plane level of the plate. In the thin plate, the heat flow is mainly in thickness direction. Similar to the example of the beam explained in section 3.3, the highest amount of heat generation occurs in the mid-level. The heat flow at the surface is negligible because the main temperature gradient is built over the thickness of the plate. Therefore a graphical representation of the outer surface would not show a heat generation.

It is apparent that the generated heat (and therefore the dissipated energy) correlates directly with the spatial distribution of the hydrostatic stress. The thermo-elastic coupling only affects those parts of the stress tensor that are associated with a volume change. Locations with a high hydrostatic stress level feature a large heat production.

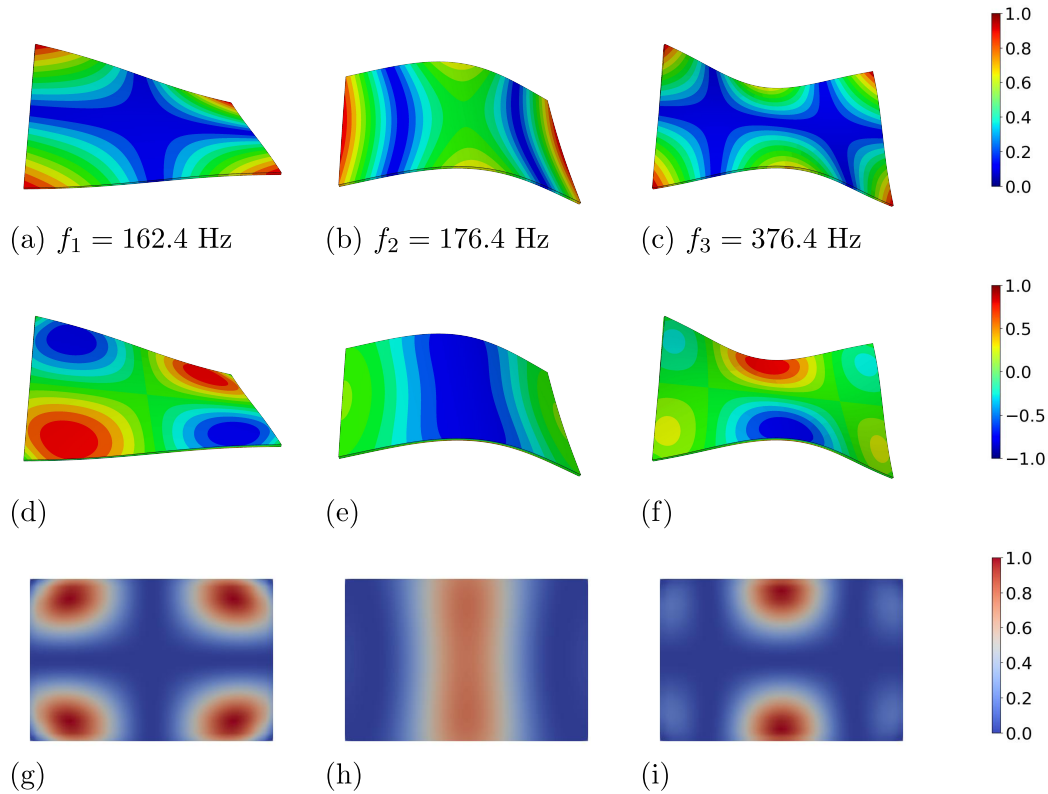


**Figure 5.5:** (a) - (c) Mode shapes of the rectangular aluminum plate 300 mm x 200 mm x 3 mm, deflection normalized to 1. (d) - (f) Distribution of hydrostatic pressure at the surface of the plate  $\sigma_{kk} = \sigma_{xx} + \sigma_{yy} + \sigma_{zz}$  (g) - (i) Spatial distribution of the dissipated energy  $\Delta Q$  in the first three eigenmodes of the plate at time  $T/4$ . A cut at mid-plane level of the plate is displayed. The values are normalized to the maximal value in each mode since they are based on relative displacements and temperature fields.

### 5.4.2.3 Comparison with Experimental Data

Figure 5.6 compares the experimental data and the simulation of the loss factor using the entropy approach. The details of the experimental procedure are explained in chapter 4.3. For reference, the analytical calculation according to Zener [65] for a beam specimen of 3 mm thickness is shown. This curve represents the case of a structure with one-dimensional heat conduction and the same thickness as the rectangular plate. Furthermore, the results are given in table 5.2, including the absolute and relative deviation of the simulated loss factor from the experiments.

Comparing the data series, it can be seen that the loss factors measured experimentally are usually higher than the simulated data. The deviation amounts to a minimum of 3 % and a maximum of approximately 35 %. This discrepancy may be explained by experimental challenges (see chapter 4.5). Every small disruptive factor in the setup causes an increase in damping. Due to the very low magnitude of the damping ratios measured in this study, the experiments are very sensitive to inaccuracies. The medium vacuum in the available vacuum chamber and small imperfections in the suspension of the plate lead to undesired dissipation effects.

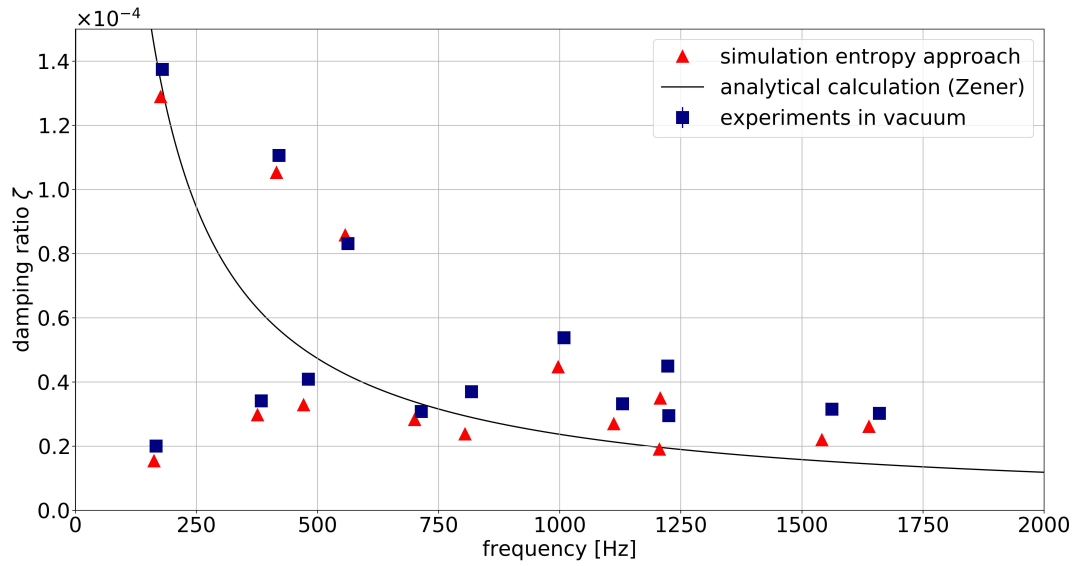
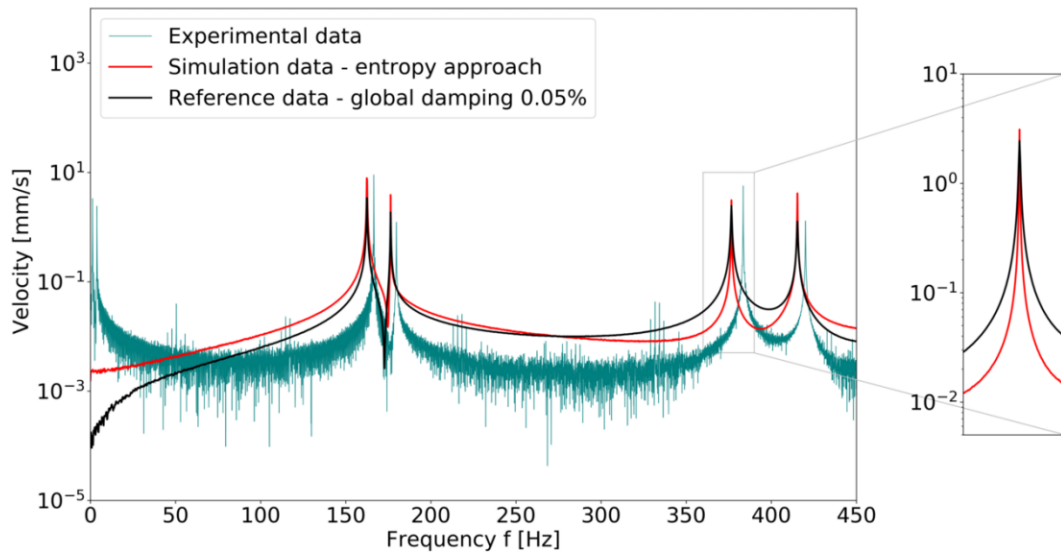
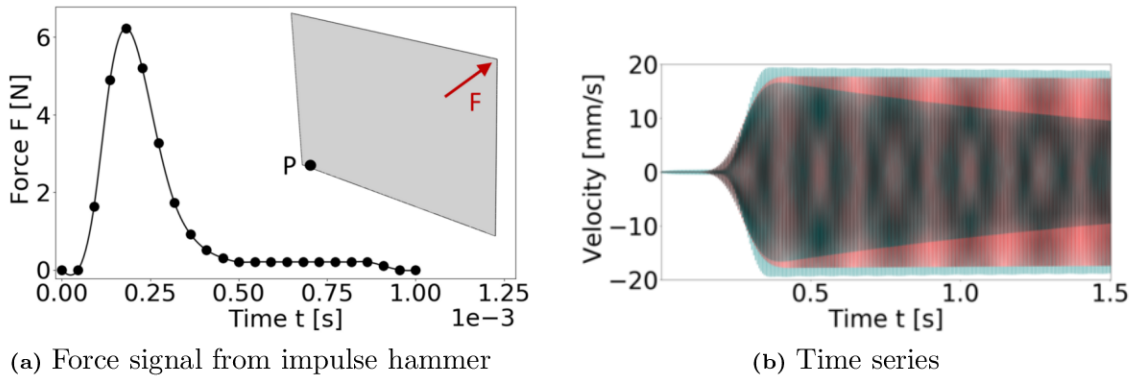


**Figure 5.6:** Comparison of experimentally determined damping ratios, simulated damping ratios with the entropy approach and for reference the analytically calculated curve for a component of thickness 3 mm according to Zener [7]

**Table 5.2:** Experimental damping ratios  $\zeta_e$  and simulated damping ratios  $\zeta_s$  for the aluminum plate 300 mm x 200 mm x 3 mm, absolute deviations and relative deviation in percent. The relative deviation is determined with reference to the experimental data.

f [Hz]	$\zeta_e$ [ $\cdot 10^{-5}$ ]	$\zeta_s$ [ $\cdot 10^{-5}$ ]	deviation abs. [ $\cdot 10^{-6}$ ]	deviation rel. [%]
162.42	1.981	1.540	4.412	22.27
176.40	13.61	12.89	7.158	5.26
376.40	3.374	2.971	4.024	11.93
415.32	10.95	10.52	4.271	3.90
471.43	4.043	3.287	7.556	18.69
557.33	8.231	8.577	3.459	4.20
700.72	3.047	2.826	2.212	7.26
804.90	3.659	2.374	1.284	35.11
997.07	5.321	4.465	8.563	16.09
1112.01	3.284	2.693	5.909	18.00
1205.84	2.920	1.903	1.017	34.83
1207.76	4.449	3.491	9.574	21.52
1541.61	2.990	2.192	7.980	26.69
1638.92	3.186	2.611	5.749	18.04

Although the deviation seems to be large in some modes, it must be taken into account that the relative differences between the mode shapes are represented very well. With the simulation approach, the correct magnitude of the damping ratios could be determined for all mode shapes and the dependence on the eigenfrequency and -form could be reflected successfully.



(c) Frequency spectrum

**Figure 5.7:** Comparison of experimental data and transient simulations with a global damping model using ( $\zeta_m = 0.0005$ ) for each mode and modal damping ratios determined with the entropy approach. The plate was excited in the upper right corner point and the time signal was measured in the lower right corner point. The shown time signals are filtered to the first eigenfrequency (162 Hz) by applying a bandpass filter in the range of 150 Hz - 170 Hz. The frequency spectrum was generated by applying a FFT to the time series.

A further simulation was performed to replicate parts of the experiments. In the physical tests the time series of the vibration velocities is recorded. To reproduce

the experiment in the simulation, a transient (i.e. time domain) analysis based on mode superposition was conducted and the results were compared directly. For the mode superposition procedure 50 eigenmodes from the previous modal analysis were considered.

As excitation a time-dependent force signal was used. Therefore the force amplitude recorded by the impulse hammer in the experiment was applied in the simulation. One node at the corner of the plate model was chosen as loading point, equivalent to the excitation of the real plate. The force signal and the applied load are shown in figure 5.7a. The time step was set to  $4.5 \times 10^{-5}$  s.

Two damping approaches were applied to the model:

- damping ratio of  $\zeta = 0.0005$  applied globally to all modes (in the further text referred to as „classical damping“)
- modal damping ratios  $\zeta_m$ , calculated by entropy approach (see table 5.2) for the individual modes, for mode 16 - 50 a modal damping of  $\zeta_m = 0.0005$  was used

A classical damping ratio of  $5 \times 10^{-4}$  was chosen based on empirical data for material damping of aluminum in the literature [2, 22].

The system response was recorded on another corner point P of the plate. In figure 5.7b the decay curve over time is shown for the experiment and the two simulations. The data series is filtered to the first eigenfrequency with a bandpass filter from 150 Hz to 170 Hz. The comparison shows that the simulation with modal damping values represents the decay behaviour of the experiment very well. The amplitudes are similar and the curves are damped weakly. The graph of the second simulation using the global damping approach reaches the same initial amplitude but decays more strongly due to the higher damping ratio.

In figure 5.7c the frequency spectrum for 0 - 500 Hz is shown for the experiment and the simulations. It was generated by applying an FFT to all three time series. First of all, it has to be noticed that there are additional frequency peaks in the experimental curve in very low-frequency ranges ( $<10$  Hz). They are caused by resonances of the elastic suspension and are comparable with rigid body modes in the case of free-free boundary conditions.

The absolute height of the peaks should not be compared directly between experiments and simulations. The frequency spectrum shows discrete data that depend on the sampling rate of the underlying time series. The procedure of the FFT is explained in detail in chapter 4.3.4.1. In the vicinity of resonance frequencies, the height of the peaks varies extremely dependent on the frequency. It can not be guaranteed, especially for the experimental data, that the exact resonant frequency is set as a sampling point. Nevertheless, the absolute heights match quite good in

the plot.

Based on the width of the peaks, a conclusion can be made about the damping behaviour. In the zoomed view the difference between the two simulations is emphasized in the example of eigenmode three. The lower modal damping results in a narrow peak, whereas the structural damping causes a wider peak.

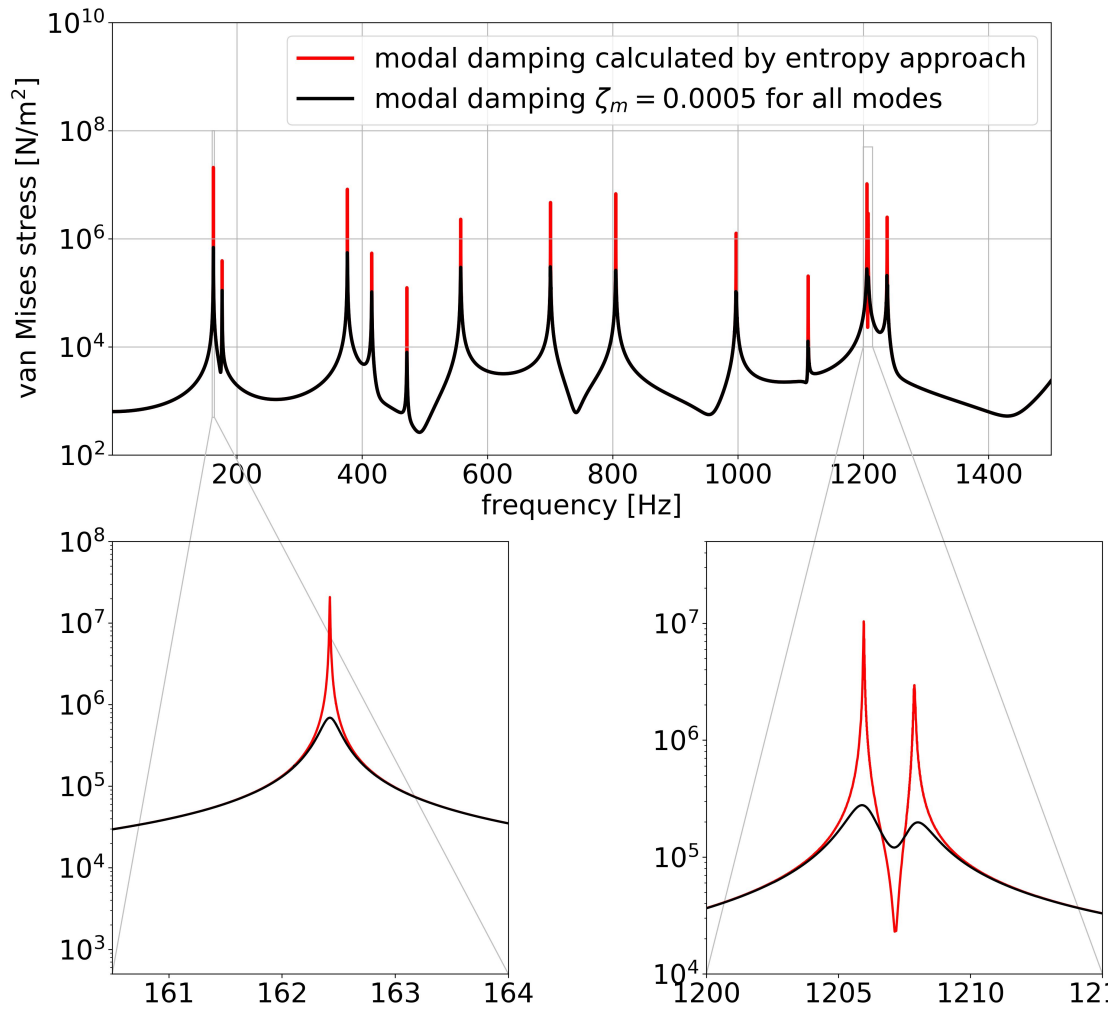
#### 5.4.2.4 Effect of the Damping Ratio on the Stresses in the Component

There can be significant effects on stresses and other strength characteristics in the component if damping parameters of the wrong order of magnitude are used. This is demonstrated by the example of the stress distribution under harmonic loading. Therefore, a steady-state dynamic analysis, i. e., a simulation in the frequency domain, is performed on the rectangular plate model. A concentrated harmonic force of 1 N is applied on one corner node of the structure (equivalent to figure 5.7a). Similar to the previous simulation, two different damping approaches were tested. First, a damping ratio of  $\zeta = 0.0005$  was applied globally to all modes, and second, modal damping ratios  $\zeta_m$  were calculated by the entropy approach for the individual modes.

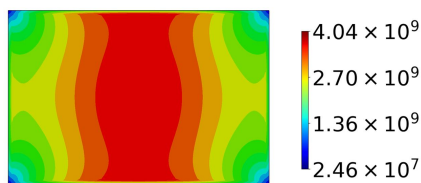
The performed frequency domain simulation is based on mode superposition. Fifty modes from a previously done eigenfrequency analysis were considered in the analysis. The frequency steps were determined by mode clustering, i.e., the intervals are smaller in the vicinity of the undamped eigenfrequencies. In this way, it is guaranteed that the system response is calculated at the resonance frequency. Therefore the height of the peaks in the frequency response spectra of both simulations can be compared directly.

As a characteristic value for the stress load of the component, the von Mises stress is used. Figure 5.8a shows the course of the von Mises stress at a corner point (point P in figure 5.7a) of the plate as a function of frequency. The simulations with the classical damping approach and the modal damping according to the entropy approach are shown for comparison. In the diagram, the frequency range up to 1500 Hz is plotted. The spatial distribution of the stress over the surface of the plate for an excitation in mode one (162 Hz) is displayed in the figures 5.8b and 5.8c.

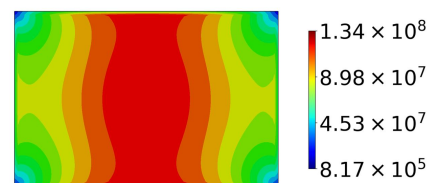
It can be demonstrated that the different damping approaches lead to significant differences in the stress peaks in the range of the resonant frequencies. The von Mises stress values of the model using the entropy approach are usually more than a power of ten larger than the reference values in the classically damped model.



(a) Frequency response spectrum from 0 Hz to 1500 Hz comparing the von Mises stress at a corner point P (see figure 5.7a) of the rectangular aluminum plate for the two applied damping approaches.



(b) Mode one ( $f_1 = 162$  Hz), modal damping approach ( $\zeta = 1.54 \times 10^{-5}$  determined by entropy approach)



(c) Mode one ( $f_1 = 162$  Hz), classical damping approach ( $\zeta = 0.0005$ )

**Figure 5.8:** Von Mises stress in the harmonically excited rectangular aluminum plate model. Compared are two damping approaches: damping ratio of  $\zeta = 0.0005$  applied to all modes and modal damping according to the entropy approach. (a) Von Mises stress in one node at corner of the plate over frequency range up to 1500 Hz. (b) - (c) Spatial distribution of the von Mises stress in the plate for excitation in eigenfrequency one  $f_1 = 162$  Hz using classical and modal damping models.

### 5.4.2.5 Comparison with Fully Coupled Simulation

Finally, it is interesting to compare the presented simplified approach to fully coupled thermoelastic simulations. As mentioned before, Serra et al. [9] developed a thermoelastically coupled FE formulation considering energy dissipation. The details of the underlying theory is given in chapter 3.4.2.

The element formulation is implemented in the FE-software package ANSYS as solid and panel elements [131]. For the modeling of the rectangular aluminum plate the type named SOLID226 is used. These volume elements with 20 nodes have quadratic interpolation functions and four DOF per node (translations  $u_x, u_y, u_z$ , temperature  $\theta$ ). The component is meshed similar to the previous simulations, i.e. in plane direction an edge length of 2 mm is applied and the structure is divided into four element layers in thickness direction.

The thermoelastically coupled element types are available for full transient (time domain) and full harmonic (frequency domain) analyses. Mode superposition procedures are not possible.

In order to determine the thermoelastic loss factors of the thermoelastically coupled model, a full harmonic analysis is performed with a point load applied sinusoidally at the corner point of the plate in the out-of-plane direction. No further boundary conditions are defined to simulate a free suspension.

The results of each frequency step include a real and an imaginary part of the solution. The complex data for the total strain energy are extracted per element and summed up over the whole structure. The loss factor is defined as the quotient of imaginary and real strain energy.

$$\eta = \frac{|\text{Im}(E_S)|}{|\text{Re}(E_S)|} \quad (5.4.1)$$

Figure 5.9 illustrates the results obtained from the fully coupled ANSYS analysis in comparison to the loss factors calculated with the simplified approach.

It is apparent from the diagram that the simplified energy approach produces only sample points at the resonant frequencies whereas the outcome of the fully coupled harmonic response analysis is one loss factor per frequency step. If the excitation frequency in the simulation matches exactly the eigenfrequency of the plate there is a pole in the curve. Therefore the absolute height of the peaks depends on the frequency discretization and is not representative. The loss factors simulated with the entropy approach should be compared with the general course of the graph. From this aspect, they agree very well with the results of the fully coupled simulations. Both the magnitude and the differences in the mode-dependent damping factors are represented accurately.

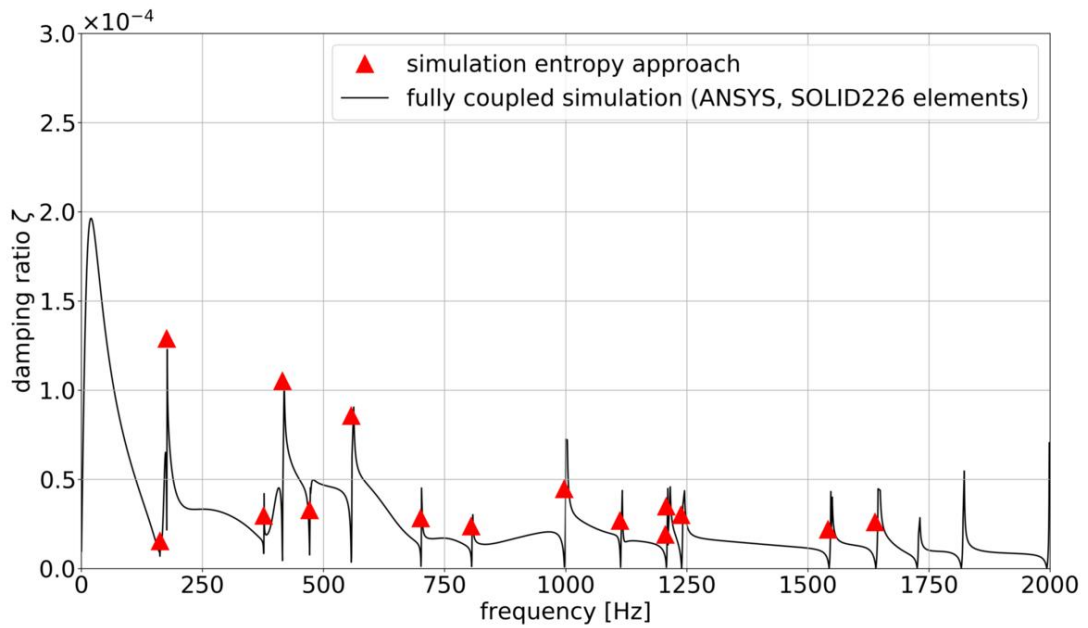


**Figure 5.9:** Comparison of the damping ratios of the modal based entropy approach with the fully coupled thermoelastic Ansys simulation for the rectangular plate.

### 5.4.3 Gearbox Casing

#### 5.4.3.1 Numerical Model

In a last step, the entropy approach was applied to the complex three-dimensional structure in the shape of a gearbox casing. The component is described in detail in chapter 4.2.

For the numerical analysis, a model with solid elements was created. Similar to the rectangular plate structure, mainly 20-node hexahedron elements with quadratic interpolation functions were used. However, due to the irregular geometry of the box, 10-node tetrahedron elements were also necessary. These elements use quadratic interpolation functions as well. Both element types have three DOF per node, the translations in three spatial directions  $u_x$ ,  $u_y$  and  $u_z$ . In total, the model was discretized by 291 320 elements with an edge length of approximately 3mm. For the steps performed in ABAQUS the element types C3D20 (hexahedron) and C3D10 (tetrahedron) are used. The FE model is displayed in figure 5.10.

#### 5.4.3.2 Generated Heat

As explained in section 5.3 the eigenmodes are calculated in ABAQUS and exported to Python. Based on the normalized strain distribution the heat generation, and the appropriate dissipated energy, in one vibration cycle are determined.

Figure 5.11 shows the correlation of the mode shapes (subfigure a-c), the hydrostatic

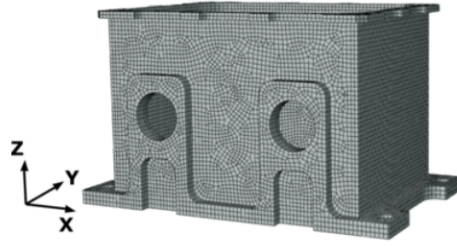


**Figure 5.10:** Discretization of the gearbox casing with hexahedron and tetrahedron solid elements. The elements C3D20 and C3D10 in ABAQUS use quadratic interpolation functions and have three **DOF** per node.

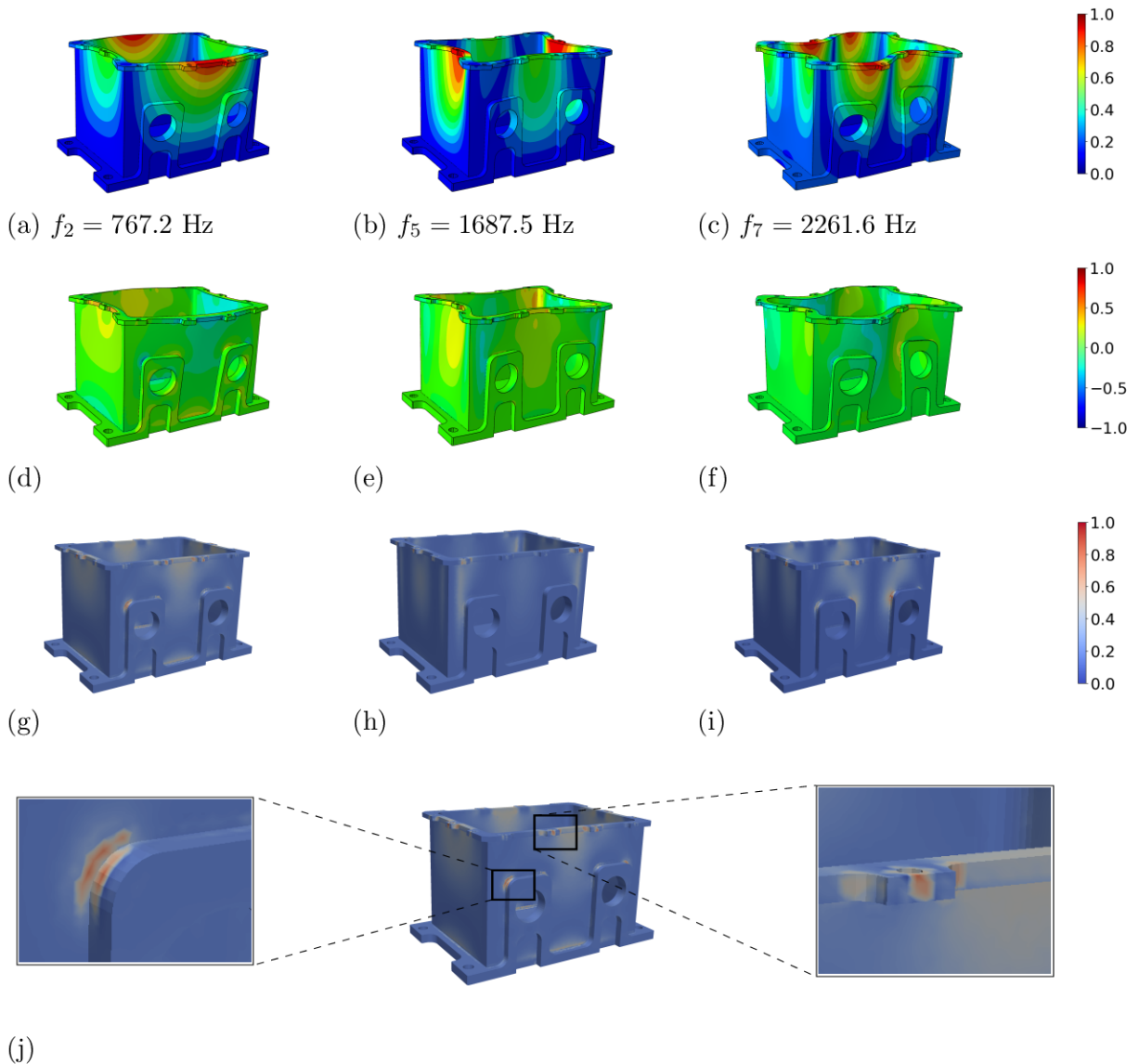


**Figure 5.11:** (a) - (c) Mode shapes 2, 5 and 7 of the box component, displacement normalized to 1 (d) - (f) Distribution of hydrostatic pressure  $\sigma_{kk} = \sigma_{xx} + \sigma_{yy} + \sigma_{zz}$  (g) - (i) Spatial distribution of the dissipated energy  $Q$  at time  $T/4$ . The values are normalized to 1 with respect to the maximum in each mode since they are based on relative displacements and temperature fields. (j) Detailed view of locations with high energy dissipation.

stress  $\sigma_{kk} = \sigma_{xx} + \sigma_{yy} + \sigma_{zz}$  (subfigure d-f) and the generated heat  $\Delta Q$  (subfigure g-i) in three specific mode shapes for the complex geometry. The eigenmodes two, five and seven were chosen as examples. Just like in figure 5.5, all data were scaled to one. The generated heat is based on the mechanical eigenmodes. These are normalized values, therefore the calculated temperature change has no significance. The generated heat  $\Delta Q$  (or equivalently the dissipated energy) is plotted at  $t = T/4$  since the vibration of the component follows a sine curve over time and the stress level, as well as the heat generation is maximal at this time.

The intensity of the thermoelastic effect depends on the relationship between the relaxation time of the temperature field and the length of the heat conduction path, as shown in chapter 3.3. For frequencies  $> 100$  Hz, the “optimal” length of the heat flow is  $< 1$  mm. Therefore the points of maximal heat generation occurs at corners, edges and holes. At these locations, large temperature gradients occur due to short geometrical distances between regions with stress differences. Furthermore, local peaks in the stress field also cause temperature gradients with short heat flow paths, which leads to local high energy dissipation. Two examples of these locations are shown graphically in the detailed plot at subfigure 5.11j.

### 5.4.3.3 Comparison with Experiments

Figure 5.12 compares the experimental values of the damping ratios  $\zeta$  with the simulated data obtained by the entropy approach. The experiments were performed on two identical components, and two measurement points were used for each eigenmode. Details concerning the experimental setup can be found in chapter 4.3. The values shown are averaged measurement results. The standard deviation is represented by bars. If no bar is visible, the standard deviation is too small to be displayed. The damping ratio of the first eigenmode has a higher value than the following. The other values remain on the same level, with a slightly decreasing trend. This course is consistent with both calculated and measured values. Usually, the experimentally measured values are always slightly higher than the calculated ones (except in the second eigenmode). The reason is mainly the systematic problems in the experimental setup, as already explained in chapter 4.5. For practical reasons, all samples were suspended in the holes at the bottom of the gearbox casing. There is no significant deformation in all the considered eigenmodes at these locations. However, they are not always the exact zero lines of the system, so there may be minor additional effects due to frictional damping. In addition, high vacuum cannot be achieved with the available vacuum chamber. Taking these facts into account, there is overall good agreement between simulation and experiment.

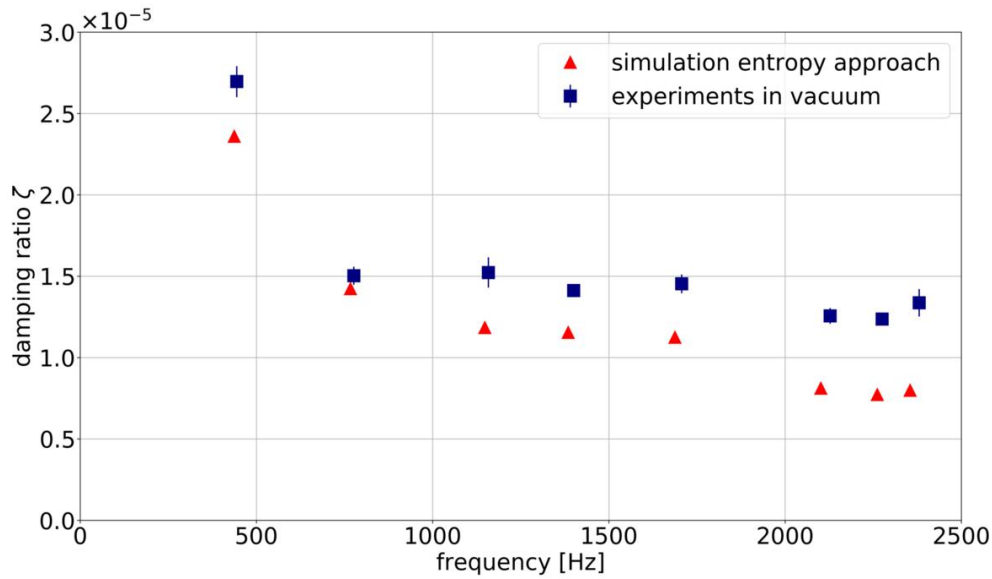


**Figure 5.12:** Comparison of the experimental data and the damping ratio determined by the entropy approach for the box component.

#### 5.4.3.4 Effect of the Damping Ratio on the Stresses in the Component

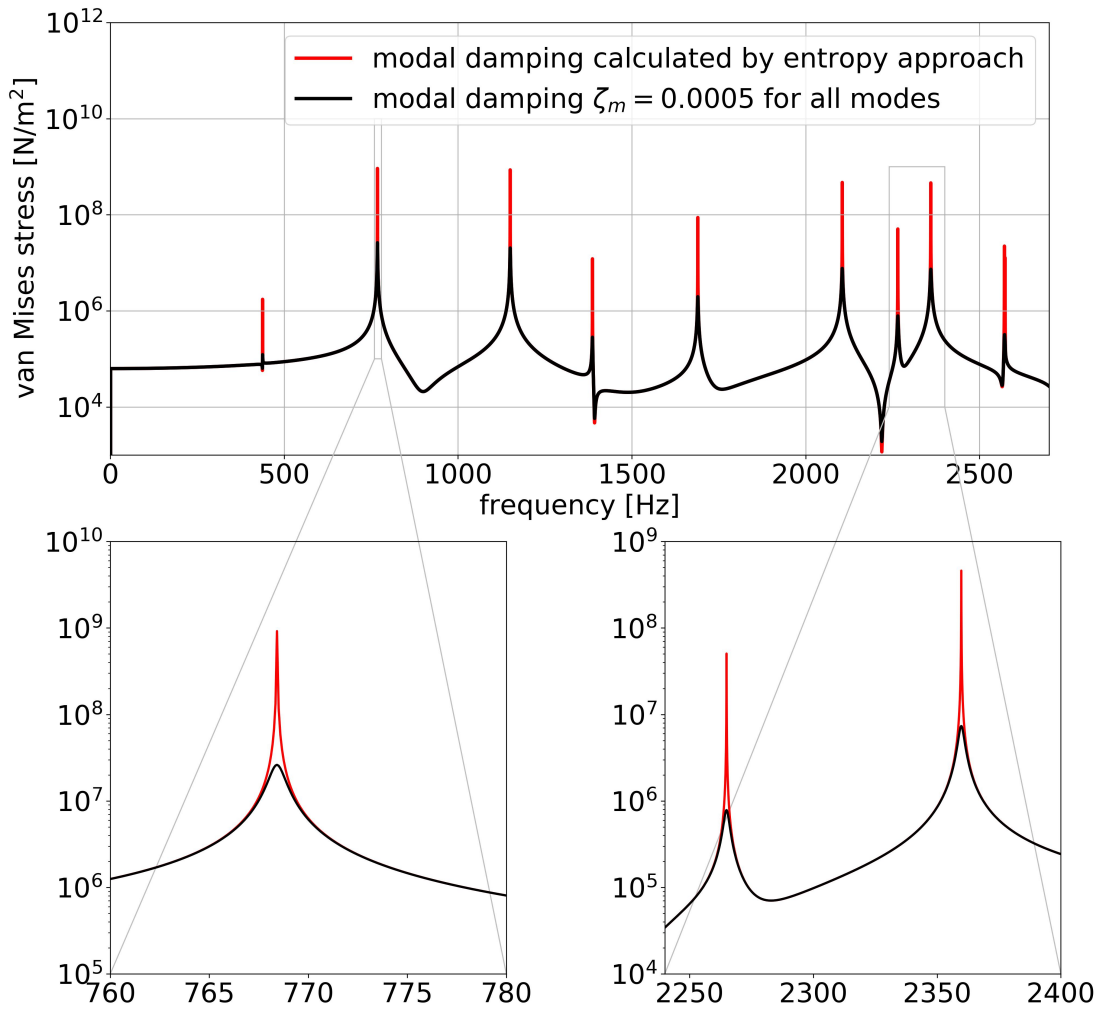
Similar to the stress analysis on the rectangular plate, the influence of the damping ratio on the stresses in the gearbox casing is studied. Therefore, a steady-state dynamic analysis, i. e., a simulation in the frequency domain, is performed on the FE model. The position of the applied loading and the node P of the analyzed stress is shown in figure 5.16. A concentrated harmonic force of 1 N is applied in the middle of the upper edge of the casing in y-direction.

As in the plate example, two different damping approaches are considered. First, a damping ratio of  $\zeta = 0.0005$  is applied globally for the whole frequency range. Furthermore, modal damping ratios  $\zeta_m$  are calculated using the entropy approach for the individual modes.

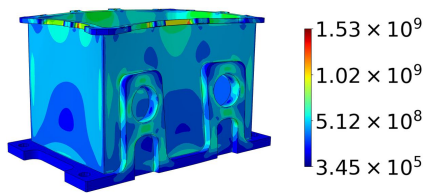
The performed frequency domain simulation is based on mode superposition. Fifty modes from a preceding eigenfrequency analysis were considered in the analysis.

The von Mises stress is used as a characteristic value for the stress load of the component. Figure 5.13a shows the von Mises stress of node P as a function of the vibration frequency. The spatial distributions of the stress in the second mode ( $f_2 = 767$  Hz) is displayed in the subfigures 5.13b and 5.13c.

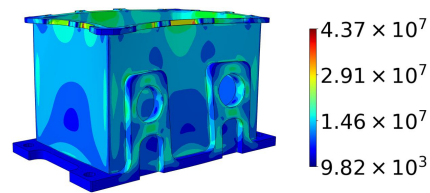
As already stated for the rectangular plate, the different damping approaches result in significant differences concerning the absolute height of the frequency peaks. Particular emphasis should be placed on the first eigenfrequency, which almost vanishes in the case of globally applied viscous damping, while a clear peak is present in the case of modal damping.



(a) Frequency response spectrum from 0 Hz to 2700 Hz comparing the von Mises stress at one node for the two applied damping approaches. The results are shown for point P (see figure 5.16)



(b) Mode one ( $f_2 = 767$  Hz), modal damping approach ( $\zeta = 1.42 \times 10^{-5}$  determined by entropy approach)



(c) Mode nine ( $f_2 = 767$  Hz), classical damping approach ( $\zeta = 0.0005$ )

**Figure 5.13:** Von Mises stress in the harmonically excited aluminum gearbox casing model. Compared are two damping approaches: damping ratio of  $\zeta = 0.0005$  applied to all modes and modal damping according to the entropy approach. (a) Von Mises stress in one node at corner of the plate over frequency range up to 2700 Hz (b) - (c) Spatial distribution of the von Mises stress in the plate for excitation in eigenfrequency one  $f_2 = 767$  Hz using classical and modal damping models.

#### 5.4.3.5 Comparison with Fully Coupled Simulation

In order to compare the results of the entropy approach with a fully coupled thermoelastic simulation, the gearbox casing was also modeled with thermoelastic solid elements in ANSYS (see chapter 3.4.2 for a theoretical description). The same mesh as described above was used. The hexahedron SOLID226 elements were already described for the case of the rectangular plate. The thermoelastically coupled tetrahedron volume elements are implemented in ANSYS under the name SOLID227. These 10-node elements have quadratic interpolation functions as well and four DOF per node ( $u_x$ ,  $u_y$ ,  $u_z$  and  $\theta$ ).

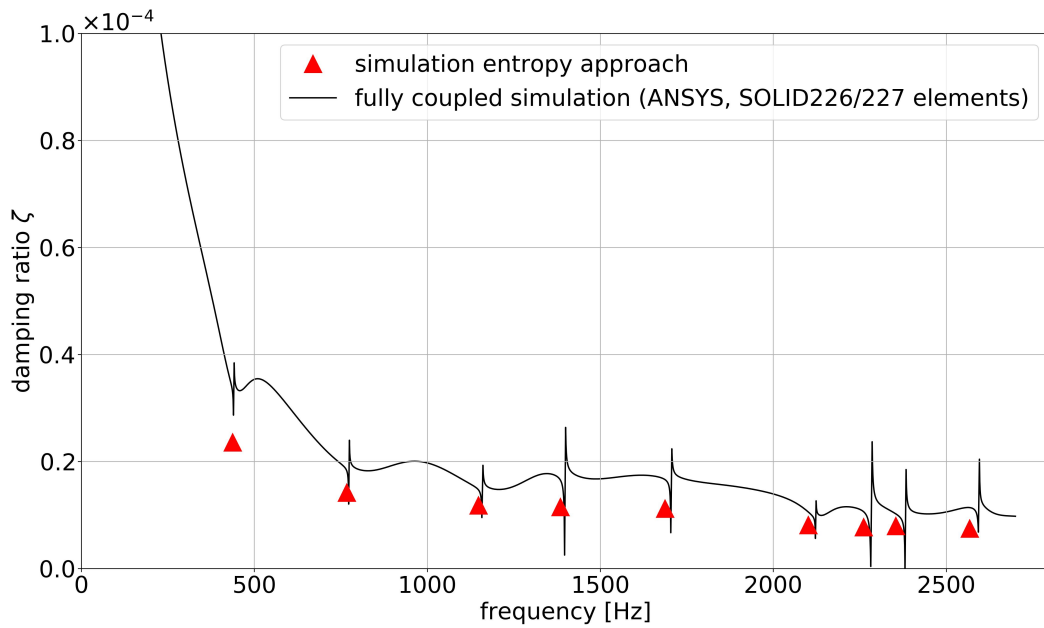
Similar to the procedure at the rectangular plate described above, a full harmonic analysis is conducted, i. e., a frequency-domain analysis using full system matrices. To simulate the free suspension, like in the experimental studies, no boundary conditions are set. A force of 100 N is applied in the middle of the upper edge of the box in the y-direction (as shown in figure 5.16). The frequency range is defined from 0 to 2700 Hz.

Figure 5.14 shows the damping ratios calculated by the entropy approach with the damping ratio curve extruded from the ANSYS harmonic simulation. In the full harmonic simulation, the system response is calculated for each frequency step. The results of each frequency step include a real and an imaginary part of the solution. The complex data for the total strain energy are extracted per element and summed up over the whole structure. The loss factor is defined as the quotient of imaginary and real strain energy. Therefore one data point is calculated for each frequency step. In contrast to this, the results of the entropy approach are determined as discrete damping ratios at the resonant frequencies.

The curve of the fully coupled simulation has poles at the resonant frequencies. Therefore an exact comparison is difficult. However, the damping values calculated by the entropy approach are close to the graph of the fully coupled simulation. Furthermore, the differences between the values of the single modes are well represented.

In the next step, the damping ratios calculated with the entropy approach were applied in a frequency-domain simulation based on modal superposition. For this purpose, the discretely determined damping ratios were used as modal damping ratios. The frequency response of this simulation was compared to the results of the fully coupled analysis.

Figure 5.15 shows a comparison of a single-point displacement in the modal based harmonic simulation with the same displacement component in the full harmonic simulation. For this analysis, a single load  $F$  in y-direction is applied harmonically at a point in the middle of the upper edge of the component, as shown in figure 5.16.



**Figure 5.14:** Comparison of the damping ratios of the modal based entropy approach with the fully coupled thermoelastic Ansys simulation for the box component.

The displacement in y-direction is determined at a node denoted by P. No support conditions are applied to the model.

The course of the curves and the width of the peaks agree very well. The absolute height of the peaks is not significant because it depends on the frequency discretization. Only at eigenfrequency 5 at approximately 1687 Hz are there inaccuracies. In this eigenmode, the measurement node P is close to a zero line (see figure 5.11 b), so that the oscillation mode cannot be reproduced well in both simulations. This leads to distortions of the results.

Note that only frequencies  $f > 200$  Hz are displayed here. The first natural frequency occurs at 437 Hz, i. e., the relevant frequency domain is covered. No boundary conditions are applied to the model to ensure comparability with the experiment. Therefore a large influence of the rigid body modes occurs at low frequencies in the full harmonic simulation.

Overall, the very good agreement of the curves shows that with the entropy approach presented here, equivalent results can be achieved as with a fully coupled calculation, with a significant reduction in computing time.

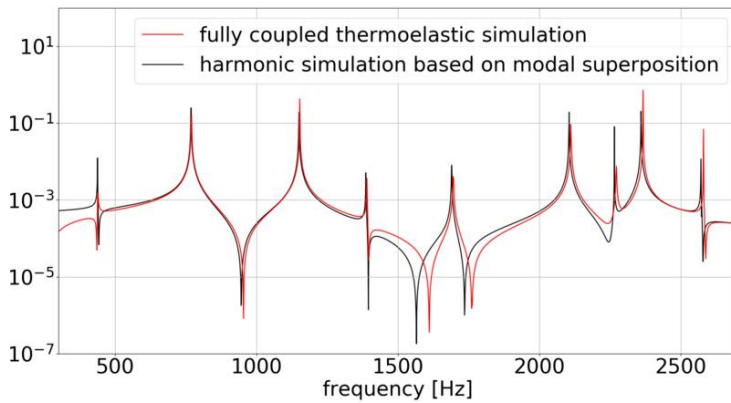


**Figure 5.15:** Comparison of displacement in  $y$ -direction of single node. Red curve: Fully coupled simulation with thermoelastic elements SOLID226. Black curve: Harmonic simulation based on modal superposition, use of modal damping ratios that were calculated with the entropy-approach.

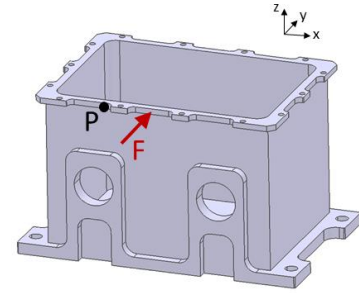


**Figure 5.16:** Excitation point of force  $F$  and measurement point  $P$  of displacement in frequency-domain analysis. No support conditions were applied.

## 5.5 Discussion

The presented entropy approach was applied to different structures. A series of thin beam structures were used for fundamental investigation of the method and comparison to analytical computations. The results of the new numerical method are comparable to the analytical solutions according to Zener [7, 65]. The numerical simulation represents the typical peak function of the loss factor over the frequency in thin beams very well. Minor deviations in the absolute value of the loss factor can be explained by the fact that the analytical calculation is based on one-dimensional heat conduction. In contrast, the simulation with the entropy approach assumes three-dimensional heat conduction.

Furthermore, the method was implemented on two components that were also part of the experimental studies, a rectangular plate and a gearbox casing. The results were analyzed in detail, considering different output parameters. For both examples, the calculated thermoelastic loss factors agreed well with the experimental results. The entropy approach results clearly represent the mode-dependent behavior of the loss factor. Compared to global material damping values from literature, it can be seen that a realistic damping approach is essential to predict deformations and stresses in the component accurately.

Additionally, the results of the entropy approach simulation are compared with fully thermoelastically coupled FE simulations. Solid elements with coupled mechanical and thermal DOF are available in the software package ANSYS and are suitable for obtaining accurate thermoelastic damping ratios. Nevertheless, simulations using these element types require enormous computing times since the thermoelastically

coupled system of equations must be solved for every time or frequency step. Therefore, the method is usually not suitable for practical use. With the entropy approach presented here, similar vibration damping and system responses in the frequency domain could be achieved with significantly lower CPU time. Table 5.3 compares the computing times for a frequency domain analysis. Both the rectangular plate structure and the gearbox casing are considered. The bottleneck in the analysis is the determination of the modal damping ratios by the method presented here. This calculation step was the only one performed on a local computer and was not parallelized, so there is still potential for improvement in this respect.

However, it must be considered that two different solution techniques are com-

**Table 5.3:** Computing time in CPU hours for a frequency-domain analysis using a direct solution procedure with fully coupled thermoelastic elements and a mode superposition solution procedure with modal damping. The modal damping ratios were determined with the entropy approach provided in this chapter. For the rectangular plate, 5000 frequency steps were analyzed and, for the box component, 2700 frequency steps were analyzed. All simulations (except for the calculation of the modal damping ratio) were run on 16 cores of a compute node with two Intel Xeon Processor E5-2650 v4 CPUs with a base clock of 2.2 GHz and 128 GB RAM.

	plate	box component
number of elements	60 000 el.	291 320 el.
fully coupled simulation SOLID226/227	34.8	1 132.3
entropy approach	1.3	11.3
eigenfrequency analysis	0.1	0.5
modal damping ratio	0.7	1.1
harmonic analysis	0.5	9.7

pared. The thermoelastically coupled elements in ANSYS require an analysis with full system matrices. In contrast, the entropy approach uses mode superposition procedures, which usually offer a great advantage in computing time but include some limitations. The analysis is restricted to linear problems, and the accuracy of the results depends on the number of considered modes.

In summary, the developed entropy approach is well suitable for calculating thermoelastic material damping in components with arbitrary geometry. The reasonable computing times make the method attractive for practical use.



# Chapter 6

## Thermoelastic damping based on modal bending energy

### 6.1 Introduction

The entropy approach presented in chapter 5 allows the calculation of thermoelastic damping in arbitrary homogeneous structures that can be discretized with solid elements. However, TED occurs very often in thin-walled components due to a short path of heat conduction in the thickness direction. Therefore, thin plates and discs were the focus of numerous studies in the past. In chapter 3.3.3, the literature review of TED in thin plates is presented separately.

Numerous authors developed methods to transform the fundamental theories of beam structures to two-dimensional plates. Usually, simple geometries such as rectangular and circular plates were considered. In most cases, the theories were applied to micro- and nanostructures since material damping is the dominant damping effect on the microscale compared to other types of damping [71, 77]. However, especially in the case of planar, thin-walled components, critical thermoelastic effects can also occur in macro-components [122, 169]. In this chapter, a simplified approach is presented to determine TED in structures that are modeled as shell structures by extending the analytical Zener formula to thin plates. The thermoelastic loss is calculated dependent on the eigenmodes and -frequencies of the component. It is integrated into the workflow of a dynamic FE simulation based on modal superposition.

A patent from the year 2017 describes the basic idea of using the analytical Zener calculation to determine local damping parameters based on the stress distribution in the component [170]. This concept is further developed in the present chapter and realized in an algorithm for application in numerical simulation methods.

The analytical approach, according to Zener [65], is valid for thin beams in the state

of pure bending. For plate structures, a reduction of the damping ratio for bending by a modal bending factor (MBF) is implemented. This factor is calculated as the bending energy and total strain energy ratio for each mode shape.

In the FE model, every shell element is considered as a plate structure, and an MBF is assigned. In this way, the proportion of bending can be represented locally, but a general MBF can also be determined by integration over the entire structure.

First, the plate theory and its extension to structural shell elements are presented. Afterwards, the method to calculate damping ratios by determining the MBF and the embedding in the FE workflow are described in detail. The results are shown using the example of the rectangular plate and compared with the approach presented in chapter 5. As an example for a thin-walled component with complex geometry, the protection plate introduced in chapter 4 is analyzed to verify the application of the method. The results are compared with experiments as well as fully-coupled thermoelastic simulations. Finally, a circular plate from a literature example is analyzed, and the results are compared to experimental reference data.

## 6.2 Fundamentals of Plate Theories and Shell Models

This section shortly presents some significant aspects of plate theories in order to provide the fundamentals for the formulation of the methodology. Furthermore, the application of the plate theory in finite element models is outlined. Since shell elements are used for the development of the MBF approach, this element type is introduced. In this chapter,  $x$  and  $y$  are defined to be the in-plane directions, and  $z$  to be the thickness direction, as shown in figure 6.1. For a more thorough treatment of shell elements and the structural models, the reader is referred to [127], [171], or [128].

### 6.2.1 Plate theory

A plate is defined as a plane structural mechanical model with a thickness dimension  $h$  that is much smaller than the other dimensions  $l_1$  and  $l_2$ , and is exposed to bending or shear stresses.

$$\frac{h}{l} \ll 1 \qquad l = \min(l_1, l_2) \qquad (6.2.1)$$

The in-plane stresses  $\sigma_{xx}$ ,  $\sigma_{yy}$  and  $\sigma_{xy} = \sigma_{yx}$  are linearly distributed over the thickness. In addition, transverse shear stresses  $\sigma_{xz} = \sigma_{zx}$  and  $\sigma_{yz} = \sigma_{zy}$  occur. It is

assumed that stresses in thickness direction can be neglected ( $\sigma_{zz} = 0$ ).

Two theories for the analysis of plate structures are distinguished:

- plates without shear deflection (Kirchhoff plate) - mainly used for thin plate structures
- plates with shear deflection (Mindlin-Reißner plate) - mainly used for thick plate structures

This section first introduces the basic equations for the Mindlin-Reißner plate theory. In a second step, the formulations are reduced to the Kirchhoff plate theory.

Concerning the material model, a homogeneous and isotropic material is assumed. The cross-sections remain straight during deformation, but not necessarily normal to the deformed middle surface. The in-plane displacements  $u_x$  and  $u_y$  are linear functions and depend on the thickness coordinate  $z$ . The transverse displacement  $u_z$  is constant and equal to the deformation  $w$ .

$$u_x(x, y, z) = z\phi_y(x, y) \quad (6.2.2)$$

$$u_y(x, y, z) = z\phi_x(x, y) \quad (6.2.3)$$

$$u_z(x, y, z) = w(x, y) \quad (6.2.4)$$

Here  $\phi_x$  and  $\phi_y$  are the rotation angles about the x and y axis of the cross-sectional fibres to the undeformed mid surface. Accordingly, the strain tensor can be divided into two parts, a bending part  $\varepsilon^b = \{\varepsilon_{xx}, \varepsilon_{yy}, \varepsilon_{xy}\}^T$  and a shear part  $\varepsilon^s = \{2\varepsilon_{xz}, 2\varepsilon_{yz}\}^T$ .

$$\{\varepsilon\} = \begin{Bmatrix} \varepsilon^b \\ \varepsilon^s \end{Bmatrix} \quad (6.2.5)$$

The bending strains are linear over the thickness of the plate and defined by the derivatives of the rotation angles, whereas the transversal shear strains are constant.

$$\begin{Bmatrix} \varepsilon_{xx} \\ \varepsilon_{yy} \\ 2\varepsilon_{xy} \end{Bmatrix} = -z \begin{Bmatrix} \frac{\partial\phi_y}{\partial x} \\ \frac{\partial\phi_x}{\partial y} \\ \frac{\partial\phi_y}{\partial y} + \frac{\partial\phi_x}{\partial x} \end{Bmatrix} \quad \begin{Bmatrix} 2\varepsilon_{xz} \\ 2\varepsilon_{yz} \end{Bmatrix} = \begin{Bmatrix} \frac{\partial w}{\partial x} - \phi_y \\ \frac{\partial w}{\partial y} - \phi_x \end{Bmatrix} \quad (6.2.6)$$

Applying the constitutive law for an isotropic material the stresses are calculated.

$$\begin{Bmatrix} \sigma_{xx} \\ \sigma_{yy} \\ \sigma_{xy} \end{Bmatrix} = -z \frac{E}{1-\nu^2} \begin{bmatrix} 1 & \nu & 0 \\ \nu & 1 & 0 \\ 0 & 0 & \frac{1-\nu}{2} \end{bmatrix} \begin{Bmatrix} \frac{\partial \phi_y}{\partial x} \\ \frac{\partial \phi_x}{\partial y} \\ \frac{\partial \phi_y}{\partial y} + \frac{\partial \phi_x}{\partial x} \end{Bmatrix} \quad (6.2.7)$$

$$\begin{Bmatrix} \sigma_{xz} \\ \sigma_{yz} \end{Bmatrix} = \frac{E}{2(1+\nu)} \begin{Bmatrix} \frac{\partial w}{\partial x} - \phi_y \\ \frac{\partial w}{\partial y} - \phi_x \end{Bmatrix} \quad (6.2.8)$$

Since energy considerations are particularly important in the current chapter, the calculation of the total strain energy is briefly presented. The total strain energy  $E_S$  is composed by the bending and shear strains defined in equation 6.2.6.

$$E_S = \frac{1}{2} \int_V \boldsymbol{\varepsilon}^T \mathbf{E} \boldsymbol{\varepsilon} \, dV \quad (6.2.9)$$

$$\begin{aligned} &= \frac{1}{2} \int_V \left[ \frac{E}{1-\nu^2} (\varepsilon_{xx}^2 + \varepsilon_{yy}^2 + 2\nu \varepsilon_{xx} \varepsilon_{yy}) \right. \\ &\quad \left. + \frac{E}{2(1+\nu)} ((2\varepsilon_{xy})^2 + (2\varepsilon_{yz})^2 + (2\varepsilon_{xz})^2) \right] dV \end{aligned} \quad (6.2.10)$$

The Mindlin-Reißner plate theory requires three independent variables: the deformation in thickness direction  $w$  and both rotation angles  $\phi_x$  and  $\phi_y$ . In plates without shear deflection, i.e., in the Kirchhoff plate theory, the independent variables are reduced to the deformation  $w$ .

The rotation angles can be defined with respect to  $w$ .

$$\frac{\partial w}{\partial x} = \phi_y \qquad \frac{\partial w}{\partial y} = \phi_x \quad (6.2.11)$$

Consequently, the shear strains  $\varepsilon_{xz}$  and  $\varepsilon_{yz}$  given in equation 6.2.6 are zero, as well as the shear stresses  $\sigma_{xz}$  and  $\sigma_{yz}$ . Therefore, the equation calculation the total strain

energy is simplified as

$$E_S = \frac{1}{2} \int_V \boldsymbol{\varepsilon}^T \mathbf{E} \boldsymbol{\varepsilon} \, dV \quad (6.2.12)$$

$$= \frac{1}{2} \int_V \frac{E}{1-\nu^2} (\varepsilon_{xx}^2 + \varepsilon_{yy}^2 + 2\nu\varepsilon_{xx}\varepsilon_{yy} - \frac{1-\nu}{2}(2\varepsilon_{xy})^2) \, dV \quad (6.2.13)$$

### 6.2.2 Shell Elements

If one of the plate theories is directly transferred into a FE formulation, the resulting element is limited to a plane mid surface and orthogonal loading. Therefore it is usually more convenient to use shell elements. The shell theory can be regarded as an extension of plate theory with additional membrane parts, i.e., shell elements behave similarly to plate elements but can also represent normal stresses and strains. Furthermore, the mid surface can be curved.

A wide variety of shell elements are available for different purposes. If the underlying plate theory, according to Mindlin-Reißner, is used, the elements usually have five or six nodal DOF, depending on whether rotation about the  $z$ -axis,  $\phi_z$ , is considered. In this chapter, again, the software package ABAQUS is used. The models are discretized with S4 shell elements. These quadrilateral elements have linear interpolation functions and four nodes with six DOF each, as shown in figure 6.1: three translational DOF and three rotational DOF.

$$u = \sum_{i=1}^n N_i u_i \quad v = \sum_{i=1}^n N_i v_i \quad w = \sum_{i=1}^n N_i w_i \quad (6.2.14)$$

$$\phi_x = \sum_{i=1}^n N_i \phi_{xi} \quad \phi_y = \sum_{i=1}^n N_i \phi_{yi} \quad \phi_z = \sum_{i=1}^n N_i \phi_{zi} \quad (6.2.15)$$

The system matrices are developed based on the weak form of the elasticity equation according to equations 3.4.7 and 3.4.12.

In this displacement-based FE approach, only first derivatives of the independent variables occur. Therefore the interpolation functions must have  $C^0$ -continuity. If the Kirchhoff plate theory without shear deformation is assumed, the interpolation function for the independent variable  $w$  have to be  $C^1$ -continuous. This results in higher order shape functions to construct a conforming element. The condition of  $C^0$ -continuity is often difficult to fulfil in practical application. Due to the simpler and more convenient formulation of shear-elastic Mindlin-Reißner plates, these elements are widely used in FE codes, even for thin structures with small deformations. Nevertheless, these elements based on a pure displacement formulation can lead to

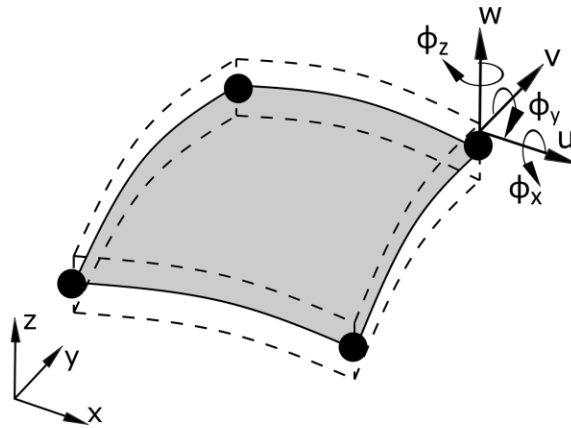


**Figure 6.1:** Four-node shell element with six **DOF** per node, as for example used in ABAQUS as S4 elements.

undesirable effects in the application. The assumption of equal interpolation functions for mid-plane deformation and rotation causes incorrect internal forces. The shear stiffness is overestimated compared to bending stiffness. This so called shear-locking effect occurs especially with decreasing thickness of the element. As a result, spurious shear forces are calculated and the deflection of the plate is approximated inaccurately.

There is a number of measures to avoid shear-locking, e.g.

- significantly higher-order interpolation functions.
- reduced integration or selective integration
- mixed elements - use of mixed interpolations for deformation, rotation and transverse shear strain, e.g. MITC-Element [172, 173]
- assumed-strain element or enhanced-assumed-strain element (EAS) [174, 175] - the kinematic equation is only fulfilled in some sample points and interpolated in between

In the S4 elements an assumed-strain approach is used. Besides the interpolation functions of the independent variables, a transverse strain field is constructed that guarantees a vanishing shear deformation with decreasing thickness. Therefore the elements behave like Mindlin-Reißner plates if the thickness is large enough and use the Kirchhoff plate theory in case of thin structures. In homogeneous elements the criterion for a “thick” shell element is an element thickness larger than  $\frac{1}{15}$  of the characteristic surface length. This length depends on the type of analysis and is defined e.g. as distance between supports in static analysis or the distance between the nodes of an eigenmode [132].

### 6.3 Method - Derivation and Implementation

The plate theory presented in chapter 6.2 is used to determine a simplified formula of the thermoelastic loss factor  $\eta$ . The basis for this is the derivation of  $\eta$  based on the rate of generated heat, as shown in chapter 3.3.1. As stated in formula 3.3.44 the thermoelastic loss factor for a beam structure is the ratio of dissipated energy  $\Delta Q$  to the total dilation energy  $W_D$ . The general definition of the loss factor  $\eta$  is the quotient of dissipated energy to total strain energy. Expanding the formula by the dilation energy  $W_D$  we get the factor  $\frac{W_D}{E_S}$ .

$$\eta = \frac{1}{2\pi} \frac{\Delta Q}{E_S} \quad (6.3.1)$$

$$\eta = \frac{1}{2\pi} \frac{W_D}{E_S} \frac{\Delta Q}{W_D} \quad (6.3.2)$$

For a beam in the state of pure bending  $\frac{W_D}{E_S} = 1$ . Usually the deformation of a plate consists of bending and shear partitions, therefore  $\frac{W_D}{E_S} \neq 1$ .

To derive the dilation energy and the total strain energy the theory of plane stress in plates is used. The following relationships characterise the state of plane stress:

$$\varepsilon_{xx} = \frac{1}{E}(\sigma_{xx} - \nu\sigma_{yy}) + \alpha(T - T_0) \quad (6.3.3)$$

$$\varepsilon_{yy} = \frac{1}{E}(\sigma_{yy} - \nu\sigma_{xx}) + \alpha(T - T_0) \quad (6.3.4)$$

$$\varepsilon_{zz} = -\frac{\nu}{E}(\sigma_{xx} + \sigma_{yy}) + \alpha(T - T_0). \quad (6.3.5)$$

In terms of the normal strains  $\varepsilon_{xx}$  and  $\varepsilon_{yy}$  the transversal strain  $\varepsilon_{zz}$  can be expressed as follows.

$$\varepsilon_{zz} = \frac{1}{1 - \nu} [-\nu(\varepsilon_{xx} + \varepsilon_{yy}) + (1 + \nu)\alpha(T - T_0)] \quad (6.3.6)$$

Furthermore, unlike in the three-dimensional solid, the relation between hydrostatic stress and volumetric strain is described by  $\sigma_{kk} = \frac{E}{1 - \nu}\varepsilon_{kk}$ . In the thermoelastically coupled heat equation (see equation 3.2.35) the coupling factor  $\beta$  is defined as  $\beta = \frac{E\alpha}{1 - \nu}$ . The thermal parts of the strain would cause nonlinear formulations in the heat equation. Since the elastic strains are significantly larger in the present problems, the thermal parts are neglected here. For the coupled heat equation of a

two-dimensional plate structure, the following formula is obtained.

$$\frac{\beta T_0}{c_V} \frac{\partial \varepsilon_{kk}}{\partial t} + \frac{\partial \theta}{\partial t} = \chi \nabla^2 T \quad (6.3.7)$$

$$\frac{E \alpha T_0}{1 - \nu} \frac{\partial \varepsilon_{kk}}{\partial t} + c_V \frac{\partial \theta}{\partial t} = \kappa \nabla^2 T \quad (6.3.8)$$

The variable  $\chi = \frac{\kappa}{c_V}$  is the thermal diffusivity. Following the derivation in chapter 3.3.2 described by equations 3.3.30 to 3.3.43, the following term for the heat transformation per cycle is obtained.

$$\Delta Q = \pi \frac{\beta^2 T_0}{c_V} \left( \int_V \bar{\varepsilon} \varphi_j dV \right)^2 \frac{\omega \omega_i}{\omega^2 + \omega_i^2} \quad (6.3.9)$$

The dilation energy  $W_D$  is calculated using the stresses and strains causing volume change. Rotational deformations are not connected to the thermal field and therefore neglected in the calculation.

$$W_D = \frac{1}{2} \int_V \sigma_{kk} \varepsilon_{kk} dV \quad (6.3.10)$$

For a plate structure, the dilation energy is

$$W_D = \frac{1}{2} \frac{E}{1 - \nu} \int_V \varepsilon_{kk}^2 dV. \quad (6.3.11)$$

Equation 6.3.2 can be written as

$$\eta = \mu_B \eta_B \quad (6.3.12)$$

where  $\mu_B$  is the MBF. The factor  $\eta_B$  gives the thermoelastic loss factor for pure bending in a beam, according to the Zener formula [65]. The MBF takes the ratio of total dilation energy to total strain energy as well as transverse strain effects into account.

Considering the plate theory, the underlying formula for thermoelastic loss (see equation 3.3.44) can be transformed into

$$\eta_{Pl} = \frac{E \alpha^2 T_0}{c_V (1 - \nu)} \sum_i \frac{\left( \int_V \bar{\varepsilon}_{kk} \varphi_j dV \right)^2}{\int_V \bar{\varepsilon}_{kk}^2 dV} \frac{\omega_i \omega}{\omega_i^2 + \omega^2}. \quad (6.3.13)$$

The eigenvectors  $\varphi_j$  form a complete orthonormal base, therefore the following re-

lation is satisfied [91].

$$\sum_{i=1}^{\infty} \frac{(\int_V \bar{\varepsilon}_{kk} \varphi_j dV)^2}{\int_V \bar{\varepsilon}_{kk}^2 dV} = 1 \quad (6.3.14)$$

The resulting equation for the thermoelastic loss in a thin plate is consistent with equation 3.3.20, Zener-like formula.

$$\eta_{Pl} = \frac{E\alpha^2 T_0}{(1-\nu)c_V} \frac{\omega_i \omega}{\omega_i^2 + \omega^2} \quad (6.3.15)$$

The MBF  $\mu_B$  is determined using the strain components of the mode shape  $\varepsilon_{ij}$ . The total dilation energy  $W_D$  is calculated according to formula 6.3.11. The total strain energy includes the shear components.

$$E_S = \frac{1}{2} \int_V \frac{E}{1-\nu^2} (\varepsilon_{xx}^2 + \varepsilon_{yy}^2 + 2\nu\varepsilon_{xx}\varepsilon_{yy}) + G((2\varepsilon_{xy})^2 + (2\varepsilon_{yz})^2 + (2\varepsilon_{xz})^2) dV \quad (6.3.16)$$

The quotient of dilation energy and total strain energy becomes:

$$\frac{W_D}{E_S} = (1+\nu) \frac{\int_V (\varepsilon_{xx} + \varepsilon_{yy})^2 dV}{\int_V \varepsilon_{xx}^2 + \varepsilon_{yy}^2 + 2\nu\varepsilon_{xx}\varepsilon_{yy} + \frac{1-\nu}{2} ((2\varepsilon_{xy})^2 + (2\varepsilon_{yz})^2 + (2\varepsilon_{xz})^2) dV} \quad (6.3.17)$$

The MBF gives the relation of the thermoelastic loss in a pure bending beam and the general thermoelastic loss in a plate under a specific deformation.

$$\eta = \mu_B \eta_B \quad (6.3.18)$$

Therefore it is defined as follows:

$$\mu_B = \frac{(1+\nu)}{(1-\nu)} \frac{\int_V (\varepsilon_{xx} + \varepsilon_{yy})^2 dV}{\int_V \varepsilon_{xx}^2 + \varepsilon_{yy}^2 + 2\nu\varepsilon_{xx}\varepsilon_{yy} + \frac{1-\nu}{2} ((2\varepsilon_{xy})^2 + (2\varepsilon_{yz})^2 + (2\varepsilon_{xz})^2) dV} \quad (6.3.19)$$

The method of using the MBF to determine the thermoelastic damping in a time-dependent FE Simulation is shown in the flowchart in Figure 6.2.

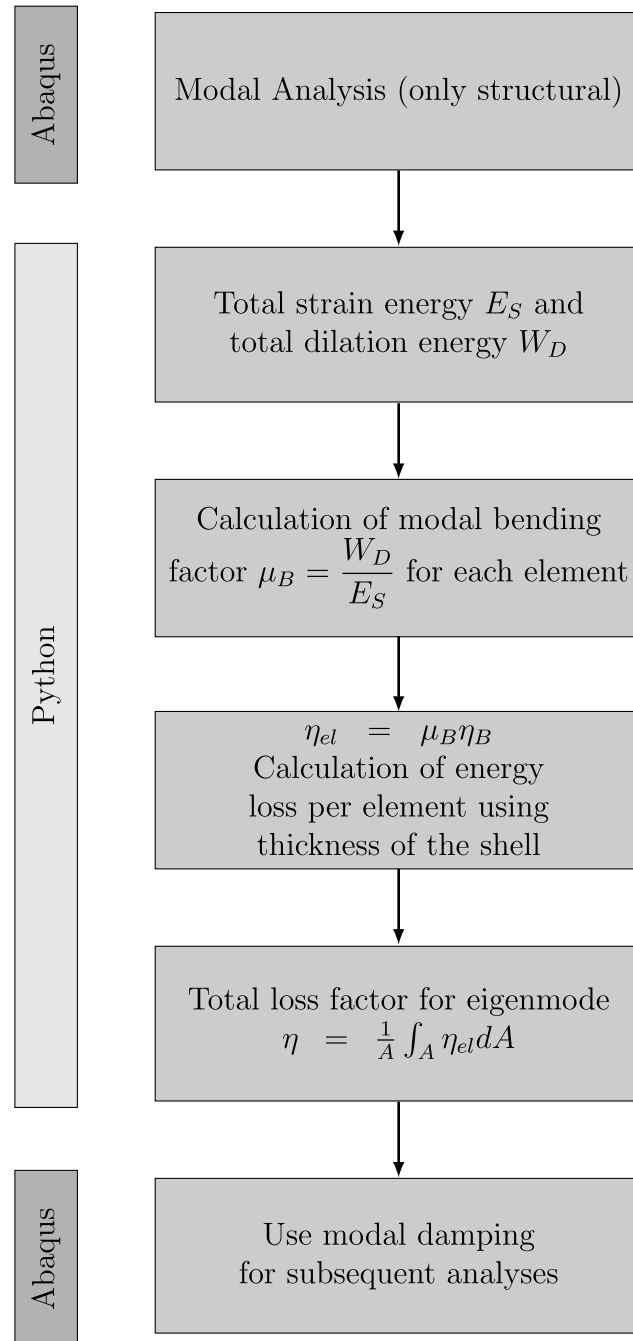


**Figure 6.2:** Flow chart for determination of the loss factor using the MBF

## 6.4 Results

### 6.4.1 Rectangular Plate

#### 6.4.1.1 Numerical Model

As a first example, the method was applied to the rectangular aluminium plate already introduced in chapter 4. For the numerical analysis, a surface geometry was generated and meshed using shell elements with a thickness of 3 mm. In ABAQUS, four-noded shell elements are implemented under the name S4. These elements use six DOF per node and linear interpolation functions. An edge length of 2 mm was chosen, similar to the solid model presented in chapter 5.4.2 leading to a total number of 15 000 elements. The plate model with the corresponding coordinate system is demonstrated in figure 6.3.

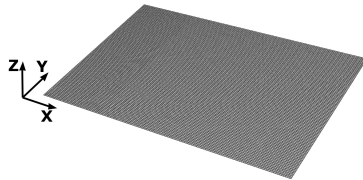


**Figure 6.3:** Shell model of the rectangular plate structure. For the numerical analyses, a model with 15 000 elements is used. The edge length is 2 mm and a thickness of 3 mm is applied.

#### 6.4.1.2 Modal Bending Factor

As can be seen from the derivation in section 6.3, the MBF  $\mu_B$  is a measure of the amount of bending during the deformation of a structure. Compared to a beam structure, which represents the state of pure bending,  $\mu_B$  can be at maximum  $\frac{1 + \nu}{1 - \nu}$ . It follows for the aluminium structures presented in this thesis ( $\nu = 0.34$ ):

$$0 \leq \mu_B \leq 2.0\bar{3} \quad . \quad (6.4.1)$$

In Figure 6.4 the spatial distribution of the normal strains, shear strains, and the MBF are demonstrated to visualize the contribution of the individual strain components to the modal bending. Eigenmode three (382 Hz) was chosen as an example. The magnitude of the deformation  $u$  is shown as well in subfigure 6.4a. The eigenvector is displacement-normalized so that the maximum displacement is unity.

The local representation of the MBF allows a statement about which elements are mainly affected by bending or mainly affected by shear or torsion. The MBF is calculated by formula 6.3.19 using the normal strain components  $\varepsilon_{xx}$  and  $\varepsilon_{yy}$  and the shear strain component  $\varepsilon_{xy}$ . Since the rectangular plate is a thin shell structure,

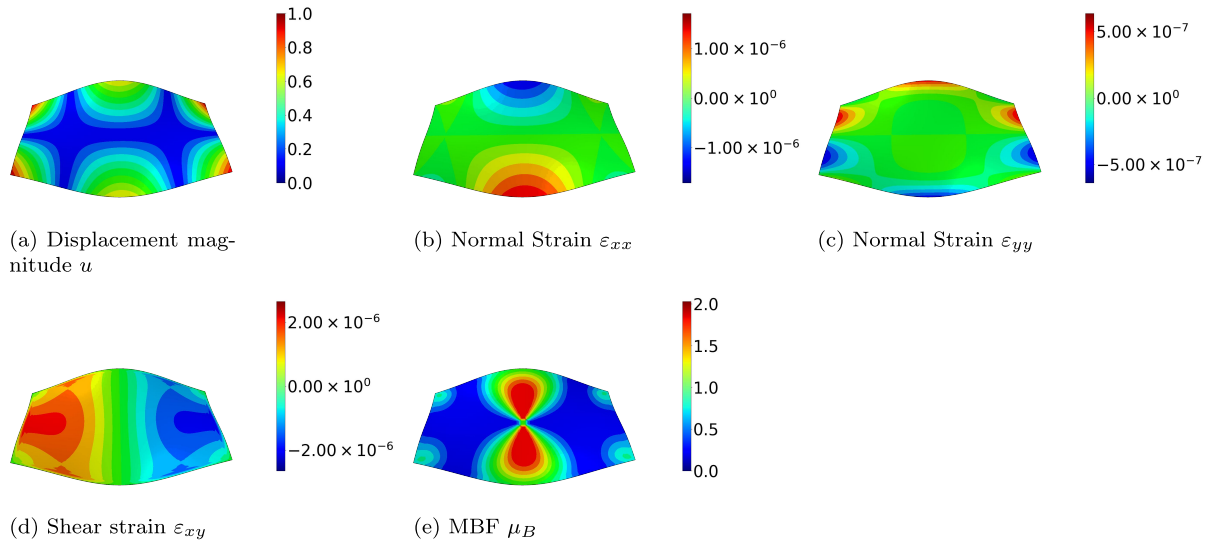


**Figure 6.4:** Relationship of the spatial distribution of the displacement magnitude  $u$  normalized so that the maximum displacement is unity, strain components  $\varepsilon_{xx}$ ,  $\varepsilon_{yy}$  and  $\varepsilon_{xy}$  and the MBF  $\mu_B$  on the example of eigenmode 3 (382 Hz) of a rectangular aluminium plate.

the elements behave according to the Kirchhoff theory, as described in section 6.2. Therefore, the shear strains  $\varepsilon_{xz}$  and  $\varepsilon_{yz}$  vanish. It should be emphasized that the values of  $\varepsilon_{xx}$  and  $\varepsilon_{xy}$  in the present eigenform are one order of magnitude higher than the values of  $\varepsilon_{yy}$ . For this reason, the strain components do not contribute to the MBF to the same extent as the normal strains. Figure 6.5 displays the MBF in comparison to the displacement of the eigenform on the example of eigenmodes one to four. The eigenvector is displayed as the displacement magnitude and again normalized to the maximum value so that the highest deflection is one. The spatial distribution of the MBF represents the amount of bending in a single deformed element and can take a value between 0 and 2.03, as mentioned before.

Furthermore, considering the MBF of the whole structure enables a classification of the mode shape. A distinction can be made between bending-dominated and torsion-dominated eigenforms. For each mode, the total MBF is given below the figure. The first mode shape is mainly characterized by torsion. With an MBF of  $\mu_B = 0.114$ , the percentage of bending energy is comparatively low. The second eigenmode is dominated by bending around one axis. The plate behaves similarly to a bending beam. This fact is reflected in the MBF value close to one. Mode shape four also shows a high amount of bending, but both axes are affected. Although the dominant deformation is bending in transversal direction,  $\varepsilon_{xx}$  and  $\varepsilon_{yy}$  range in the same order of magnitude. Therefore, the MBF exceeds a value of one that characterizes a bending beam. Mode shape three is a mixed mode with an MBF of 0.47, i.e., 47% bending energy. Figure 6.6 shows a comparison of all considered modes. On the left the deformed shape is plotted, in combination with the MBF of the whole structure. The MBF has a minimum of 0.114 (mode one) and 1.719

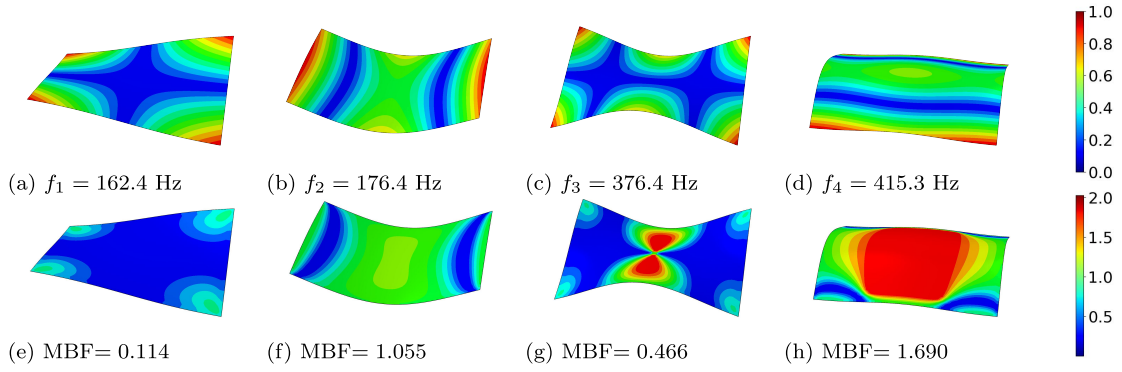


**Figure 6.5:** (a) - (d) mode shapes of rectangular aluminium plate 300 x 200 x 3 mm, displacement magnitude normalized to 1 (e) - (h) local distribution of MBF on aluminium plate

(mode nine). The highest values occur mainly in the eigenmodes, which can already be visually identified as bending (2, 4, 9, 15).

- mode 2 -  $f_2 = 176.4$  Hz - MBF  $\mu_B = 1.055$
- mode 4 -  $f_4 = 415.3$  Hz - MBF  $\mu_B = 1.69$
- mode 9 -  $f_9 = 997.1$  Hz - MBF  $\mu_B = 1.719$
- mode 15 -  $f_{15} = 1638.9$  Hz - MBF  $\mu_B = 1.703$

In addition to the experimentally studied eigenfrequencies, also mode 23 with  $f_{23} = 2235$  Hz and an MBF of  $\mu_B = 1.618$  is shown as a further example of a bending mode shape.

#### 6.4.1.3 Comparison of the MBF Approach with Experiments

In Figure 6.7 and table 6.1 the damping ratios calculated with the presented approach are compared to the damping ratios measured experimentally in vacuum. As a reference, the graph of the analytical approach for thermoelastic loss of a bending beam according to Zener [7] is given as well. The damping values should be interpreted in relation to this curve. To get the damping ratio of each eigenmode, this theoretical value is reduced or expanded by the corresponding MBF. Therefore the values are located above the analytical graph if  $\mu_B > 1$  and below the curve if  $\mu_B < 1$ .

The experimental damping ratios are usually slightly higher than the simulated data. This result may be explained by the circumstances of the experimental setup, as already explained in chapter 4. The measurements are very sensitive to minor deviations in the suspension of the components or the ambient air pressure.

The relationships are demonstrated again on the right-hand side using the example of eigenmode five. The MBF is 0.636, therefore the damping ratio of the reference curve is reduced to 63%. The result of  $\zeta = 3.19 \times 10^{-5}$  is slightly below the experimental value of  $\zeta = 4.04 \times 10^{-5}$ . Since the rectangular plate structure was also

used as an example for the entropy approach presented in chapter 5 the results are plotted in the diagram as well. A comparison of both methods is discussed in the following section.

**Table 6.1:** Comparison of the experimental damping ratios  $\zeta_e$  and simulated damping ratios for the aluminum plate 300 mm x 200 mm x 3 mm. Both, the simulated data according to the MBF approach  $\zeta_{s,2D}$  and the entropy approach  $\zeta_{s,3D}$  are demonstrated together with the relative deviation in percent. The relative deviation is determined with reference to the experimental data.

f [Hz]	$\zeta_e \quad [\cdot 10^{-5}]$	$\zeta_{s,2D} \quad [\cdot 10^{-5}]$	deviation rel. $\zeta_{s,2D} \quad [\%]$	$\zeta_{s,3D} \quad [\cdot 10^{-5}]$	deviation rel. $\zeta_{s,3D} \quad [\%]$
162.42	1.981	1.66	16.20	1.540	22.27
176.40	13.61	14.11	3.67	12.89	5.26
376.40	3.374	2.93	13.16	2.971	11.93
415.32	10.95	9.63	12.05	10.52	3.90
471.43	4.043	3.19	21.10	3.287	18.69
557.33	8.231	6.46	21.52	8.577	4.20
700.72	3.047	2.74	10.08	2.826	7.26
804.90	3.659	1.92	47.53	2.374	35.11
997.07	5.321	4.08	23.32	4.465	16.09
1112.01	3.284	2.20	33.01	2.693	18.00
1205.84	2.920	1.25	57.19	1.903	34.83
1207.76	4.449	2.63	40.89	3.491	21.52
1541.61	2.990	1.77	40.80	2.192	26.69
1638.92	3.186	2.46	22.79	2.611	18.04

#### 6.4.1.4 Comparison of the MBF Approach with the Entropy Approach

In the figures 6.7 and 6.8 and table 6.1 the results of the modal bending approach are compared to the results of the entropy approach presented in chapter 5 for the rectangular plate. As shown in figure 6.7 the results of both approaches are approximately equivalent. Mostly, the values of the damping ratios are almost exactly the same. This relation is evident, for example, in mode five, which can be seen in the zoom on the right. In some cases, the results of the entropy approach are slightly higher than those of the MBF approach, e.g., in mode two (176 Hz) or mode four (415 Hz). The reason for this is probably the different concepts of heat conduction in the two methods. The MBF approach assumes one-dimensional heat conduction based on the Zener theory for thin beams. Although transverse shear strains are considered, the heat flow is only possible in thickness direction. This is certainly the dominant dimension of thermal conduction, but heat flows can also occur in-plane directions to a minor extent. The entropy approach assumes three-dimensional heat conduction and considers these small effects.

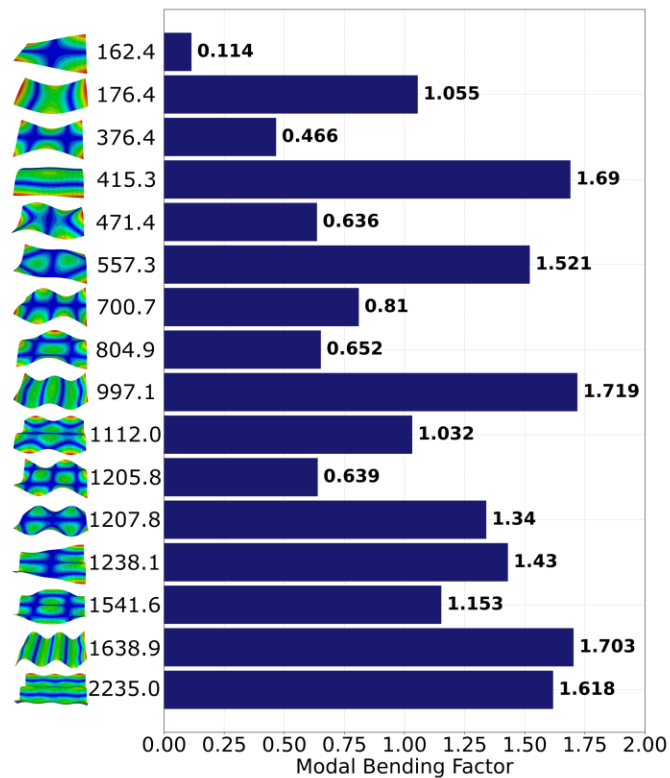


**Figure 6.6:** Overview of the modal bending factors (MBF) of the eigemodes considered in experiment and simulation for the rectangular plate.

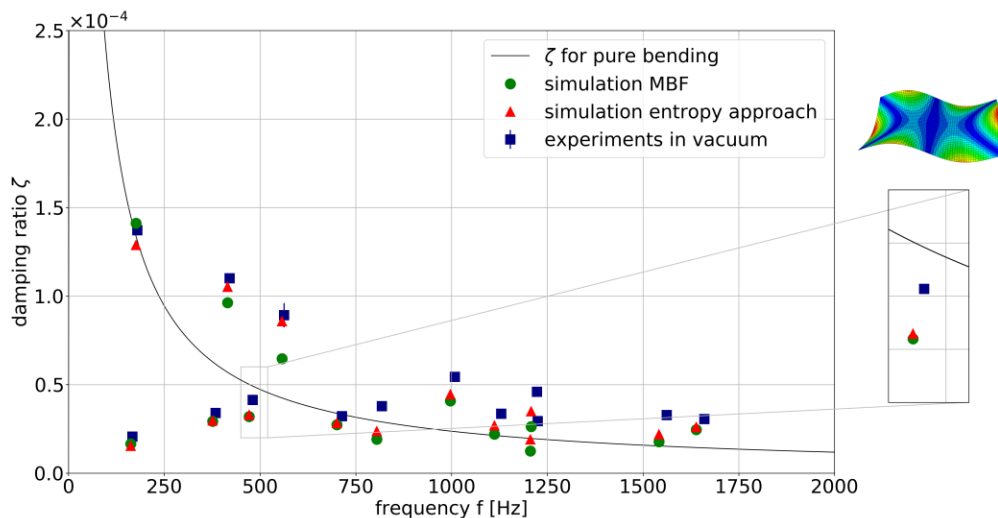


**Figure 6.7:** Comparison of experimentally determined damping ratios (in vacuum), simulated damping ratios using the entropy approach (see chapter 5), and simulated damping ratios using the MBF approach on the example of the rectangular aluminum plate. For reference, the analytical solution for a component with a thickness of 3 mm is demonstrated as continuous curve.

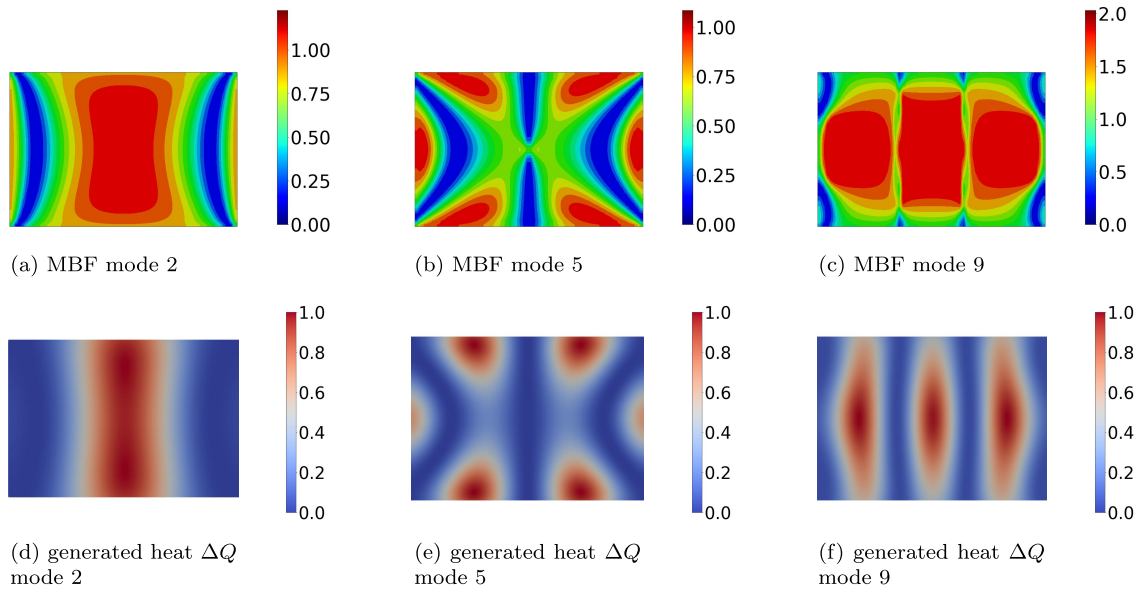


**Figure 6.8:** Comparison of the spatially distributed modal bending factor (MBF) with the generated heat  $\Delta Q$  calculated by the entropy approach for three eigenmodes of the rectangular plate.

In table 6.1 the relative deviation to the experimental data for both simulation approaches is demonstrated. Except for mode one and two, the MBF approach leads to larger differences.

Comparing the spatial distribution of the MBF with the spatial distribution of the generated thermal energy, clear correlations can be seen. At the locations where a high degree of bending deformation occurs, much energy is converted into heat and thus dissipated. This relationship is shown in figure 6.8 at the example of modes one, five, and nine.

## 6.4.2 Protection Plate

### 6.4.2.1 Numerical Model

In order to model the protection plate structure with shell elements, the Computer Aided Design (CAD) model is reduced to a mid surface. The component has a uniform thickness, and a two-dimensional plate is generated representing the mid-layer of the thickness. This surface is meshed using quadrilateral shell elements with four nodes each. The displacement is approximated by linear interpolation functions. Each node has six DOF: three translational displacements  $u_x$ ,  $u_y$ ,  $u_z$  and three rotational DOF  $\phi_x$ ,  $\phi_y$  and  $\phi_z$ . An edge length of 1 mm was intended, but it could not be realized everywhere due to the irregular geometry. In total, 80 722 elements are generated. The shell thickness is set to 1 mm. In ABAQUS, the four-noded shell elements are implemented under the name S4. The model is demonstrated in figure 6.9.

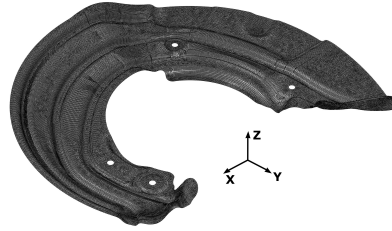


**Figure 6.9:** Shell model of the protection plate. For the numerical analysis, a model with 80 722 elements and an approximate edge length of approximately 1 mm is used. The shell thickness is set to 1 mm.

#### 6.4.2.2 Modal Bending Factor

The protection plate is manufactured from the same aluminum alloy as the rectangular plate. Therefore, the condition  $0 \leq \mu_B \leq 2.0\overline{3}$  also holds for this plate. Figure 6.10 shows the spatial distribution of the strain components  $\varepsilon_{xx}$ ,  $\varepsilon_{yy}$  and  $\varepsilon_{xy}$  as well as the MBF for the protection plate on the example of eigenmode one ( $f_1 = 31.8$  Hz).

For comparison, the mode shape is also demonstrated in subfigure 6.10a with the magnitude of the displacement  $u$ . Similar to the results of the rectangular plate, all eigenmodes are displacement-normalized with a maximal magnitude of one. Although the eigenmodes have a well-defined deformation in which the zero lines are clearly visible, the strain components are irregularly distributed. This can be explained by the geometry of the sheet with ridges, grooves, and holes. It is difficult to derive a clear relationship between the distribution of the strain components and the eigenmode. The distribution of the MBF is accordingly irregular. There are neither areas with very high MBF values nor areas with very low ones. For the entire component, the modal bending factor is 0.596.

The same effect also occurs in the other mode shapes. Figure 6.11 shows the spatial distribution of the MBF in comparison to the eigenvector on the example of modes one to four. The displacement of the mode shape is given as magnitude and normalized so that the maximum is unity. The MBF can get a maximum of 2.03, but neither very high nor very low values occur. In all of the shown eigenmodes, the MBF is in the mid-range between 0.48 and 0.66.

#### 6.4.2.3 Comparison of the MBF Simulation with Experiments

In figure 6.12, the comparison of the simulated damping ratios according to the MBF approach with the experimental data recorded in vacuum is demonstrated. For reference, the analytical calculation based on the theory of Zener [7] is given as well. Since all analyzed mode shapes have a modal bending factor between 47% and 77%, the simulation values follow the course of the Zener curve with a relatively constant distance. The experimental data agree well with the simulations. As already stated

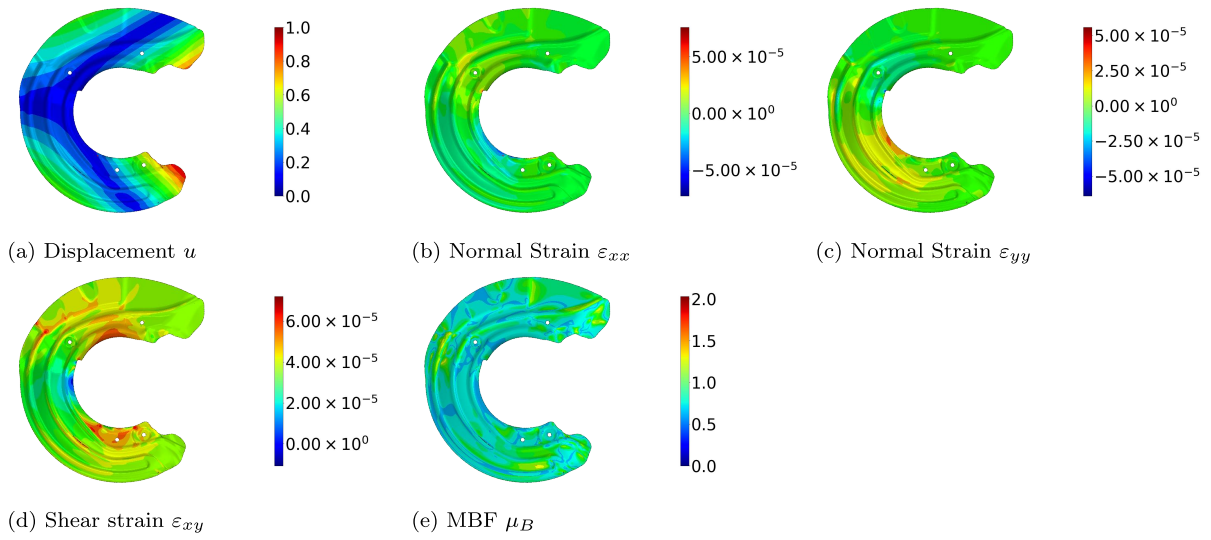


**Figure 6.10:** Relationship of the spatial distribution of displacement  $u$  normalized to 1 mm, strain components  $\varepsilon_{xx}$ ,  $\varepsilon_{yy}$  and  $\varepsilon_{xy}$  in  $\text{N}/\text{mm}^2$  and the MBF  $\mu_B$  on the example of eigenmode 1 (33 Hz) of a protection plate.

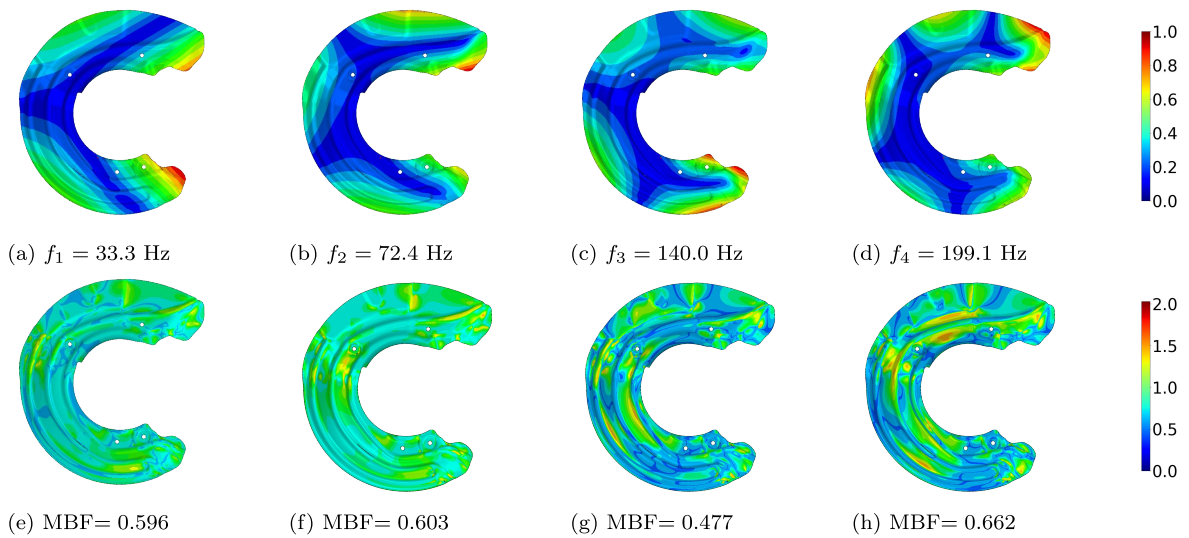


**Figure 6.11:** (a) - (d) mode shapes of aluminium protection plate, displacement magnitude normalized to 1 (e) - (h) local distribution of MBF

in the other examples, the measured damping ratios are always slightly higher than the calculated ones.

Two eigenmodes should be highlighted here. The experimental damping ratio of mode six ( $f_6 = 260.7$  Hz) and mode nine ( $f_9 = 419.9$  Hz) are significantly higher than the MBF simulation. One possible explanation could be inaccuracies in the experimental setup so that undesired additional damping effects occur, e.g., due to the suspension. However, this case can be considered not probable, since the experiments were repeated on two components and no deviation occurred (see chapter 4). It is possible that heat flows occur due to the strain distribution in these two eigenmodes, which are not reflected by the model assumptions in the MBF approach. Based on the Zener theory, only one-dimensional heat conduction in the thickness direction is modeled by this method. Possible heat flows at the surface are not considered, and lower energy dissipation is calculated.

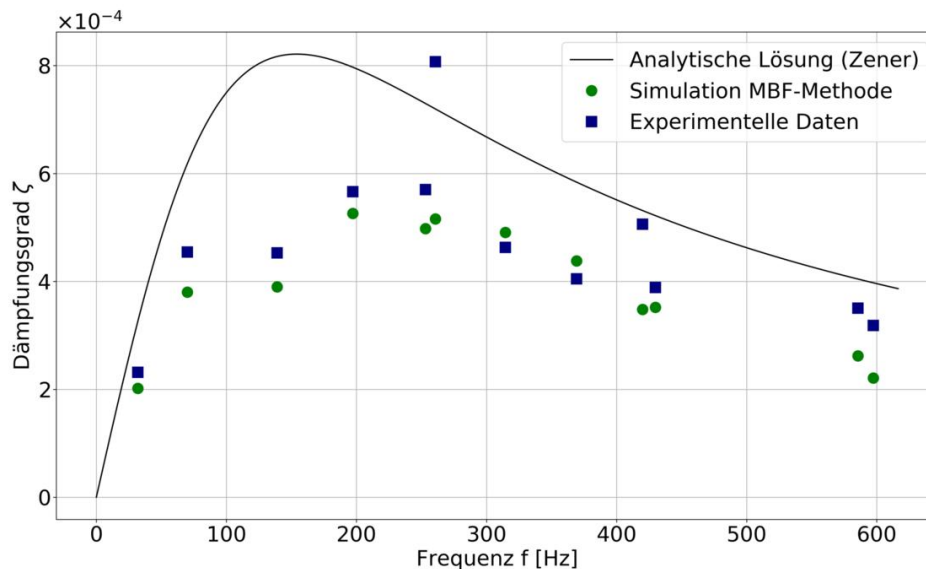


**Figure 6.12:** Comparison of the MBF simulation results for the protective plate with experimental results. For comparison, the analytical solution according to Zener [7] is plotted as continuous curve.

#### 6.4.2.4 Comparison of the MBF Simulation with a Fully Thermoelastically Coupled Simulation

As further verification of the developed approach, the results are compared with a fully thermoelastically coupled simulation using the elements described in chapter 3.4.2. The thermoelastic element formulation in ANSYS is implemented for solid and panel elements but not for shell elements. Therefore a new volume model of the protection plate is built for this simulation. The CAD structure is meshed with volume elements. Thermoelastic solid elements are implemented in ANSYS under

the name SOLID226. These hexahedron elements have 20 nodes with four DOF each (Translational displacements  $u_x$ ,  $u_y$ ,  $u_z$ , and temperature  $\theta$ ), and quadratic interpolation functions. The edge length in the in-plane direction of the plate is approximately 1 mm, as in the shell model. In thickness direction, two element layers are applied. Therefore, the number of elements is nearly doubled to 160 852 elements. In order to be able to evaluate the simulations, it should be noted that the thermoelastic elements in ANSYS are based on the theory of three-dimensional heat conduction.

Similar to the simulation procedure described in chapters 5.4.2.5 and 5.4.3.5 a full harmonic analysis is conducted, i.e., a frequency-domain analysis using full system matrices. For the excitation, a location with a high out-of-plane deflection in all mode shapes was chosen (see figure 6.13). A force of 1 N is applied in the z-direction. To simulate a free suspension, no further boundary conditions are set. The frequency range is defined from 0 Hz to 700 Hz with a frequency step of 1 Hz.

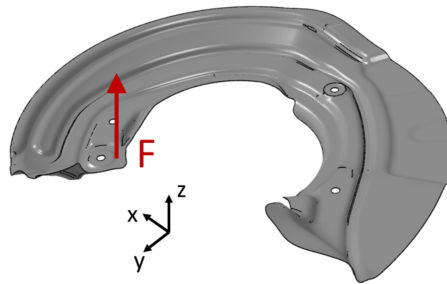


**Figure 6.13:** Excitation point of force  $F$  in the full thermoelastically coupled simulation in frequency-domain for the protection plate. The load is applied in z-direction. No boundary conditions are set.

For each frequency step, the complex data of the strain energy are extracted element-wise and summed up over the whole model. In order to calculate the loss factor, the imaginary part is divided by the real part.

$$\eta = \frac{|\text{Im}(E_S)|}{|\text{Re}(E_S)|} \quad (6.4.2)$$

Therefore, one loss factor per frequency step is obtained that can be transformed into the damping ratio.

In the case of resonance, i.e., the excitation frequency matches the eigenfrequency, poles occur in the curve of the fully coupled simulation. The absolute height of these peaks depends on the frequency discretization. When comparing the MBF simulated loss factors with the damping ratio curve of the ANSYS simulation, the poles should be neglected. Nevertheless, a statement can be made concerning the basic trend of the curve.

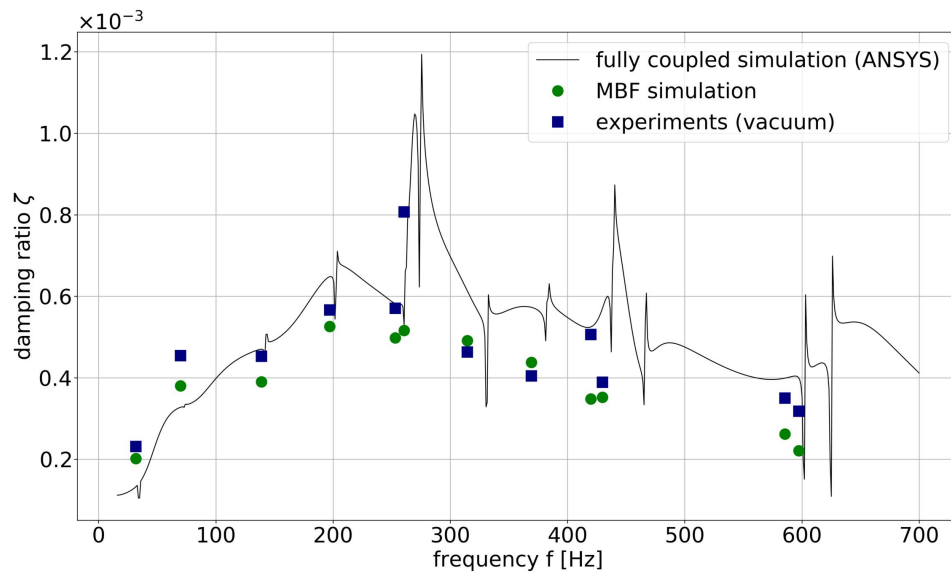


**Figure 6.14:** Comparison of the MBF simulation of the protective plate with the fully thermoelastically coupled simulation in ANSYS.

For the first two eigenmodes, the damping ratio values of the MBF method are higher than the ANSYS curve. Afterward, the relation reverses. With increasing frequency, the difference enlarges, and the ANSYS calculation shows a significantly higher damping ratio than the MBF simulation. It is also noticeable that frequency shifts occur in the higher frequency range between the two simulations.

In terms of both frequencies and damping characteristics, the MBF values are in better agreement with the experiments. Probably, the structural dynamic behavior of the thin sheet is not adequately represented by a solid model.

Nevertheless, eigenmodes six and nine should be emphasized. In section 6.4.2.3 significantly higher experimental data compared to the MBF-simulation were noticed for these modes. In the course of the ANSYS curve, an increase of the damping ratio in the range of these frequencies can also be observed. Therefore it can be concluded that these mode shapes induce strains leading to heat flows that can not be analyzed with a model based on a one-dimensional heat conduction.

### 6.4.3 Application on a Literature Example

In the previous analyses and discussions, own experiments were used to validate the models, all conducted under the same boundary conditions in the same laboratory. Thereby, systematic errors in the experiment are not definitely excluded. In order to perform validation on external, independent data, the method presented in this chapter is applied to a literature example. Furthermore, the applicability to another material than the aluminum alloy is tested. The experimental study provided

in Cagnoli et al. [122] was chosen as a reference since the experimental setup is described in detail in the publication, and the dimensions of the test sample are given. Similar to the experiments presented in chapter 4, the authors installed the test setup within a vacuum chamber in order to avoid air and radiation damping. The excitation is realized electromagnetically in the vacuum chamber. A thin circular disc is used as a test sample with a support in the middle point. This position corresponds to nodal support for multiple, but not all, eigenmodes. Therefore some modes are not included in the experimental data. The experiments are conducted per eigenmode, and the results are given as modal loss factors. The disc has a diameter of 75.58 mm with a thickness of 0.51 mm and a frequency range up to 5000 Hz was measured. Unfortunately, the material properties are not explicitly given in the publication, just the material specification ( $\alpha$ -brass, 64% Cu, 36% Zn). The parameters demonstrated in table 6.2 are assumed for the brass alloy according to [176].

parameter	value	unit
Young's modulus $E$	$1.06 \times 10^{11}$	N/m <sup>2</sup>
Poisson's ratio $\nu$	0.33	
density $\rho$	8420	kg/m <sup>3</sup>
thermal conductivity $\lambda$	107	W/mK
heat capacity $C_p$	368	J/K
thermal expansion coefficient $\alpha$	$1.87 \times 10^{-5}$	K <sup>-1</sup>

**Table 6.2:** Material parameters of brass alloy with 64% Cu and 36% Zn [176]

To apply the MBF approach, first, a finite element model was built. The circular disc was modeled and meshed in ABAQUS using S4 shell elements. As described above, these four-noded shell elements have linear interpolation functions and six DOF per node. The average edge length is approximately 1 mm, resulting in 5654 elements in total. Different from the experiment, no boundary conditions are applied in the eigenfrequency analysis to get results for all mode shapes. In the considered frequency range from 0 Hz to 5000 Hz 28 eigenmodes were calculated. However, due to the double symmetric geometry, the modes usually occur in pairs with the same frequency. If these doubled frequencies are neglected, 15 simulated modes are available compared to ten experimental modes.

Figure 6.15 shows the first four eigenmodes of the circular plate with the according MBF plot. The visual representation of the MBF, as well as the total MBF value, clearly demonstrate that modes one and three are relatively low affected by bending. The modal deformation includes a large percentage of shear. Mode shape two should be particularly emphasized. The double symmetrical circular structure allows a deformation with so-called synclastic curvature, i.e., pure bending about

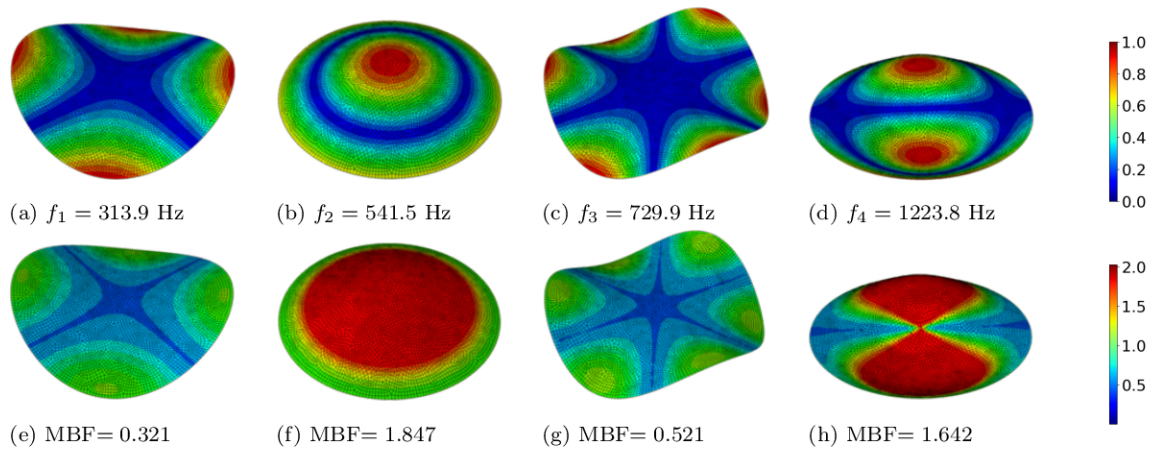


**Figure 6.15:** (a) - (d) mode shapes of the circular brass disc with a diameter of 75.58 mm and a thickness of 0.51 mm, the displacement magnitude is normalized to the maximal value (e) - (h) local distribution of **MBF** on the brass disc

two axes. Therefore, most of the elements exhibit the highest possible **MBF** of 1.985 for the brass plate with a Poisson's ratio of 0.33.

Figure 6.16 compares the experimental loss factors of Cagnoli et al. [122] with the simulated results using the **MBF** method. Although not every mode shape is considered in the experimental results, all modes of the frequency range up to 5000 Hz are shown.

Two types of modes shapes can be distinguished. In the first group (mode 1, 3, 5, 6, 9, 12, 14), the sinusoidal deflection is formed in the azimuthal direction, whereas the center of the plate is undeformed. In the reference, these modes are called "butterfly modes." For these eigenvectors, a low **MBF** is calculated, leading to a low loss factor. The other group shows sinusoidal deflections in the radial direction (mode 2, 8) or a combination of both. These deformations include a higher amount of bending energy, and therefore, larger thermoelastic loss factors occur.

The simulated loss factors agree excellently with the experiments. The effect of slightly higher measuring results observed in the previous sections does not occur here. A possible explanation could be found in the experimental conditions. The authors describe a vacuum chamber providing a pressure below  $10^{-6}$  mbar. In combination with the study concerning air pressure presented in chapter 4, it can be concluded that the remaining gas in the vacuum chamber has a significant effect on the measured loss factors.

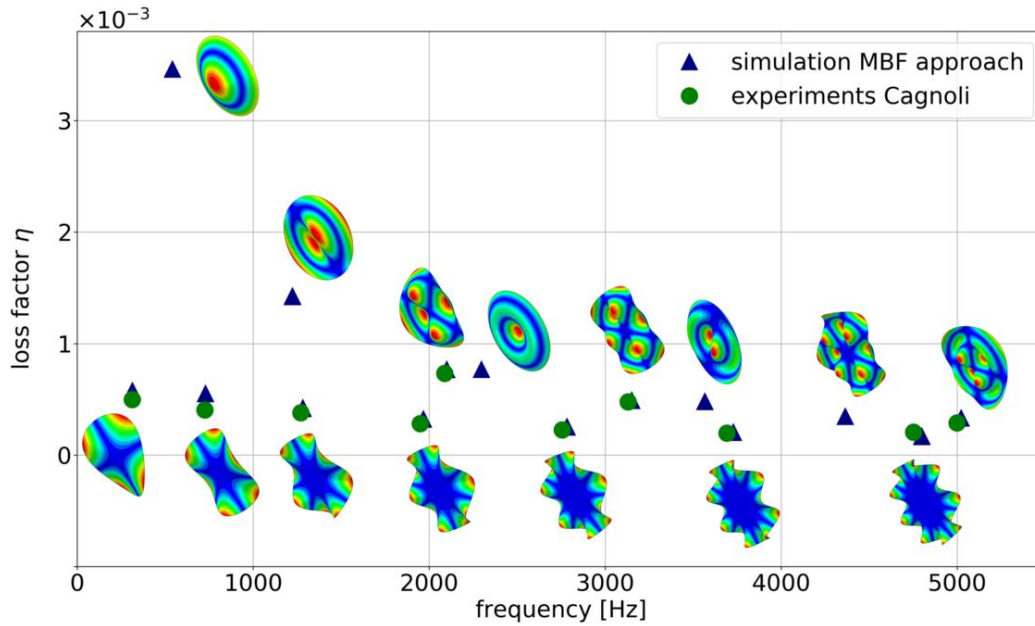


**Figure 6.16:** Comparison of the MBF simulation results for the circular disc with experimental results according to Cagnoli et al. [122].

## 6.5 Summary and Discussion

The developed MBF approach is an efficient method for the determination of thermoelastic damping in thin-walled structures that can be modeled with shell elements. It is based on the reduction of the damping ratio calculated analytically for the state of pure bending. Therefore a quantitative computation of the bending amount in a deformed structure is necessary, given by the modal bending factor (MBF).

The method was applied to a thin rectangular plate, and the simulated damping ratios were compared with experimental data and with the results of the entropy approach presented in chapter 5.

The agreement with the measured data is very good, although the deviations for some modes are slightly larger than those of the entropy approach.

However, concerning the computing time, the MBF method proves to be more efficient, although a comparison of different structural models is difficult. Considering only the simulation of the damping ratios based on the eigenmodes, the MBF simulation is approximately ten times faster, as demonstrated in table 6.3.

Furthermore, the approach was applied to a protection plate from the automotive industry. The results of the damping ratios match well with the experimental data and the results of fully thermoelastically coupled simulations. Sporadic deviations can be explained by the reduced one-dimensional heat conduction model in the plate

structure.

Compared to the full coupled simulation, a significant improvement of the computing time is achieved (see table 6.4).

Regarding the practical applicability, it should be emphasized that the code was entirely developed in Python without additional packages or libraries. Therefore it can be run directly in ABAQUS. The integration into a simulation process in practice would be straightforward.

**Table 6.3:** Computing time in CPU seconds of the damping ratios of the rectangular aluminum plate using the MBF approach in comparison to the entropy approach presented in chapter 5. The MBF approach was applied to a shell model and the entropy approach to a solid model with four element layers in thickness direction. Therefore, the models have a different number of elements. The computing times were measured for the simulation of 15 eigenmodes.

	MBF	entropy approach
number of elements	15 000	60 000
eigenfrequency analysis	87	153
modal damping coeff.	325	3628

**Table 6.4:** Computing times in CPU seconds for a harmonic analysis of the protection plate using the MBF approach and mode superposition compared with a fully thermoelastically coupled harmonic analysis. The thermoelastic elements SOLID226 in ANSYS are used. The modal based harmonic analysis are also conducted in ANSYS for reasons of comparability using SHELL181 elements (four nodes, linear interpolation functions). In the harmonic analysis, a frequency range of 0 Hz to 700 Hz was considered using 700 steps. Except for the determination of the damping ratios, all simulation were run on 16 cores of the same computer system.

	SHELL181	SOLID226
computing time total	8 178	1 487 650
eigenfrequency analysis	113	
modal damping ratio	6780	
harmonic analysis	1285	



# Chapter 7

## Conclusion and Outlook

### 7.1 Summary and Conclusion

The objective of the thesis was the development of simulation methods for the integration of thermoelastic damping in finite element analyses. It focused on a realistic representation of the dissipation effects, verified by validating the models on experimentally determined data. For this purpose, a test setup was developed to measure material damping in vibrating components. Furthermore, the computational efficiency of the developed methods has been considered with respect to practical applicability.

Concerning thermoelastic energy dissipation, several literature references provide empirical, material-dependent values, usually based on experiments. However, the data shows considerable variations for the same material. Also, only general damping parameters are given, without considering the frequency, excitation amplitude, vibration mode, or environmental conditions.

Analytical calculations of thermoelastic damping are possible for simple geometries by solving the coupled thermoelastic differential equations. Simplified analytical formulas were first developed for thin beam structures using the theory of one-dimensional heat conduction. Further developments extended the approach to other geometries, such as rectangular and circular discs, as well as rings. For more complex samples, numerical solutions are required. Regarding numerical methods, formulations for finite elements exist, including both mechanical and thermal degrees of freedom, and result in system matrices with thermoelastic coupling terms. However, the numerical solution of the fully coupled systems of equations involves considerable computational effort.

This fosters the development of efficient simulation methods that enable thermo-

elastic damping simulation in complex geometries without a full solution of thermoelastically coupled problems. Two approaches were developed to include thermoelastic damping in time-dependent Finite Element Simulations based on mode superposition, one for the application to thin plate structures modelled with shell elements and one for volume structures modelled with solid elements. Therefore, different algorithms were formulated to evolve the thermoelastic loss factor from the mechanical mode shapes and eigenfrequencies of the structure. In subsequent analyses in the time and frequency domain, the loss factor is applied as modal damping. Therefore, the time-dependent simulations can be performed entirely using elastic finite elements without thermal degree of freedom. Both methods are shortly summarized in figure 7.1.

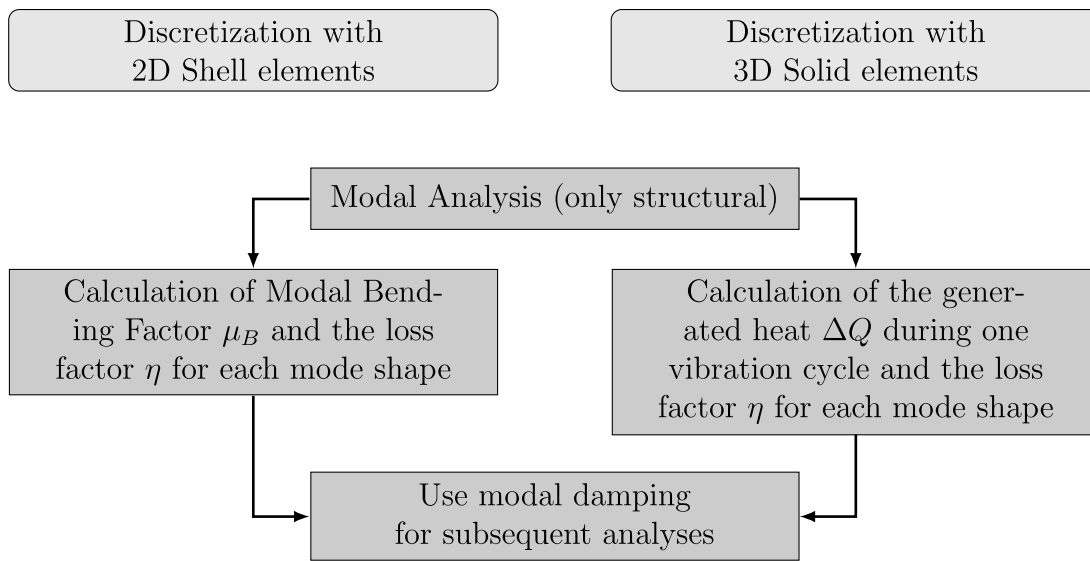


**Figure 7.1:** Flow chart for numerical solution procedure

The following paragraphs provide an overview of the main steps and findings involved in developing the simulation approaches and the experimental studies.

## Experiments

- An experimental setup was refined in order to measure material damping, excluding other sources of energy dissipation. Air and radiation damping was avoided by conducting the experiments within a vacuum chamber. Furthermore, a suspension and measurement scheme tailored to the specific mode shapes inhibited friction losses on the support locations. The samples were excited with an automatic impulse hammer controlled from outside the vacuum chamber, and the vibration velocity was recorded contactless using a Laser Doppler vibrometer. The damping ratio  $\zeta$  was calculated by fitting an exponential function on the decay curve.

- Three experimental samples were used: a thin rectangular plate, an actual protection plate from the automotive industry, and a box geometry based on a gearbox casing. All components were made from the same aluminum alloy (AlMg4.5Mn0.7).
- It has been shown that the material damping ratio in vacuum does not depend on the excitation amplitude. Furthermore, a nonlinear dependency of the damping ratio on the air pressure could be measured.
- The measurements were conducted in the ventilated and the evacuated vacuum chamber to compare the damping ratios in air and vacuum. All experiments were repeated on several measurement points and up to four identical components. While a considerable variation of the measurement results in air was observed, the tests in vacuum showed excellent reproducibility.
- The measured damping ratios depend on the eigenfrequency and -form. Values of  $2.0 \times 10^{-5}$  to  $1.4 \times 10^{-4}$  for the rectangular plate,  $2.3 \times 10^{-4}$  to  $8.1 \times 10^{-4}$  for the protection plate and  $1.2 \times 10^{-5}$  and  $2.6 \times 10^{-5}$  for the gearbox casing were achieved. Overall, material damping in the plate structure was higher than in the volume structure.
- Compared to the simulated values, the experimental data showed slightly stronger damping. One reason for this could be imperfections in the experiment, such as the remaining air pressure in the vacuum chamber of approximately 5 mbar.

### **Thermoelastic damping based on generated heat**

- The method represents a generalized approach for the use in three-dimensional solid elements, which can be applied to a wide range of geometries. First, the deformation in the eigenmodes of the system was transformed into a temperature field by thermoelastic coupling. The heat fluxes, leading to an increase in entropy and energy dissipation, were determined by solving the three-dimensional heat conduction equation over one oscillation cycle. Finally, the thermoelastic loss factor was obtained from the quotient of converted thermal energy to total strain energy. The method is referred to as “entropy approach”.
- The eigenfrequency analysis and the subsequent time and frequency domain calculations were performed in the finite element software ABAQUS. The development of the entropy approach in order to determine modal damping ratios was done in Python, using the FEM library FEniCS.
- The approach was first implemented on thin beam structures and compared with analytical solutions according to Zener [65], showing good agreement.

However, the maximum loss factors of the analytical calculation were not achieved in the simulation, which is due to the different modeling assumptions. The simulation method implies three-dimensional heat conduction, whereas the analytical formula assumes one-dimensional conduction in the thickness direction.

- The entropy approach was tested on the rectangular plate, as well as the gearbox casing. The experimental data could be reproduced very well in the simulation, especially the relative difference in the damping ratio between the modal shapes. Compared to classical damping models, a much better agreement with the experimental measurements was obtained.
- Compared with fully coupled thermoelastic simulations, a significant improvement in the computing time was achieved with comparable prediction quality. Nevertheless, solution methods with full system matrices vs. modal superposition methods are compared, and the fundamental differences should be taken into account. The modal superposition technique restricts the application of the method to the linear domain. Furthermore, the accuracy of the results depends on the number of considered modes.

### **Thermoelastic damping based on modal bending energy**

- The second method was developed to simulate modal damping ratios in thin plate structures modeled with two-dimensional shell elements. The fraction of strain energy stored in the bending deformation could be determined by simulating a modal bending factor (MBF). The maximum thermoelastic damping effect occurs in the state of pure bending and can be calculated analytically as a function of the component thickness. The MBF can determine the actual thermoelastic damping per modal shape.
- The method enabled the visualization of the spatial distribution of the dissipated energy in the component by calculating elemental MBF. It was demonstrated that a high fraction of bending energy leads to high thermoelastic damping. The modal bending factor allows a quantitative classification of the eigenmodes with respect to their damping behavior.
- The approach was applied to the rectangular plate and the protection plate. A direct comparison to the entropy approach was possible for the rectangular plate. Some modal damping ratios showed a slightly larger deviation from the experimental results than the entropy approach, but there was still a very good agreement. Furthermore, the computing time of the MBF approach was even faster. The match with the experimental data was good for the protection

---

plate, although a more significant deviation occurred in two modes. It is possible that the modeling approach assuming one-dimensional heat conduction is not unconditionally suitable for more complex geometries.

- Finally, the MBF method was applied to a circular disc component presented in literature for which experimental results were available. Besides a further validation of the model on external data, the circular disc also includes the case of a synclastic mode shape with pure bending around two axes. Therefore the maximal possible MBF could be calculated, and the example enables an illustrative presentation of the method

Overall, it can be concluded that two suitable methods for efficient numerical calculation from thermoelastic damping on a modal basis were developed. The methods were applied on simple geometries and complex components and validated on experimental data.

## 7.2 Outlook

There are still plenty of open research questions concerning material damping, as well as damping phenomena in general in modeling and simulation.

The methods shown in this thesis were developed and tested on aluminum. In chapter 6, the application of the method to brass was demonstrated. It can be assumed that both approaches are suitable for metallic materials. The transfer of the simulation methods to non-metallic materials with a higher damping potential, such as elastomers or other plastics would be a promising concept.

In recent years, several studies have examined material damping in advanced composite materials, such as carbon-fiber-reinforced composites [177–181]. In principle, extending the entropy approach to such heterogeneous materials should be possible as long as suitable FE models are available. However, it must be taken into account that, due to internal boundaries causing friction, the thermoelastic effect is not the dominant damping mechanism anymore.

The MBF method has been tested on plates with one layer of elements. Therefore, it could be interesting to consider layered plates, such as sandwich structures. Furthermore, the formulation of the MBF can be extended if anisotropic material properties are considered. A similar concept has been proposed in [111], although not in the context of FE simulation.

In the analysis of the generated heat during a mechanical vibration in chapter 5, it has been shown that a large part of the energy dissipation occurs at thin edges and corners, i.e., at places with short heat conduction paths. Future research could focus on developing surface structures with respect to thermoelastic energy dissipation.

The surface geometry can be optimized to allow maximum energy dissipation by explicitly calculating the heat conduction.

Furthermore, all observations in this work are limited to linear analyses since the methods are based on modal superposition. Further work would certainly be required to develop methods for nonlinear problems.

Finally, it should be emphasized that the prediction of material damping is one component in a comprehensive damping model, which is necessary to perform realistic simulations of vibration processes. The methods presented in this thesis should be combined with damping models concerning joint damping effects and acoustic radiation.

# Bibliography

- [1] Verein Deutscher Ingenieure e.V. *Werkstoff- und Bauteildämpfung, Blatt 1-5*. Berlin, August 2004.
- [2] C. W. De Silva. *Vibration Damping, Control, and Design*. Mechanical and Aerospace Engineering Series. CRC Press, 2007. ISBN: 9781420053227.
- [3] BMW Group PressClub, BMW AG. *BMW Gen5 Hochintegrierte E-Antriebs-einheit Schnittmodell*. 2020. URL: <https://www.press.bmwgroup.com/deutschland/photo/compilation/T0338848DE/der-neue-bmw-ix3>.
- [4] Siemens AG, München/Berlin. *Gas turbine rotor in high speed balancing facility*. 2016. URL: <https://press.assets.siemens.com/content/siemens/press/ui/en/search.html#/asset/sid:db400db7-446b-4c2b-91f8-0209e0f7ae7e>.
- [5] V. Forgacs. *Millennium Bridge with St. Paul's Cathedral in the background*. 2019. URL: <https://unsplash.com/photos/xgP7VQ6mRG8>.
- [6] C. T.C. Nguyen. “Micromechanical resonators for oscillators and filters”. In: vol. 1. 1995.
- [7] C. Zener. “Internal Friction in Solids. I. Theory of Internal Friction in Reeds”. In: *Physical Review* 52 (3 1937), pp. 230–235.
- [8] C. Zener, W. Otis, and R. Nuckolls. “Internal friction in solids III. Experimental demonstration of thermoelastic internal friction”. In: *Physical Review* 53.1 (1938), pp. 100–101.
- [9] E. Serra and M. Bonaldi. “A finite element formulation for thermoelastic damping analysis”. In: *International Journal for Numerical Methods in Engineering* 78.6 (2009), pp. 671–691.
- [10] D. Fang, Y. Sun, and A. K. Soh. “Advances in Thermoelastic Damping in Micro- and Nano- Mechanical Resonators: a Review”. In: *Journal of Solid Mechanics and Materials Engineering* 1 (1 2007), pp. 18–34.
- [11] S. McAdams et al. “The psychomechanics of simulated sound sources: Material properties of impacted thin plates”. In: *The Journal of the Acoustical Society of America* 128.3 (2010), pp. 1401–1413.

- [12] C. Guist. “Anforderungen an die Modellqualität im Maschinenbau: Vortrag an der Bauhaus-Universität Weimar”. Weimar, 18.12.2020.
- [13] A. S. Nowick and B. S. Berry. *Anelastic relaxation in crystalline solids*. Vol. 1. Materials science series. New York: Academic Press, 1972. ISBN: 9780125226509.
- [14] B. J. Lazan. *Damping of materials and members in structural mechanics*. Pergamon Press, 1967.
- [15] A. Nowick. “Anelastic Phenomena in Metals and Nonmetallics”. In: *Internal Friction, Damping, and Cyclic Plasticity*. ASTM International, 1965.
- [16] J. L. Snoek. “Effect of small quantities of carbon and nitrogen on the elastic and plastic properties of iron”. In: *Physica* 8.7 (1941), pp. 711–733.
- [17] C. Zener. “Mechanical Behavior of High Damping Metals”. In: *Journal of Applied Physics* 18.11 (1947), pp. 1022–1025.
- [18] C. Zener. *Elasticity and Anelasticity of Metals*. Chicago University Committee on Publications in the Physical Sciences. University of Chicago Press, 1948.
- [19] M.S.Blanter I.S.Golovin H.Neuhauser H.-R.Sinning. *Internal friction in metallic materials*. 2007, p. 83. ISBN: 9783540687573.
- [20] T.-S. Kê. “Stress Relaxation across Grain Boundaries in Metals”. In: *Physical Review* 72.1 (1947), pp. 41–46.
- [21] L. Cremer, M. Heckl, and B. A.T. Petersson. *Structure-borne sound: Structural vibrations and sound radiation at audio frequencies*. Springer Berlin Heidelberg, 2005.
- [22] V. Adams and A. Askenazi. *Building better products with finite element analysis*. 1. ed. Santa Fe, NM: OnWord Press, 1999.
- [23] L Gaul, A Schmidt, and S Bograd. “Experimentelle Ermittlung von Kennwerten zur Werkstoff-und Fügestellendämpfung sowie deren Berücksichtigung in Finite-Elemente-Berechnungen”. In: *Forschungsvereinigung Verbrennungskraftmaschinen (FVV) Heft* 859 (2008).
- [24] C. F. Beards. “The damping of structural vibration by controlled interfacial slip in joints”. In: *Journal of Vibration and Acoustics, Transactions of the ASME* 105.3 (1983).
- [25] A.D. Nashif, D.I.G. Jones, and J.P. Henderson. *Vibration Damping*. Wiley-Interscience publication. Wiley, 1991. ISBN: 9780471867722.
- [26] H. Wentzel. *Modelling of frictional joints in dynamically loaded structures: a review*. KTH Solid mechanics, Royal Institute of technology, 2006.

- 
- [27] R. A. Ibrahim and C. L. Pettit. “Uncertainties and dynamic problems of bolted joints and other fasteners”. In: *Journal of Sound and Vibration* 279 (2005).
- [28] L. Gaul and R. Nitsche. “The role of friction in mechanical joints”. In: *Applied Mechanics Reviews* 54.2 (2001).
- [29] J. Chen et al. “A study of friction microslip modeling for dynamic analysis of bladed discs with root joints”. In: *Proceedings of the Institution of Mechanical Engineers, Part C: Journal of Mechanical Engineering Science* 233.8 (2019).
- [30] A. T. Mathis et al. *A Review of Damping Models for Structures with Mechanical Joints* 1. 2020.
- [31] J. Geisler. *Numerische und experimentelle Untersuchungen zum dynamischen Verhalten von Strukturen mit Fügstellen*. Friedrich-Alexander-Universitaet Erlangen-Nuernberg (Germany), 2010.
- [32] L. Gaul, A. Schmidt, and S. Bograd. “Werkstoff-und Fügstellendämpfung II-Modellierung von Werkstoff-und Fügstellendämpfung in der FEM”. In: *FVV-Abschlussbericht Vorhaben 984* (2011).
- [33] S. Bograd, A. Schmidt, and L. Gaul. “Joint damping prediction by thin layer elements”. In: 2008.
- [34] S. Bograd et al. *Modeling the dynamics of mechanical joints*. 2011.
- [35] A. Schmidt, S. Bograd, and L. Gaul. “Measurement of joint patch properties and their integration into finite-element calculations of assembled structures”. In: *Shock and Vibration* 19 (5 2012).
- [36] M. C. Junger and D. Feit. *Sound, structures, and their interaction*. Second edition. An MIT Press classic. Cambridge, Massachusetts and London, England: The MIT Press, 1986.
- [37] F. Fahy and P. Gardonio. “Sound and Structural Vibration—Radiation, Transmission and Response”. In: *Noise Control Engineering Journal* 55.3 (2007).
- [38] H. M. Westergaard. “Water pressures on dams during earthquakes”. In: *Transactions of the American society of Civil Engineers* 98.2 (1933), pp. 418–433.
- [39] C. Conca, A. Osses, and J. Planchard. “Added mass and damping in fluid-structure interaction”. In: *Computer Methods in Applied Mechanics and Engineering* 146.3-4 (1997).

- [40] D. Yano et al. “Vibration analysis of viscoelastic damping material attached to a cylindrical pipe by added mass and added damping”. In: *Journal of Sound and Vibration* 454 (2019), pp. 14–31.
- [41] A. S. Dehkharghani et al. *A Review of Available Methods for the Assessment of Fluid Added Mass, Damping, and Stiffness with an Emphasis on Hydraulic Turbines*. 2018.
- [42] Z. Zhang and F. Xu. “Added mass and damping effects on vibrating bridge decks in still air”. In: *Journal of Wind Engineering and Industrial Aerodynamics* 191 (2019), pp. 227–238.
- [43] G. R. Sinambari. *Ingenieurakustik: Physikalische Grundlagen und Anwendungsbeispiele*. 5th ed. Wiesbaden: Springer Fachmedien Wiesbaden GmbH, 2014.
- [44] Stephen A. Hambric, Shung H. Sung, and D. J. Nefske, eds. *Engineering vibroacoustic analysis: Methods and applications*. Chichester, West Sussex, United Kingdom: John Wiley & Sons Inc, 2016.
- [45] Kirkup. “The Boundary Element Method in Acoustics: A Survey”. In: *Applied Sciences* 9.8 (2019), p. 1642.
- [46] S. Marburg. “Boundary Element Method for Time-Harmonic Acoustic Problems”. In: *Computational Acoustics*. Ed. by Manfred Kaltenbacher. Vol. 579. CISM International Centre for Mechanical Sciences Ser. Cham: Springer International Publishing, 2017, pp. 69–158.
- [47] A. K. Chopra. *Dynamics of Structure eBook, Global Edition*. Pearson Education, 2016.
- [48] C. Petersen. *Dynamik der Baukonstruktionen*. Vieweg+Teubner Verlag, 2000. ISBN: 9783528081232.
- [49] R.W. Clough and J. Penzien. *Dynamics of Structures*. McGraw-Hill, 1993.
- [50] D. Inman. “DAMPING MODELS”. In: *Encyclopedia of Vibration*. Ed. by S. Braun. Oxford: Elsevier, 2001, pp. 335–342.
- [51] J.W.S. Rayleigh. *The theory of sound*. The theory of sound Bd. 1. 1877.
- [52] A. L. Kimball and D. E. Lovell. “Internal Friction in Solids”. In: *Phys. Rev.* 30 (6 1927), pp. 948–959.
- [53] T. Theodorsen and I.E. Garrick. *Mechanism of Flutter: A Theoretical and Experimental Investigation of the Flutter Problem*. NACA R-685. U.S. Government Printing Office, 1940.
- [54] R.E.D. Bishop and D.C. Johnson. *The Mechanics of Vibration*. University Press, 1960.

- 
- [55] W. W. Soroka. “Note on the Relations Between Viscous and Structural Damping Coefficients”. In: *Journal of the Aeronautical Sciences* 16 (1949), pp. 409–410.
- [56] T. K. Caughey. “Vibration of dynamic systems with linear hysteretic damping”. In: *Proceedings of the Fourth US National Congress of Applied Mechanics*. 1962, pp. 87–98.
- [57] T. J. Reid. “Free Vibration and Hysteretic Damping”. In: *Aeronautical Journal* 60 (1956), pp. 283–283.
- [58] R. W. Clough and J. Penzien. *Dynamics of Structures*. McGraw-Hill, 1993.
- [59] M. A. Biot. “Thermoelasticity and irreversible thermodynamics”. In: *Journal of Applied Physics* 27.3 (1956), pp. 240–253.
- [60] W. Nowacki. *Thermoelasticity*. Vol. 3. International series of monographs in aeronautics and astronautics. Division 1: Solid and Structural Mechanics. Addison-Wesley Publishing Company, 1962.
- [61] W. Nowacki. “Problems of thermoelasticity”. In: *Progress in Aerospace Sciences* (1970).
- [62] H. Parkus. *Thermoelasticity*. 2nd ed. Vienna: Springer Wien, 1976.
- [63] E. B. Tadmor, R. E. Miller, and R. S. Elliott. *Continuum mechanics and thermodynamics: From fundamental concepts to governing equations*. Reprinted with corr. Cambridge: Cambridge University Press, 2013.
- [64] W. Nowacki. “Basic Relations and Equations of Thermoelasticity”. In: *Thermoelasticity* 15 (1986), pp. 1–67.
- [65] C. Zener. “Internal friction in solids II. General theory of thermoelastic internal friction”. In: *Physical Review* 53.1 (1938), pp. 90–99.
- [66] P. Chadwick. “On the propagation of thermoelastic disturbances in thin plates and rods”. In: *Journal of the Mechanics and Physics of Solids* 10.2 (1962), pp. 99–109.
- [67] P. Chadwick et al. “Thermoelasticity. The dynamical theory”. In: *Progress in solid mechanics* 1 (1960), pp. 263–328.
- [68] P. Chadwick. “Thermal damping of a vibrating elastic body”. In: *Mathematika* 9.1 (1962), pp. 38–48.
- [69] J. B. Alblas. “On the general theory of thermo-elastic friction”. In: *Applied Scientific Research* 10.1 (1961), pp. 349–362.
- [70] J. B. Alblas. “A NOTE ON THE THEORY OF THERMOELASTIC DAMPING”. In: *Journal of Thermal Stresses* 4.3-4 (1981), pp. 333–355.
-

- [71] R. Lifshitz and M. L. Roukes. “Thermoelastic damping in micro- and nanomechanical systems”. In: *Physical Review B* 61 (8 2000), pp. 5600–5609.
- [72] F. L. Guo and G. A. Rogerson. “Thermoelastic coupling effect on a micro-machined beam resonator”. In: *Mechanics Research Communications* 30.6 (2003).
- [73] Y. Sun, D. Fang, and A. K. Soh. “Thermoelastic damping in micro-beam resonators”. In: *International Journal of Solids and Structures* 43.10 (2006), pp. 3213–3229.
- [74] W. Zuo et al. “Thermoelastic damping in asymmetric three-layered microbeam resonators”. In: *Journal of Applied Mechanics, Transactions ASME* 83.6 (2016).
- [75] L. Yang et al. “Thermoelastic damping in bilayer microbeam resonators with two-dimensional heat conduction”. In: *International Journal of Mechanical Sciences* 167 (2020).
- [76] Y. Fu, L. Li, and Y. Hu. “Enlarging quality factor in microbeam resonators by topology optimization”. In: *Journal of Thermal Stresses* 42.3 (2019).
- [77] Y. Fang et al. “Thermoelastic damping in flexural vibration of bilayered microbeams with circular cross-section”. In: *Applied Mathematical Modelling* 77 (2020).
- [78] Z. Hao and F. Ayazi. “Thermoelastic damping in flexural-mode ring gyroscopes”. In: *American Society of Mechanical Engineers, Micro-Electro Mechanical Systems Division, (Publications) MEMS*. Vol. 7 MEMS. 2005, pp. 335–343.
- [79] S.J. Wong, C.H.J. Fox, and S. McWilliam. “Thermoelastic damping of the in-plane vibration of thin silicon rings”. In: *Journal of Sound and Vibration* 293.1-2 (2006), pp. 266–285.
- [80] S. T. Hossain, S. McWilliam, and A. A. Popov. “An investigation on thermoelastic damping of high-Q ring resonators”. In: *International Journal of Mechanical Sciences* 106 (2016), pp. 209–219.
- [81] G. Cagnoli and P. A. Willems. “Effects of nonlinear thermoelastic damping in highly stressed fibers”. In: *Physical Review B - Condensed Matter and Materials Physics* 65.17 (2002).
- [82] R. Haddadzadeh Hendou and A. Karami Mohammadi. “Transient analysis of nonlinear Euler-Bernoulli micro-beam with thermoelastic damping, via nonlinear normal modes”. In: *Journal of Sound and Vibration* 333.23 (2014), pp. 6224–6236.

- 
- [83] S. Salajeghe, S. E. Khadem, and M. Rasekh. “Nonlinear analysis of thermoelastic damping in axisymmetric vibration of micro circular thin-plate resonators”. In: *Applied Mathematical Modelling* 36.12 (2012), pp. 5991–6000.
- [84] S. B. Kim and J. H. Kim. “Quality factors for the nano-mechanical tubes with thermoelastic damping and initial stress”. In: *Journal of Sound and Vibration* 330.7 (2011).
- [85] A. S. Vahdat and G. Rezazadeh. “Effects of axial and residual stresses on thermoelastic damping in capacitive micro-beam resonators”. In: *Journal of the Franklin Institute* 348.4 (2011), pp. 622–639.
- [86] S. K. De and N. R. Aluru. “Theory of thermoelastic damping in electrostatically actuated microstructures”. In: *Physical Review B - Condensed Matter and Materials Physics* 74.14 (2006).
- [87] R. C. Shieh. “Thermoelastic vibration and damping for circular timoshenko beams”. In: *Journal of Applied Mechanics, Transactions ASME* 42.2 (1975).
- [88] R. C. Shieh. “Eigensolutions for coupled thermoelastic vibrations of timoshenko beams”. In: *Journal of Applied Mechanics, Transactions ASME* 46.1 (1979).
- [89] D. V. Parayil, S. S. Kulkarni, and D. N. Pawaskar. “Analytical and numerical solutions for thick beams with thermoelastic damping”. In: *International Journal of Mechanical Sciences* 94-95 (2015), pp. 10–19.
- [90] L. D. Landau, E. M. Lifshitz, et al. *Theory of elasticity*. Vol. 7. 3. Pergamon Press, Oxford New York, 1986.
- [91] I. N. Bronstein et al. *Taschenbuch der Mathematik*. Ed. by überarbeitete und erweiterte Auflage 5. Frankfurt am Main: Verlag Harri Deutsch, 2001.
- [92] V. K. Kinra and K. B. Milligan. “A Second-Law Analysis of Thermoelastic Damping”. In: *Journal of Applied Mechanics* 61.1 (1994), p. 71.
- [93] J. E. Bishop and V. K. Kinra. “Some improvements in the flexural damping measurement technique”. In: *ASTM Special Technical Publication*. 1169. Publ by ASTM, 1992, pp. 457–470.
- [94] J. E. Bishop and V. K. Kinra. “Elastothermodynamic damping in laminated composites”. In: *International Journal of Solids and Structures* 34.9 (1997), pp. 1075–1092.
- [95] A. Duwel et al. “Engineering MEMS resonators with low thermoelastic damping”. In: *Journal of Microelectromechanical Systems* (2006).
- [96] S. A. Chandorkar et al. “Multimode thermoelastic dissipation”. In: *Journal of Applied Physics* (2009).
-

- [97] Z. Hao. “Thermoelastic damping in the contour-mode vibrations of micro- and nano-electromechanical circular thin-plate resonators”. In: *Journal of Sound and Vibration* 313.1-2 (2008), pp. 77–96.
- [98] Z. Hao, Y. Xu, and S. K. Durgam. “A thermal-energy method for calculating thermoelastic damping in micromechanical resonators”. In: *Journal of Sound and Vibration* 322.4-5 (2009), pp. 870–882.
- [99] Y. Tai, P. Li, and W. Zuo. “An entropy based analytical model for thermoelastic damping in micromechanical resonators”. In: vol. 159. Trans Tech Publications Ltd, 2012, pp. 46–50.
- [100] Y. Tai and P. Li. “An analytical model for thermoelastic damping in microresonators based on entropy generation”. In: *Journal of Vibration and Acoustics, Transactions of the ASME* 136.3 (2014).
- [101] Y. Tai et al. “Entropy generation and thermoelastic damping in the In-plane vibration of microring resonators”. In: *Entropy* 21.7 (2019), p. 631.
- [102] J. Ignaczak and W. Nowacki. “The plane dynamic problem of thermoelasticity”. In: *Proc. Vibr. Probl.* Vol. 4. 1961, p. 2.
- [103] J. Ignaczak and W. Nowacki. “Transversal vibration of a plate, produced by heating”. In: *Archiwum Mechaniki Stosowanej* 13 (1961), pp. 651–667.
- [104] J.E. Lagnese and J.-L. Lions. *Modelling Analysis and Control of Thin Plates*. Vol. 1. Edition. Springer, 1989, pp. 25–40.
- [105] J. E. Muñoz Rivera and Y. Shibata. “A linear thermoelastic plate equation with Dirichlet boundary condition”. In: *Mathematical Methods in the Applied Sciences* 20.11 (1997).
- [106] Z. Y. Liu and M. Renardy. “A note on the equations of a thermoelastic plate”. In: *Applied Mathematics Letters* 8.3 (1995).
- [107] C. D’Apice. “Convexity considerations and spatial behavior for the harmonic vibrations in thermoelastic plates”. In: *Journal of Mathematical Analysis and Applications* 312.1 (2005).
- [108] J. U. Kim. “On the Energy Decay of a Linear Thermoelastic Bar and Plate”. In: *SIAM Journal on Mathematical Analysis* 23.4 (1992), pp. 889–899.
- [109] Y. Enomoto. “On a thermoelastic plate equation in an exterior domain”. In: *Mathematical Methods in the Applied Sciences* 25.6 (2002).
- [110] J. G. Simmonds. *Major Simplifications in a current linear model for the motion of a thermoelastic plate*. Tech. rep. 4. 1999, pp. 673–679.

- 
- [111] A. Norris and D.M. Photiadis. “Thermoelastic relaxation in elastic structures, with applications to thin plates”. In: *Quarterly Journal of Mechanics and Applied Mathematics* 58.1 (2005), pp. 143–163.
- [112] A. Norris. “Dynamics of thermoelastic thin plates: A comparison of four theories”. In: *Journal of Thermal Stresses* 29.2 (2006), pp. 169–195.
- [113] B. H. Houston et al. “Thermoelastic loss in microscale oscillators”. In: *Applied Physics Letters* 80.7 (2002), pp. 1300–1302.
- [114] B. H. Houston et al. “Loss due to transverse thermoelastic currents in microscale resonators”. In: *Materials Science and Engineering A* 370.1-2 (2004), pp. 407–411.
- [115] D. M. Photiadis et al. “Thermoelastic loss observed in a high Q mechanical oscillator”. In: *Physica B: Condensed Matter* 316-317 (2002), pp. 408–410.
- [116] A. H. Nayfeh and M. I. Younis. “Modeling and simulations of thermoelastic damping in microplates”. In: *Journal of Micromechanics and Microengineering* (2004).
- [117] Y. Sun and H. Tohmyoh. “Thermoelastic damping of the axisymmetric vibration of circular plate resonators”. In: *Journal of Sound and Vibration* (2009).
- [118] Y. Sun and M. Saka. “Thermoelastic damping in micro-scale circular plate resonators”. In: *Journal of Sound and Vibration* 329.3 (2010), pp. 328–337.
- [119] P. Li, Y. Fang, and R. Hu. “Thermoelastic damping in rectangular and circular microplate resonators”. In: *Journal of Sound and Vibration* 331.3 (2012), pp. 721–733.
- [120] Y.-P. Tai, P. Li, and W.-L. Zuo. “Thermoelastic damping in MEMS torsion resonators in consideration of coupling effect between torsion and bending”. In: *Zhendong yu Chongji/Journal of Vibration and Shock* (2014).
- [121] T. H. Metcalf et al. “Thermoelastic damping in micromechanical resonators”. In: *Applied Physics Letters* 95.6 (2009), p. 61903.
- [122] G. Cagnoli et al. “Mode-dependent mechanical losses in disc resonators”. In: *Physics Letters, Section A: General, Atomic and Solid State Physics* 382.33 (2018), pp. 2165–2173.
- [123] D.W. Nicholson. *Finite Element Analysis: Thermomechanics of Solids*. CRC Press, 2003.
- [124] M. R. Eslami et al. *Theory of Elasticity and Thermal Stresses: Explanations, Problems and Solutions*. Solid Mechanics and Its Applications. Springer Netherlands, 2013.
-

- [125] S. Appel and J. Wijker. “Structural Modelling for Thermoelastic Analysis”. In: *Springer Aerospace Technology*. 2022.
- [126] J. H. Choi and I. Lee. “Finite element analysis of transient thermoelastic behaviors in disk brakes”. In: *Wear* 257.1-2 (2004).
- [127] K.-J. Bathe. *Finite element procedures*. Prentice Hall, Pearson Education, Inc., 2006.
- [128] O. C. Zienkiewicz, R. L. Taylor, and J. Z. Zhu. *The finite element method: its basis and fundamentals*. Elsevier, 2005.
- [129] T. J. R. Hughes. *The Finite Element Method*. Prentice-Hall, 1987.
- [130] R. De Borst et al. *Nonlinear finite element analysis of solids and structures*. John Wiley & Sons, 2012.
- [131] Inc. ANSYS. *Ansys Mechanical APDL, Release 2021 R2, Theory Reference*. United States, July 2021.
- [132] Dassault Systèmes. *ABAQUS/Standard User’s Manual, Version 2020*. English. United States: Dassault Systèmes Simulia Corp, 2020.
- [133] Nathan M Newmark. “A method of computation for structural dynamics”. In: *Journal of the engineering mechanics division* 85.3 (1959), pp. 67–94.
- [134] H. M. Hilber, T. J. R. Hughes, and R. L. Taylor. “Improved numerical dissipation for time integration algorithms in structural dynamics”. In: *Earthquake Engineering & Structural Dynamics* 5.3 (1977), pp. 283–292.
- [135] C. Petersen. *Dynamik der Baukonstruktionen*. Vieweg+Teubner Verlag, 2013.
- [136] GLEICH Aluminium GmbH. *Technisches Datenblatt: G.AL Formenbauplatten, G.AL C210R*. 2019. URL: <https://gleich.de/wp-content/uploads/2020/11/produktdatenblatt-g-al-c210r-gesaegte-aluminium-gussplatte.pdf>.
- [137] BMW Group PressClub, BMW AG. *BMW 3er Coupé Hinterachse*. 2006. URL: <https://www.press.bmwgroup.com/deutschland/photo/detail/P0024478/bmw-3er-coup-hinterachse-05/2006>.
- [138] K. Rötger, H. ; Bennewitz. “Ueber die innere Reibung fester Körper; Absorptionsfrequenzen von Metallen im akustischen Gebiet”. In: *Physikalische Zeitschrift* 37.16 (1936).
- [139] C. Zener. “Internal friction in solids”. In: *Proceedings of the Physical Society* 52.1 (1940).
- [140] W. E. Baker, W. E. Woolam, and D. Young. “Air and internal damping of thin cantilever beams”. In: *International Journal of Mechanical Sciences* (1967).

- 
- [141] N. Granick and J. E. Stern. *Material Damping of Aluminum by a Resonant-Dwell Technique*. Tech. rep. NATIONAL AERONAUTICS and SPACE ADMINISTRATION GREENBELT MD GODDARD SPACE . . . , 1965.
- [142] P. Gudmundson and C. Wüthrich. “Die Werkstoffdämpfung von Stählen bei hohen Dehnungsamplituden”. In: *Materialwissenschaft und Werkstofftechnik* 17.8 (1986).
- [143] R. F. Gibson and R. Plunkett. “A forced-vibration technique for measurement of material damping - Internal damping of beam specimens in resonant flexural vibration is found from measurements of input acceleration and resulting specimen-bending strain”. In: *Experimental Mechanics* 17.8 (1977).
- [144] R. A. Buser and N. F. de Rooij. “Resonant silicon structures”. In: *Sensors and Actuators* 17.1-2 (1989).
- [145] T. V. Roszhart. “The effect of thermoelastic internal friction on the Q of micromachined silicon resonators”. In: *Technical Digest, 1990 Solid-State Sensor and Actuator Workshop*. 1990, pp. 13–16.
- [146] K. Y. Yasumura et al. “Quality Factors in Micron- and Submicron-Thick Cantilevers”. In: *Journal of Microelectromechanical Systems* 9.1 (2000), pp. 117–125.
- [147] R. N. Candler et al. “Investigation of energy loss mechanisms in micromechanical resonators”. In: *TRANSDUCERS 2003 - 12th International Conference on Solid-State Sensors, Actuators and Microsystems, Digest of Technical Papers*. 2003.
- [148] R. N. Candler et al. “Impact of geometry on thermoelastic dissipation in micromechanical resonant beams”. In: *Journal of Microelectromechanical Systems* (2006).
- [149] R. Abdolvand et al. “Thermoelastic damping in trench-refilled polysilicon resonators”. In: *TRANSDUCERS 2003 - 12th International Conference on Solid-State Sensors, Actuators and Microsystems, Digest of Technical Papers*. Vol. 1. 2003.
- [150] R. Abdolvand et al. “Quality factor in trench-refilled polysilicon beam resonators”. In: *Journal of Microelectromechanical Systems* 15.3 (2006).
- [151] C. Muller et al. “Experimental evidence of thermoelastic damping in silicon tuning fork”. In: *Procedia Chemistry*. Vol. 1. 1. 2009.
- [152] E. Cesarini et al. “A “gentle” nodal suspension for measurements of the acoustic attenuation in materials”. In: *Review of Scientific Instruments* 80.5 (2009), p. 053904.
-

- [153] A. V. Dmitriev, D. S. Gritsenko, and V. P. Mitrofanov. “Non-axisymmetric flexural vibrations of free-edge circular silicon wafers”. In: *Physics Letters, Section A: General, Atomic and Solid State Physics* 378.9 (2014).
- [154] C. Gibert et al. “Modal tests and analysis of a radial impeller at rest: Influence of surrounding air on damping”. In: *Proceedings of the ASME Turbo Expo*. Vol. 7. PARTS A AND B. 2012.
- [155] O. P. Hentschel et al. “Analysis of an experimental setup for structural damping identification”. In: *Journal of Theoretical and Applied Mechanics (Poland)* 54.1 (2016), pp. 27–39.
- [156] Polytec. *Portable Digital Vibrometer PDV-100, User Manual*. Ed. by Polytec GmbH. Waldbronn, Germany, 2009.
- [157] H.-E. Albrecht et al. *Laser Doppler and Phase Doppler Measurement Techniques*. 2003.
- [158] E. P. Tomasini. *Laser Doppler Vibrometry: A Multimedia Guide to Its Features and Usage*. Berlin, Heidelberg: Springer Berlin / Heidelberg, 2020.
- [159] M. Meyer. *Signalverarbeitung: Analoge und digitale Signale, Systeme und Filter*. 9., korrigierte Auflage. Springer eBook Collection. Wiesbaden: Springer Vieweg, 2021. ISBN: 9783658328016.
- [160] J. M. Giron-Sierra. *Signals and Data, Filtering, Non-stationary Signals, Modulation*. Softcover reprint of the hardcover 1st edition 2016. Vol. volume 1. Signals and Communication Technology. Singapore: Springer, 2017. ISBN: 9811096422.
- [161] D. G. Stephens. *Investigation of air damping of circular and rectangular plates, a cylinder, and a sphere*. Washington, D.C.: National Aeronautics and Space Administration, 1965.
- [162] M. Wesolowski and E. Barkanov. “Air damping influence on dynamic parameters of laminated composite plates”. In: *Measurement: Journal of the International Measurement Confederation* 85 (2016).
- [163] B. D. Coleman and W. Noll. “Erratum: Foundations of linear viscoelasticity”. In: *Reviews of Modern Physics* 36.4 (1961), p. 1103.
- [164] B. D. Coleman and W. Noll. “The thermodynamics of elastic materials with heat conduction and viscosity”. In: *Archive for Rational Mechanics and Analysis* 13.1 (1963), pp. 167–178.
- [165] B. D. Coleman and V. J. Mizel. “Existence of caloric equations of state in thermodynamics”. In: *The Journal of Chemical Physics* 40.4 (1964), pp. 1116–1125.

- 
- [166] G. Hütter. “Coleman-Noll Procedure for Classical and Generalized Continuum Theories”. In: *Encyclopedia of Continuum Mechanics*. Springer, Berlin, Heidelberg, 2020, pp. 316–323.
- [167] W. Thomson. “On the Dynamical Theory of Heat, with numerical results deduced from Mr Joule’s Equivalent of a Thermal Unit, and M. Regnault’s Observations on Steam”. In: *Transactions of the Royal Society of Edinburgh* 20.2 (1853), 261–288.
- [168] A. Logg, K.-A. Mardal, and G. Wells. *Automated solution of differential equations by the finite element method: The FEniCS book*. Vol. 84. Springer Science & Business Media, 2012.
- [169] L. Zoghaib and P. O. Mattei. “Damping analysis of a free aluminum plate”. In: *JVC/Journal of Vibration and Control* 21.11 (2015), pp. 2083–2098.
- [170] C. Guist. “Verfahren zur Ermittlung der Dämpfung eines Bauteils”. Pat. DE 10 2015 214 437. 2017.
- [171] M. Bischoff. “Finite Elements for Plates and Shells”. In: *Encyclopedia of Continuum Mechanics* (2020), pp. 898–920.
- [172] K.-J. Bathe, M. L. Bucalem, and F. Brezzi. “Displacement and stress convergence of our MITC plate bending elements”. In: *Engineering Computations* (1990).
- [173] E. N Dvorkin and K.-J. Bathe. “A continuum mechanics based four-node shell element for general non-linear analysis”. In: *Engineering computations* (1984).
- [174] J. C. Simo and M. S. Rifai. “A class of mixed assumed strain methods and the method of incompatible modes”. In: *International Journal for Numerical Methods in Engineering* 29.8 (1990), pp. 1595–1638.
- [175] U. Andelfinger and E. Ramm. “EAS-elements for two-dimensional, three-dimensional, plate and shell structures and their equivalence to HR-elements”. In: *International Journal for Numerical Methods in Engineering* 36.8 (1993), pp. 1311–1337.
- [176] B. S. Berry. “Precise investigation of the theory of damping by transverse thermal currents”. In: *Journal of Applied Physics* 26.10 (1955).
- [177] T. L. Attard, L. He, and H. Zhou. “Improving damping property of carbon-fiber reinforced epoxy composite through novel hybrid epoxy-polyurea interfacial reaction”. In: *Composites Part B: Engineering* 164 (2019).
-

- [178] Z. Xu et al. “Additive manufacturing of two-phase lightweight, stiff and high damping carbon fiber reinforced polymer microlattices”. In: *Additive Manufacturing* 32 (2020).
- [179] M. J. Le Guen et al. “The damping-modulus relationship in flax-carbon fibre hybrid composites”. In: *Composites Part B: Engineering* 89 (2016).
- [180] L. Ma et al. “Modal characteristics and damping enhancement of carbon fiber composite auxetic double-arrow corrugated sandwich panels”. In: *Composite Structures* 203 (2018).
- [181] H. Li et al. “Modeling of amplitude-dependent damping characteristics of fiber reinforced composite thin plate”. In: *Applied Mathematical Modelling* 80 (2020).

# Appendix A

## Measurement and Excitation Schemes of the Components

## A.1 Rectangular Plate

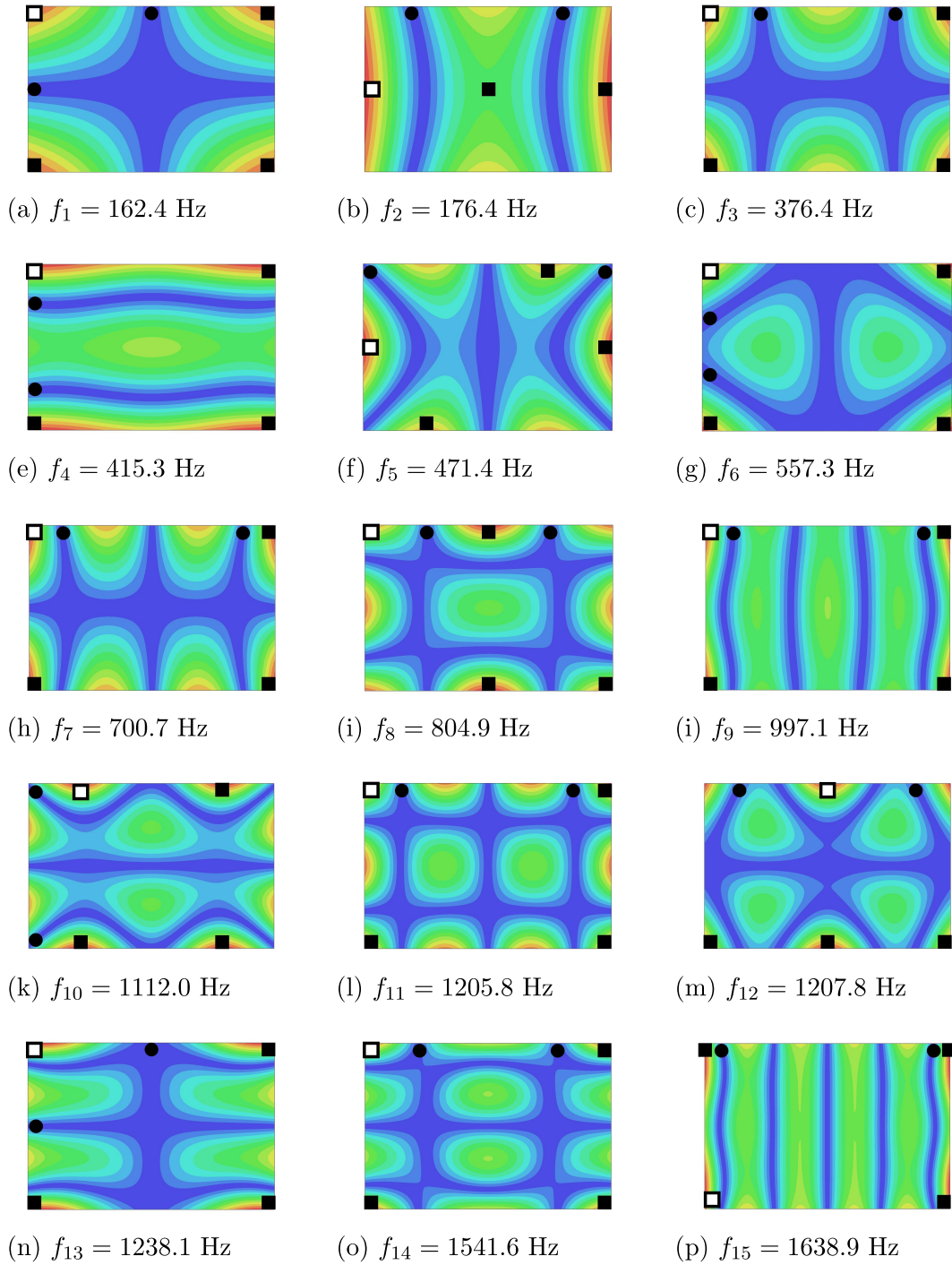


**Figure A.1:** Measurement schemes for the eigenmodes of the rectangular plate. The locations for the suspension (●) are in the nodal lines. The excitation (◻) and measurement (◼) points are at the locations with high deflections.

## A.2 Protection Plate

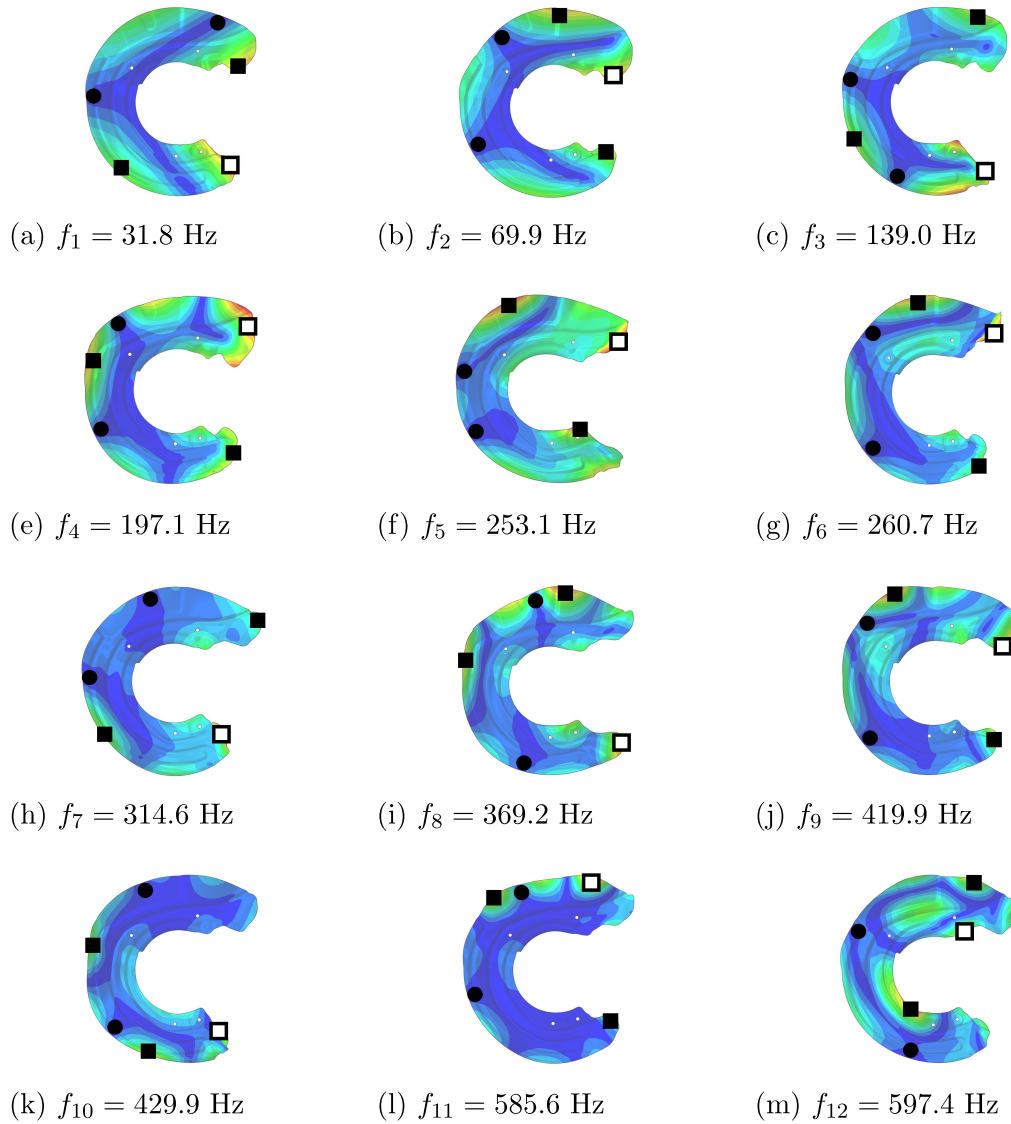


**Figure A.2:** Measurement schemes for the eigenmodes of the protection plate. The locations for the suspension (●) are in the nodal lines. The excitation (◻) and measurement (◼) points are at the locations with high deflections.

### A.3 Gearbox Casing

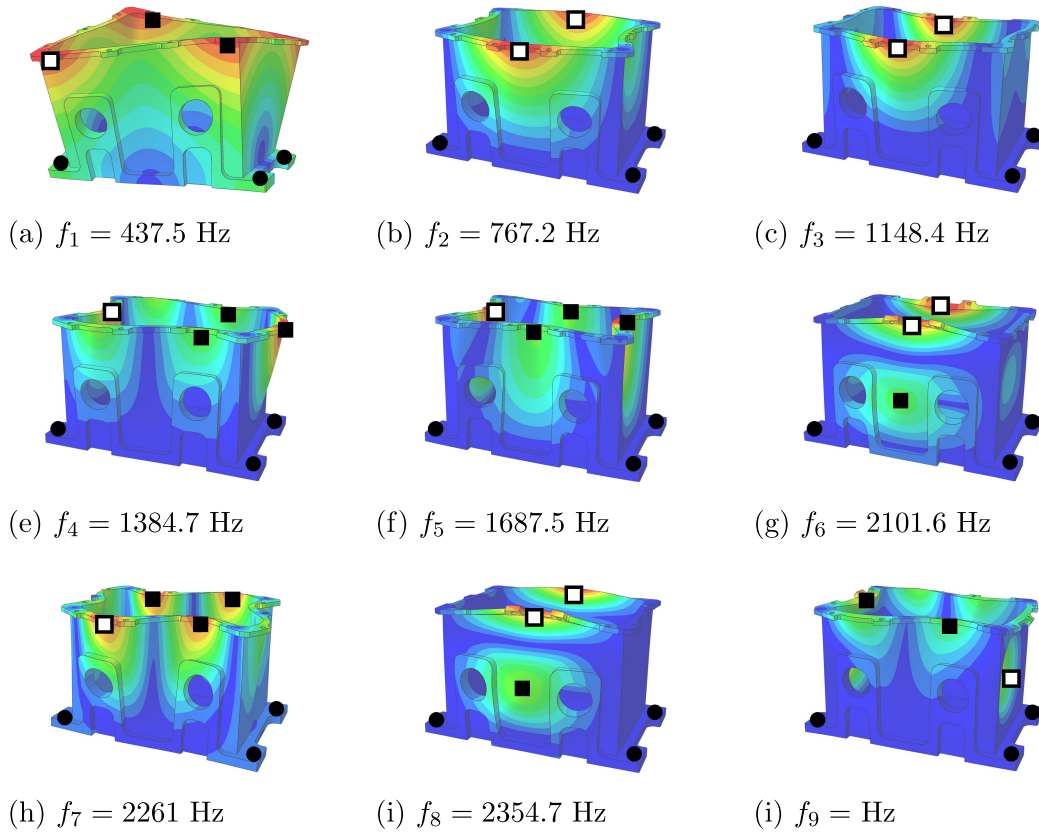


**Figure A.3:** Measurement schemes for the eigenmodes of the gearbox casing. The locations for the suspension (●) are in the nodal lines. The excitation (□) and measurement (■) points are at the locations with high deflections.

# Publications by the Author

## Peer-Reviewed Journal Paper

Zacharias, C.; Könke, C.; Guist, C. (2022): A New Efficient Approach to Simulate Material Damping in Metals by Modeling Thermoelastic Coupling. In: *Materials* 15 (5), S. 1706. DOI: 10.3390/ma15051706.

## Conference Proceedings and Contributions

Zacharias, C.; Könke, C.; Guist, C. (2021): Thermoelastic Modeling Concepts for Material Damping in two and three-dimensional Elements. In: *Proceedings of the 27th International Congress on Sound and Vibration, ICSV27*, 11-16 July 2021. Gliwice: Silesian University Press.

Zacharias, C.; Könke, C.; Guist, C. (2019): Simplified approaches in the modelling of thermoelastic damping. *ECCOMAS Young Investigators Conference (YIC2019)*. Krakau, 05.09.2019.

Zacharias, C.; Könke, C. (2018): Experimental and Numerical Studies on Material and Joint Damping. (Posterbeitrag). *Thüringer Werkstofftag 2018*. Weimar.

Zacharias, C., and Könke, C. (2017): Experimental and Numerical Studies of Thermoelastic Damping. In: *Proceedings of the 7th GACM Colloquium on Computational Mechanics for Young Scientists from Academia and Industry*.